UNIVERSITÀ DEGLI STUDI DI TRIESTE

XXXIII CICLO DEL DOTTORATO DI RICERCA IN

SCIENZE DELLA TERRA, FLUIDODINAMICA E MATEMATICA.
INTERAZIONI E METODICHE

Finanziatore del progetto: ICTP - International Centre for Theoretical Physics

Use of the Regional Climate Model RegCM4 to assess circulation, precipitation and temperature patterns sustaining the Tagliamento glacier (southeastern Alps) at 21 ka.

Settore scientifico-disciplinare: **GEO/12**

DOTTORANDA
Costanza Del Gobbo Costanza Del Gobbo

COORDINATORE
Prof. Stefano Maset Stefano Maset

SUPERVISORE DI TESI
Dr. Filippo Giorgi Filippo Giorgi

CO-SUPERVISORE DI TESI
Dr. Renato R. Colucci

ANNO ACCADEMICO 2019/2020

To the brave women
and wise men of my family

Abstract

The Last Glacial Maximum (LGM) is a global event that occurred 26 to 21 ka BP. It was characterised by the expansion of ice sheets, mountain glaciers, permafrost and sea ice and was associated with a mean sea level drop of about 120 m. The environment was deeply modified by decreased temperature (3 to 6 °C globally) and different precipitation regimes compared with today's conditions. In the southeastern Alps, the Tagliamento glacier expanded into the Friuli plane with a piedmont lobe, which was one of the most representative piedmont lobes in the southern Alps. Evidence of this event is today recognisable from the large set of well-preserved moraines released by the major glacier advances.
Mountain glaciers are inherently sensitive to changes in climate conditions and are strongly affected by temperature and precipitation variations. Due to this factor glaciers are considered crucial climate indicators both on the local and on the global scale and for short as well as long time periods. For the Tagliamento glacier during the LGM, the physical processes leading to its extension and mass balance are not yet fully understood. Contributions likely derive from reduced snowmelt and evaporation related to lower temperature, changes in regional circulations leading to increased precipitation (e.g. enhanced southerly flow impinging over the Alps) or increased convection especially during the transition seasons. Disentangling these contributions is thus important for a full understanding of the dynamics of the glacier.

The low elevation and relatively small accumulation basin of the Tagliamento glacier make it an ideal case study for the application of a high-resolution regional climate model, which can provide climate information at fine spatial scales. Therefore this thesis combines a high-resolution regional climate model (RCM), the ICTP RegCM4 model system, with LGM topography, vegetation and glacier morphology reconstructed from paleoclimate proxies. The primary aim of the thesis is to improve our knowledge about the atmospheric circulation and thermodynamic conditions that sustained the Tagliamento glacier at the LGM, with particular attention to changes in precipitation patterns. A multiple nesting approach is adopted, with the RegCM4 run at high spatial resolution (12 km) over a greater Alpine domain, with boundary conditions from an intermediate resolution (50 km) RegCM4 simulation, itself driven by the PMIP3/CMIP5 compliant Earth system model developed by the Max Planck Institute for Meteorology (MPI-ESM-P). Two 20-year long simulations are conducted and inter-compared, one for the climate state at the LGM standard (21 ka BP) and one for pre-industrial conditions. In order to validate and customise the RegCM4 simulation, an experiment forced with ERA-Interim observations reanalysis data is performed and compared with observational precipitation and temperature datasets. For the LGM simulation orbital parameters and greenhouse gas concentrations are set at the LGM values. It is stressed that this is one of the few applications of RCMs to paleoclimate studies today.

The results show that RegCM4 at 12 km of resolution is able to capture the seasonality and spatial variability of the atmospheric circulation patterns which were responsible for the development and maintenance of the main glaciers in the southeastern Alps, Apennines and Balkans at the LGM, with simulated climate fields compatible with available proxies and other model reconstructions. LGM temperatures are simulated to be about 6.6 °C lower than at pre-industrial times, with drier conditions over the study domain, especially north of the alpine chain, and with the southern alpine region relatively wetter than the northern alpine foreland due to increasing southerly moist flow. Stratiform and convective precipitation contributed to feed the Tagliamento glacier, with the predominance of convective phenomena from late spring to early autumn, while during the rest of the year southerly and westerly stratiform precipitation prevailed, as originated from a cyclonic circulation. In the southeastern Alps, summer precipitation often occurred as snowfall, limiting extensive melting phenomena, and in general precipitation (both liquid and solid) was higher than in the whole alpine chain. These conditions favoured the development of a large piedmont glacier in a southerly exposed, low elevation basin.

This project represents a step forward in the framework of paleoclimate studies, adding new high-resolution quantitative information about the atmospheric circulation feeding glacier formation at the LGM and paving the way for several future developments.

Acknowledgements

First of all, I would like to thank my supervisors. So, thank you, Filippo and Roberto, for your support, your patience and your knowledge during these three (and a bit more) unconventional PhD years. In particular thank you, Roberto, for coming up with the idea of the *Colucci Mechanism*, that led to this PhD and thank you, Filippo, for believing in me for this project.
This work would not have been possible without the help of Johann Jungclaus from the Max Plank Institute for Meteorology, who provided the MPI-ESM-P data, fundamental to force our RCM simulations.
I wish to thank the ICTP and its people, for having been a safe place and a kind company. You all represent a unique heterogeneous mix where I always felt confident and at home.
In particular, my sincere thanks to Graziano, for the (many) hours spent fixing my codes and figuring out how to adapt RegCM for my work. Without your help, I wouldn't have even started my simulations! Thank you also to Johannes who with incredible kindness never hang up my calls, all the times my computer crashed.
Thanks to my personal computer that surprisingly survived these last eleven months of home-working. Now you can rest a bit.

My most sincere gratitude goes to Marco and Adriano who have always been present for the last three years. Thank you, Adriano, for your almost continuous work as a personal scientific and IT consultant and for being a really good friend! You've brought the mountains a little closer with our talks about mountaineering, climbing, hiking and now also skiing. Obviously, huge thank you to Anna and Sofia for having been patient for all the hours Adriano spent reading my thesis.
Words are not enough to express the loving support that Marco has given me since we started our journey together. With the years things change and we grow, and you are always here with me. Thanks for the past and future adventures which I am sure we will share!

Author's note

This thesis is available with high-resolution images and hyperlinks at `http://users.ictp.it/~cdel_gob/PhD_thesis/PhD_thesis_final.pdf` or by requesting it to costanza.delgobbo@gmail.com.

Contents

Chapter 1

Introduction

1.1 Project Objectives and Overview

This project aims at improving the understanding of the main mechanisms and scale interactions that led to the formation and maintenance of the Tagliamento glacier, in the southeastern Alps, during the Last Glacial Maximum (LGM, 26 to 19 ka BP; Clark et al., 2009; Hughes et al., 2013), with particular attention to precipitation patterns. The project follows a modelling approach based on the use of the International Centre for Theoretical Physics (ICTP) Regional Climate Model RegCM4.7 (Giorgi et al., 2012).

One of the most significant challenges in climate modelling is to reduce the uncertainties related to precipitation patterns, especially at smaller scales (Kirtman et al., 2013). In this project, we study the area of the Julian Alps, which is one of the wettest regions in Europe (Isotta et al., 2014). Here a small number of glaciers, characterised by small accumulation basins, still survive at low altitudes due to high accumulation rates (Colucci, 2016; Colucci and Žebre, 2016).
Within the international climate monitoring programmes, mountain glaciers changes are considered as high-confidence climate indicators (Colucci and Guglielmin, 2015; Haeberli et al., 2007). In particular, small glaciers are important indicators of short term variations in the climate system, both on the local and on the global scale (Kuhn, 1995), due to their sensitivity to topo-climatic conditions (Hughes and Woodward, 2008). These elements make the southeastern Alps a unique case study for the application of a high-resolution climate model focused on the atmosphere-cryosphere interactions.

Previous works on the North-Atlantic and European LGM have already investigated the large scale atmospheric circulation mainly by means of low-resolution climate models (Laîné et al., 2009; Merz et al., 2015), proxy data (Luetscher et al., 2015; Monegato et al., 2017) and recently also high-resolution climate models (Pinto and Ludwig, 2020; Strandberg et al., 2011). These studies highlight a strengthening and, in most of the cases, a southward shift of the Atlantic storm track associated with a marked latitudinal pressure gradient over Europe. According to Luetscher et al.

(2015), this pressure gradient forced the moist air masses from the subtropical moisture reservoir across the Alps, leading to the main precipitation over the European Alps at the LGM.

In this thesis, we focus on the precipitation distribution through the year at the LGM, to explore the hypothesis that supports higher precipitation during late-Spring to early-Autumn in the southeastern Alps. If this is the case, we expect the sea level pressure pattern to present a semi-permanent high-pressure system over the Fennoscandian ice-sheet and a corresponding low-pressure system between the Western Mediterranean Sea and the Gulf of Genoa. This pressure configuration would develop as a consequence of the Rossby-wave breaking of the jet stream over Western Europe (Luetscher et al., 2015). In this framework, we propose two main mechanisms to explain the origin of the precipitation in the southeastern Alps that led to the formation of the Tagliamento glacier:

(i) the orographic lifting of southerly air masses, which were forced to move from the Mediterranean and Adriatic regions towards the Alpine reliefs by the marked latitudinal pressure gradient. This mechanism was proposed by Luetscher et al. (2015) and Monegato et al. (2017) but has never been explored with a high-resolution Regional Climate Model (RCM);

(ii) the emergence of small-scale convective phenomena, triggered by the abundance of melt-water in the glacier's foreland. These phenomena are primarily of convective nature and thus, we expect them to have a greater impact during the summer.

In order to validate these mechanisms, a chain of three climate models was devised. The Max Planck Institute for Meteorology Earth System Model in Paleo Mode (MPI-ESM-P; Stevens et al., 2013), compliant with PMIP3/CMIP5 protocols (Paleoclimate Modelling Intercomparison Project; Braconnot et al., 2012), provides the pre-industrial and LGM large-scale framework for pre-industrial and LGM time, where the Regional Climate Model RegCM4.7 is nested in two steps of increasing resolution (50 km and 12 km). The MPI-EMS-P is a widely used Earth system model that has already been successfully employed in the study of the European LGM (e.g. Pinto and Ludwig, 2020). In particular, Ludwig et al. (2016) analysed five PMIP3 models and the MPI-ESM-P showed an overall behaviour in line with the models' ensemble average. Still, a northern position of the North Atlantic jet stream was observed compared with the other four models. However, recently Kageyama et al. (2020) presented some preliminary results of the PMIP4/CMIP6 experiment, where the average jet stream position is further north than in the PMIP3/CMIP5 simulations, having a pattern close to the MPI-ESM-P jet.

In order to adapt the RegCM4.7 to work for LGM conditions over the southeastern Alpine region, we calibrated the RegCM4.7, forced with ERA-Interim data (Dee et al., 2011), against present-day observations. Next, we nested the tuned RegCM4.7 within both the MPI-ESM-P pre-industrial control run (PC) and LGM run. The LGM runs were provided with an *ad hoc* reconstruction of the land-use dataset for the LGM conditions. Finally, we compared the simulation forced with the pre-industrial data against the LGM simulation to find the differences between the LGM and the pre-industrial climate.

Regional climate models applied to the paleoclimate field have recently started gaining increasing attention (Ju et al., 2007a; Ludwig et al., 2018; Strandberg et al., 2011). This work fits well in this context and has the potential to provide a basis for other similar studies. The advantage of using a modelling approach for a paleoclimate study is that it allows to extend the domain of study beyond the limits of the proxies distribution and at the same time, the wide range of proxy data enables the validation of the model results.

Beyond testing and customisation of the RegCM4.7 system for LGM conditions over the southeastern Alpine region, this thesis aims at exploring the interactions between the glacier surface and the atmosphere in order to provide the grounds for future development of a coupled dynamic ice-sheet model. Indeed, in order to understand the anthropic effects on the Earth's ecosystems, it is necessary to enhance our knowledge about natural climate variability on both long and short time scales. In this framework, paleoclimate simulations provide crucial information on how the different climate system components react to the natural climate variability and which physical laws regulate climate-related processes.

1.1.1 The Structure of this Thesis

This thesis is structured in 7 chapters. In the upcoming sections of the current chapter a general overview of climate models and Last Glacial Maximum is given. Chapter 2 presents the ecological setting of the domain at the LGM, with particular attention to glaciers and vegetation distribution. The methods are presented in chapter 3 which, for first, introduces the models used and presents the nesting chain of the models. Then describes the spin-up and simulations phases and concludes with an analysis of the main problems and correction applied to the data. In chapter 4 the discussed topic is the analysis of the atmospheric circulation over the domain and the difference between the LGM and pre-industrial runs, while chapter 5 presents the method used for the Equilibrium-Line Altitude calculation and its analysis. The results are discussed and related to other studies in chapter 6. To conclude, chapter 7 gives a summary of this project and of the future prospects.

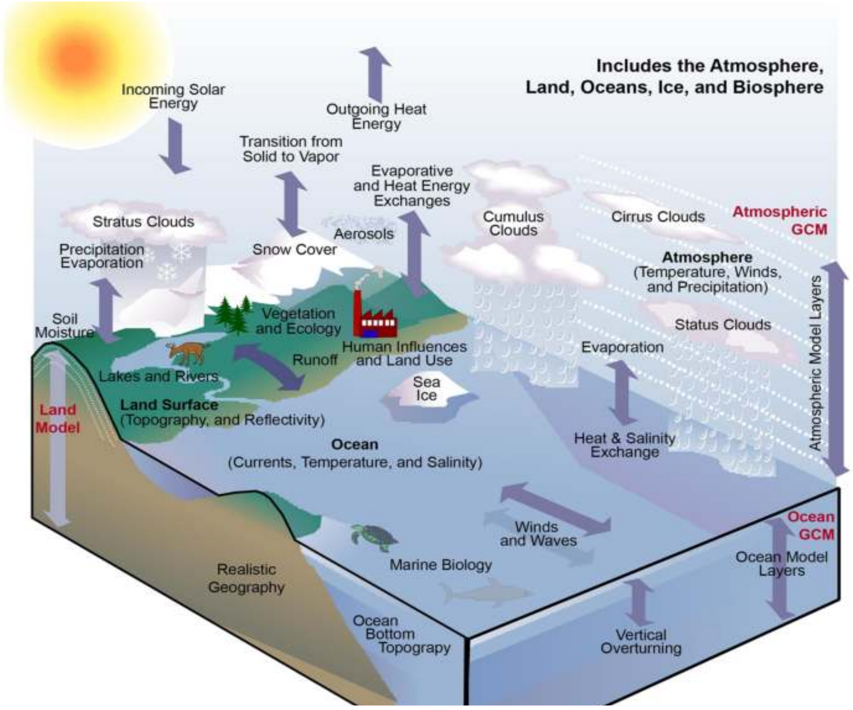

FIGURE 1.1: A representation of the complexity of interaction within the climate system and consequently of the most advanced climate models. From: Karl and Trenberth (2003).

1.2 Climate Models: An Overview

Climate is defined as the average weather conditions (e.g. temperature, precipitation, humidity) of a particular region for a time period generally longer than 20–30 years. The climate system is constituted by a large number of components characterised, in their turn, by a multitude of processes happening at different temporal and spatial scales (figure 1.1). Climate models have proven to be a useful tool to investigate the climate system and to assess a wide range of scientific questions since they have specialised into a great number of different typologies.

Climate models are constituted by two main components: one representing the dynamics and one the physics of the system. Sets of partial differential equations (PDEs), which aim to solve the extreme complexity of the climate system following a numerical approach, embody the dynamics. The set of equations, which is incomplete due to the essence of the climate system, includes the fundamental laws of nature such as conservation of mass, energy and momentum, the principles of thermodynamics and biological knowledge. Discretisation in space and time of these equations determines the resolution of the output but also influences the solution stability.

By the mean of full equations, it is possible to represent only some processes; the others require to be approximated through conceptual models (often referred to as parameterisation; Flato et al., 2013). This technique constitutes the physic component of the model and is used to represent processes that occur at scales that are smaller than the grid-cell (e.g. convection) or to simplify extremely complex mechanisms (e.g. biochemical processes in vegetation).

Since 1970's, Global Climate Models have become increasingly comprehensive of the different elements that compose the climate system by coupling atmosphere, oceans, sea ice, land (e.g. vegetation, soil type, soil moisture, snow and groundwater), aerosol, bio-geochemistry (as the carbon cycle, sulphur cycle, and ozone; Flato, 2011) and in some cases continental ice sheets. These extremely complex models represent the current state-of-the-art models and are called Earth System Models (ESMs; Flato et al., 2013).

Climate models can be classified according to different peculiarities as their spatial coverage, the levels of complexity they include, or the number of dimensions. The two main types of climate models are represented by the Global Climate Models (GCMs) and the Regional Climate Models (RCMs).

Global Climate Models

Global Climate Models or General Circulation Models and Earth System Models are used to study the Earth's climate on a global scale. They simulate the complex and non-linear interactions between the components of the Earth's climate system. The prime application of these models constitutes in simulating past and future responses of the climate system to external forcing.

A simple version of the ESMs are the Earth System Models of Intermediate Complexity (EMICs), which are often applied to explore climate feedbacks and sensitivities on long time scales (Flato et al., 2013). EMICs are used to test new ESMs components such as ice sheets (Goosse et al., 2010) and ocean sediment models (Ritz et al., 2011) and to investigate climate response on millennial timescales (Zickfeld et al., 2013).

GCMs and ESMs use a three-dimensional grid with some tens of vertical layers divided between ocean and atmosphere, while the horizontal resolution usually spans from 100 to 500 km. The high number of grid-cells and the complexity of the simulated processes determine high computational times, which exclude (with the current technology) the possibility to increase the spatial and temporal resolution in order to detect local climate futures. For this reason, in the late 1980s, the first Regional Climate Model (RCM) was developed (Dickinson et al., 1989; Giorgi, 1990; Giorgi and Bates, 1989) and through the downscaling techniques, it became possible to capture small scale climatic features. Two main downscaling techniques exist: Dynamical and empirical-statistical. The first technique is physically based but computationally expensive: a low-resolution climate model forces a high-resolution limited area climate model by providing the initial and time-dependent boundary conditions. The second refers to the use of statistical relationships between low-resolution model output and high-quality observed weather data in order to predict local climate variables with high resolution (Tang et al., 2016).

Regional Climate Models

In the last three decades, the RCMs have seen a significant development with a wide variety of applications, spanning from process studies to paleoclimate and centennial future climate projections, with resolutions from about 50 km to less than 5 km in the case of convection-permitting simulations (Giorgi, 2019).

Regional Climate Models are Limited Area Models (LAMs), which produce high-resolution data over a limited domain by dynamically downscaling coarser climate fields. The main idea is that the GCM simulates the global circulation driven by large scale forcings (as radiation, aerosols, greenhouse gasses changes) and the RCM is then nested into the GCM. Therefore, the RCM addresses the sub-GCM grid-scale processes as those occurring due to complex topography, coastlines, inland bodies of water, land cover distribution, or dynamical processes occurring at the mesoscale (Giorgi, 2019). In addition to GCMs data, also global reanalysis or RCMs themselves can provide the initial and time-dependent lateral boundary conditions (LBCs) to drive the RCMs. Typically, the required variables for the RCM prognostic equations are wind components, temperature, water vapour and surface pressure. It is also necessary to provide the lower boundary conditions: The Sea Surface Temperature (SST) for the ocean-atmosphere interface and the surface characteristics and initial soil moisture content for the land.

The transition between LBCs and RCM is provided by mean of a standard relaxation technique in the so-called buffer zone (Davies and Turner, 1977): a stripe of cells on the edge of the domain where the boundary conditions and the driven model reach a dynamic equilibrium, after a spin-up time of about 5 to 10 days; (Giorgi et al., 1993; Laprise et al., 2008). In the buffer zone, the small scale-features characteristic of the RCM smoothly develop towards the domain interiors.

In a one-way nesting, the RCM can inherit GCM's systematic errors since it is not supposed to correct the errors present in the large-scale forcing fields (Giorgi, 2019). For this reason, it is a good practice to examine in detail the input data and to exclude either the buffer zone and the spin-up period before analysing the RCM's output.

1.2.1 Added Value

The large number of applications of RCMs highlights the wide acceptance they have in the scientific community, but at the same time, questions arise about the additional information they provide to the GCM, the so-called Added Value (AV). The assessment of the AV is often difficult as RCMs can both improve or worsen the information of the GCM simulations (Giorgi et al., 2015).

RCMs has shown to provide an AV compared to the GCMs for small-scale, topography and parameterisation-dependent processes as orographic precipitation and storm activity (Ludwig et al., 2019). Ciarlo et al. (2020) and Kanamitsu and De Haan (2011) showed that the AV is not spatially homogeneous but tends to be higher over areas of complex topography as the Alps or the Pyrenees and lower in flat areas as central Europe (Gómez-Navarro et al., 2013; Prömmel et al., 2010). This is caused by the RCMs resolution, which enables to capture sub-GCM grid-scale processes (Giorgi et al., 2015) which are often triggered by complex topography.

Studies about the AV focused on the Holocene and the Last Glacial Maximum, (Armstrong et al., 2019; Gómez-Navarro et al., 2013; Ludwig et al., 2019, 2017; Russo and Cubasch, 2016) proved that RCMs increase the information related to small scale processes also in the paleoclimate field.

To summarise, GCMs and RCMs perform a complementary task by providing different information for a given region (Giorgi, 2019). Thus, a careful evaluation of the meaning of the RCMs data is required: When large-scale processes over flat terrain prevail, the RCM does not necessarily add value to the GCM.

1.2.2 Climate Model Evaluation

Climate models are the primary tool for investigating the climate system, thus it is crucial to evaluate their performance. Before the release of a climate model, the singular model's components need to be tested (e.g. the atmospheric module is tested with sea surface temperature prescribed; Flato et al., 2013). Then all the modules are evaluated together, and a first parameters adjustment is performed in order to make the model able to capture large-scale climatic features.

The last step is the *model customisation* where the parameters are regulated to match the observational data for a particular region. It does not exist at the moment a systematic parameter optimisation methods applicable to coupled climate models (Neelin et al., 2010) rather, model customisation involves trade-offs, and for this, it represents an important source of uncertainty.

Evaluation of climate model simulations is normally performed by comparing the model output with corresponding observationally-based estimates (Ban et al., 2014), proxy data (Armstrong et al., 2019; Ludwig et al., 2017), multimodel ensembles (Kageyama et al., 2020), or using quantitative statistical measures (Smiatek et al., 2016). When model performance is assessed through observation, the quality, the resolution and how the observations are processed is crucial.

1.2.3 Paleoclimate Model Studies

Paleoclimate modelling is focused on two main targets: The understanding of the processes influencing the climate system on a long time scale and the comparison of

the recent past with the present-day climate. The understanding of the mechanisms that have driven climate changes in the past makes it possible to project future climate states. Indeed, the same climate models, with modified prescribed forcings, are used to simulate present-day climate, future scenarios, and paleoclimate.
The wide range of proxy data available for the past (e.g. ice cores, volcanic and lake deposits, exposure times of periglacial rocks, fossil-pollen) enables the validation of the model results (Braconnot et al., 2012) and at the same time, models help to fill the spatio-temporal gaps between proxies, that for their nature are sparse and discontinuous (Jansen et al., 2007). Alternatively, to calibrate paleoclimate runs, scientists use control runs. These highlight the changes that are independent of either natural variability or variation in the external forcing but are only related to the model physics and parameterisation.

In paleoclimate studies, different paths can be pursued in order to maintain computer costs low. One choice is to perform geologic timescales simulations with simple models which, to the detriment of high temporal and spatial resolution, simulate the climate change over long timescales (Farnsworth et al., 2019). In this way, it is possible to catch the long term mechanisms involved in the climate system. On the other hand, short simulations (few hundreds of years) with complex models as ESMs and RCMs can be performed to obtain a more detailed representation of the physics of the climate processes (Kageyama et al., 2018). A typical experiment is to produce short time slices every few thousand years (Kutzbach and Guetter, 1986).
Recently, the use of RCMs in paleoclimate studies is gaining importance as proved by the works of Kageyama et al. (2005), Renssen et al. (2001) and Strandberg et al. (2011), ludwig2017impacts, LUDWIG201834, LUDWIG2020 In particular Ludwig et al. (2020) could reach the fine resolution of 8.5 km over the Alps and Carpathians.

1.3 The Last Glacial Maximum

The term Last Glacial Maximum (LGM) is used to refer the to time, during the last glacial cycle (0 to 150 ka BP; Lisiecki and Stern, 2016), of maximum global ice volume (Hughes et al., 2013). It is considered to have been a global event (figure 1.2.a), and it is conventionally defined from sea-level records (Peltier and Fairbanks, 2006) and oxygen isotope stratigraphy of ocean sediments (figure 1.2.b; CLIMAP Project Members, 1976, 1981). Indeed, as the continental ice expands, there is an exchange of water between the ice masses and the oceans. This exchange of water is responsible for the sea-level change (figure 1.3) and together with the temperature drives the isotopic signal of ice and sediment cores (figure 1.2.b and c). The $\delta^{18}O$ provides us with integrated information about the global status of the oxygen isotopic composition of the marine sediments but covers any regional climate variability signature. Therefore, the LGM can be outlined as a global event, which corresponds to a minimum in

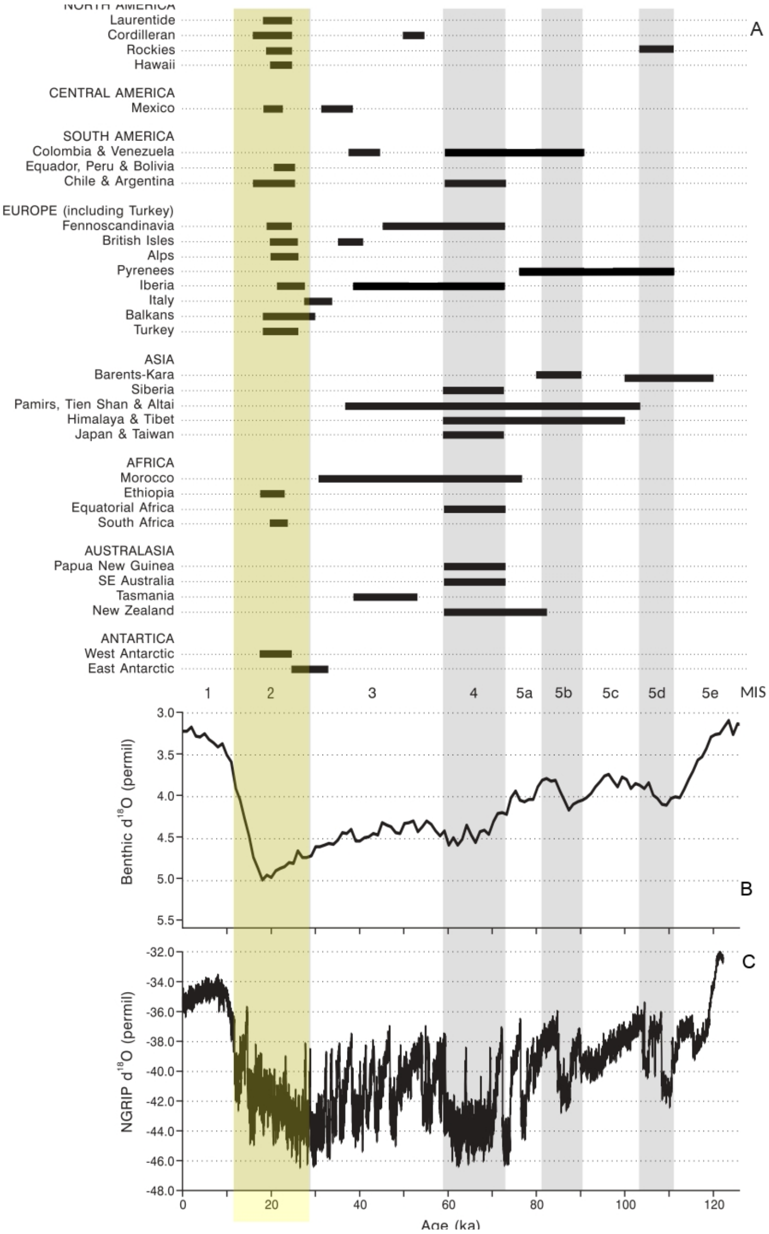

FIGURE 1.2: Modified from Hughes et al. (2013). In yellow the LGM, in grey the previous glaciations. a) An overview of the timing of the maximum glacier extension from several regions around the wold during the last glacial cycle. b) The marine oxygen isotope record based on Lisiecki and Raymo (2005) and c) the Greenland $\delta^{18}O$ based on NGRIP (2004).

global sea-level and a maximum in marine oxygen isotope records occurred at about 21 cal ka BP (CLIMAP Project Members, 1976; Yokoyama et al., 2000).

Only in the last decade, the scientific community has agreed that both mountain glaciers and ice sheets had reached their maximum extension not synchronously with the *global* LGM (Hughes et al., 2013; Monegato et al., 2017).

Hughes et al. (2013) have shown that the European Alps and the Laurentide Ice Sheet

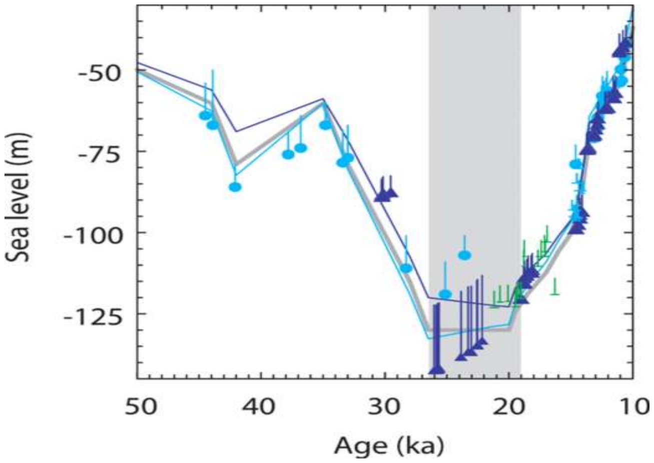

FIGURE 1.3: From Clark et al. (2009). Sea-level predictions (blue and light blue lines) compared to relative sea level data for different locations (light blue circles, blue triangle, green dashes, and ligth-blue dashes) and eustatic sea-level timeseries (gray line). The vertical gray bar indicates the time of the LGM (for more details see Clark et al., 2009).

(LIS) had one major event at MIS2 (Marine Isotope Stage 2 –29.0 to 12.0 ka BP), corresponding to the LGM, while other glaciated regions as the Fennoscandian Ice Sheet also had earlier pulses (figure 1.2.a). Terrestrial stratigraphy and speleothems isotope records (Luetscher et al., 2015) showed that the maximum extent of the European glacier was reached in different moments and not synchronously with the LGM inferred from ocean $\delta^{18}O$ sediment data (Gillespie and Molnar, 1995). Consequently, it is more appropriate to affirm that an extended global glaciation occurred during the MIS2 (Clark et al., 2009), instead of attributing to the LGM a precise date for the entire Earth.

1.3.1 Triggers and Termination of the LGM

The LGM occurred as a consequence of changes in the orbital configuration of the Earth (Bowen, 2009; Thackray et al., 2008), which caused variations in the Earth insolation (figure 1.4.b) as well as in the atmospheric and ocean circulation. Increased precipitation and lower surface temperature (figure 1.4.a) acted as a trigger for the onset of several extensive ice sheets in North America, North Europe, Antarctica and several glaciers in all continents.

According to Clark et al. (2009), the primary triggers of the growth of the ice sheets to their *local* LGM positions have been the high latitude Northern Hemisphere insolation, the SST in the tropical Pacific, and the atmospheric CO_2 concentration (figure 1.4). Indeed, between 33 to 29 ka BP, Northern Hemisphere summer insolation declined and CO_2 slightly dropped by about 15 ppm. In particular, low levels of insolation occurred at about 45°N (figure 1.4.b) in correspondence to the LIS southern margin. This reduced the ablation rate of the LIS, leading to a glacial advance that caused a

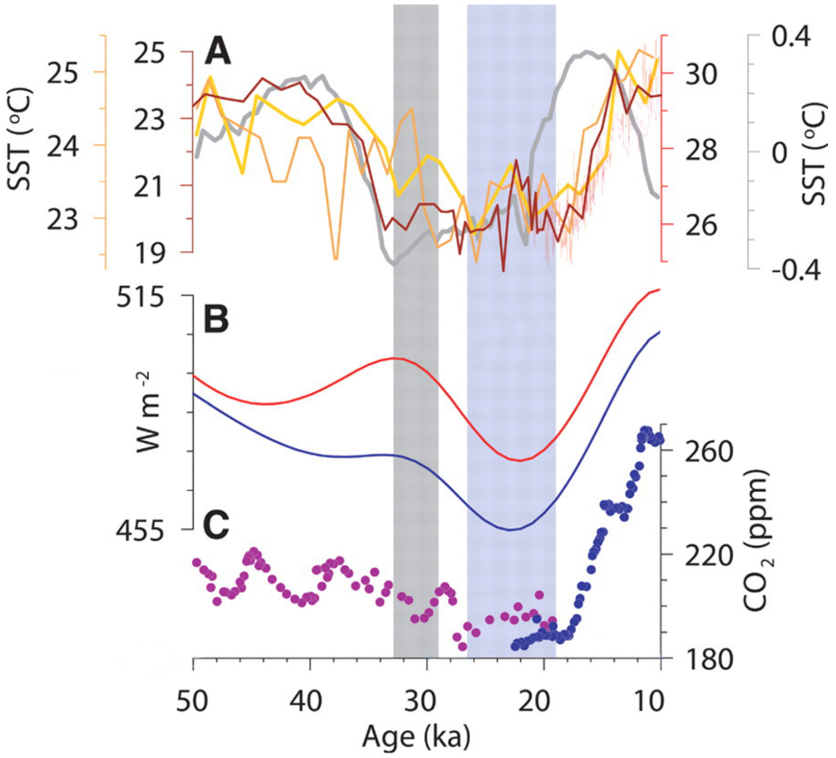

FIGURE 1.4: Modified from Clark et al. (2009). Different climate forcings pattern at the LGM: a) SST records compared to simulations data (NINO3 index; gray line); b) 21June to 20 July insolation at 45° and 65° (red and blue line respectively Laskar et al., 2004); c) Atmospheric CO_2 from Ahn et al. (2004) in purple and Ahn and Brook (2014) in blue.

first LGM drop in the sea-level (~40 m; Clark et al., 2009). At about the same time (38 to 30 ka BP), the eastern equatorial Pacific cooled down by 2 to 4 °C (Feldberg and Mix, 2003; Martínez et al., 2003), while the western sector had already cooled 30 kyr earlier (Lea, 2000), resulting in a La Niña-like SST field (Clark et al., 2009; Koutavas, 2002).

The ice sheet waxing at the beginning of the LGM occurred under three main forcings. On the contrary, the LGM termination, that began synchronously (at 19 to 20 ka BP) for several mountain glaciers and ice sheets worldwide (Schaefer, 2006), was controlled only by the increased summer ablation caused by an enhanced in northern insolation (Clark et al., 2009).

1.3.2 Global Effects of the LGM

The effect of the onset of the LGM ice sheets on the climate system has been intense: On one side the water trapped within continental ice lowered the sea level by about 120 to 130 m (Clark et al., 2009; Yokoyama et al., 2000), drastically modifying the shape of the ocean basins (Clark and Mix, 2002).
At 31 ka BP the onset of the LGM was marked by an abrupt sea-level fall by about

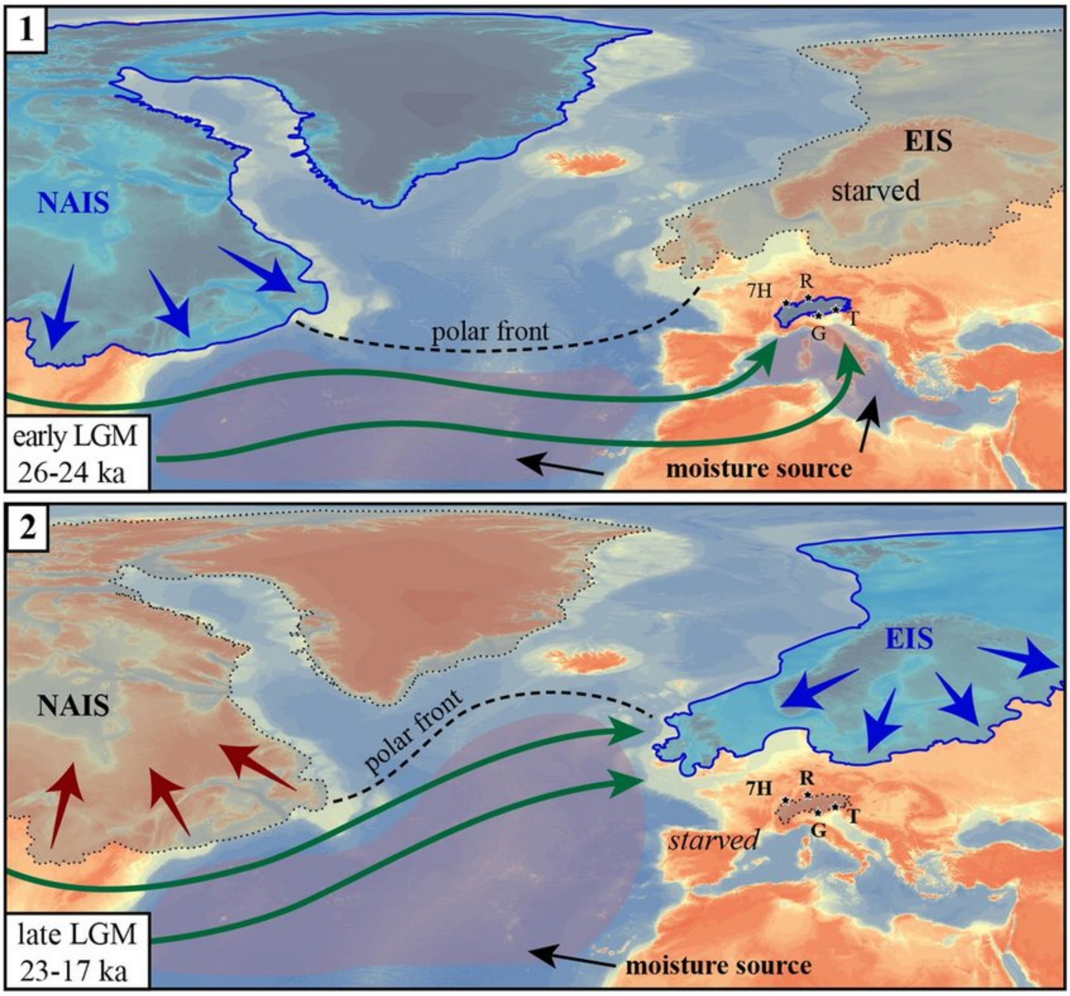

FIGURE 1.5: From Monegato et al., 2017. Schematic representation of the changes in the atmospheric circulation generated by the onset (1) and retreat (2) of the NAIS and the consequent effects on the ice masses over Europe. 7H: speleothems data. R: Rhine Glacier. G: Garda Glacier. T: Tagliamento Glacier.

40 m in less than two millennia (Yokoyama et al., 2018). Then, between 29 ka BP and 21 ka BP the sea-level slowly continued to fall to −134 m (Lambeck et al., 2014) with respect to the pre-LGM sea level. Subsequently, from 20 ka BP, with the highest rate between 16.5 ka BP and 8.2 ka BP, the deglaciation took place at an average rate of 12 m kyr^{-1} (Lambeck et al., 2014). The massive release of freshwater from the waning land ice masses altered not only sea-level and salinity but also oceanic deep convection, ocean circulation, heat transport, sea ice and the global atmospheric circulation (Masson-Delmotte et al., 2013).

At the LGM, the atmospheric circulation underwent deep modifications under the forcing of the ice sheets (Bowen, 2009) and colder global average temperatures. In literature, there is still significant disagreement on the global average of the annual mean temperature at the LGM, but the estimates range from 6 to 3 °C colder than pre-industrial time, depending on employed climate models and proxy dataset (Annan and Hargreaves, 2013; Braconnot et al., 2007).

The perturbation that the ice sheets caused on the global atmospheric circulation was transmitted to remote regions through mechanisms (Masson-Delmotte et al., 2013) as the meridional shift of the Northern Hemisphere westerlies linked to the onset of semi-permanent anticyclonic circulation over the ice bodies. An example is the effect the expansion of the North American Ice Sheet (NAIS) had on the North Atlantic jet stream, which was pushed southward at about 42° (figure 1.5; Florineth and Schlüchter, 2000; Monegato et al., 2017). Another consequence of the growth of the ice sheets was the orographic effect that influences the stationary wave patterns (Abe-Ouchi et al., 2007) and trade wind systems (Timmermann et al., 2004). On the local scale, the ice sheets produced strong katabatic winds directed from the interior to the margins of the ice body (Masson-Delmotte et al., 2013).

The waxing ice sheets that reached previously vegetated regions increased the albedo, leading to colder temperature as a consequence of the snow-albedo feedback. The vertical growth of the ice sheet determined a further cooling (lapse-rate effect) but also caused a decrease in the precipitation and accumulation rates (elevation-desert effect; Oerlemans, 1980). The glacioisostatic phenomena played the counter effect: the weight of the ice sheet led the underlying bedrock to subside, reducing the altitude of the ice sheet and consequently increasing the temperature (Berg et al., 2008). The glacioisostatic rebound has been acting in Scandinavia since the deglaciation began, as evidenced by the shorelines (Colgan et al., 2019).

In summary, the onset of the LGM profoundly modified the environment, influencing all the components of the climate system through its network of multiple feedbacks.

Chapter 2

LGM in the European Alps

During the LGM the atmospheric and environmental conditions were drastically different compared to today. Extended glaciers covered the Alps, the temperature was 3 to 6 °C colder than in the pre-industrial time (Annan and Hargreaves, 2013), and the air-masses circulating over Europe followed different patterns (Luetscher et al., 2015; Monegato et al., 2017). Convection was reduced as a consequence of the limited energy available. The Alps were located over a boundary that divided the dry central Europe, dominated by westerly winds from the South alpine region, characterised by southerly and enriched in moisture air masses. This dynamic favoured the glaciers expansion, but also deeply modified the vegetation distribution in Europe.

In this chapter a brief overview of the climatic and environmental conditions over Europe at the LGM will be provided, with a focus on the aspects of particular relevance for this thesis.

2.1 LGM atmospheric circulation over Europe

Recent studies (e.g. Luetscher et al., 2015; Monegato et al., 2017) suggest that the LGM alpine glaciers expansion occurred as a consequence of the maximum expansion of the North Atlantic Ice Sheet (NAIS) which, by pushing the polar front southward, modified the atmospheric circulation over the Atlantic ocean and Mediterranean sea. Model simulations performed by Laîné et al. (2009) show a thinning of the storm track in the northwestern Atlantic and an increased synoptic activity between the Azores Islands and the Iberian Peninsula. Laîné et al. (2009) suggest that the increased baroclinicity, together with the orography, modified by the ice sheet expansion, forced the southeasterly displacement of the North Atlantic storm track and jet.

During MIS 3 (59 to 29 cal ka BP; Voelker et al., 1998) and MIS 4 (74 to 59 ka BP; Martinson et al., 1987) the Polar Front was located north of 46°N, and the circulation was prevailing westerly over Europe, causing ice buildup in Scandinavia and Central Europe. At the LGM the shift of the Polar Front from 46 to 40°N (Laîné et al., 2009) led to increased precipitation over southwestern Europe and much drier conditions over central and northern Europe. The modification of the storm-track also led to frequent southerly flow incursions passing over the Mediterranean sea and reaching the southern Alps. This flow became enriched in moisture over the sub-tropical moisture reservoir, an area that was less affected by the change in the insolation that concurred to trigger the LGM (Luetscher et al., 2015). Indeed, in the tropics and sub-tropics the sea surface temperature experienced only a limited drop compared to the high latitudes and maintained the necessary energy to provide moisture for precipitation (Luetscher et al., 2015). As these air masses reached the Alps, abundant orographic precipitation led to the formation and maintenance of extended glaciers in this area.

The differential insolation and temperature changes in the tropics and sub-tropics compared to the mid and high-latitudes, determined a steepening of the temperature and pressure gradients, which together with a semi-permanent blocking over the Fennoscandian ice sheet, probably increased the synoptic activity in the North Atlantic mid-latitudes and along the jet stream axis (Luetscher et al., 2015). This steep gradient was also the main mechanism that forced the air masses to move from the subtropics to the Alps.

Only when the NAIS began to wane the Eurasian ice sheet started growing, triggered by the polar front, which at that time moved back to about 46°N (Monegato et al., 2017).

2.2 Environmental reconstructions

The study of the past climate constitutes an essential step in order to better understand the present and future climate evolution and to discriminate anthropogenic and natural processes.

Direct observations and instrumental records go back only a couple of centuries, thus in order to extend the record beyond this (short) time, it is fundamental to be able to read the natural climate archives. These indirect measures of past climate, often referred to as climate proxies, can provide the scientists with huge amounts of information from the time they have formed. The paleo-climatic proxies can be of lithological/mineralogical origin, can be produced by geochemical processes occurring in a small range of environmental conditions or can be constituted by the remains of organisms that lived in specific temperature ranges.

The main weakness of climate proxies is their discontinuous and sparse spatial distribution and the concrete possibility that they undergo erosion, weathering, and alteration. To overcome this problem and increase the reliability of paleoclimate reconstructions it is advisable to use multiple proxies.

In the framework of this thesis two categories of proxies are particularly important: glaciers and their related forms and processes, and vegetation. In this section an

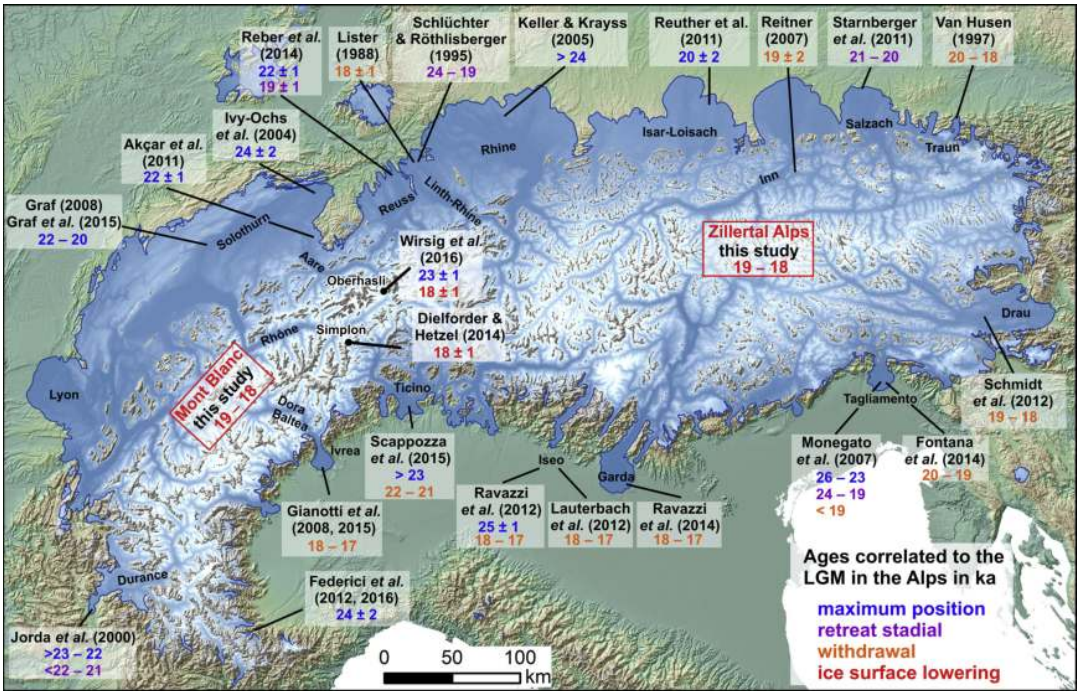

FIGURE 2.1: From Wirsig et al. (2016). The different times of advance and retreat of the alpine glaciers at the LGM.

environmental reconstruction for these two climate indicators, based on the available literature will be presented, while in the next chapter (3.2.2) how these information have been used to create the input data for the model simulations will be explained.

2.2.1 The LGM Alpine glaciers

The glacial cycles in the European Alps have been largely documented by means of geomorphological mapping (Ehlers and Gibbard, 2004), trim-lines, and geological and geochemical studies. Only recently all these data were used for glaciers reconstructions implemented by means of glacier models or Geographic Information System (GIS) applications.

Glacier Advance

The typical LGM alpine landscape was characterised by long valley glaciers which flowed from extended accumulation areas like high elevation ice domes and ice fields (Florineth, 1998; Florineth and Schlüchter, 2000). Florineth and Schlüchter (2000) reconstructed the paleo-atmospheric circulation patterns and hypothesised the presence of three major ice-domes in the Swiss Alps, located South of the present climate divide in correspondence of high precipitation areas. Kelly et al. (2004) completed the theory of Florineth and Schlüchter (2000) and suggested that several glaciers in the western Alps and the majority of the glaciers in the eastern and southern Alps originated not from an ice-dome, but rather from ice-fields. Indeed the mountainous reliefs present in these regions constrained the ice to follow the topography.

From the ice-domes and ice-fields, the ice was then canalised by the alpine valleys (Kelly et al., 2004) and flowed outward. As these long valley glaciers reached the lowlands, the ice spread out in piedmont lobes, leading to the formation of moraines, hummocky ground and other morphological forms both in the northern and southern Alpine forelands (Penck and Brückner, 1909).

Model reconstructions (Kuhlemann et al., 2008) estimated the Equilibrium-Line Altitude (ELA) in the southern Alps on average at 1300 m a.s.l., with values down to 1000 m a.s.l. in the Julian Prealps, while on the northern alpine slopes the ELA was at approximately 1100 m a.s.l.. The ELA depression associated with the LGM glaciers with respect to the LIA (Little Ice Age) was about 1000 to 1500 m (Ivy-Ochs et al., 2006a,b, 2008), with the lowest values in the western Alps (Federici et al., 2016).

Luetscher et al. (2015) studied the speleothems formed in different caves across the Alps at the LGM and observed that their data supported advection of moist air from the South. The interaction between the synoptic circulation and the insulation decline at 29 ka BP caused differences in the ice build-up in the Alps, with a non-uniform glacier advance and withdrawal (figure 2.1). Luetscher et al. (2015) suggests that the LGM glacier expansion was predominantly fed by precipitation occurring between spring and autumn. This was inferred by the presence of liquid water, which is necessary for the growth of the speleothems.

The Southeastern Alpine Glaciers

The Alpine glaciers were characterised by an initial advance around 26 to 24 ka BP, corresponding to the GS-3 stadial, and a second minor advance at 23 to 22 ka BP (Monegato et al., 2017). The glaciers advance at the LGM has occurred almost synchronously across the Alpine chain, but the withdrawal of the Tagliamento system began earlier than in other alpine sectors, probably due to its small and low-elevation catchment basin (Monegato et al., 2017). Between 22 and 19.5 ka BP the Tagliamento glacier rapidly reacted to the climate variations and retired within the inner valleys, leaving several recessional moraines (Fontana et al., 2014b).

In the southeastern Alps the Equilibrium-Line Altitude (ELA) was estimated for the LGM at about 1200 m a.s.l. (Colucci et al., 2014; Žebre et al., 2014), in the Prealps at 1000 to 1150 (Monegato, 2012), while in the Po river basin the ELA was attested on average at 1920 m a.s.l. (Kettner and Syvitski, 2008).

There is no evidence for a transfluence from the Drava to the Tagliamento catchment (Monegato et al., 2007; Seguinot et al., 2018), thus the Tagliamento basin was delimited by an area corresponding to the south-central part of Julian and Carnic Alps.

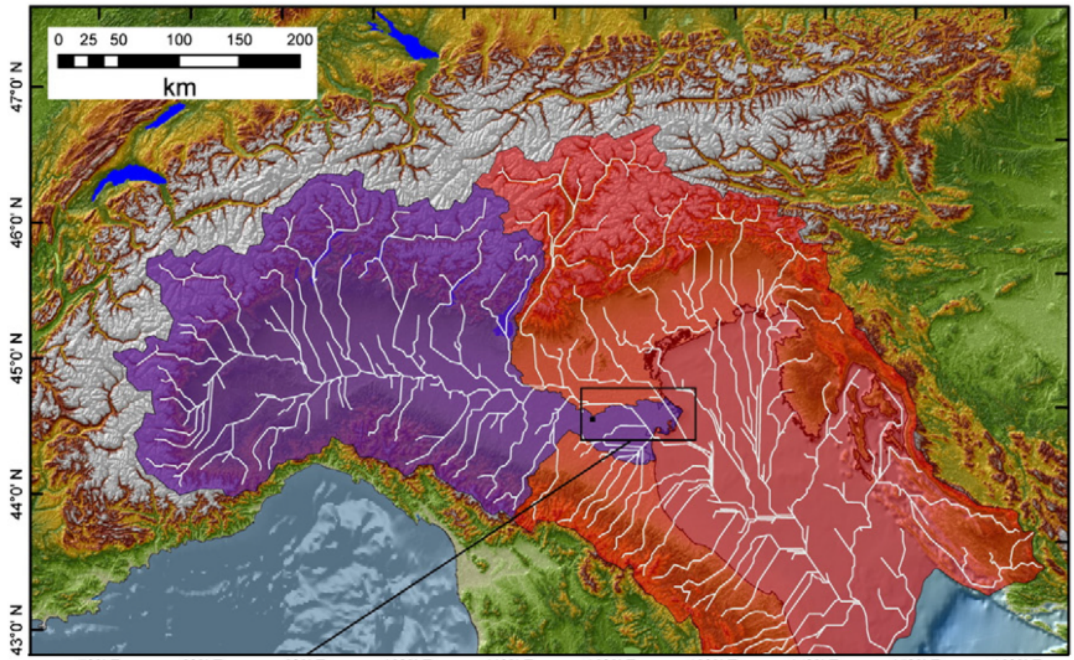

FIGURE 2.2: Modern (violet) and LGM (pink) drainage basin of the Po River (modified from Kettner and Syvitski, 2008; Maselli et al., 2011). In white are represented the reconstructed river network during the LGM. The black box shows the present-day location of the Po River delta.

The Adriatic alluvial Plain

The major glaciated basins in the southern Alps had piedmont lobes with large outwash fans, which merged in the Adriatic Plain (Fontana et al., 2014a; Monegato et al., 2007; Ravazzi et al., 2012). The Adriatic Plain was a wide alluvial plain occupied by the Po River and its Appenninic and Dinaric tributaries (figure 2.2; Correggiari et al., 1996; Fontana et al., 2014b; Trincardi et al., 1996). These rivers transported large volumes of sediments that fed a vast system of depositional megafans occasionally cut through by channel complexes (Fontana et al., 2008, 2014b).
Over this region the moisture gradient increased from the semiarid Adriatic alluvial Plain towards a wide braided river area, whose water was supplied by the LGM glaciers. Ground water availability together with orographic precipitation (Luetscher et al., 2015) were the main drivers for the vegetation development in the southeastern Alps.

Deglaciation

The deglaciation occurred after the LGM, starting from about 21 to 19 ka BP (Ivy-Ochs et al., 2004), with still-stand phases and some readvances. From this moment the piedmont lobes rapidly disappeared (van Husen, 2000) and the ice progressively retired, firstly into the valleys and, later, in the high-altitude cirque glaciers (Penck and

Brückner, 1909; van Husen, 2000). The landscape in the lowlands was punctuated by lakes and bogs and in the mountains a dendritic network of valley glaciers developed. According to Penck and Brückner (1909), as the piedmont lobes desegregated the lateglacial begun.

2.2.2 Vegetation

A close set of interactions exists between climate system and land surface. Atmosphere, soil, and vegetation are related by two-ways feedbacks, which can significantly modify the structure of local climate (Sato et al., 2015), in terms of rates of change and spatial distribution of climate components. Terrestrial ecosystems store 2.1 to 3.6 times more carbon than the atmosphere (Sato et al., 2015), thus it is fundamental to take into account the mechanisms that cause sinking and releasing of carbon in terrestrial environments in the climate models. Moreover, the land surface controls the partitioning of available energy, between sensible and latent heat flux and the partitioning of available water between evaporation and runoff (Pitman, 2003). For this reason, it is fundamental to study the distribution of vegetation, glaciers, soil and water bodies corresponding to the time we want to simulate with climate models.

In general, the domain was colder and drier than today and the taxa characterising the environment reflected this fact. The vegetation at the LGM has been studied by means of pollen records extracted from lakes, caves and geological deposits and is detailed in the appendix A, distinguishing between northern and southern Alps, and Apennines.
In short, central Europe was characterised by a glacial desert in the proximity of the Fennoscandian ice sheet (Sirocko et al., 2016), and by a boreal forest and a dry steppe in the northern alpine foreland (Duprat-Oualid et al., 2017; Fuhrmann et al., 2020). In the southern Alps the vegetation was influenced by the high alpine elevations as well as by the proximity to the sea. Thus a wide range of taxa could adapt in the different sectors of the southern part of the domain. Glaciers and snow melt water favoured the growth of forests in the piedmont areas (Monegato et al., 2015), the higher elevation regions were characterised by a dry alpine tundra (Ravazzi et al., 2012) and the Apennines area was mainly steppic (Tzedakis, 2005; Watts et al., 1996).

Chapter 3

Climate Simulations

The aim of this project is to improve the understanding of the evolution of the Tagliamento glacier during the LGM. In order to obtain the climatic conditions, and in particular the precipitation pattern for the LGM in the southeastern Alps, a modelling approach was employed.
This chapter begins with the description of the models used to carry out the experiment (section 3.1) and proceeds with the preprocessing phase (section 3.2), through the definition of the domain, the model customisation, the nesting and the definition of an appropriate land-use dataset for the past. Section 3.3 details the setup of the simulations, such as the parameterisation, the resolution, and the main schemes used. Finally, section 3.4 describes the statistical analysis performed on the outputs of the simulations, along with the corrections that the data required to be used in this study.

3.1 Models

In the framework of this project a chain of three climate models was devised. The Max Planck Institute for Meteorology Earth System Model (see section 3.1.1 Stevens et al., 2013) compliant with the PMIP3/CMIP5 protocols (Paleoclimate Modelling Intercomparison Project; Braconnot et al., 2012) provides the large-scale framework for pre-industrial and LGM time, on which the Regional Climate Model RegCM4.7 (section 3.1.2) is nested in two steps of increasing resolution: first at 50 km, then a second time at 12 km.

3.1.1 GCM: MPI-ESM-P

The large scale simulations were performed by the Max Plank Institute using their Earth System Model, the MPI-ESM-P, whose atmospheric general circulation model is the ECHAM. It is branched from an early version of the European Centre of Medium–Range Weather Forecast (ECMWF) model (Roeckner et al., 1989) and is written in Fortran90. The modular structure of the MPI-ESM-P makes it possible to couple different Earth system components models, such as the land surface model JSBACH

(Thum et al., 2011), which describes the land-based processes for the carbon cycle or the ECHAM that simulates the small-scale fluid dynamics as well as the large-scale circulation (Shi and Lohmann, 2016).

MPI-ESM-P uses a gaussian grid to calculate non linear equation terms and some physical parameterisation. MPI-ESM-P's grid is defined by an almost regularly distributed set of grid points. According to the chosen model resolution the grid-size can span from $0.5\,^{\circ} \times 0.5\,^{\circ}$ to $3.8\,^{\circ} \times 3.8\,^{\circ}$ in horizontal. The vertical coordinate is flexible, and uses a sigma-hybrid coordinates which follows the terrain in the lower troposphere and that progressively flatten towards the stratosphere.
MPI-ESM-P allows to chose between two methods to define the orbital parameters: one extremely precise for today's climate, and one based on Kepler's laws for paleoclimate studies (Giorgetta et al., 2013). This allows to take into account the periodic changes in the Earth's and Sun reciprocal configuration that forced the Pleistocene ice ages.

In the framework of this thesis, it is important to highlight that the MPI-ESM-P simulations, performed in the context of PMIP3/CMIP5 experiment, were kindly provided by the Max Plank Institute. The Max Plank Institute performed a 150 years long simulation at the LGM standard (21 ka BP) and PC, sharing a time slice of the last 20 years for each simulation time. The horizontal resolution of these simulations is $1.9\,^{\circ} \times 1.9\,^{\circ}$, with 47 vertical layers.

3.1.2 RCM: ICTP RegCM4.7

The regional climate model RegCM4.7 was originally developed at the National Centre for Atmospheric Research (NCAR; Dickinson et al., 1989; Giorgi, 1990; Giorgi and Bates, 1989) and now is maintained by the ICTP Earth System Physics section with the support of a worldwide community of scientists, the so-called Regional Climate Research Network, or RegCNET (Giorgi et al., 2006). RegCM is used by several institutions and research groups for a wide range applications, from process studies (Van Vuuren et al., 2011) to paleoclimate (Ju et al., 2007b) and future climate simulations (Jia et al., 2014). Indeed the RegCM system is a community model: it is public, open source, portable, and can be applied to any region of the world.
The evolution of RegCM is continuous both in terms of software code and physics representations (Giorgi et al., 2012), indeed new features and schemes are routinely added through the frequent revisions of the code. RegCM is mainly written in the Fortran programming language and is compliant with the Fortran 2003 ANSI standard. RegCM reads and writes files in the netCDF format (Elguindi et al., 2014).
The dynamical core of the RegCM is similar to the NCAR Mesoscale Model 4 and 5 (MM4, MM5; Grell et al., 1994) and thus is a hydrostatic, compressible, terrain-following sigma-vertical coordinate model based on an Arakawa B-grid in which

wind and thermodynamical variables are horizontally staggered (Giorgi et al., 2012). Several schemes and parameterisations are offered in order to represent the complexity of the climate system.
From the RegCM4.5 release, a non-hydrostatic core was implemented, which allows to run in convection-permitting mode and to increase the resolution up to 1 to 3 km. RegCM now is a fully coupled regional earth system model and can be coupled with models of the ocean (Turuncoglu et al., 2013), lakes (Small et al., 1999), aerosol (Solmon et al., 2006), desert dust (Zakey et al., 2006), chemistry (Shalaby et al., 2012), hydrology (Coppola et al., 2003), and land processes (Oleson et al., 2008).

The RegCM model system is composed by a preprocessor, RegCM itself and a postprocessor. The preprocessor has two components: Terrain and ICBCs (Initial and Boundary Conditions). The terrain component produces a representation of the topography, with coastline and elevation, but includes also the sea surface temperature, which acts as the lower boundary condition for the ocean-atmosphere interface, and surface characteristics and initial soil moisture content that are the lower boundary over the land.
The Initial and time dependent Boundary Conditions are three-dimensional isobaric meteorological data that can be provided by GCMs/ESMs, global reanalysis or RCMs (Elguindi et al., 2014). As RegCM is a sigma-vertical coordinate model and the ICBC are in isobaric coordinates, an interpolation from pressure levels to sigma levels is performed. The required variables for the RegCM initial and lateral boundary conditions are 6–hourly zonal and meridional wind components, air temperature, water vapour content and surface air pressure.

3.1.3 CLM4.5

Starting from the 1980s, in order to represent the interactions existing between the climate system and the land surface, to quantify the concepts of ecological climatology, and to understand how natural and human changes in vegetation and land use affect the climate, Land Surface Models (LSM) were embedded into long-term climate simulations.
LSM are generally constituted by a module which treats the physical aspects of the atmosphere-land surface exchanges, in terms of water and energy, a module which simulates the biological and bio-geochemical processes, and a model that considers the influence of the CO_2 over climate and plants (Sato et al., 2015).
Among the various available LSMs, for this project, the Common Land Model version 4.5 (CLM4.5; Oleson et al., 2013) and BATS (Biosphere-Atmosphere Transfer Scheme; Dickinson et al., 1993) were used. BATS is an older LSM which is only required to initialise the simulations, while the main calculations related to the land-use are performed with CLM. CLM4.5 is coupled with RegCM since version 4, and represents

a fundamental aspect for this thesis as it allows to represent the different land-use from PC to LGM.

Tile Approach

One key highlight of CLM4.5 is the ability to represent sub-grid processes, thanks to a tile approach in which each grid-cell, land units, snow/soil columns, and plant functional types (PFTs) are hierarchically nested (Oleson et al., 2013). Every surface grid-cell can be subdivided into any number of tiles, each tile containing a single land unit (Dai et al., 2003), and every land unit holding a number of columns. In particular, the vegetated land units are further subdivided into patches of plant functional types, each with its own canopy height and leaf and stem area index.

The most generic units identify the macroscopic characteristics of an environment and are: glacier, lake, urban, vegetated, and crop. The second sub-grid level is constituted by the columns, which present a multiple layer structure for soil and snow, optimised to reproduce high-resolution physical and chemical variations in all layers (Dai et al., 2003; Oleson et al., 2013). The third sub-grid level is constituted by the 24 plant functional types (PFTs, table 3.1), a classification of plant species based their optical properties, capability of water uptake, effect on heat, moisture and momentum fluxes, and photosynthetic parameters for vegetation and crops (Lavorel et al., 2007). The PFTs have to be associated to the column levels in order to model the bio-geophysical processes, which regulate the plants physiology and the exchanges between plants and the surroundings.

Every tile responds to the mean conditions of the atmosphere above the grid-cell to which the tile belongs to. In turn, the atmospheric grid box receives heat and moisture fluxes which are weighted among all the tiles in the grid box, according to the PFTs distribution.

Input Data

In order to define the PFTs and distinguish the land units, before running the CLM over the desired domain, a detailed dataset with the surface characteristics is needed. This data can be acquired though satellite remote sensing and global field surveys (for the present-day; Dai et al., 2003) or from proxies (for the past). A preprocessing phase is fundamental, in order to extrapolate from the raw data the parameters and initial conditions required by CLM. These include:

Land surface Soil colour, soil texture, land units and the portion of each land units corresponding to every PFT in each grid-cell have to be defined. The information has to be aggregated to the model's spatial resolution (Oleson et al., 2013).

Soil and vegetation Vegetation parameters can be time variant or invariant. Invariant parameters are the morphological and optical parameters and physiological

	PFT - Vegetated Land Unit
Tree	Needleleaf Evergreen Tree - Temperate
	Needleleaf Evergreen Tree - Boreal
	Needleleaf Deciduous Tree - Boreal
	Broadleaf Evergreen Tree - Tropical
	Broadleaf Evergreen Tree - Temperate
	Broadleaf Deciduous Tree - Tropical
	Broadleaf Deciduous Tree - Temperate
	Broadleaf Deciduous Tree - Boreal
Shrub	Broadleaf Evergreen Shrub - Temperate
	Broadleaf Deciduous Shrub - Temperate
	Broadleaf Deciduous Shrub - Boreal
Grass	C_3 Arctic Grass
	C_3 Grass
	C_4 Arctic
	C_3 Unmanaged Rainfed Crop
	C_3 Unmanaged Irrigated Crop
	PFT - Crop Land Unit
Rainfeed	Rainfed Corn
	Rainfed Temperate Cereals
	Rainfed Soybean
Irrigated	Rainfed Corn
	Rainfed Temperate Cereals
	Rainfed Soybean

TABLE 3.1: PFTs for vegetated land-units are divided into trees, shrubs, and grasses. The C_3, unmanaged irrigated crop needs the activation of the irrigation module. PFTs for crop land-units are divided by feeding method: rain or irrigation. Temperate cereals include wheat, barley, and rye.

properties of plants (Dai et al., 2003; Oleson et al., 2013), while time variant parameters include green Leaf Area Index (LAI) and Steam Area Index (SAI). Soil parameters are derived from a depth-varying percentage of sand and clay.

Model initialisation The initialisation of the model requires temperature and moisture data. Each land unit has its own initial temperature, which is applied to 15 soil layers for vegetated and glacier units, and to 10 layers for lake units. If snow is present, the snow layers are initialised according to the snow depth, and further calculations regarding the snow water equivalent are performed.

Atmospheric coupling An atmospheric model coupled with CLM provides the atmospheric forcing to the model. With the atmospheric forcing, the land model calculates surface energy, constituent, momentum, and radiative fluxes, by mean of soil and snow hydrologic states from the previous step; these fluxes are then used to calculate the hydrology of soil and snow that are passed back to the atmospheric component.

Since RegCM is already tightly integrated with its CLM, all the necessary CLM configuration is defined from the RegCM namelist at the beginning of the simulation.

3.2 Preprocessing

Figure 3.1 shows the workflow followed in this thesis. As seen in section 3.1, climate and land surface models require several different datasets as initial and boundary conditions. Only once the datasets that contain meteorological and land surface information are ready, a series of model simulations can start. The first simulations aim at finding the right model parameters and settings to tune the RegCM for the chosen domain (section 3.2.3). Once the model customisation is deemed satisfactory, the *real* simulations can begin (section 3.3). However, a careful evaluation of the outputs is always required (section 3.4).

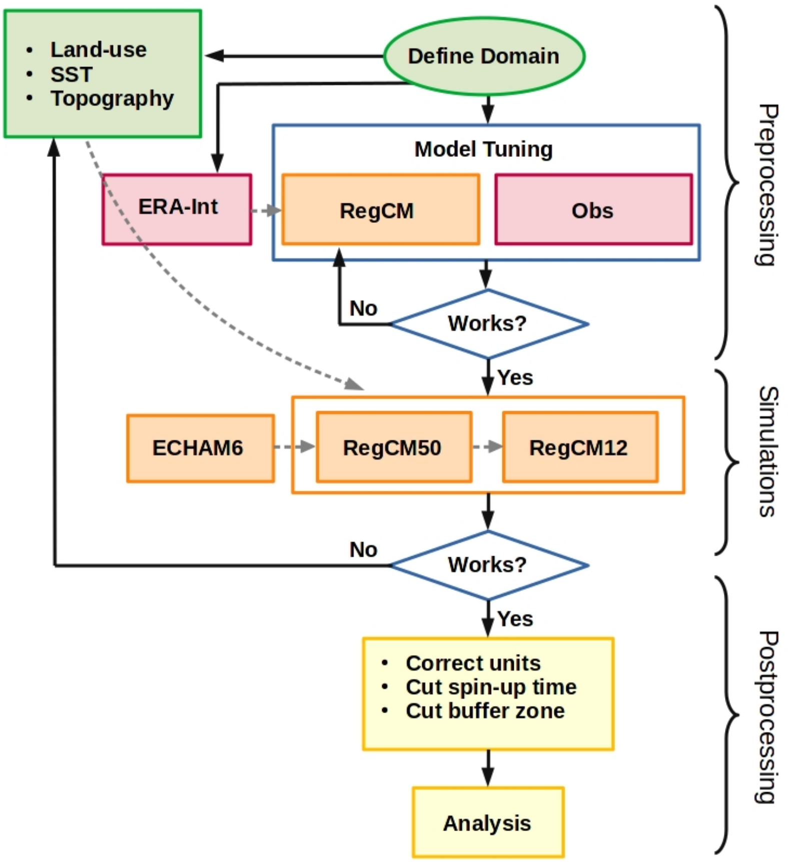

FIGURE 3.1: Flowchart representing the preprocessing, simulation and postprocessing phases carried out in this project. The dashed grey arrows indicate the input data that are used to force RegCM. The models are represented in orange, observation and reanalysis datasets in red, and in green the datasets prepared in the preprocessing phase. Two check points are present: one for the model customisation and one to validate the simulations.

3.2.1 The study domain

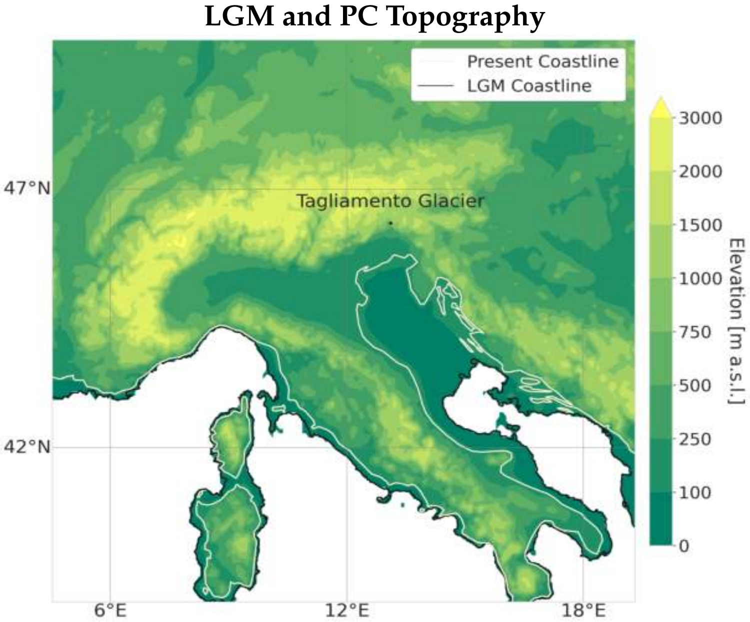

FIGURE 3.2: Coastlines comparison plotted above the LGM topography. In white the present-day coastline and in black the LGM coastline. The elevation difference between the two coastlines is equal to 120 m.

The choice of the simulation domain requires considerations about the atmospheric circulation, the topography and the model behaviour. The domain should include the area where the main regional forcings affect the climate of a given region (Giorgi et al., 2015). To avoid mismatches between the resolutions of the driving and nested models when interpolating the LBCs onto the RCM grid, it is advisable to avoid defining the domain boundaries over complex terrain. Indeed, RegCM has the tendency to produce artefacts if important orographic elements are cut by the domain boundary (Giorgi et al., 2015). Another important aspect to consider is the vicinity of the domain boundary with the area of interest, in order to minimise possible boundary effects. Indeed the stabilisation of the nested model fields that develop from the driving model happens within the fist cells near the boundary.

Consequently, the domain chosen for this study was extended in order to cover the Alpine and Balkan mountain chains in their full extent, as well as a large part of the Apennines. In order to avoid the boundary effect, the boundaries were set more than 10 grid-cells far from the southeastern alpine region in the high-resolution simulation. The resulting domain extends between 4 and 20 °E and from 38.5 to 50 °N. Figure 3.2 shows the simulation domains at 12 km.

3.2.2 LGM Land-use Reconstruction

Adapting the RegCM4.7 model to work for LGM conditions over the southeastern Alpine region requires solving some challenges such as the reconstruction of vegetation, glaciers and topography of the LGM, owing to the lack of direct observations for this past period. Ludwig et al. (2017) and Merz et al. (2015) pointed out the importance of using realistic representation of glacial boundary conditions (ice sheet, SSTs and vegetation) to run regional (paleo-) climate simulation. Thus, in order to correctly represent the landscape at the time of the simulations a whole set of preprocessing tools was produced.

Normally, for building their initial and boundary conditions, climate models that simulate present day climate can rely on datasets built from direct observations of the Earth's surface. These datasets represent the distribution of plant, soil texture, soil colour, ice, topography, coastline, and urban areas. Satellite and direct observations are blended together and interpolated to a gridded and georeferenced map (Hird et al., 2017; Langford et al., 2016), which is then used to run the present-day simulations. Unfortunately, paleoclimate studies cannot rely on any direct observation. Hence, information about terrain and vegetation have to be inferred from proxies and paleoclimate reconstructions.

In the framework of this thesis, observational datasets were used for the model customisation and pre-industrial simulations, while for the LGM we employed environmental reconstructions from proxies, that are detailed in the chapter 2, appendix A and in the next sections.

LGM Coastline

As illustrated in section 1.3.2, Clark and Mix (2002) assessed the eustatic sea level net decrease at the LGM between 120 and 130 m.

To produce the map representing coastline and topography for the LGM, the maps representing land elevation and bathymetry had to be modified and merged. The datasets employed in this operation are two datasets normally used by RegCM for present-day simulations. These two datasets are:

Land elevation Global Multi-resolution Terrain Elevation Data 2010 (GMTED2010; Danielson and Gesch, 2011) produced by the U.S. Geological Survey (USGS) and the National Geospatial-Intelligence Agency (NGA).

Bathymetry ETOPO1 (Amante and Eakins, 2009), produced by the National Geophysical Data Center (NGDC).

GMTED2010 and ETOPO1 are structured with the origin (i.e. the 0 m a.s.l.) at the present-day coastline, but the GMTED2010 values increase upward, while the ETOPO1 values increase downward. In order to compose the final coastline and elevation map the GMTED2010 was increased by 120 m (Clark and Mix, 2002) and the bathymetry map ETOPO1 was reduced by 120 m (Clark and Mix, 2002). Finally, these maps were merged together, to include those lands that outcropped at the LGM and that were submerged as the glacial melting begun about 21 to 19 ka BP (Ivy-Ochs et al., 2004).

The spatial resolution of the produced maps corresponds to the resolution of the original elevation models and is equal to 30 arcsec. In the domain, the maximum altitude is 4749 m a.s.l., while the minimum is 0 m a.s.l.. The produced map is shown in figure 3.2, where it is possible to appreciate how the northern Adriatic was affected by the sea level change.

RegCM's preprocessor tool then interpolates the produced topography to the two desired model resolutions of 12 and 50 km.

LGM Glaciers

For the glacier extent across the domain, the data produced by Ehlers and Gibbard (2004) was employed. This work analyses the Quaternary glaciation worldwide, but we selected only the Alps, the Apennines, the Balkans and the southern margin of the Fennoscandian ice sheet at the LGM. In this study, the height of glaciers was not considered. Indeed, considering the RegCM4 model resolution and the topography smoothing applied by the model, which does not allow us to capture narrow valleys, we think that adding the glaciers topography would not modify significantly our results.

LGM Vegetation

As exhaustively presented in section 2.2.2 and appendix A, several studies aim at defining the bioma characteristic of Europe during the Last Glacial (115 to 14.7 cal ka BP; Dahl-Jensen et al., 2013). The effect of complex orography and continentality, which strongly control the climate of Europe, affecting precipitation, humidity, and temperature, make this task particularly difficult.

Even though the domain chosen for this study is not particularly large, it includes several different climatic regions. Hence, the first step for the vegetation reconstruction required to divide the domain in sub-regions (figure 3.3):

a) northern Alpine,

b) southern Alpine,

    b.1) Southwestern and southeastern Alps

    b.2) West Garda Sector

c) Pyrenees, Apennines and Balkans,

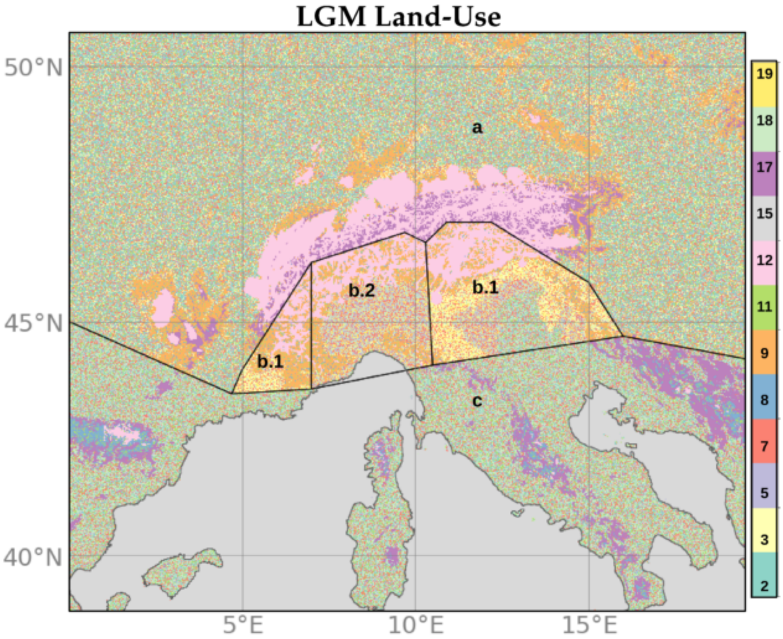

FIGURE 3.3: Reconstructed vegetation map. The black lines divide the sub-regions: (a) northern Alpine, (b.1) southwestern and eastern Alps, (b.2) West Garda Sector, and (c) Pyrenees, Apennines and Balkans. Every plant type is defined according to its corresponding BATS code, as shown in the colour scale on the right. In particular, glaciers are represented in pink. The percentage of every plant type for each sub-region and altitudinal band is shown in tables 3.2 and 3.3.

The boundary between northern and southern Alps replicates the Alpine weather divide used by Becker et al. (2016).
Each region is further divided into altitudinal bands chosen specifically for each area (table 3.2), according to latitudinal range, average slopes aspect, and air temperature. Then, a bioma, made by an association of plant types (table 3.3) is assigned to each altitudinal band based on a literature review. The plant types in every bioma are (spatially) randomly distributed.
A precise reconstruction of the vegetation distribution is extremely important, since the land surface models drive the exchange on energy and water fluxes between the atmosphere and the land surface. Every PFT is defined by optical properties, capability of water uptake, effect on heat, moisture and momentum fluxes. Thus the PFT distribution strongly affects the simulation outputs, in particular air temperature and evaporation.

The method employed to define the bioma was developed following a trial and error approach, in order to avoid that the simulated fields replicate the PFTs distribution generating non-uniform gradients in the model outputs. The bioma are defined to ensure spatial variability to the vegetation and continuity between adjacent regions. In this way water and energy fluxes patterns do not show large contrasts between sub-regions and elevation bands.

Regions		**Bioma**	**Altitudinal Bands**
Northern Alps		Boreal Steppa	0 to 700 m
		Forest - Tundra	700 to 800 m
		Tundra	800 to 1200 m
		Desert	> 1200 m
Southern Alps	Western and Eastern Sector	Steppa	0 to 110 m
		Steppa - Forest	110 to 130 m
		Boreal Forest	130 to 700 m
		Forest - Tundra	700 to 900 m
		Tundra	> 900 m
	West Garda Sector	Steppa	0 to 110 m
		Steppa - Forest	110 to 700 m
		Forest - Tundra	700 to 900 m
		Tundra	> 900 m
Mediterranean		Steppa	0 to 900 m
		Tudra	900 to 1500 m
		Desert	> 1500 m
North Africa		Steppa - Forest	0 to 300 m and 1200 to 1500 m
		Temperate Forest	300 to 120 m
		Steppa	> 1500 m
Desert		Steppa	1000 to 1500 m
		Desert	0 to 1000 m and > 1500 m

TABLE 3.2: Subdivision of every region into altitudinal bands and the corresponding bioma.

As input data, RegCM requires two land-use datasets: one based on the CLM standards (table 3.1) and one based on the BATS standards (Dickinson et al., 1993). The input in BATS format (figure 3.3) is thus defined as a two dimensional NetCDF file where the plant types are (spatially) randomly distributed according the to percentage attributed to sub-regions and altitudinal bands. The CLM input, on the other side, requires a three dimensional NetCDF file where the three dimensions are latitude, longitude and PFT. The PFT levels are defined by a percentage of a given PFT in every grid-cells, so that the sum of the various PFT layers in a singular cell is 100 %. As both CLM and BATS include the glacier distribution in their land-use representations, the ice extent was defined according to the work of Ehlers and Gibbard (2004).

Another important aspect of the vegetation is its evolution through the year, which is described by the time-variable Leaf Area Index and Steam Area Index variables. Ideally, we would use satellite data, but since they are not available for the LGM, we substitute them with present-day analogues. For each plant type in the vegetation map, a corresponding present-day location with similar climatic characteristics of the LGM was identified. The choice fell to those regions that maintain the daily light cycle trough the year, since the domain of study is at a mid latitude. For each of these present-day locations, the LAI and SAI time-varying properties are assumed to be valid for the corresponding LGM vegetation cells. In this way, the LGM vegetation is based on real-world, present-day, high-quality data.

Bioma	**Plant Type**	%	**BATS**	**CLM**
Steppa	Short Grass	20	2	14
	Deciduous Broadleaf Tree	10	5	8
	Semi-Desert	15	11	1, 14
	Deciduous Shrub	35	17	11
	Tall Grass	20	7	14
Boreal Steppa	Short Grass	35	2	13
	Tall Grass	15	7	13
	Deciduous Broadleaf Tree	10	5	9
	Semi-Desert	10	11	1, 13
	Evergreen Needleleaf Tree	10	3	3
	Tundra	10	9	12, 13
	Deciduous Shrub	10	17	12
Steppa-Forest	Deciduous Broadleaf Tree	20	5	8, 9
	Tall Grass	25	7	13, 14
	Deciduous Shrub	25	17	11, 12
	Mix Woodland	15	18	2, 3, 4, 8, 9, 10, 11, 12
	Forest/Field	15	19	2, 3, 4, 8, 9, 10, 11, 12, 13, 14
Temp. Forest	Deciduous Broadleaf Tree	20	5	8
	Tall Grass	15	7	14
	Deciduous Shrub	10	17	11
	Mix Woodland	20	18	2, 4, 8, 10, 11
	Forest/Field	10	19	2, 4, 8, 10, 11, 14
	Evergreen Neadleleaf Tree	25	3	2
Boreal Forest	Evergreen Needleleaf Tree	40	3	3, 4
	Tall Grass	20	7	13
	Deciduous Shrub	10	17	12
	Mix Woodland	20	18	3, 9, 10, 12
	Forest/Field	10	19	3, 9, 10, 12, 13
Forest-Tundra	Evergreen Needleleaf Tree	25	3	3, 4
	Tundra	50	9	12, 13

	Deciduous Shrub	10	17	12
	Evergreen Shrub	10	9	12
	Deciduous Broadleaf Tree	5	5	9
Tundra	Desert	10	8	1
	Tundra	80	9	12, 13
	Semi-Desert	10	11	1, 13
Desert	Desert	80	8	1
	Semi-Desert	20	11	1, 13
Glaciers	Glaciers	100	12	1
Ocean	Ocean	100	15	1

TABLE 3.3: Percentages of plant types per every bioma with the corresponding BATS (Wilson et al., 1987) and CLM codes (Oleson et al., 2013).

3.2.3 RegCM4.7 model customisation

In order to adapt the RegCM4.7 to work for LGM conditions over the southeastern Alpine region, we calibrated the model, forced with ERA-Interim data (Dee et al., 2011), against present-day near-surface air temperature (i.e. the temperature at the height of 2 m) and total precipitation observations.

ERA-Interim is a reanalysis dataset produced by the European Centre for Medium-range Weather Forecasts (ECMWF). It is uniform in time and space, physically coherent and consistent with observations. The ERA-Interim dataset is produced from weather model simulations of the past, constrained by observations. As a consequence, ERA-Interim produces very high quality and consistent boundary conditions. For this reason, it is often used for the so called *perfect boundary simulations* that are used for validating the outputs of regional climate models.

The E-OBS (Haylock et al., 2008) gridded observational dataset was used as reference during the customisation phase of the RegCM simulations. E-OBS covers the whole European and Mediterranean region and consequently the entire simulated domain. Two other precipitation dataset, EURO4M (Isotta et al., 2014) and ARCIS (Pavan et al., 2018), were used as a further check for the southeastern Alps. These datasets are characterised by very high station density, high-resolution and high-quality, which are important factors especially when validating precipitation.

11 test simulations were performed with a model resolution of 12 km on a Lambert Conformal Conic projection. Model customisation was manually performed by simulating 5-year chunks and comparing them, after the removal of a 1-year spin-up period and the buffer zone, with precipitation and temperature observations from the E-OBS dataset (Haylock et al., 2008) for the randomly chosen period 1980-1985. Modelled near-surface air temperature and total precipitation were assessed by

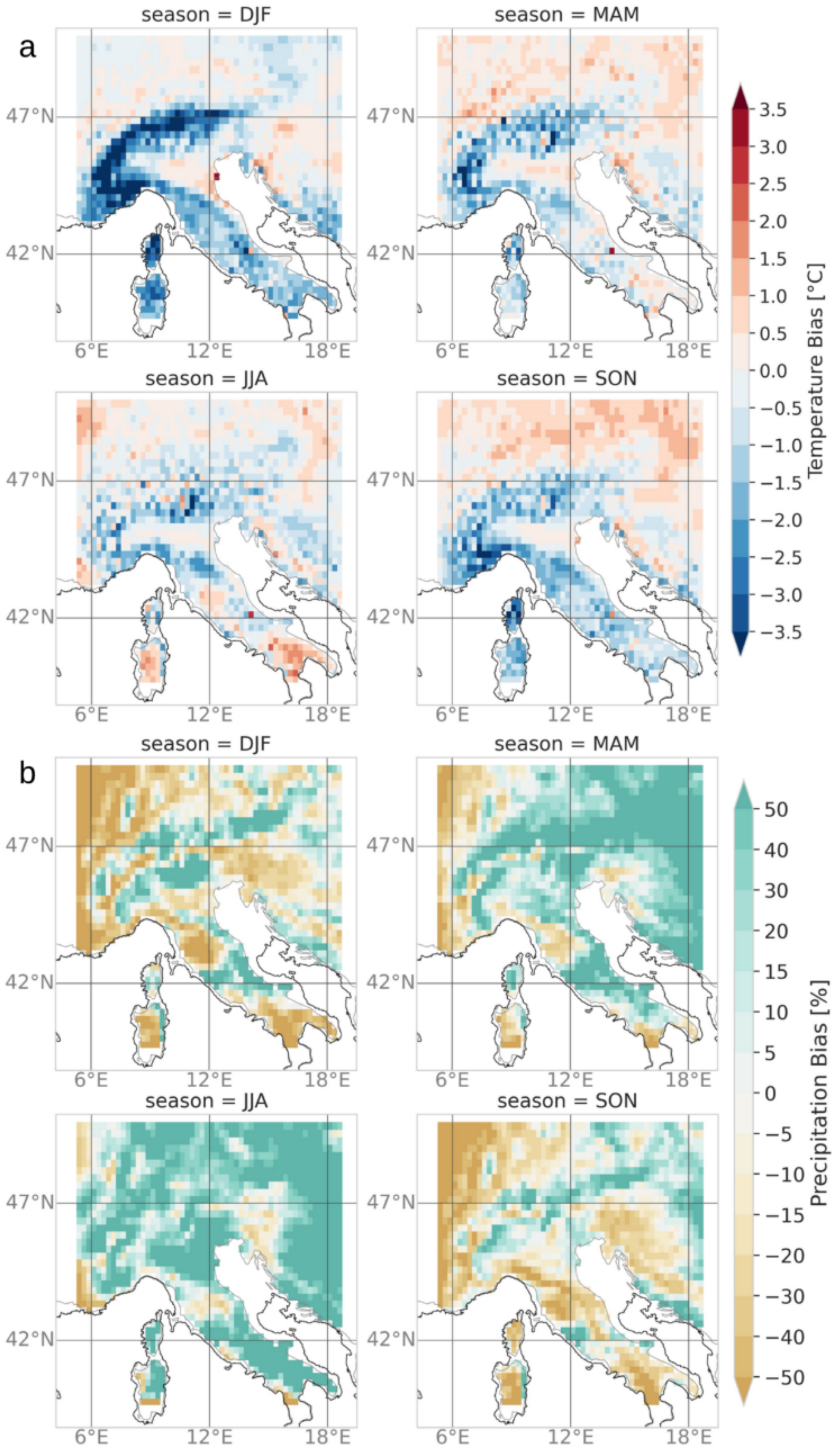

FIGURE 3.4: Difference between present-day RegCM simulation forced with ERA-Interim data and the observational dataset E-OBS, for near-surface air temperature (a) and precipitation (b), in the period 1980-1985. This difference is calculated from the best simulation among 11 tests.

means of seasonal averages and calculating the bias for both the variables. Figures 3.4 shows the spatial distribution of the mean seasonal model biases for near-surface air temperature and total precipitation compared to the E-OBS dataset. The RegCM4 model data have been interpolated onto the 0.22° E-OBS grid. The optimisation of the RegCM4 model system was performed by testing different values in the moisture (Pal et al., 2000) and Tiedtke (Tiedtke, 1996) cumulus schemes (table 3.4).

Model customisation was managed with particular attention for the southeastern Alps where the Tagliamento glacier, the object of study of this thesis, is located. Indeed, partly high bias is found in the western Alps, while the southeastern Alps shows more contained differences between E-OBS and modelled data (3.4).

In general the RegCM4 underestimates the observed temperatures during all the seasons, with largest bias during winter and over the Alps. On the contrary, RegCM4 in the flat regions slightly overestimates the temperatures. Both the pattern and the values of the temperature bias are in line with the results obtained by Smiatek et al. (2016) who run 13 high-resolution RCMs in the alpine region within the CORDEX experiment Giorgi et al., 2009. Concerning the precipitation, RegCM4 produces wetter conditions (+50 %) compared to the observed data in particular during spring and summer, while in autumn and winter the RegCM model locally underestimate the precipitation. A similar behaviour was also noted by Kotlarski et al. (2014) in the framework of the EURO-CORDEX project, who assessed a set of RCM simulations driven by ERA-Interim data.

The model biases shown in figure 3.4 are thus considered reasonable in the context of regional climate model simulations in the Alpine region (Kotlarski et al., 2014; Smiatek et al., 2016) and can be partially explained with the shortage of weather stations at high elevation, a lack in the gauge undercatch correction in the observed data (Adam and Lettenmaier, 2003) and also by the natural climate variability since, for the model customisation we simulated 5 years only.

Sheme	**Parameter**	**Value**	Description
Explicit moisture (Pal et al., 2000)	qck1land	5.0×10^{-4}	Autoconversion Rate for Land
	qck1oce	2.5×10^{-4}	Autoconversion Rate for Ocean
	cevaplnd	1.0×10^{-3}	Raindrop evaporation rate coefficient land
	cevapoce	1.0×10^{-3}	Raindrop evaporation rate coefficient ocean
Tiedtke Cumulus (Tiedtke, 1996)	entrpen_lnd	1.75×10^{-3}	Entrainment rate for penetrative convection
	rhebc_lnd	0.9	Critical rh below cloud for evaporation iconv=4

TABLE 3.4: RegCM4 schemes and parameters modified during the customisation phase and their final configuration.

3.2.4 Nesting the RCM into the ESM

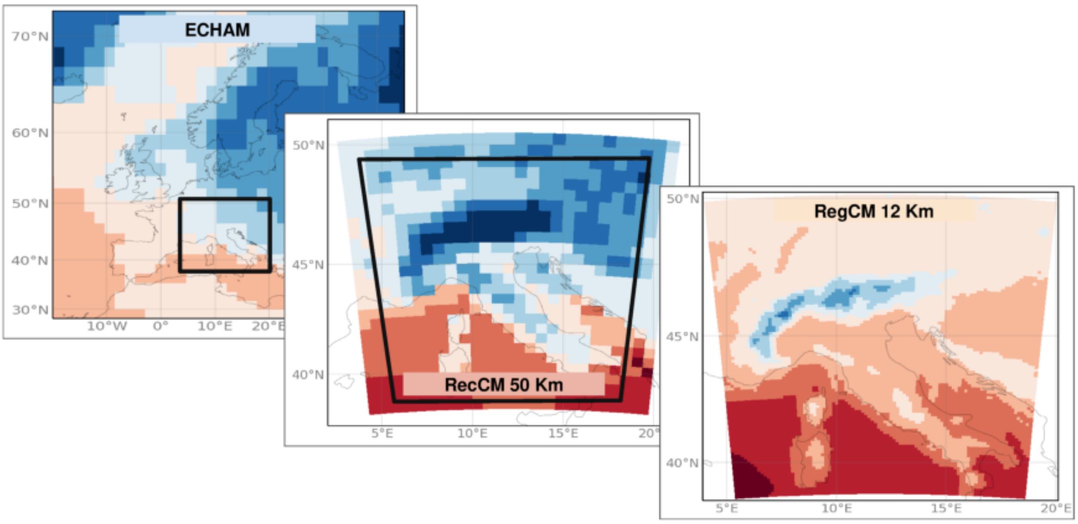

FIGURE 3.5: The applied nesting chain. The models are represented from the low-resolution MPI-ESM-P to the high-resolution RCM RegCM4.7. The black boxes indicate the domain of the higher-resolution simulations.

Figure 3.5 shows the applied nesting chain. Whenever a small-scale, high-resolution simulation is nested into a larger-scale, low resolution simulation, there is a risk of introducing artifacts and inconsistencies. The larger the ratio between the resolutions of the driving and the nested models, the higher this risk is. According to Denis et al. (2003), this ratio should be lower than about 12. However, the maximum ratio used in most RCM applications is about 10, in order to obtain good downscaling abilities (Giorgi et al., 2015) without additional artifacts. If the resolution ratio is higher than this value, it is advisable to pursue a multiple nested approach, where an intermediate resolution RCM is forced by a ESM and, in turns, drives a second high-resolution RCM (Giorgi et al., 2015).

The driving MPI-ESM-P simulation was performed by the MPI with a resolution of $1.9\,^{\circ} \times 1.9\,^{\circ}$, about 200 × 150 km considering the domain average latitude and longitude, while the desired output resolution is 12 km. In this case the resolution ratio would fall between 12.5 and 16.7 , far too high for a good downscaling. Thus an intermediate simulation was set with a resolution of 50 km. In this way, the resolution ratio between MPI-ESM-P and the intermediate RegCM simulation ranges from 3 to 4, while the second nesting has a ratio of 4.3.
The nested fields require a given amount of cells to develop their patterns. The band of cells on the boundary of the nested simulation is called buffer zone and its width is dependent upon the chosen lateral boundary condition scheme. The domains of the two RegCM simulations were spaced by a band of grid cells that allowed the 50 km simulation to reach the stability for its fields before driving the high-resolution simulation. The employed lateral boundary condition scheme is

based on the relaxation, exponential technique, with 5 dot and cross point slices on the relaxation boundary, and 3, 2 and 1 nudge values for high, medium and low range respectively.

Before starting the simulations, the MPI-ESM-P data needed to be converted from GRIB (GRIdded Binary), a data format that stores weather and climate data as grid-point values expressed in binary form, to NetCDF (Network Common Data Form), the format required by the RegCM model system for the input data. The grid was then converted from spectral to grid-point and divergence and vorticity were transformed to the respective zonal and meridional wind components. These operations were performed with the Climate Data Operators software (CDO; Schulzweida, 2019).

3.3 Simulation set-up

Once the preprocessing phase was completed, four 20 years long simulations were performed: two for the PC and two for the LGM, at 50 km and 12 km of resolution. As detailed in section 3.2.4, the simulations at 50 km resolution were employed to drive those at 12 km of resolution. The simulations were ran on the ICTP ARGO cluster (`http://argo.ictp.it/`) using, on average, 120 processor cores.

Among the different customisation options, it was found that the best results were obtained by coupling the Boundary layer scheme from McCaa and Bretherton (2004) and the cumulus convection scheme over land and ocean from Tiedtke (1996). The simulations were performed with constant greenhouse gasses, whose values are shown in the table 3.5 for both PC and LGM. The orbital parameters calculated according to the equation proposed by Berger (1978) for the PC and LGM are the eccentricity of the Earth's elliptical orbit about the Sun, the obliquity of the Earth's equatorial plane with respect to the Earth's orbital plane and the longitude of perihelion. To the orbital PC values a lag of 20 kyr (the maximum allowed by the model) was set in order to obtain the LGM orbital configuration (table 3.6). According to Clark et al. (2009), the insolation changed between the LGM and the PC by 40 W m^{-2} at the latitude of 45°N.

	CO_2	CH_4	N_2O
PC	280	650	270
LGM	185	350	200

TABLE 3.5: Greenhouse gasses values at PC ad LGM.

3.4 Postprocessing

The model outputs required a careful evaluation before starting the analysis of the results. Indeed, some problems were detected only running short, 5-years long

	Year (A.D.)	Eccentricity	Obliquity	Longitude of Perihelion
PC	1850	0.016764	23.4593	280.327
LGM	-20000	0.018800	22.7986	278.768

TABLE 3.6: Orbital parameters for the PC and LGM simulations

simulations. Moreover, once the final simulations were completed, the data required some corrections with the aim to compare LGM and PC datasets.

3.4.1 Troubleshooting

The final version of the PC and LGM simulations was reached after three previous problematic simulations. More in detail, the problems were caused by:

Plant type distribution scheme It turned out to be particularly important to introduce the concept of the bioma, defined by a random distribution of different plant types for sub-regions and altitudinal bands (section 3.2.2). Indeed the application of a singular plant type per sub-region (or even for a small portion of sub-region) determined contrived patterns for several variables of the model outputs. The choice of the bioma, on the contrary, solved this problem by allowing a smooth transition between regions with different bioma, given the fact that the percentage of the plant types that constitute the bioma are progressively scaled from one climatic region to another.

Sea Surface Temperature in the north Adriatic The ESM resolution is too coarse to capture the Adriatic basin as a sea. Thus the MPI-ESM-P temperature calculated for the North Adriatic shows values typical of the land surface. Temperature over land is on average characterised by more extreme values, both colder and warmer than over the sea. Thus the MPI-ESM-P surface temperature was bias corrected with ERA-Interim data, which, being calculated from high-resolution models and observations, is able to capture the Adriatic sea and to pass the information to the new MPI-ESM-P-modified SST dataset.

RegCM-interpolated topography The topography NetCDF file is produced by downscaling a high-resolution Digital Elevation Model (DEM) to the resolution required by the model. The downscaling applies an interpolation technique to the input DEM, hence LGM and PC domain files do not only differ by 120 m of elevation, but being produced from two different datasets with a non linear process they show slightly different topographic features. This makes it impossible to compare LGM and PC datasets, as the climatic variables are highly sensitive to orography. Thus the LGM topography file was created by directly modifying the PC RegCM-produced topography. The method, detailed in section 3.2.2, was applied on the RegCM-interpolated domain file of the PC.

Once these problems were fixed the final 20-years long simulations were run.

3.4.2 Variables

Aim of this thesis it to study the LGM in the southeastern Alps, but to do this it is important to also study the difference from a reference time, the pre-industrial. For the sake of clarity, before comparing the LGM and PC simulations the units of some variables were converted: Temperature was converted from Kelvin to Celsius, while all the fluxes expressed in $\mathrm{kg^2\,m^{-1}\,s^{-1}}$ (precipitation, evaporation, melting and runoff) were converted to $\mathrm{mm\,d^{-1}}$.
In order to compare LGM and PC sea level pressure and near-surface air temperature it was required to take into account the 120 m of altitudinal difference occurred between the two historical times due to the sea-level change. Thus, concerning the sea level pressure, 11 hPa were added to the PC values. This value was calculated considering the atmospheric pressure decrease as a linear function of the elevation change. Indeed the atmospheric pressure decreases to about 500 hPa within the first 5.5 km in the troposphere. The PC near-surface air temperatures were reduced by 0.78 °C, using the environmental lapse rate of 0.65 °C/100 m.
The LGM elevation has been used as a reference and the PC sea-level pressure and near-surface air temperature were rescaled to the LGM elevation. In this way it was possible to compare PC and LGM data.

Annual, seasonal and monthly averages over the 20 years simulation were calculated for every variable, after the removal of a 1-year spin-up period and the buffer zone. The main tools produced to analyse the data are the maps of averaged values for PC, LGM and their anomalies as well as line-plots showing the monthly variability of the individual variables. The results of the simulations, after the application of the postprocessing, are presented in the chapter 4.

Chapter 4

Analysis of the Climate simulations

In this chapter, the results obtained during the development of this PhD project will be discussed. Finally, after a postprocessing phase, two datasets, one for the PC and one for the LGM, were analysed and compared. In this chapter we pass through the main variables that describe the atmospheric circulation in the MPI-ESM-P (section 4.1) and RegCM4 (section 4.2), validate the model simulations versus land global observations (CRU; Harris et al., 2013) and reanalysis data (ERA-Interim; Dee et al., 2011) and qualitatively assess the RegCM4 added value (section 4.4). Evaluation of models performance (section 4.1.1 and 4.2.1) was performed by comparing ERA-Interim/CRU observations and pre-industrial data. Even if these two datasets refer to different times, we assume that the climate conditions differences are minimal. Hereafter, the differences between LGM and PC simulations are referred to as *anomaly* and the difference between the observation/reanalysis dataset and the climate models are named *bias*.

4.1 MPI-ESM-P

In the current section, the MPI-ESM-P model simulations are analysed for the PC and LGM runs. PC simulation is compared with present-day observations for temperature and precipitation and reanalysis data for wind fields. The LGM model results are compared with the PC and are then analysed in relation to other modelling studies and proxy-based reconstructions, in order to assess the large scale atmospheric forcing that was used to drive the RegCM4 model simulations over the southeastern Alps.

4.1.1 MPI-ESM-P Model Validation

From the comparison of ERA-Interim and pre-industrial 200 hPa wind fields (figure 4.1), only small differences emerge. The jet stream position in the Atlantic Ocean is placed slightly northern in ERA-Interim data than in the PC. Winds are mainly westerly and northwesterly in both the simulations and no blocking is recorded over Scandinavia. This is the main difference with the LGM simulation. The MPI-ESM-P model tends to slightly underestimate the maximum wind speed in particular over North Africa and during summer along Scandinavia.

An analysis of the 850 hPa winds (figure 4.2) highlights a larger model bias compared to the 200 hPa levels (figure 4.1). In particular, in the ERA-Interim dataset the jet stream branch that blows along the Scandinavian coast is much stronger than in the PC simulation and is present all year-round with a southwest-northeast direction. In the ERA-Interim data the wind field over the Iberian and Mediterranean regions is weaker than in the PC, probably due to differences in the North Atlantic jet stream pattern. This bias is minimum in autumn. Winter is the month with the largest bias, that is likely caused by the southern position of the North Atlantic jet in the MPI-ESM-P dataset. This causes an anticyclonic curvature in the PC winds over central Europe and a cyclonic circulation south of Iceland. In both ERA-Interim and PC datasets central Europe is hit by strong westerly winds. At this pressure level the winds reach Europe from west/southwest and this differs from the LGM when 850 Pa winds were mainly westerly/northwesterly.

For what concerns the temperatures (figure 4.3), the CRU and PC values follow similar patterns and present similar values, but the PC shows smaller details compared to the observation that, on the contrary, better represent the topography-induced effect. Differently from temperatures, precipitation (figure 4.4) reveals a larger bias between CRU observational dataset and PC model output. PC model simulation captures much fewer details than the observation as a consequence of its coarser resolution. PC patterns are thus smoother both in the spatial patterns and for what concerns values distribution. In particular, the largest bias is recorded along the western coast, Pyrenees, Alps, Apennines and Balkans, proving that the orographic precipitation is largely affected by the model bias. Nevertheless, even if the detail is low, the PC simulation shows a wet region in the Alps. The MPI-ESM-P model tends to underestimate summer precipitation and overestimate winter precipitation.

4.1.2 MPI-ESM-P: PC vs. LGM Winds

The wind analysis was performed at two different pressure levels, 200 hPa and 850 hPa, in order to capture aspects of both the lower and upper troposphere. At 200 hPa the domain is interested by westerly and northwesterly winds both at LGM and PC (figure 4.1). The LGM 200 hPa winds (figure 4.1) are strongly influenced by the Scandinavian Ice Sheet, which blocks the eastward passage of air masses particularly during summer, when the snow cover is minimum and the albedo difference between the ice sheet surface and the bare ground is maximum. Westerly air masses from the Atlantic Ocean bend around the southern margin of the Scandinavian Ice Sheet. This

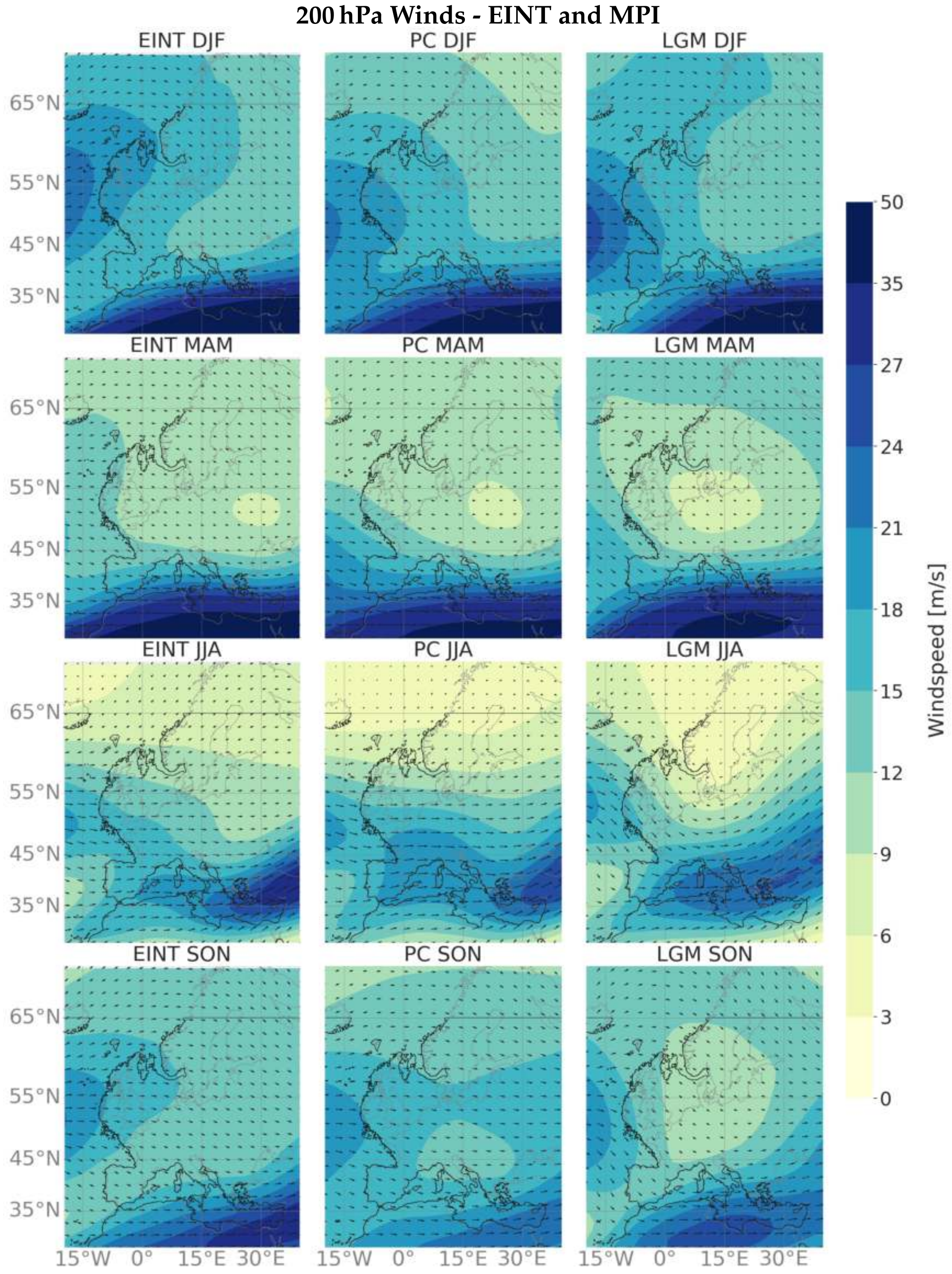

FIGURE 4.1: ERA-Interim (left) and MPI-ESM-P 200 hPa wind field for PC (center) and LGM (right) seasonal means.

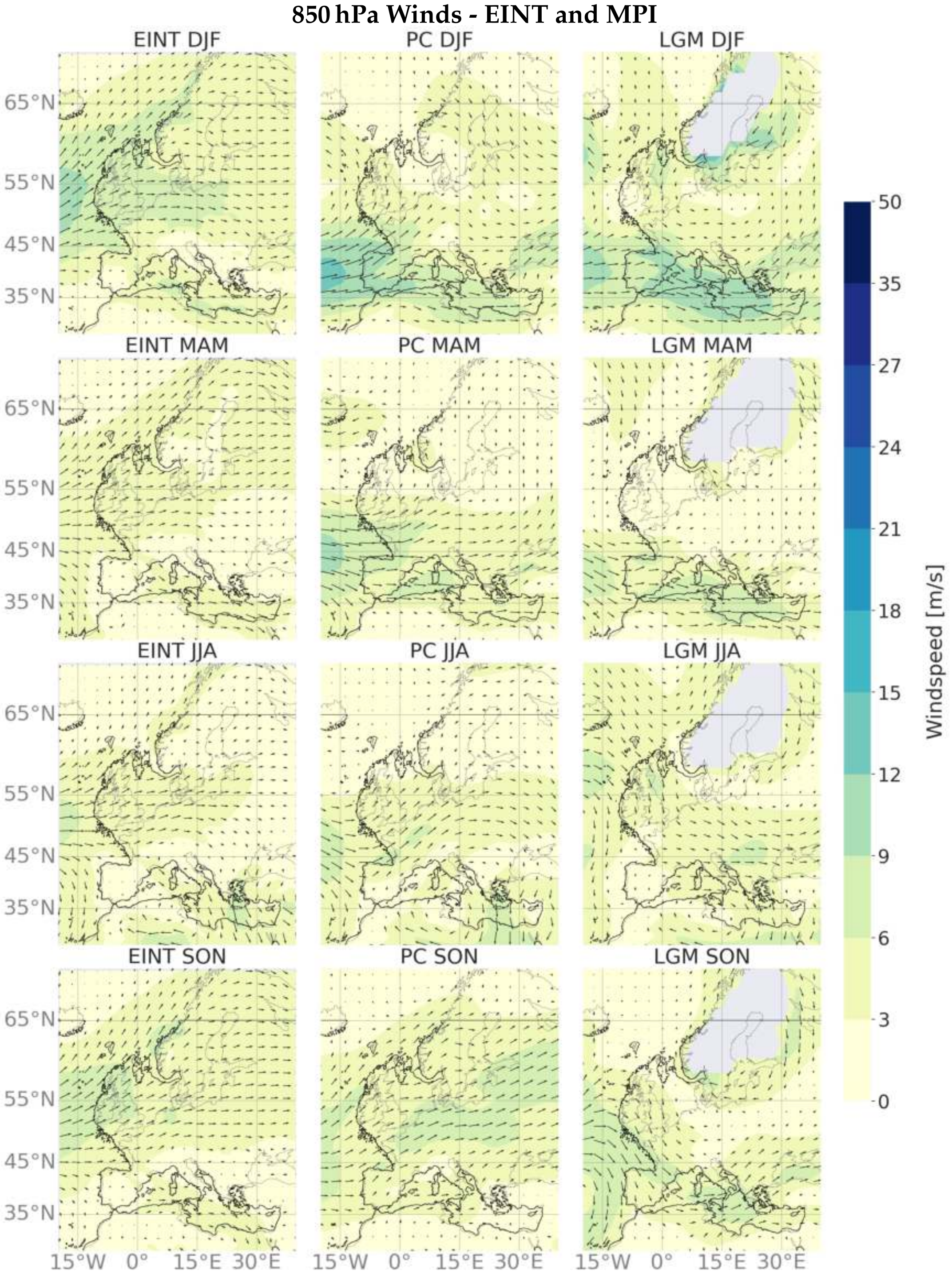

FIGURE 4.2: ERA-Interim (left) and MPI-ESM-P 850 hPa wind field for PC (center) and LGM (right) seasonal means. The grey area corresponds to the Scandinavian Ice Sheet.

is consistent with Ludwig et al. (2016), who noted that the MPI-ESM-P storm track produced increased precipitation in Island and western Scandinavia as a consequence of the Scandinavian Ice Sheet blocking. The same pattern, but with weaker winds and southerly displaced, also happened in autumn during the LGM. In particular, LGM summer and autumn present enhanced winds between North Africa and the Mediterranean basin. While winter is the season with the smallest LGM-PC anomaly, but is also characterised by stronger average 200 hPa windspeed over the domain.
In figure 4.1, the location of maximum windspeed in the Atlantic region corresponds to the upper-level North Atlantic jet stream. The PMIP3 project models analysed by (Ludwig et al., 2016) reproduced two main jet stream pattern across the Atlantic ocean: one characterised by strong zonal winds towards Europe and one, typical of the MPI-ESM-P model (the one used to force the RegCM4 simulations in this study), characterised by southwest-northeast tilt of the jet across the Atlantic region that bents southward over Europe and descends in the Mediterranean region. In both cases, the North Atlantic jet stream is primarily driven by the stationary wave pattern arising from an orographic barrier as the NAIS and secondly by greenhouse gasses concentration, orbital forcing and SST (Merz et al., 2015). In figure 4.1 the position of the jet stream is consistent with what highlighted by Ludwig et al. (2016) for MPI-ESM-P LGM simulations.

The wind field in the lower troposphere (figure 4.2) shows marked differences between PC and LGM. As for the upper-level winds, the Scandinavian Ice Sheet influences the wind field generating at 850 hPa an anticyclonic circulation in the vicinity of ice sheet southern and eastern margins. This wind pattern is often related to enhanced dust storm activity and loess deposition as reported by Florineth and Schlüchter (2000) and Schaffernicht et al. (2020).
Concerning the LGM low-level jet, stronger westerly and northwesterly winds entered the Mediterranean basin compared to the PC, when the wind had a more southwesterly component. At the LGM the strongest winds in Europe occurred over the Mediterranean basin and not over central Europe as at the PC, indicating a southward shift of the jet stream over Europe between the two time periods. Thus, even if among the ESMs, the MPI-ESM-P do not simulate a southward shift of the North Atlantic jet over the Atlantic ocean (Ludwig et al., 2016), however, it produces a southward displacement directly over Europe. During LGM spring and summer the air masses in the Mediterranean region were purely zonal, while in autumn and winter they were characterised by a northwesterly component that brought cold polar air in the western Mediterranean as hypothesised by (Kuhlemann et al., 2008).
At the LGM, during all the seasons, but in summer, the storm track split over the Adriatic Sea, with one branch directed north around the eastern Alps, towards the Scandinavian Ice Sheet as suggested by Florineth and Schlüchter (2000), Ludwig et al. (2016) and Monegato et al. (2017). During summer the westerlies in central Europe

were particularly strong and a cyclonic circulation developed on the North African coast.

4.1.3 MPI-ESM-P: PC vs. LGM Temperature

The MPI-ESM-P reproduces colder temperature at the LGM compared to the PC (figure 4.3), with annual mean values being 0.6 °C and 9.5 °C for the LGM and PC respectively, with an average anomaly equal to 8.9 °C. This value is higher compared with the global reconstruction of Annan and Hargreaves (2013) and Strandberg et al. (2011), but can be accepted considering that the MPI-ESM-P domain is clipped and centred on Europe and for a large part it is influenced by the presence of the LGM Scandinavian Ice Sheet. Also the In particular, at the LGM over the Scandinavian Ice Sheet temperatures were more than 20 °C colder than at the PC, while in the Mediterranean realm the anomaly was much smaller (−4 to −5 °C), in agreement with pollen-based data (Bartlein et al., 2010) and climate model simulations (CCSR1, LMDZLR, HadAM Jost et al., 2005).

Summer anomalies fit with the proxy reconstruction performed by (Wu et al., 2007) better than winter anomalies, fact that was also observed by Jost et al. (2005). Indeed the MPI-ESM-P tends to overestimate the winter temperature anomaly. Across the domain there is an evident temperature anomaly gradient, also found by Strandberg et al. (2011), who simulate the LGM climate using the Community Climate System Model 3 (CCSR1) (Collins et al., 2006). This gradient is caused by the combined effect of increased albedo and surface elevation of the Scandinavian Ice Sheet and the latitudinal insolation difference, with the sub-tropics being less affected by changes in orbital parameters than the sub-polar region (Luetscher et al., 2015).

It was also observed, in agreement with the CCSM3 simulation (Strandberg et al., 2011), that a largest seasonal anomaly occurred in winter (−10.2 °C compared to the −7.5 °C of summer) probably as a consequence of the sea-ice albedo feedback.

4.1.4 MPI-ESM-P: PC vs. LGM Precipitation

The MPI-ESM-P simulated precipitation anomaly denotes drier condition at the LGM compared to the PC particularly over the Scandinavian Ice Sheet (−80 %), eastern (−40 %) and central Europe (−30 %) during all the seasons but summer, when central Europe was wetter compared with the PC. On the contrary, the Iberian peninsula at the LGM was always wetter than at the pre-industrial time as well as the Mediterranean region and North Africa, indicating changed position of the Atlantic westerly winds.

When compared to proxy data the precipitation values produced by the MPI-ESM-P model determine too humid conditions along the western Iberian coast (Ludwig et al., 2016) particularly during winter (figure 4.4. An analogous pattern was also found

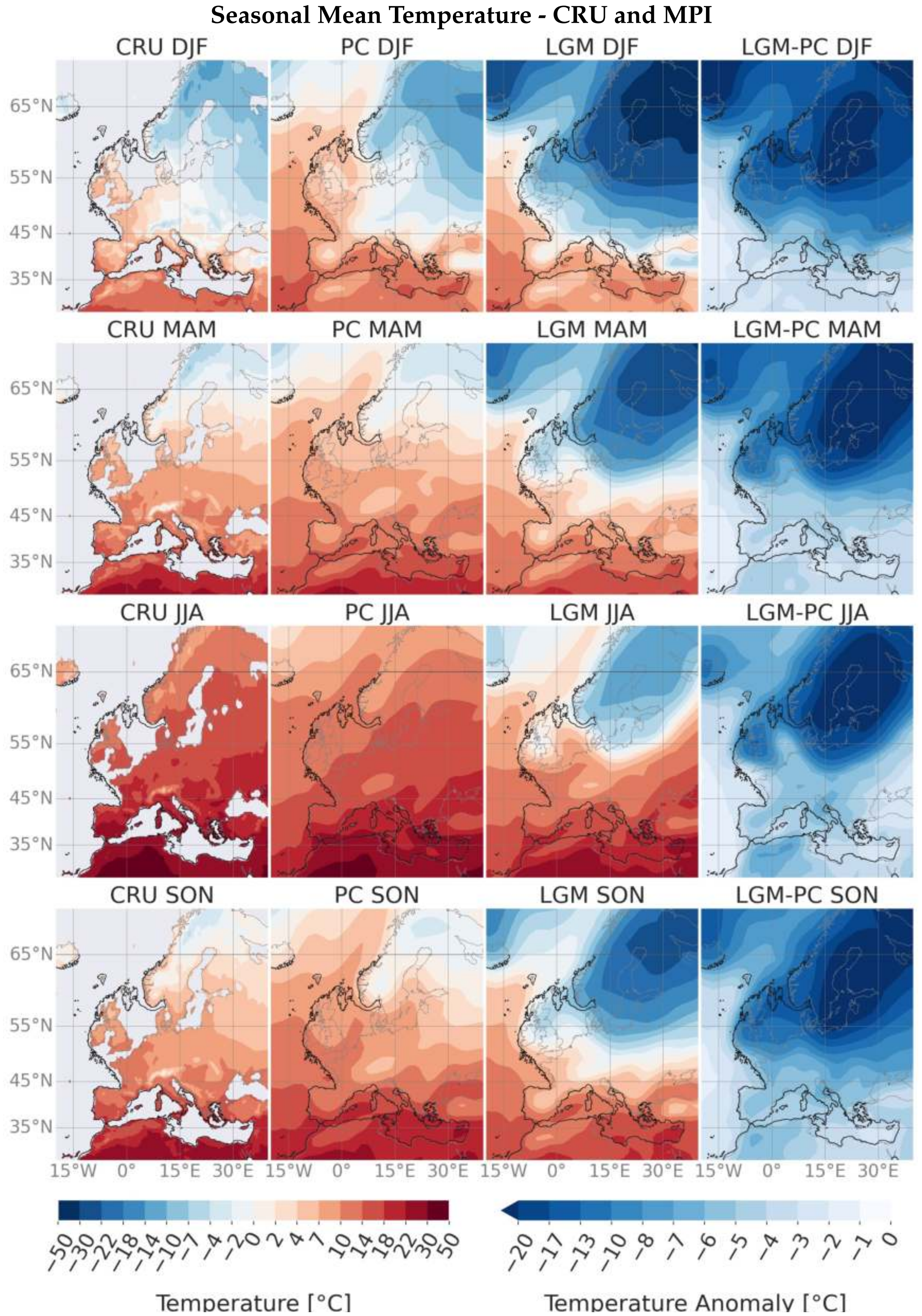

FIGURE 4.3: CRU (left) and MPI-GCM-P seasonal mean temperature in °C for PC (center-left), LGM (center-right), and anomaly (right).

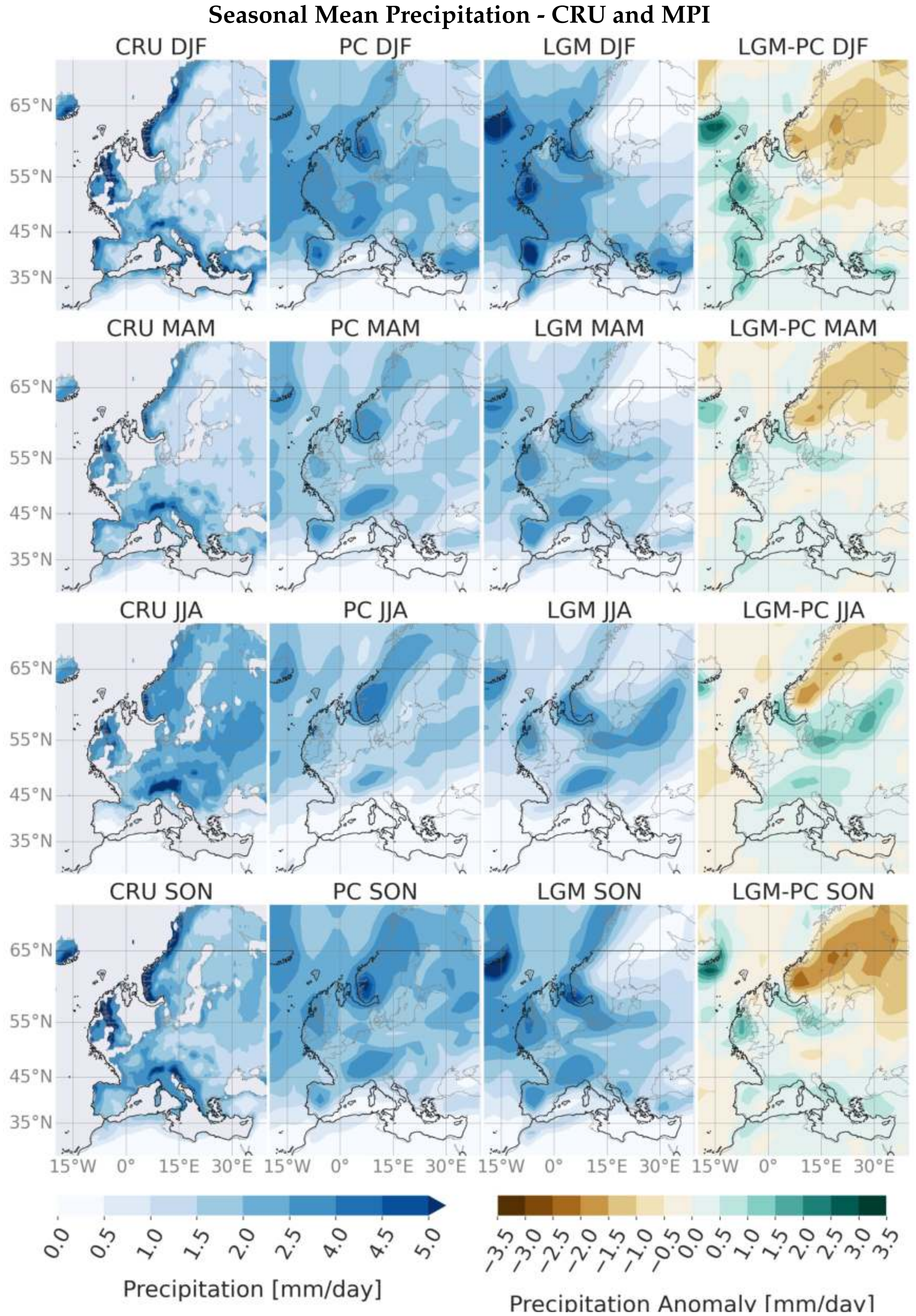

FIGURE 4.4: CRU (left) MPI-GCM-P seasonal mean precipitation in or PC (center-left), LGM (center-right), and anomaly (right).

by Strandberg et al. (2011). During spring, summer and autumn the southern flank of the Scandinavian Ice Sheet presented a positive precipitation anomaly. This was also found by (Ludwig et al., 2016) analysing four ESMs (included the MPI-ESM-P) and the increased precipitation was attributed to the branch of the Mediterranean jet that, passing east of the Alps, caused orthographic precipitation on the Scandinavian Ice Sheet margin. The 20-years chunk from the LGM MPI-ESM-P simulation we are analysing shows stronger precipitation anomaly compared with other PMIP3 models (Ludwig et al., 2016), and in general the MPI-ESM-P model presents differences when compared with proxy (Annan and Hargreaves, 2013; Bartlein et al., 2010) due to both uncertainties in the proxy reconstructions and modelling parameterisations (Ludwig et al., 2018). Compared with the proxy reconstruction of Wu et al. (2007), the LGM MPI-ESM-P simulation is characterised by slightly wetter conditions.

4.2 RegCM4

In the current section, we followed the same approach pursued in section 4.1. First we analyse the RegCM4 PC model simulation with the CRU observations (temperature and precipitation) and ERA-Interim reanalysis data (winds), and then PC and LGM RegCM4 model outputs are compared.

4.2.1 RegCM4 Model Validation

The RegCM4 pre-industrial wind fields both at 200 hPa (figure 4.5) ad 850 hPa (figure 4.6) generally show a behaviour in line with the ERA-Interim dataset for what concerns wind speed and wind directions. Only a small difference in the wind direction is found in summer and autumn, when the ERA-Interim winds are more zonal than the PC ones.
In the upper troposphere the circulation over the domain is dominated by northwesterly winds and no information is added to the MPI-ESM-P PC data. On the contrary, in the lower troposphere, where the wind field is closer to the topography, the RegCM4 PC output is more detailed than the MPI-ESM-P model data.
In the PC model simulations winds at 850 hPa are stronger than in ERA-Interim data, particularly over the Alps and in the Po Valley, and descend the Italian peninsula with a northwest-southeast direction. The ERA-Interim data highlights the development of a lee-side cyclone in the Gulf of Genoa, always but in winter. These difference in the PC and ERA-Interim wind patterns are possibly ascribable to the different North Atlantic jet between the two datasets (section 4.1.2).

With regards to the temperature (figure 4.7), the CRU dataset, having a resolution lower than the RegCM, shows slightly warmer temperatures than the PC in particular over the mountain chains. In general, PC RegCM simulation correctly represents

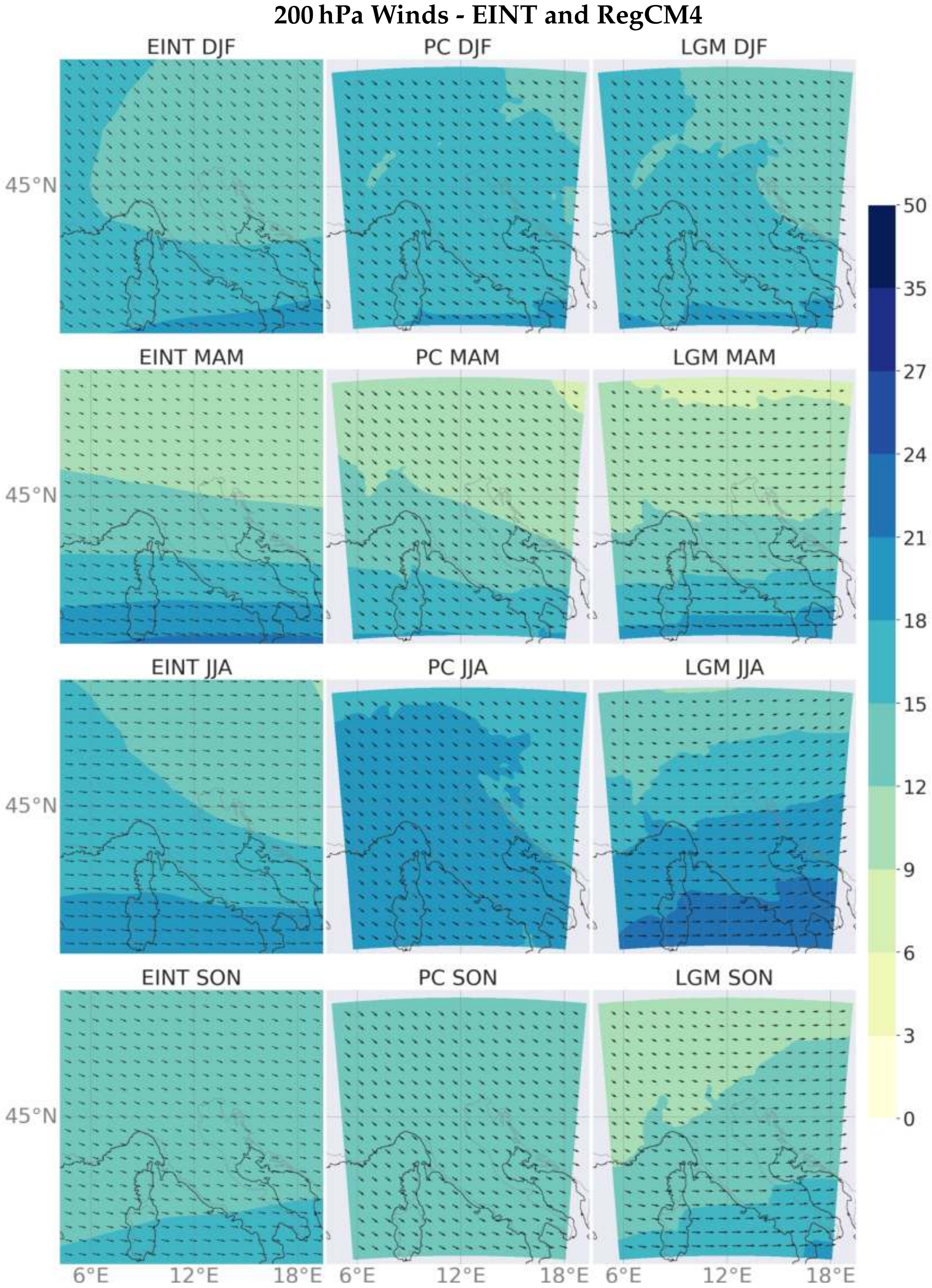

FIGURE 4.5: ERA-Interim (left) and RegCM4 200 hPa wind field for PC (center) and LGM (right) seasonal means.

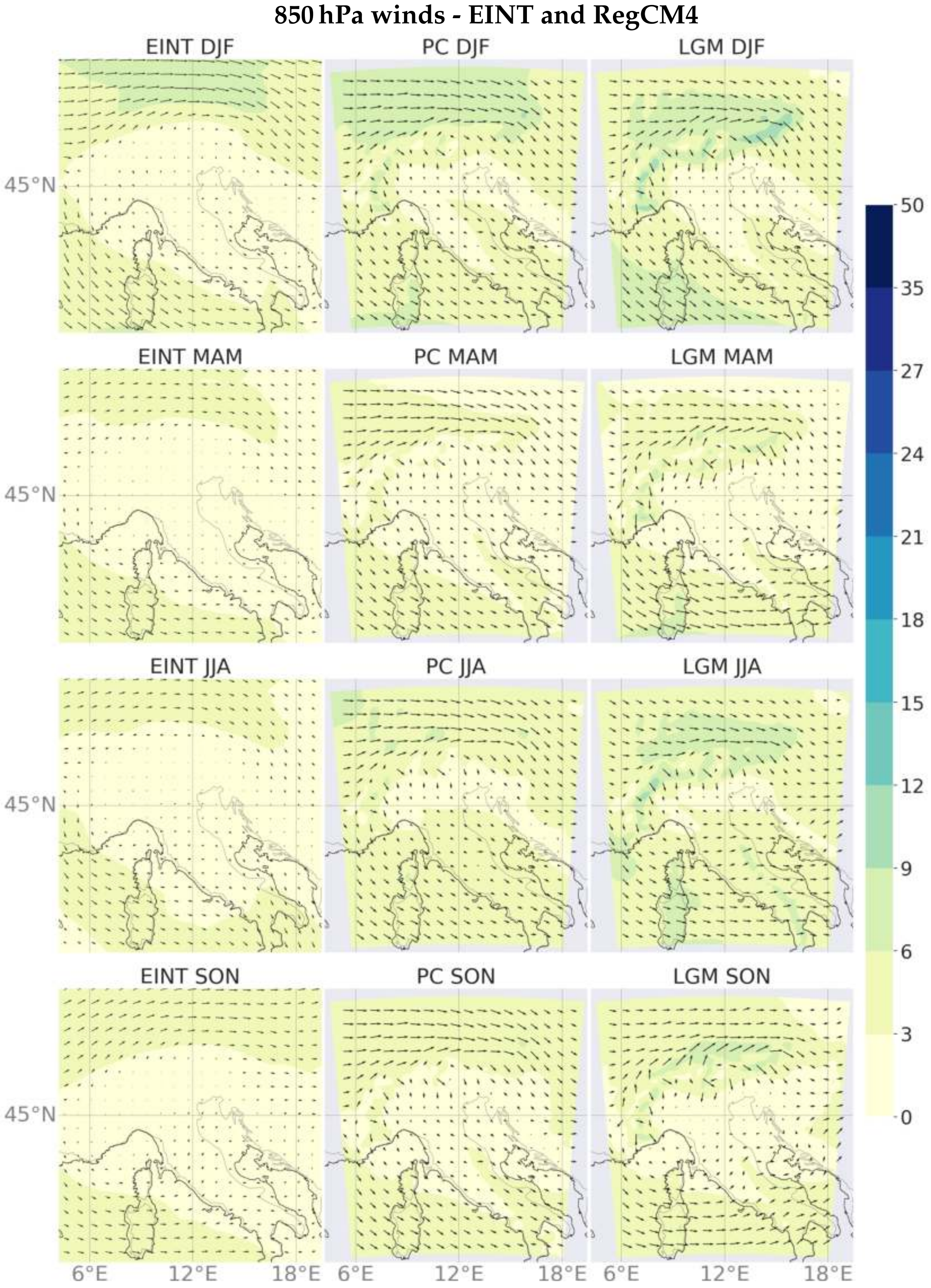

FIGURE 4.6: ERA-Interim (left) and RegCM4 850 hPa wind field for PC (center) and LGM (right) seasonal means.

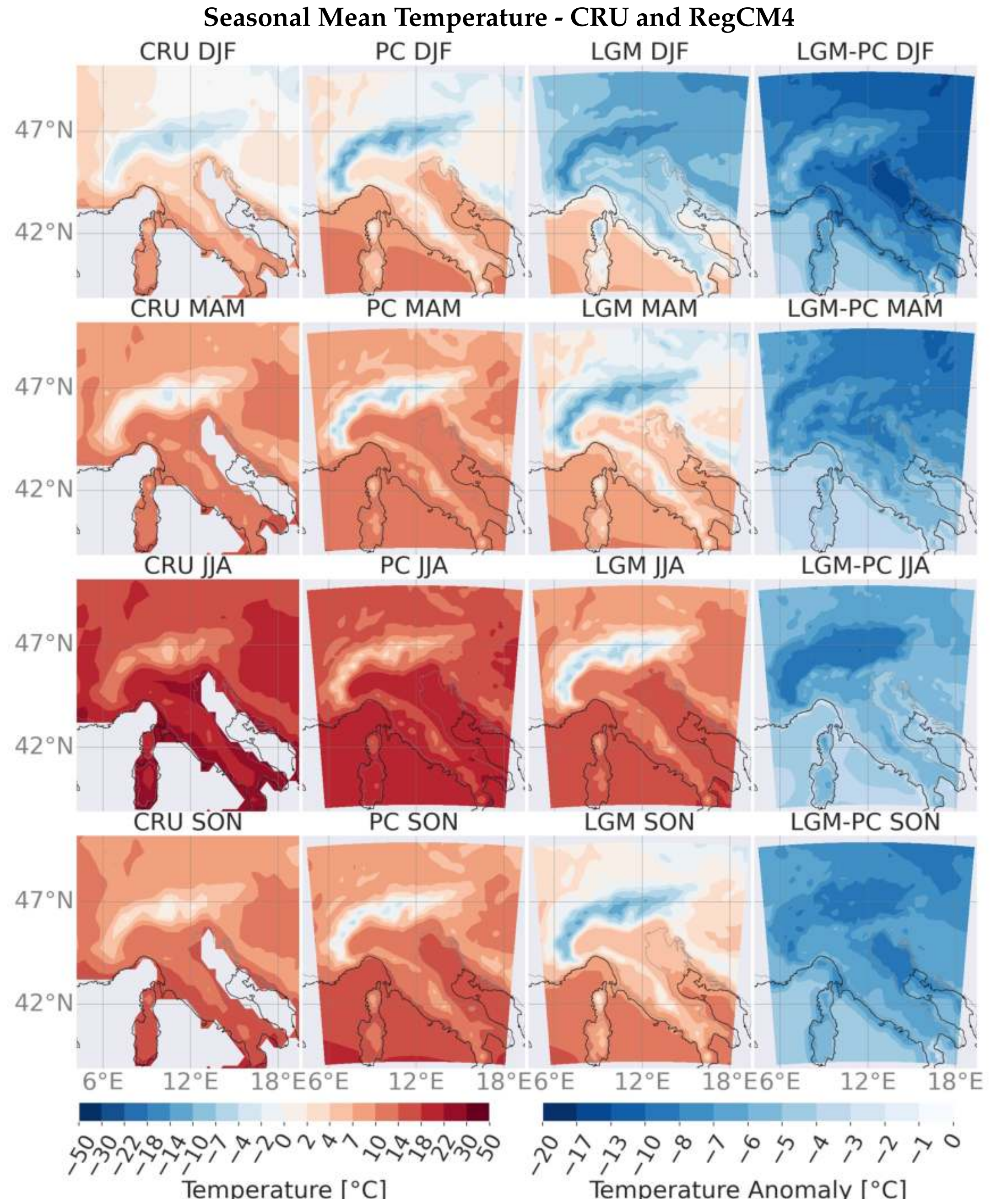

FIGURE 4.7: CRU (left) and RegCM4 seasonal mean temperature in °C for PC (center-left), LGM (center-right), and anomaly (right).

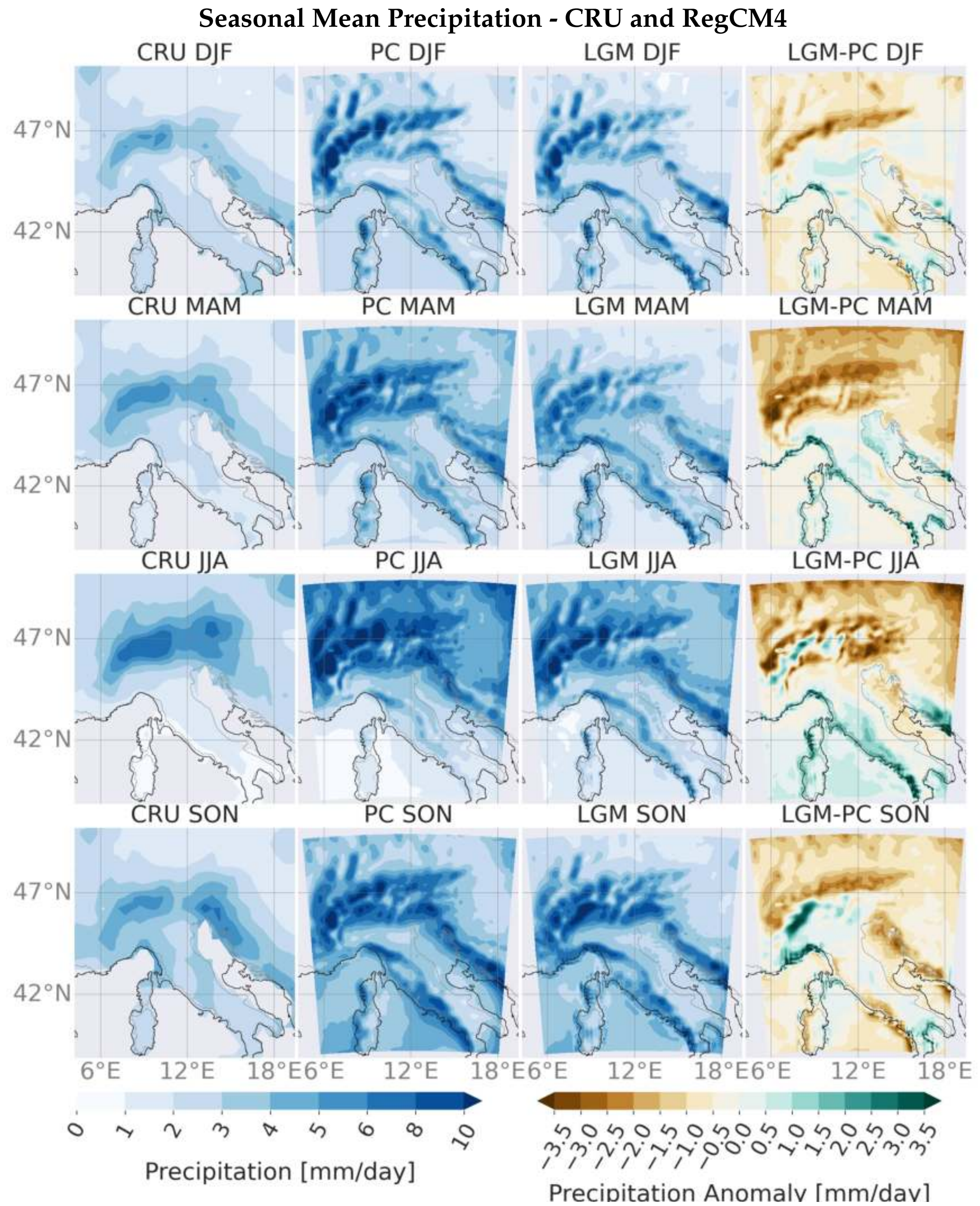

FIGURE 4.8: CRU (left) RegCM4 seasonal mean precipitation in or PC (center-left), LGM (center-right), and anomaly (right).

temperature patterns with latitudinal and altitudinal gradients, but underestimate summer and mountain temperatures. This in particular could be caused by the lag of about 150 yr between PC and present-day observations.

RegCM4 precipitation (figure 4.8) shows for the PC much higher values over central Europe and the mountains than the observations, but the Tagliamento basin, the area focus of the model customisation, presents smaller bias compared to other sectors of the domain. In general RegCM4 overestimate the precipitation almost everywhere, but the LGM-PC difference is in line with proxy reconstructions (Bartlein et al., 2010), with only slightly wetter LGM condition in the Apennines at the LGM compared to the PC (Ludwig et al., 2020).

4.2.2 RegCM4 Climate Variables

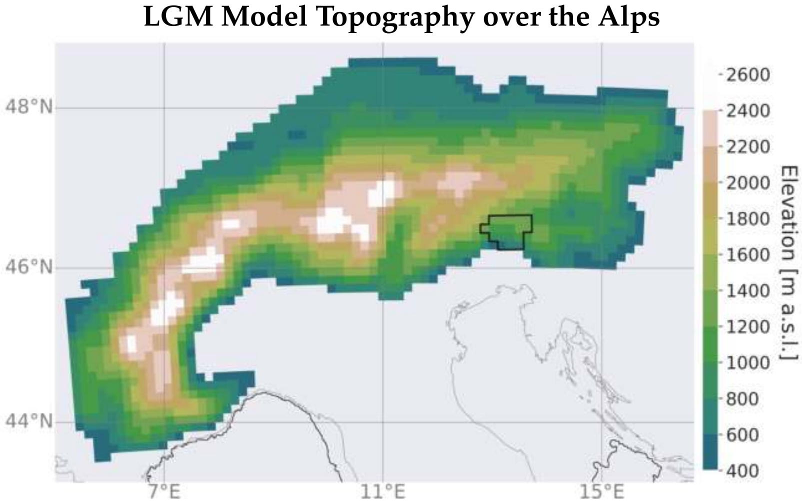

FIGURE 4.9: Topography of the Alps as interpolated by the RegCM4. In the black polygon, the Tagliamento basin. The resolution is 12 km. PC coastline is represented in grey and LGM coastline is represented in black.

The RegCM4 simulations outputs are described and analysed starting from the domain scale and increasing the focus down to the Alps and the Tagliamento glacier basin (figure 4.9). Maps representing the monthly means for different variables (table 4.1) are studied as well as line-plots representing the monthly mean quantities averaged in diverse elevation bands in the whole domain, in the Alps and the Tagliamento basin.

Concerning the anomaly, one has to consider the fact that LGM and PC elevations differ by 120 m a.s.l.. Thus, when comparing LGM and PC grid-cells, one compares two points with the same horizontal coordinates but with different elevations. For near-surface air temperature and sea level pressure, that are highly sensitive to the elevation above the sea level, a correction has been applied (see section 3.4.2). The LGM elevation has been used as a reference to produce the line-plots of a specific altitudinal band for both LGM and PC data. Only in this way it was possible to compare precisely the same locations. The elevations below 120 m a.s.l. have not been included in the line-plots, but are present in the maps.

In this analysis, one big warning concerns the model resolution. It is equal to 12 km, that even though is a high-resolution for a regional climate model, causes a smoothing of the topography. This procedure affects in particular smaller topographic features such as valleys and mountaintops. For example, the grid-cell containing the highest peak in the Alps (4810 m a.s.l.), has an elevation value of only 2730 m a.s.l..

Variable	**Abbreviation**	**Units**
Sea Level Pressure	psl	hPa
Precipitation	pr	$\mathrm{mm\,d^{-1}}$ or %
Convective Precipitation	prc	$\mathrm{mm\,d^{-1}}$ or %
Winds	-	$\mathrm{m\,s^{-1}}$
Near Surface Air Temperature	tas	°C
Surface Snow Melt	snm	$\mathrm{mm\,d^{-1}}$
Surface Snow Amount	snw	$\mathrm{kg\,m^{-2}}$
Evaporation	evap	$\mathrm{mm\,d^{-1}}$
Surface Runoff	mrros	$\mathrm{mm\,d^{-1}}$
Total Runoff	mrro	$\mathrm{mm\,d^{-1}}$

TABLE 4.1: Main analysed variables. All the variables are expressed with the same units of their anomalies, except for pr and prc, whose anomalies are expressed in percentage and PC and LGM values in $\mathrm{mm\,d^{-1}}$.

4.2.3 Sea Level Pressure

In order to make the comparison between LGM and PC possible and to calculate the PSL anomaly, it was required to take into account the 120 m a.s.l. of elevation difference between LGM and PC. The pre-industrial PSL values have been corrected by adding 11 hPa to the model output, as explained in section 3.4.2.

The LGM simulations showed a permanent high-pressure system over the north-eastern sector of the domain and a low-pressure system over the Tyrrhenian and the Mediterranean Sea during the coldest months (from October to April). On the contrary, during the summer months, a local high-pressure system developed over the Alpine reliefs, with highest values in the western sector (figure 4.10).

It must be noted that such topography-related features often develop in weather and climate models as a result of the interpolation applied in the postprocessing phase in order to calculate the sea level pressure from the surface pressure. Thus, these features can potentially be independent of the atmospheric patterns. In particular, in RegCM4 the mean sea level pressure is calculated according to Källen (1996), with a

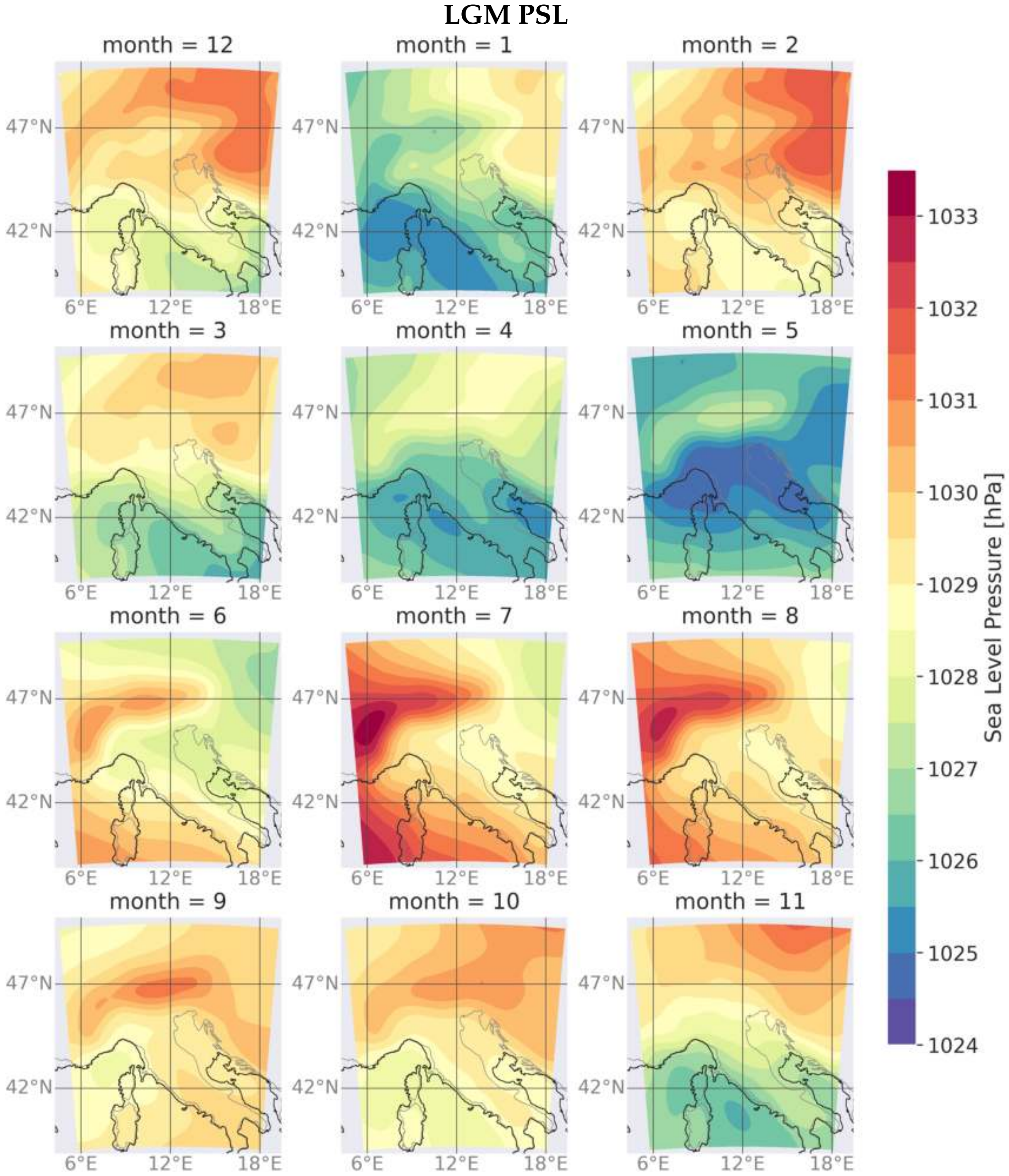

FIGURE 4.10: LGM monthly mean sea level pressure averaged over 19 years.

constant lapse rate of 6.5 K km^{-1}, that is eventually modified for very warm and very cold surface temperatures. Finally, the sea level pressure is smoothed by means of a Gauss-Siedel filter.

In general, the LGM sea level pressure showed higher values with a more pronounced NE-SW gradient compared to pre-industrial times except for summer when the high-pressure was over the Alpine chain in both simulation times. The PSL patterns observed during LGM spring are delayed by one month compared to the PC ones. In particular, the low-pressure system over centre Italy and the Adriatic Sea at the PC developed in April while at the LGM in May. However, the maximum values are observed in both the simulations in July.

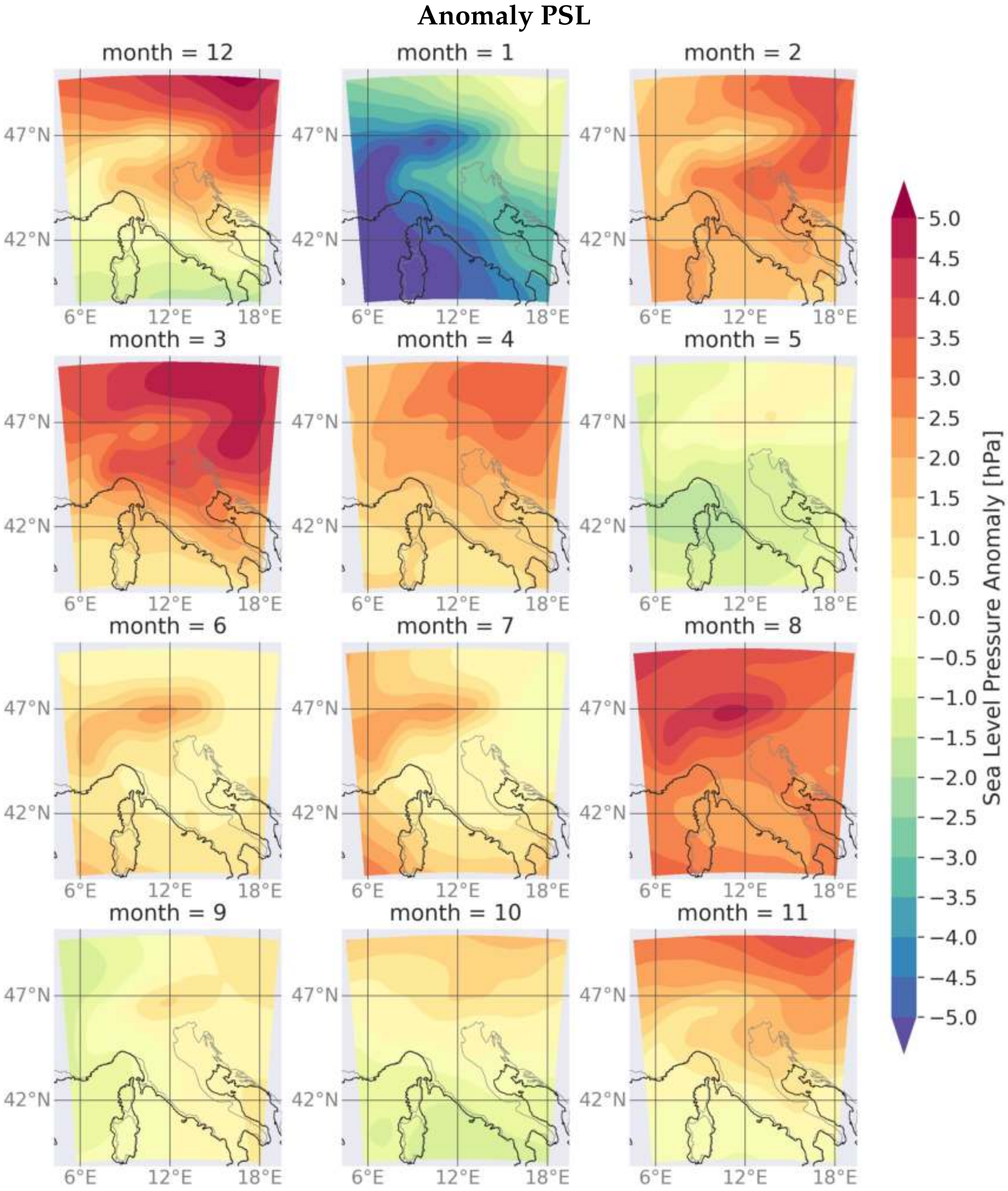

FIGURE 4.11: Monthly mean sea level pressure anomaly averaged over 19 years.

The LGM monthly mean sea level pressure (figure 4.10) shows a smooth transition from month to month, with a smaller spread (4.4 hPa) between the month with the lowest average PSL (May - 1025.8 hPa) and the month with the highest average PSL (July - 1030.2 hPa), if compared with the PC values, when the spread was equal to 5.5 hPa, with minimum values in April (1014.0 hPa) and maximum in January (1019.5 hPa). These data highlight the different annual cycle of LGM and PC. The LGM shows two well distinct situations between summer and winter, while the PC presents a persistent high-pressure system over the western Alps. Thus, only during summer both the LGM and PC were characterised by a similar pattern of sea level pressure with the presence of a local high-pressure system over the Alpine reliefs. As already explained, this topography-related pattern may be attributable to both atmospheric processes or model artefacts. However, this difference in the PSL annual cycle leads to months characterised by a large LGM-PC anomaly, as for January which, at the LGM, shows the lowest winter values, while at the PC presents the highest winter (and yearly) values (figure 4.11).

The largest gradient in sea level pressure anomaly between the LGM and the PC occurred during winter and early spring (figure 4.11), when the temperature over the Fennoscandian ice sheet was extremely low (Broccoli and Manabe, 1987; Cohmap Members, 1988; Kutzbach et al., 1991; Kutzbach and Guetter, 1986; Peyron et al., 1998), and the heat capacity of the Tyrrhenian sea prevented a rapid cooling of the sea surface temperature. Indeed, these pressure patterns could potentially be linked to the marked surface temperature gradient over the domain: The contrasts between extended glaciated and snow-covered areas as the Fennoscandian ice sheet(winter) or the Alps (summer) and the warmer sectors as the Tyrrhenian Sea (winter) or ice and snow-free low-altitude areas (summer).

4.2.4 Precipitation

In terms of precipitation patterns (figure 4.12), the simulations are in agreement with proxy reconstructions (Bartlein et al., 2010; Wu et al., 2007) and other RCM studies (Ludwig et al., 2020; Strandberg et al., 2011). LGM climate conditions were much more arid than in pre-industrial times, with a difference of 13 % in the precipitation throughout the domain, 17 % over the Alps, and 21 % over the Tagliamento basin. The RCM simulation added significant information to the ESM data, in particular for what concerns the distinction between convective and stratiform precipitation and the precipitation in the central Italy. Differently, the ESM could capture, rather with small detail, the precipitation over the Alps and Balkans but the maximum average values are lower than in the RCM output.

At the LGM, Central Europe was 20 to 40 % drier than at pre-industrial times (figure 4.13), while the southern alpine domain was locally wetter, in particular on the Italian coast and peninsula from April to September. Figure 4.12.a shows also a large positive anomaly along the Italian western coast and over Sardinia and Corsica, which is probably caused by the high vertical step in the LGM model topography in correspondence to the coast in these areas. In particular, over Sardinia and Corsica the anomaly propagated from the western coast towards the interior of the islands, leading to the formation of a series of artefacts.

The yearly cumulative precipitation (figure 4.12.a) present a similar pattern compared to the work of (Ludwig et al., 2020; Strandberg et al., 2011), but our values are larger in particular in the western Alps. The highest values are located in the northern foreland of western and central Alps and southern Balkans, but also the southeastern

Alps presented a particularly wet spot. In table 4.2 the Tagliamento basin showed higher average values than the rest of the Alps and the domain, for LGM ad PC. However, both LGM and PC simulations differ from the present-day observations (Isotta et al., 2014) that attest to the southeastern Alps the highest yearly precipitation amount in the Alps (figure 4.12.b).

	LGM [mm/yr]			**PC [mm/yr]**		
	Mean	**Min**	**Max**	**Mean**	**Min**	**Max**
Dom	1240	289	4911	1416	607	5237
Alps	1802	780	4398	2183	981	5237
Tj	2131	1135	2777	2685	1568	3203

TABLE 4.2: Cumulative precipitation means, minima and maxima in the domain (Dom), Alps and Tagliamento basin (Tj).

Convective and Stratiform Precipitation

Precipitation outputs of RegCM4 are the total precipitation (PR), given by the sum of convective and stratiform precipitation, and the convective precipitation (PRC). Thus, stratiform precipitation is simply calculated by subtracting the convective precipitation from the total precipitation.

LGM convective precipitation was generally weaker with respect to pre-industrial times, with a marked reduction (50 %) particularly over Central Europe and the Alps (figure 4.14). This may be a consequence of the lower LGM temperatures with respect to the PC temperatures (see section 4.2.7), that lead to a more stable atmosphere. However, analogously to the PC, LGM convective precipitation dominated over the stratiform precipitation, in particular during the summer months and over the sea (figure 4.16). During winter over land and at the highest elevation all year-round the precipitation was mainly stratiform.

In order to explore the LGM and PC atmospheric stability the vertical lapse rate was studied. The pre-industrial simulation shows an almost constant value through different seasons, which is close to the environmental lapse rate (6.5 °C km^{-1}). The LGM lapse rate, instead, shows two well-defined types: During summer the average lapse rate is 8.3 °C km^{-1} (value typical of unstable conditions), while during winter it is equal to4.7 °C km^{-1} (value typical of stable conditions). These values were extracted from the near-surface air temperature at different elevations and could be affected by local topography-induced effects. However summer convective precipitation anomaly can be explained with a more unstable atmospheric conditions.

Table 4.3 compares LGM and PC percentage of convective precipitation with respect to the total precipitation. It emerges that during the PC convection was stronger than in the LGM, and in both the simulations summers presented values above the yearly

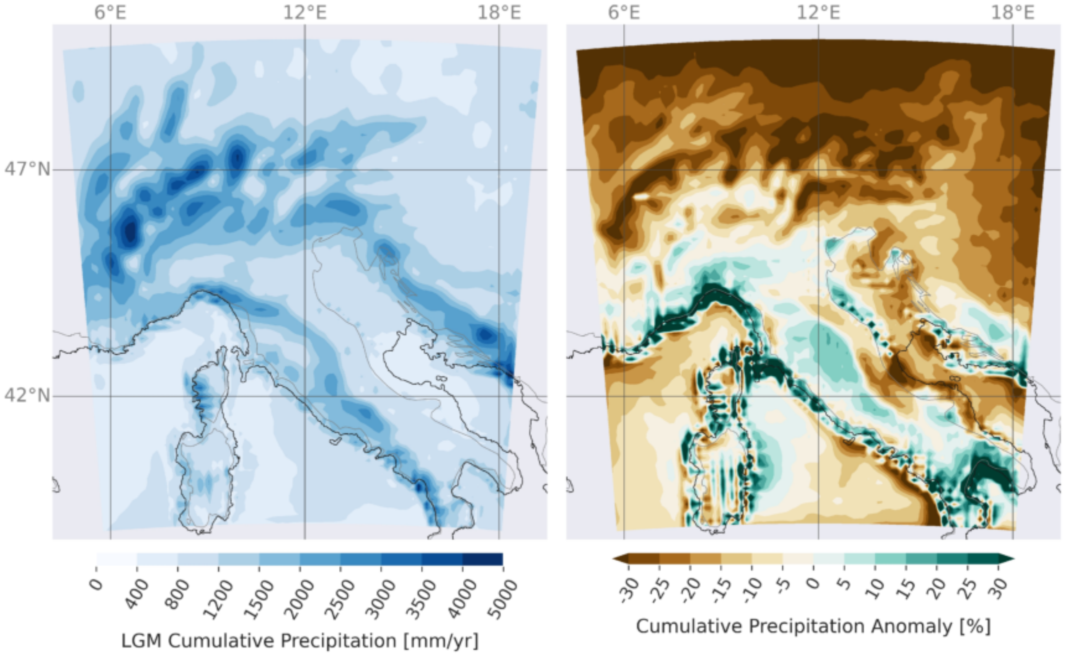

a) Cumulative PR

b) Observation: PR

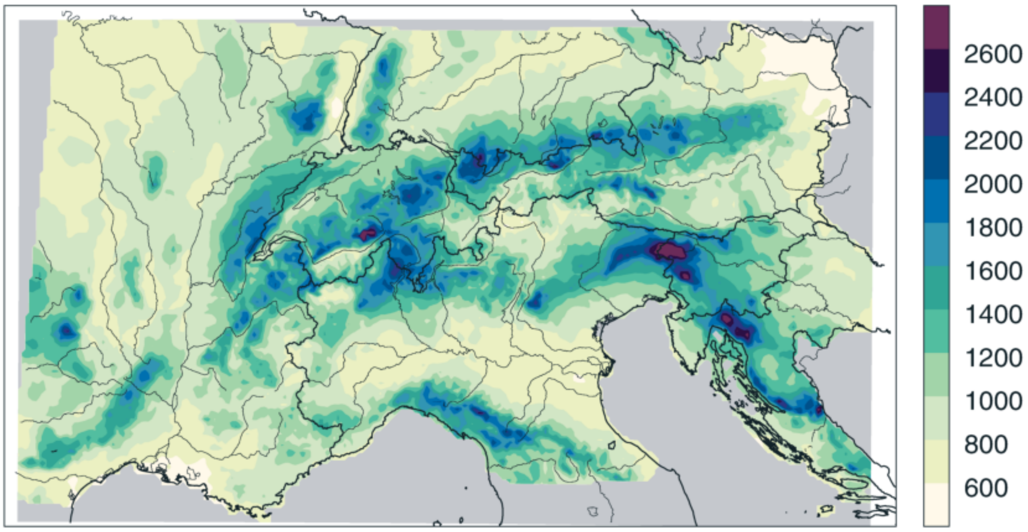

FIGURE 4.12: (a) Yearly cumulative precipitation at the LGM (left) and yearly cumulative precipitation anomaly (right). The precipitation anomaly presents some artefacts, evidenced by high positive anomalies over Sardinia, Corsica, and Tyrrhenian coast. (b) From Isotta et al. (2014). Mean annual precipitation in mm yr^{-1} for the period 1971–2008.

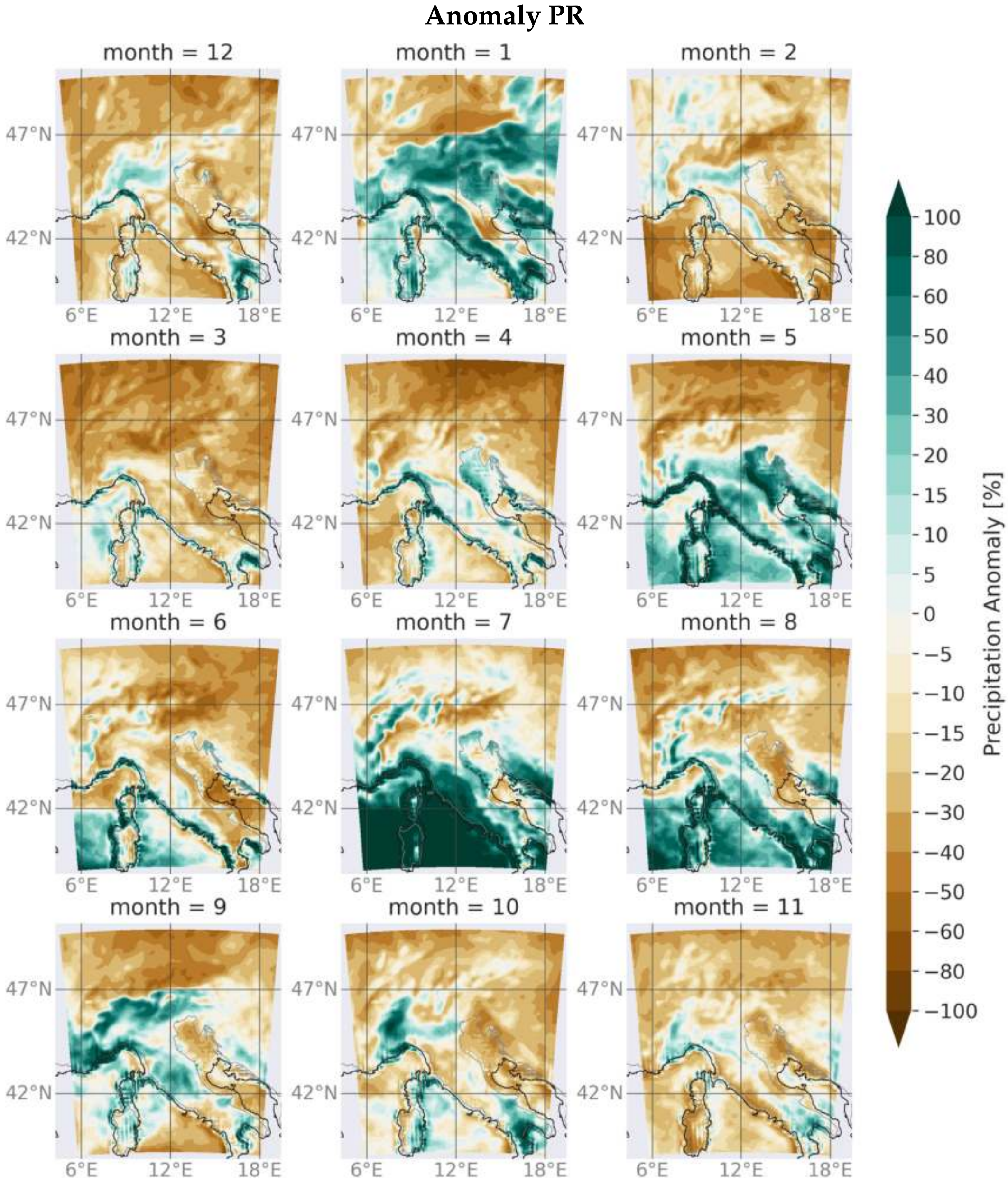

FIGURE 4.13: Monthly mean precipitation anomaly averaged over 19 years.

average. Considering the whole domain, the LGM during winter was characterised by more stratiform precipitation than convective, while in the PC convection was always predominant. The situation was different in the Alps that presented predominance of convection only during summer at the LGM, while in the PC convection was above 50 % always but during winter.

Figure 4.15 shows a positive stratiform precipitation anomaly that highlights possible increased synoptic activity in the domain during the LGM when compared with the PC. Concerning only stratiform precipitation the south alpine domain was generally wetter than in the PC, with the exclusion of the higher Apennine regions. On the contrary, the North alpine domain was drier or presented small anomaly, with the

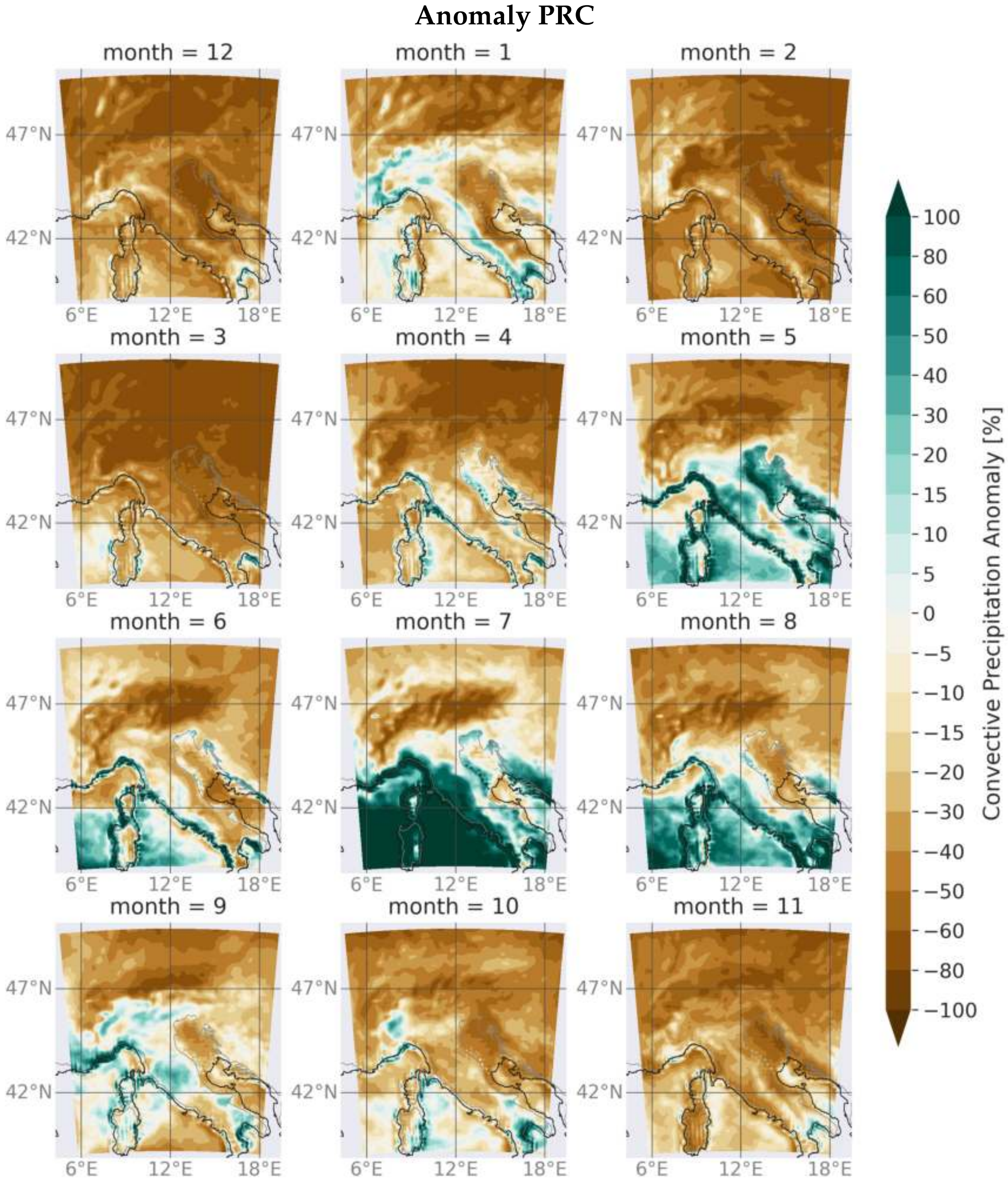

FIGURE 4.14: Monthly mean convective precipitation anomaly averaged over 19 years.

exclusion of the summer, wetter than in the PC. As shown by table 4.2 the Alps were characterised mainly by stratiform precipitation, which may give important information on the origin of the air masses involved in the synoptic activity. Considering that the Alps constitute an orographic barrier for the air masses, one can say that the precipitation in the southern Alps during DJF, MAM and JJA, were originated in the Mediterranean region. July and August were the only months that showed positive stratiform precipitation anomaly in the whole domain, also North of the Alps. Fact that can be explained *i)* by higher geopotential elevation during summer, that allowed the southerly air masses to pass over the Alps or *ii)* by the

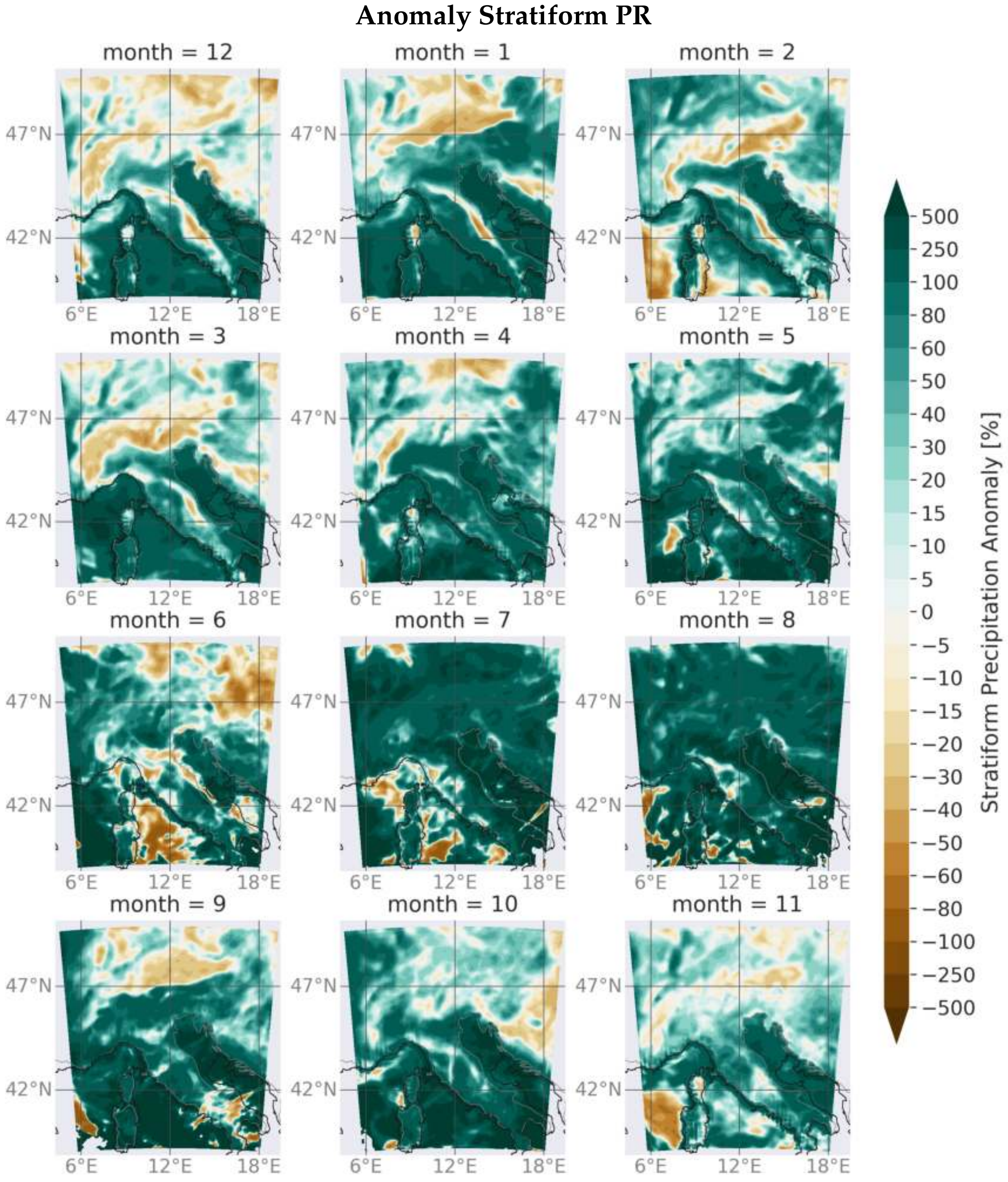

FIGURE 4.15: Monthly mean stratiform precipitation anomaly averaged over 19 years.

influence of Atlantic perturbations in the north alpine foreland.

The synoptic precipitation was less intense than the convective precipitation for both LGM and PC, and for this reason the total precipitation anomaly (figure 4.13) is mainly negative, almost copying the convective precipitation pattern (figure 4.14). During the warmest months, from May to August, the total and convective precipitation anomaly over the sea was positive (figures 4.13 and 4.14), showing a relation with the Mediterranean jet, that in summer was completely westerly over the Italian peninsula as highlighted also by the wind-field (section 4.2.5). This precipitation mostly affected the western Apennines and the southern Balkans, which were in the

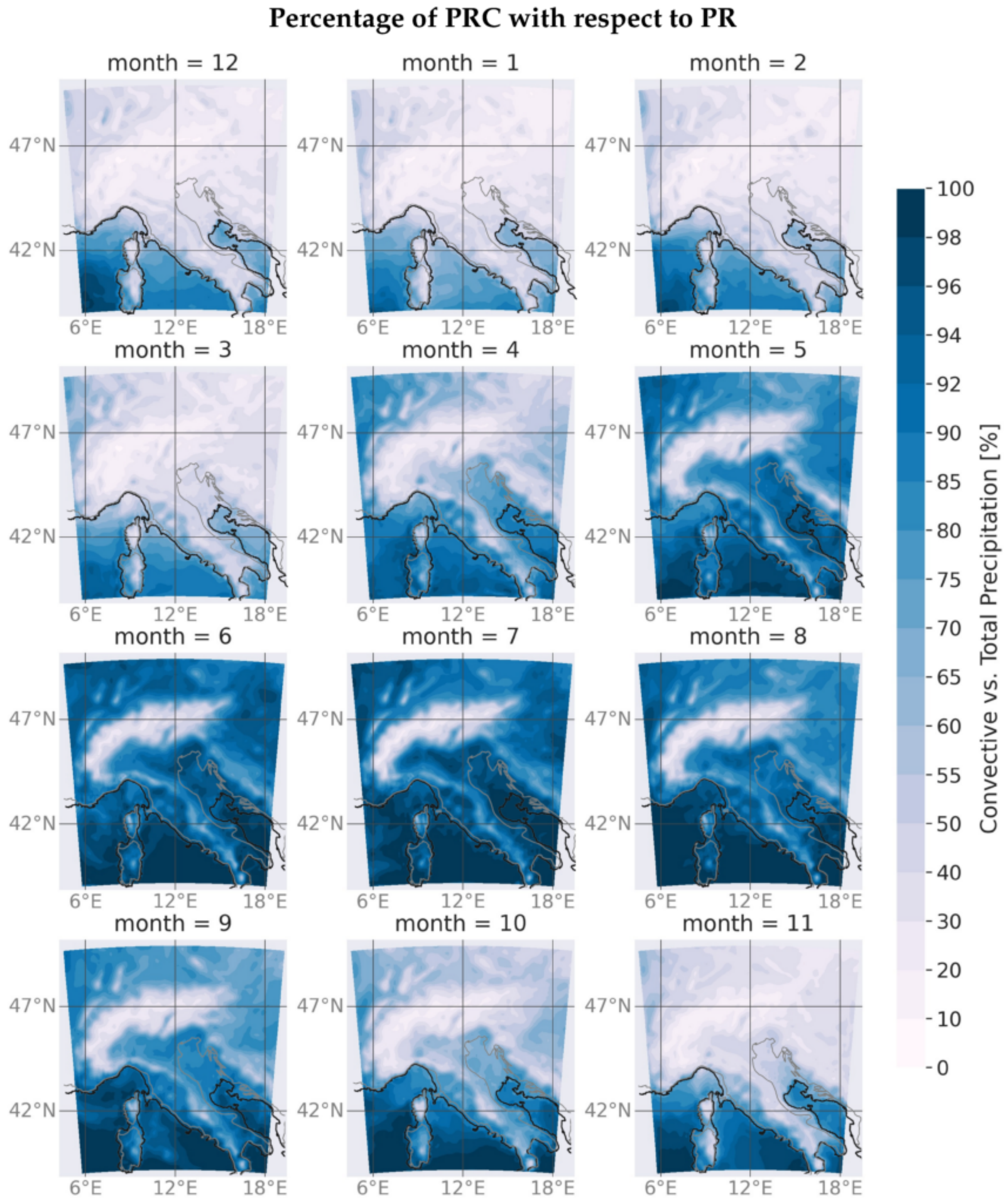

FIGURE 4.16: Percentage of the monthly mean convective precipitation with respect to the total precipitation averaged over 19 years. Darker blue shades indicate strong convection, lighter blue shades are for stratiform precipitation.

upwind side with respect to the Mediterranean jet. In general, during all seasons, the Apennines and the Balkans presented drier and wetter sectors, compared to pre-industrial times, being influenced by both stratiform and convective precipitations. Stratiform precipitation presented positive anomaly almost everywhere in the domain (figure 4.15), convective precipitation, which was more intense than the stratiform precipitation, showed positive anomaly only in the upwind-side of Apennines and Balkans (figure 4.16).

	LGM [%]			PC [%]		
	Dom	**Alps**	**Tj**	**Dom**	**Alps**	**Tj**
YR	66	40	38	79	59	55
DJF	44	23	17	62	35	28
MAM	66	40	36	82	60	55
JJA	87	61	62	94	83	86
SON	67	39	35	80	55	52

TABLE 4.3: Percentage of yearly and seasonal convective precipitation out of total precipitation, in the domain (Dom), Alps and Tagliamento basin (Tj).

Considering the whole domain, January and July presented the largest total precipitation anomaly between LGM and PC (figure 4.13), showing an inverse pattern for northern and southern alpine regions in January and a significant positive anomaly (>100 %, with $< 1\,\mathrm{mm\,d^{-1}}$ at the PC and 0.2 to $2\,\mathrm{mm\,d^{-1}}$ at the LGM) over the sea in July.

Stratiform, convective and total precipitation patterns suggest that at the LGM the Alps acted as a barrier for the southerly air masses, leading to a drier northern alpine foreland and a relatively wetter southern Alpine domain. This precipitation pattern supports the theory proposed by Florineth and Schlüchter (2000), Luetscher et al. (2015) and Monegato et al. (2017) that the LGM atmospheric circulation was dominated by a southward displacement of the westerly jet stream in the North Atlantic, causing the moist air masses originated over the Atlantic Ocean and the sub-tropical moisture reservoir, to flow across the Mediterranean region and then towards the Alps.

Focus on the Alps and Tagliamento basin

Large monthly variability characterised the Alpine region and the Tagliamento basin, even though these areas were mainly drier than at the PC. From both monthly maps (figure 4.13) and line-plots of the annual cycle (figure 4.17) emerges that March was the driest month over the domain, and in particular over the Alps and the Tagliamento basin.

In the Alps, the precipitation amount was highly dependent on the elevation, showing different annual cycles for the elevations above and below 1000 m a.s.l. (figure 4.17). Below this level, the annual cycle was bell-shaped around July, reflecting the trend of stratiform and convective precipitations, that had in June and July respectively their minimum and maximum value. Above 1000 m a.s.l., the curve was asymmetrical, with increasing precipitation from March to the period July-September, due to the influence of the stratiform precipitation, that respect to convection presented a skewness towards autumn at the higher elevations. Convective and stratiform precipitation had an opposite behaviour with the altitude: convection showed its maximum values at the lower elevations, where stratiform precipitation was at its minimum. Considering the total precipitation, the monthly average increased from 400 to 1800 m a.s.l. and decreased at the highest elevations, being the Alps mainly affected by stratiform precipitation.

The PC data showed a bell-shaped curve below 1400 m a.s.l. and a curve that grew from January to June, and that flattened during Summer and Autumn at higher elevations (figure 4.18). However in general, June presented the highest average precipitation values. At lower elevations, LGM and PC precipitation annual cycles showed bell-shaped curves, but the maximum precipitation in the LGM was delayed by one month with respect to the PC and the change to non-bell-shaped patterns occurred at a higher elevation for the PC.

Considering the whole year, the LGM climate in the Alps was 17 % drier, with less convective precipitation (-43 %) than during the PC. Over the Alps the stratiform precipitation were predominant on convective precipitation, always but in summer

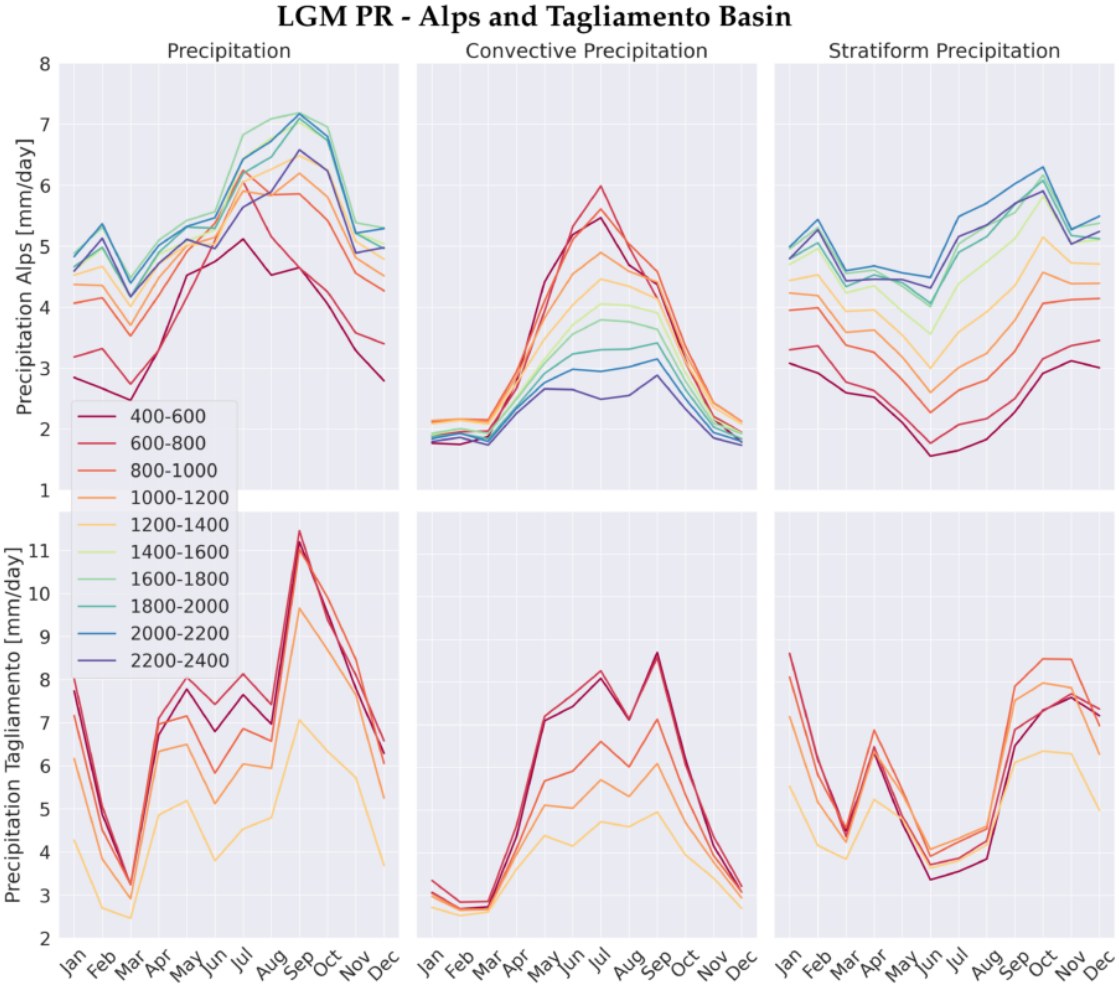

FIGURE 4.17: LGM monthly mean total, convective and stratiform precipitation for the Alps (above) and Tagliamento basin (below). The colours represent different elevation bands.

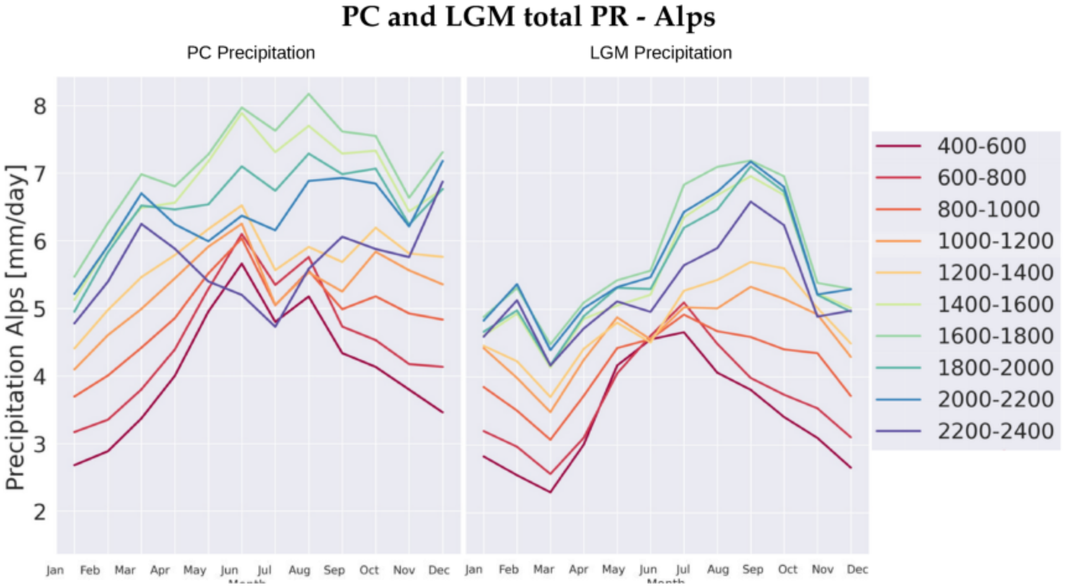

FIGURE 4.18: PC (left) and LGM (right) monthly mean total precipitation for the Alps. The colours represent different elevation bands.

(table 4.3). Convective precipitation showed its highest values at the Alps margins. Similarly to pre-industrial times, at the LGM the precipitation over the Alps increased from East to West, with a relatively wet area in the southeastern Alps all year-round (figure 4.19). This wet spot was located in the southern part of the Tagliamento glacier basin and was characterised by highly variable stratiform precipitation during the whole year and convective precipitation from late spring to early autumn (figure 4.17). A positive anomaly in the precipitation occurred in the Adriatic region (figure 4.13) during the late spring when melting and surface runoff were at their maximum (section 4.2.9 and section 4.2.10). Further North of the Adriatic region, the southeastern Alps showed positive precipitation anomalies during early autumn and in January. Thus, late spring, early autumn and January mark positive precipitation anomalies close and over the Tagliamento glacier basin, supporting the idea of different annual cycles between LGM and PC.

The Tagliamento basin shows, at all the elevations from 400 to 1400 m a.s.l., a precipitation pattern characterised by maximum precipitation in September, as already seen above 1000 m a.s.l. in the rest of the Alps (figure 4.17). Differently from the rest of the Alps, the precipitation amount decreased from the lowest (400 m a.s.l.) to the highest elevations (1400 m a.s.l.), in particular during late spring to summer. The average monthly precipitation amount in the Tagliamento basin was higher than the average precipitation amount in the Alps for the same altitudinal bands and even for higher alpine elevations. The only exception occurred in March, which showed particularly low values.

These elements prove that the Tagliamento basin had climatic characteristics typical

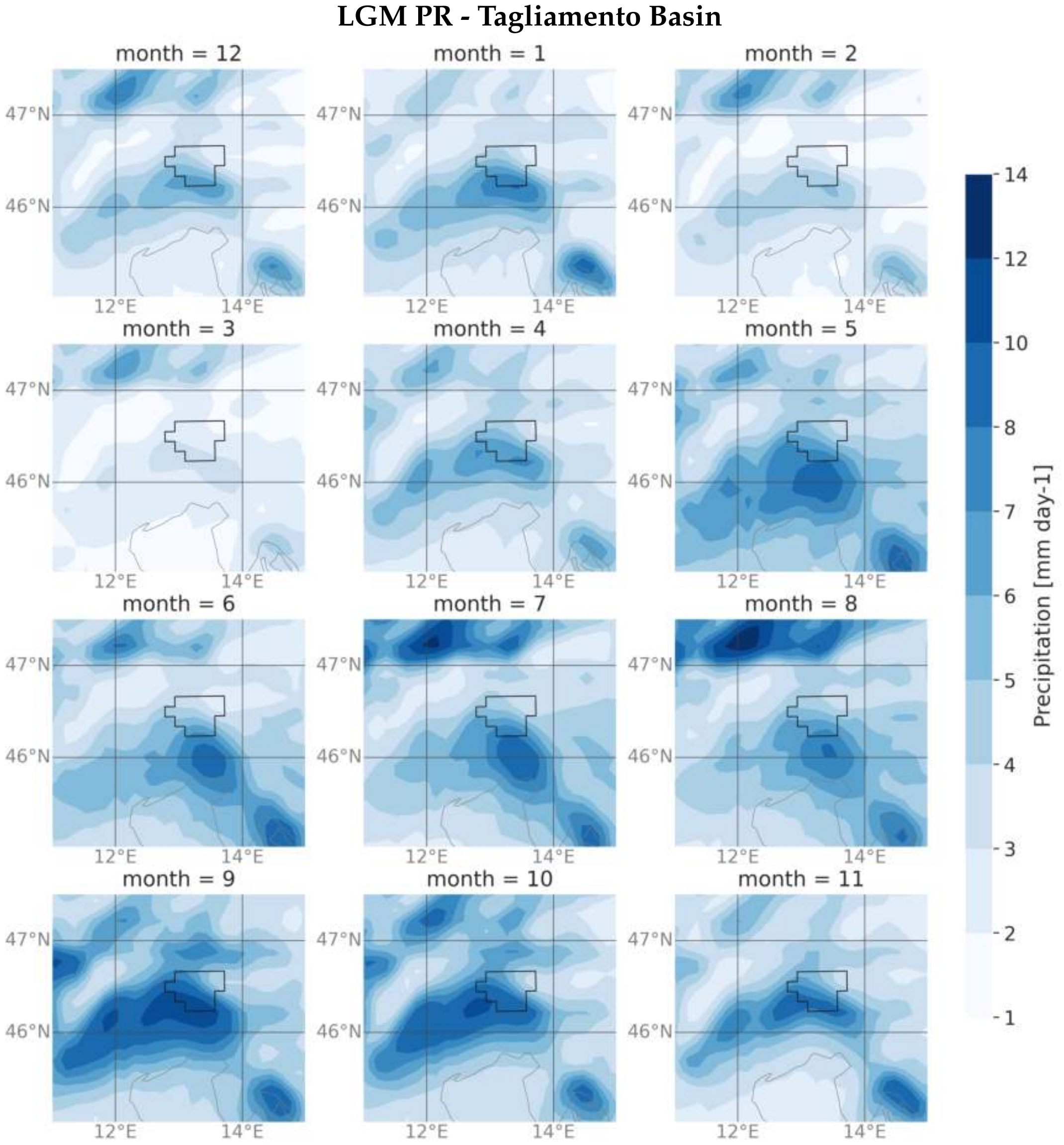

FIGURE 4.19: LGM monthly mean precipitation of the southeastern Alps, averaged over 19 years. The black polygon indicates the Tagliamento basin.

of higher elevation areas in the Alps, which might explain the presence of a glacier at such a low altitude. Similarly to the whole Alpine chain, the LGM annual cycle anticipated by one month the PC curve, but in both the simulation autumn is markedly wetter than the other seasons. Considering the average monthly temperature (section 4.2.7) and the surface snow amount maps (section 4.2.8) it is likely that this autumn precipitation occurred in the form of snowfalls, interrupting the melting season and feeding the Tagliamento glaciers.

4.2.5 Winds

In this section it is analysed the wind at 850 hPa, representative for the lower troposphere, where the orographic-related phenomena occur. Winds at lower pressure

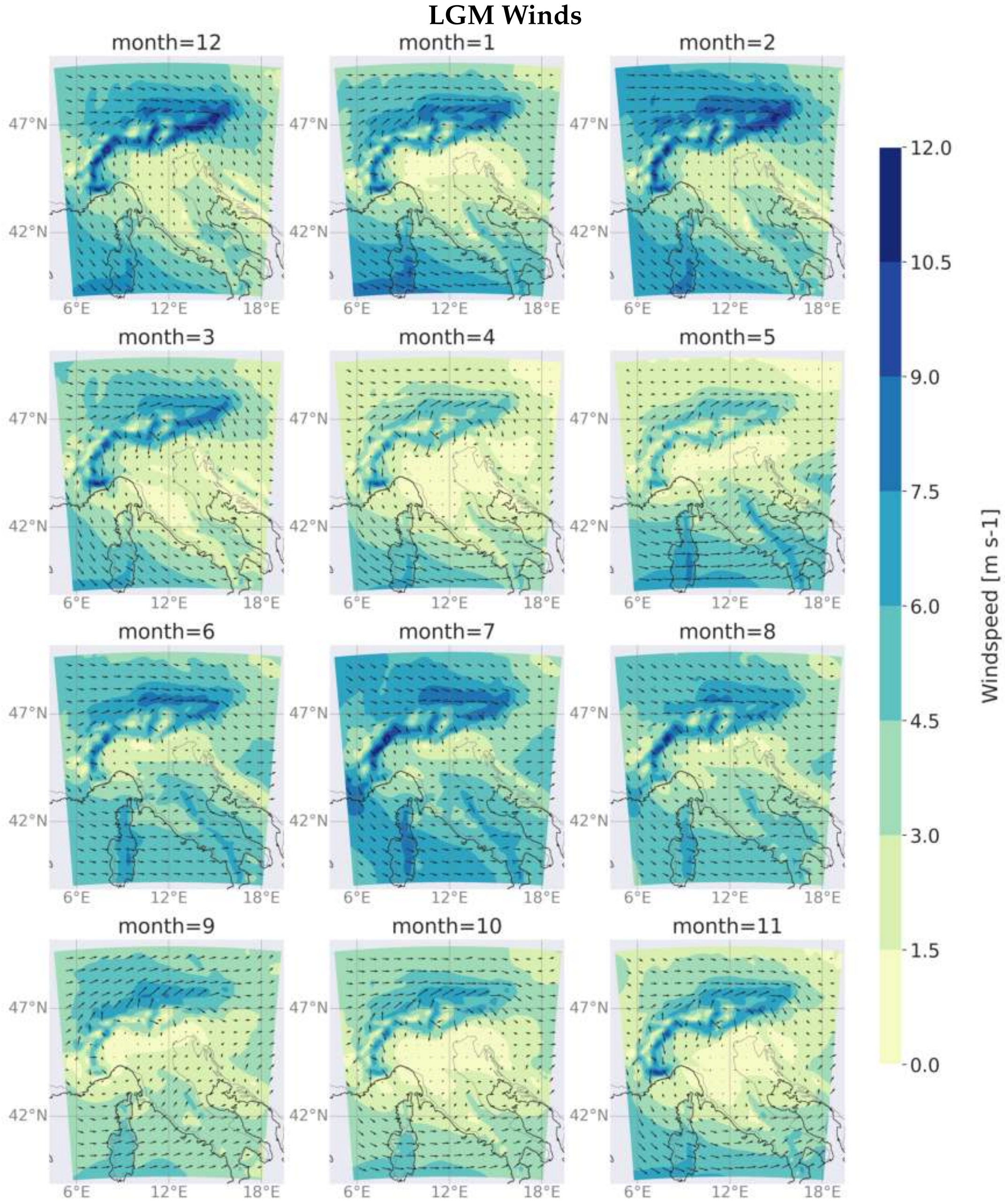

FIGURE 4.20: LGM monthly mean 850 hPa wind direction (arrows) and speed (colours) averaged over 19 years.

levels were also considered but are not shown. The 700 hPa winds together with the winds at the sigma levels between 0.725 and 0.825 were examined to ensure no interpolation error occurred in the 850 hPa winds due to interference of airflows and topography. Likewise, the 200 hPa (figure 4.6) and 500 hPa were analysed, but they did not add information to the ESM simulations (section 4.1.2).

At the LGM, the atmospheric circulation over the domain was characterised mostly by north-westerly winds (figure 4.20), originated from the North Atlantic jet as shown in figure 4.2. The Alps constitute an orographic barrier which split the westerly winds

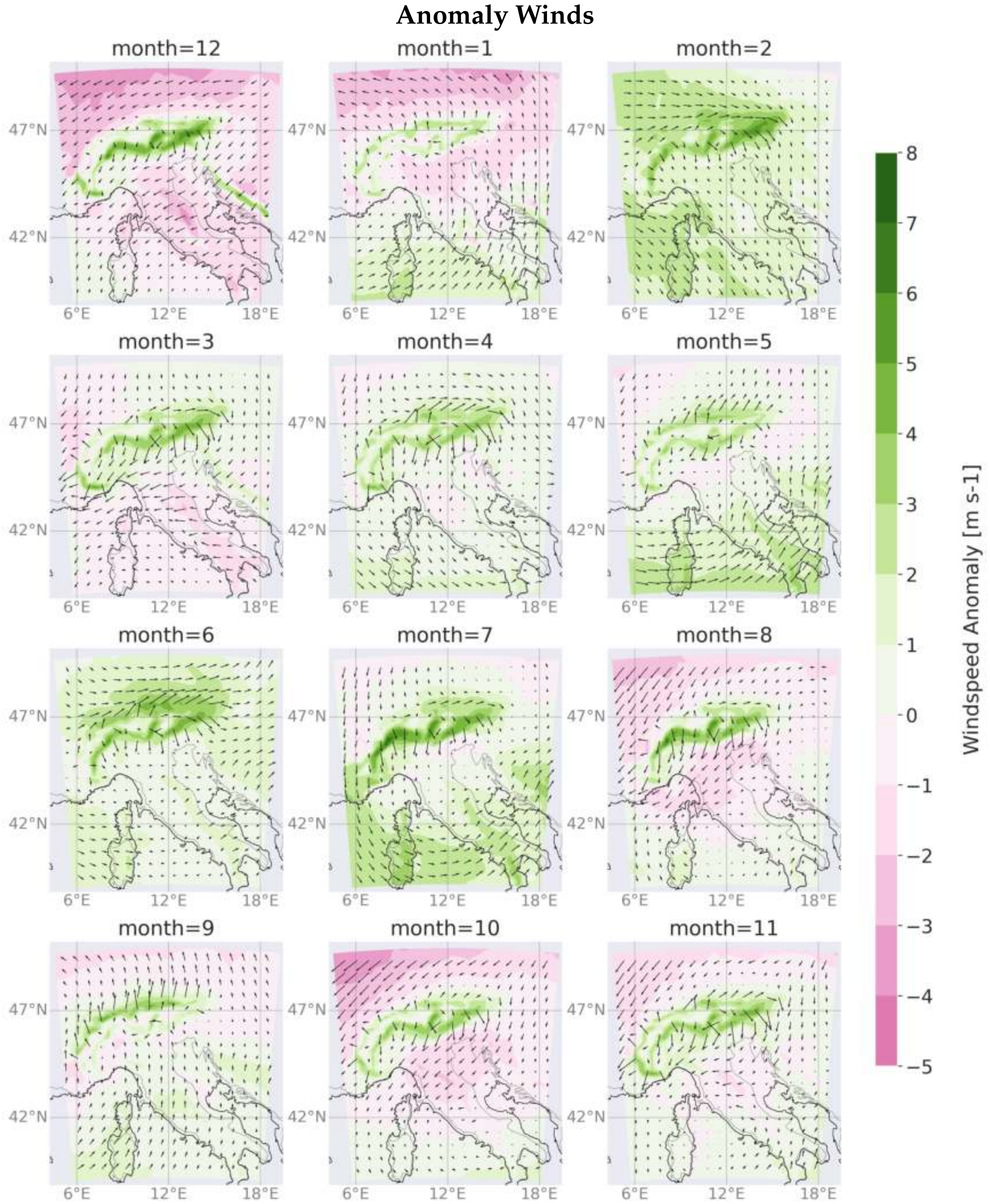

FIGURE 4.21: Monthly mean 850 hPa wind direction anomaly (arrows) and speed (colours) anomaly averaged over 19 years.

into two components: one flowing eastward parallel to northern alpine foreland and one flowing south of the Alps with different directions according to the month (figures 4.2, 4.6 and 4.20). From December to March, except for January, the southern branch of westerly winds was directed towards south-east both flowing over the Tyrrhenian Sea and descending from the Alps along the Italian peninsula. From April to November, instead, this flow turned eastward crossing the Apennine chain. In particular, during summer this wind-flow was purely westerly along the whole Italian peninsula. At the same time, in the intermediate seasons, a cyclonic circulation

developed between the Gulf of Genoa and the Po Valley, causing a return flow over central Italy directed towards north-east. As suggested by Florineth and Schlüchter (2000) and Ludwig et al. (2016) this north-easterly flow could have branched from the Mediterranean jet over the Adriatic Sea. According to Ludwig et al. (2020), the southern alpine foreland, the Po Valley, and the northern sector of the Apennines, being in the lee-side of the Alps, present less intense winds compared to other parts of the domain, especially when the cyclone developed in these areas (figure 4.20).
January, even if is in the middle of winter, presented wind and precipitation characteristic (section 4.2.4) of an intermediate season, with higher precipitation than at the PC in the southern Alps, westerly winds in the southern Italy and extremely weak winds in the Po Valley Plain.
Over the Alps, the LGM wind-field was always stronger than at the PC (figure 4.21). At the LGM, the winds were weaker than at pre-industrial times north of the Alps, in particular from late summer to winter, and stronger in the Mediterranean region, supporting the idea of a southward shift of the Atlantic jet-stream (Luetscher et al., 2015; Monegato et al., 2017) and the development of a cyclonic circulation over the Tyrrhenian Sea (Kuhlemann et al., 2008).
In spring, with the development of the cyclonic circulation (figure 4.20), the North Adriatic and Friulian Plain were wetter than at pre-industrial times (figure 4.13). In summer, when the westerlies of Atlantic origin were located slightly more north than during the rest of the year, the cyclonic circulation was weaker and the air masses brought precipitation more to the south than in spring, in the Italian peninsula and over the southern Balkans. In the southeastern Alps, the precipitation was mainly focused on the Friulian Plane and the Pre-Alps and presented a smaller positive precipitation anomaly compared to the Apennines and Balkans. Only in January and September, when the wind anomaly showed a marked and pure northward direction, a positive precipitation anomaly was present in the whole southern alpine region (figure 4.13).
The highest average wind speed at the 850 hPa level occurred during winter and summer over the Alps. The wind pattern over the Alps showed a wind-field that diverged in correspondence of the main Alpine ridge due to the formation of katabatic flows (figure 4.20) that generated as a consequence of the strong thermal gradient between the extended glaciers over the Alps and the warmer surrounding planes. This phenomenon is particularly intense during summer when the snow cover at low altitude is minimum and the thermal gradient is maximum. The katabatic winds cooled and dried the Po Valley and Friulian Plains, especially during the warmest months. The katabatic winds presented a strong southward component, always but in September when the southerly flow is so strong to reach the Alps rich in moisture, bringing precipitation.

Alternatively, the katabatic winds may reflect the high-pressure system that developped over the Alps as a consequence of the interpolation of the surface pressure into sea level pressure (see section 4.2.3).
Stronger winds and dryer climatic conditions, associated with reduced vegetation cover, represent a favourable environment for dust storm and loess deposition (Ludwig et al., 2020; Schaffernicht et al., 2020).

4.2.6 Relative Humidity

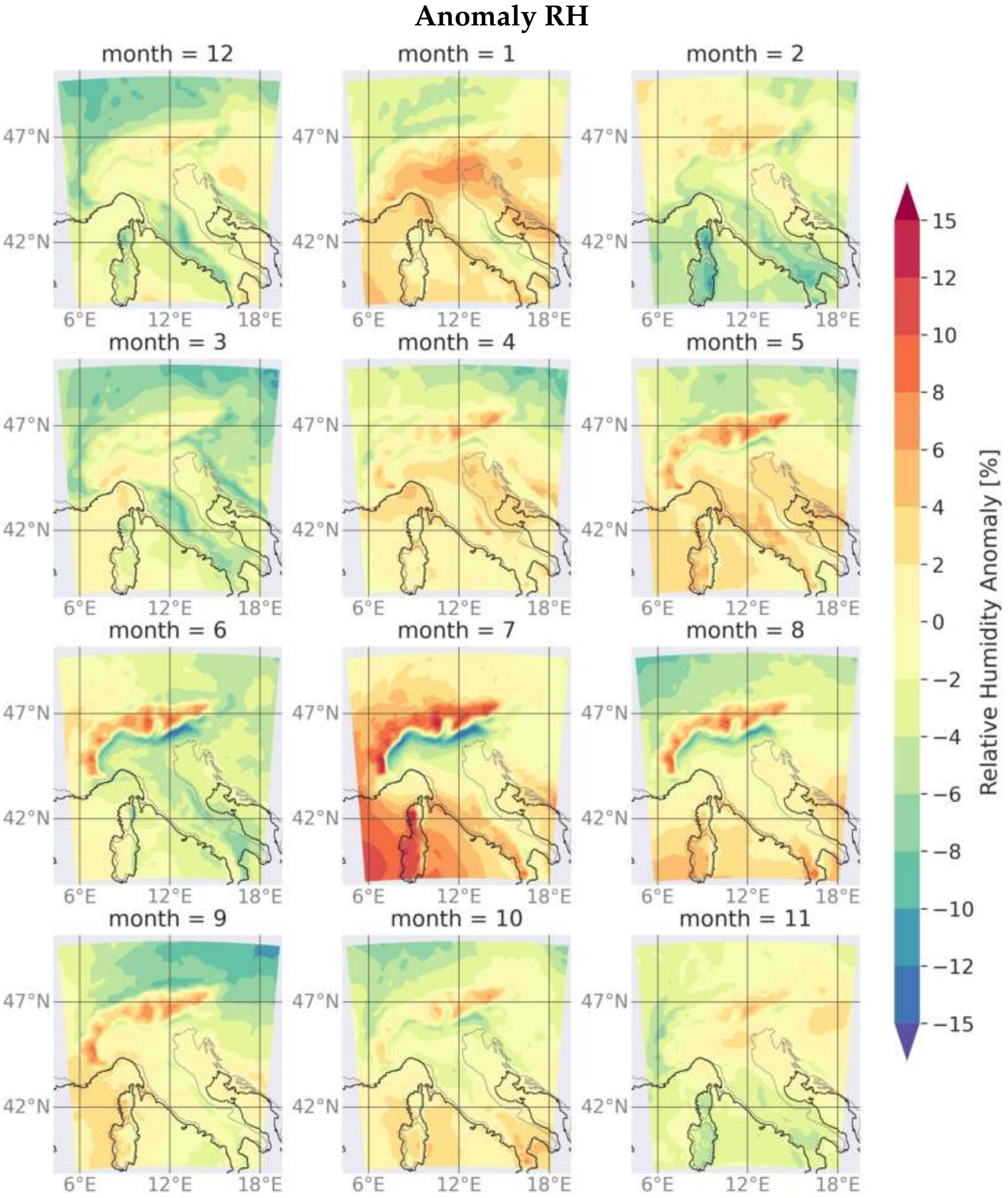

FIGURE 4.22: Monthly mean relative humidity anomaly averaged over 19 years.

The relative humidity anomaly (figure 4.22 is interesting if analysed with winds and precipitation. Indeed, the months characterised by the development of the cyclonic circulation in the Po Valley Plane, as January and April, show positive relative humidity anomalies in the plane South of the Alps. When the atmospheric circulation over central Italy was purely westerly, as during summer, the Alps showed the highest RH levels, while the lowest values occurred in the Po Valley Plane. This may be related to different factors or a combination of them: *i)* the strong katabatic winds descending from the Alpine reliefs as a consequence of the marked temperature gradient between the mountains and the plane (section 4.2.6) or *ii)* the blocking acted by the Alps with respect to the moisty Atlantic air masses coming from NW. This second hypothesis is also supported by the positive RH anomaly presents particularly in July, North of the Alps and West.

In general, the Alps tend to protect the air masses in the lee-side with respect to the erosion exerted by the NW airflow. Thus, these protected air masses can maintain their water content.

4.2.7 Near-Surface Air Temperature

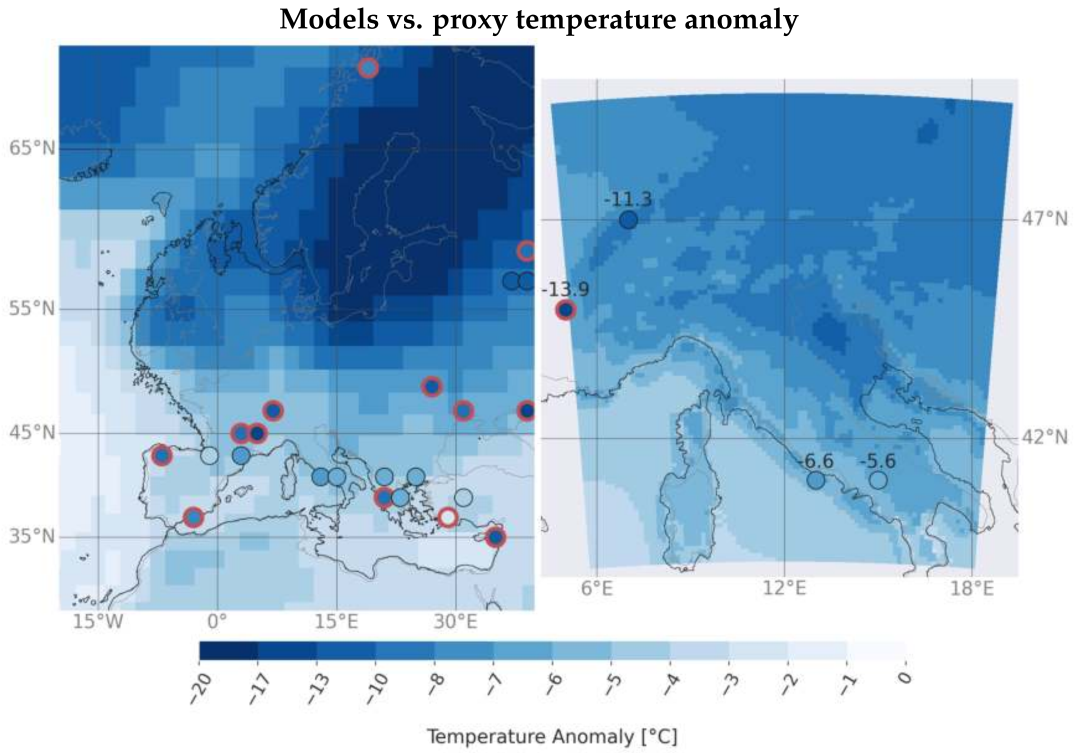

FIGURE 4.23: MPI-ESM-P (left) and RegCM4 (right)temperature anomaly (LGM-PC) compared with proxy reconstruction from Bartlein et al. (2010). The red circles indicate model LGM-PC anomaly falls out of the error range for the proxies.

The near-surface air temperature during the LGM was always lower than in the pre-industrial times (figure 4.24) in agreement with proxy reconstructions (Bartlein et al., 2010; Wu et al., 2007, 4.23) and climate models (Kageyama et al., 2020; Strandberg

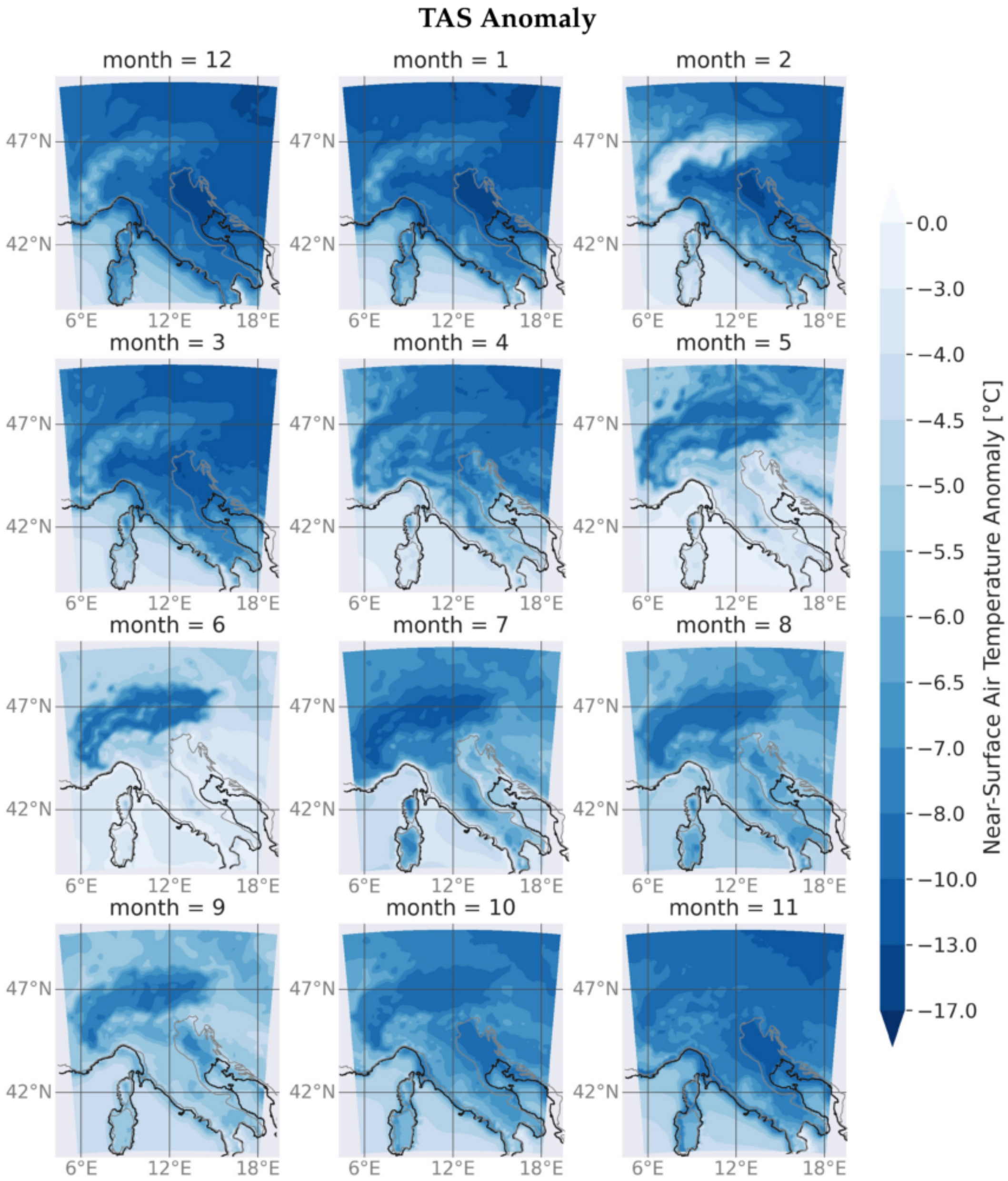

FIGURE 4.24: Monthly mean near-surface air temperature anomaly averaged over 19 years.

et al., 2011). The spatial patterns of the temperature anomaly fits well with the data of (Ludwig et al., 2020) in particular for the summer, when a large anomaly was present over the Alps. In general it was observed over the Alps an underestimation of the temperature, which is possibly caused by the topography smoothing performed by the RegCM4. Indeed, RegCM4 leaves almost unchanged the topography in the planes but reduces the maximum elevation in the Alps (figure 4.9). The same behaviour was also observed when CRU observation were compared with PC simulation (section 4.2.1)

As observed also for the MPI-ESM-P model simulation (4.1.3) and by (Strandberg

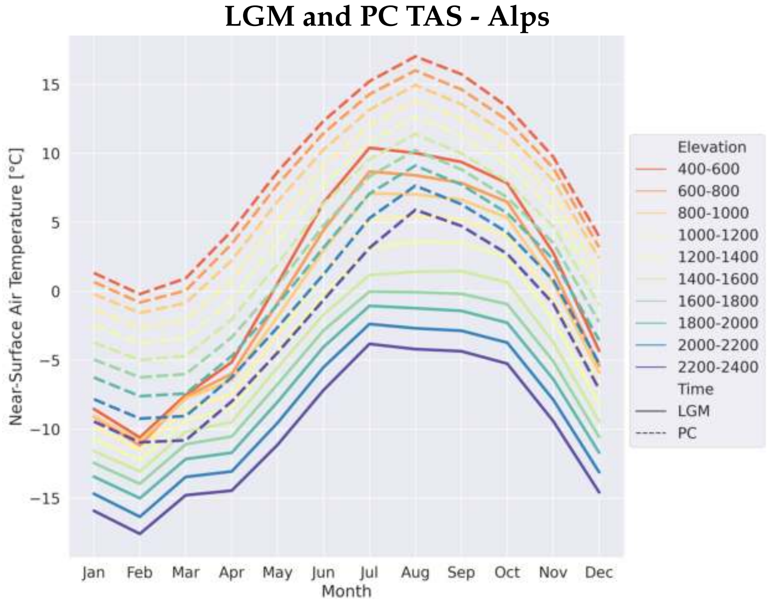

FIGURE 4.25: Monthly mean near-surface air temperature of LGM (solid) and PC (dashed) over the Alps. The colours represent different elevation bands, with the reference of the LGM topography.

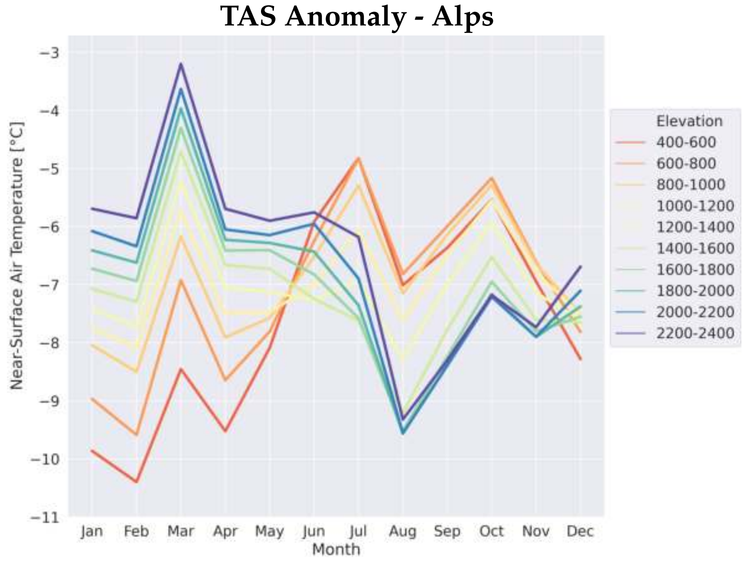

FIGURE 4.26: Monthly mean near-surface air temperature anomaly over the Alps. The colours represent different elevation bands, with the reference of the LGM topography.

et al., 2011), the largest anomaly between LGM and control-run occurred in winter (−8.30 °C on average). In particular, the NE sector of the domain feels the influence of the cold air masses around the Fennoscandian ice sheet during the LGM and the northern Adriatic undergoes the effect of the modification of the coastline between the two simulation times (figure 4.24). The temperature anomaly in the Adriatic is caused by different thermal inertia between water and land, since during the LGM the northern Adriatic was above the sea level and at the PC was submerged. The large

TAS anomaly in the north-eastern alpine foreland and the Adriatic region mainly regards the lower altitudes.

The monthly map present two different local maxima in the TAS anomaly: One in NE Europe in winter and the other in the Alps during summer. This may reflect the fact that the coldest spots of the domain have changed between the LGM and pre-industrial times: At the LGM one was located in the proximity of the Fennoscandian ice sheet an the other over the Alps, but after the ice sheet has waned, the only annual local minimum in TAS remained was over the Alps.

Over the domain, June and September were the months with the smallest monthly mean anomaly with less than 5 °C between LGM and PC on average, and in the Alps also February showed a similar characteristic. During the coldest months, in particular in February, the monthly mean anomaly is smaller over the Alps than in the rest of the domain, on the contrary, during the warmest months, in particular in July, the anomaly is larger over the Alps. The near-surface air temperature anomaly over the Alps shows an E-W gradient, with the highest temperature anomaly over the Eastern Alps (figure 4.24). This seasonal difference likely arises from the different amount and distribution of snow on the ground. Indeed, during winter, the snow covered the Alps both at the PC and LGM, while at lower elevations the snow was present at the LGM, but only occasionally at the PC. During summer the extended Alpine glaciers were only present at the LGM, and the planes were snow-free in both the simulation times. Also the zonal gradient in the Alps can be explained by the snow cover. Indeed, the Western Alps at the LGM and PC presented an extended snow cover, while in the Eastern Alps the snow cover has strongly reduced at the PC.

The annual cycle depicted in figure 4.25 shows different patterns for LGM and PC in the Alpine region. A bell-shape characterises the annual cycle of pre-industrial times, which is symmetrical around the highest TAS, occurring in July. Differently, the LGM curve shows a peak in June, with a steep increase of TAS during MAM and a steep decrease of TAS after September. During summer the average temperatures were almost constant, but slightly different trends characterised different elevation bands. Winter was longer than in pre-industrial times as highlighted by the change in the inflection points of the curves (figure 4.25), which occur earlier in the control-run (February) than in the LGM (March).

The Tagliamento basin presented similar characteristics of the rest of the Alps, with June being the warmest month until 800 m a.s.l. and a more bell-shaped pattern around July for the highest elevations.

As observe also by (Strandberg et al., 2011), in the Alps, above 1600 m a.s.l., the monthly mean temperatures were always below 0 °C, preventing melting phenomena. This elevation is above the model elevation of the Tagliamento basin, which during late-spring to early-autumn showed monthly average temperatures above 0 °C at all the elevations. In the Tagliamento basin at the PC, the average monthly

TAS were below 0 °C for 1 (at 400 to 600 m a.s.l.) to 5 (at 1200 to 1400 m a.s.l.) months per year, compared the 6 to 9 of the LGM at the same altitudes of the PC. Being TAS and melting related (Wake and Marshall, 2015), one can say that the hydrological year at the LGM presented a melting season with a different length of summer and winter compared to pre-industrial times (section 4.2.9).

At the elevations below 1000 m a.s.l., TAS anomaly presents maxima (minima) during winter (summer). In contrast, the elevations above 1200 m a.s.l. show the opposite (figure 4.26). The intermediate altitudinal bands present hybrid characteristics with less variability through the seasons. This may indicate that the influence of the Fennoscandian ice sheet , that regards mainly the low altitudes, is stronger in winter, while the contrast between the extended Alpine glaciers at the LGM and the almost ice and snow-free Alps of the pre-industrial times prevails in summer. Noteworthy is the fact that the elevation of the LGM ELA (1300 m a.s.l., Kuhlemann et al., 2008; Monegato, 2012) is closed to the elevation that separates the two anomaly patterns described above.

The altitudinal variation of the annual range of TAS (difference between the mean of the warmest month and the mean of the coldest month) calculated at four altitudinal bands (500-1000, 1000-1500, 1500-2000, 2000-2500 m a.s.l.) was studied for the Alpine region. It resulted that the pre-industrial times presented an almost constant annual range of TAS through the five altitudinal bands with a mean range of 16.68 °C and a standard deviation of 0.19 °C. The LGM, in contrast, has a mean range of 15.89 °C and a standard deviation of 2.26 °C, showing a larger temperature variability related to the elevation. The smallest LGM annual temperature range is recorded at the highest elevation, likely due to the permanent snow coverage (13.88 °C, from 2000 to 2500 m a.s.l.), while the largest temperature range is recorded at the lowest altitudes (19.47 °C, from 500 to 1000 m a.s.l.; table 4.4).

Elevation	**LGM Yearly TAS Range**	**PC Yearly TAS Range**
500-1000	19.47	16.81
1000-1500	16.22	16.46
1500-2000	14.01	16.54
2000-2500	13.88	16.91
Mean	15.89	16.68
St. Dev.	2.26	0.19

TABLE 4.4: LGM and PC yearly temperature range, given by the difference between the average TAS of the warmest month and average TAS of the coldest month.

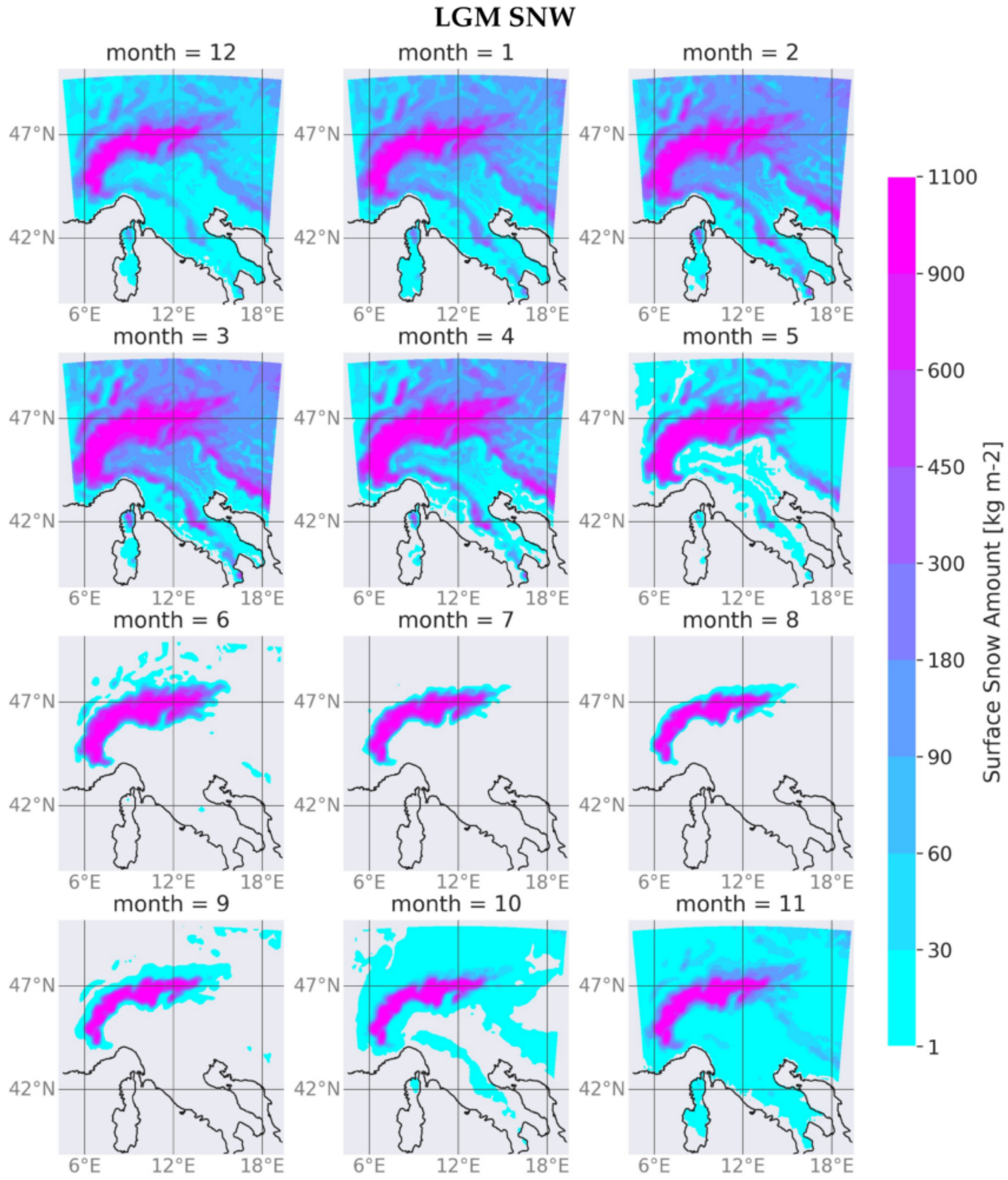

FIGURE 4.27: Monthly mean surface snow amount averaged over 19 years.

4.2.8 Surface Snow Amount

At the LGM, on average, snow was present almost over the whole domain from October to May, with the only exclusion of the low-altitude areas in the southern part of the domain (figure 4.27).

In the Alps, at the LGM, the surface snow amount increased from September to March between 400 and 1000 m a.s.l., to April between 1000 and 1600 m a.s.l. and to May above 1600 m a.s.l. (figure 4.28). The Tagliamento basin showed a similar trend, with the peak in surface snow amount that was reached later as the elevation increased. In the Tagliamento basin, the surface snow amount was always higher compared to the entire Alpine chain, with the exclusion of the highest altitudinal

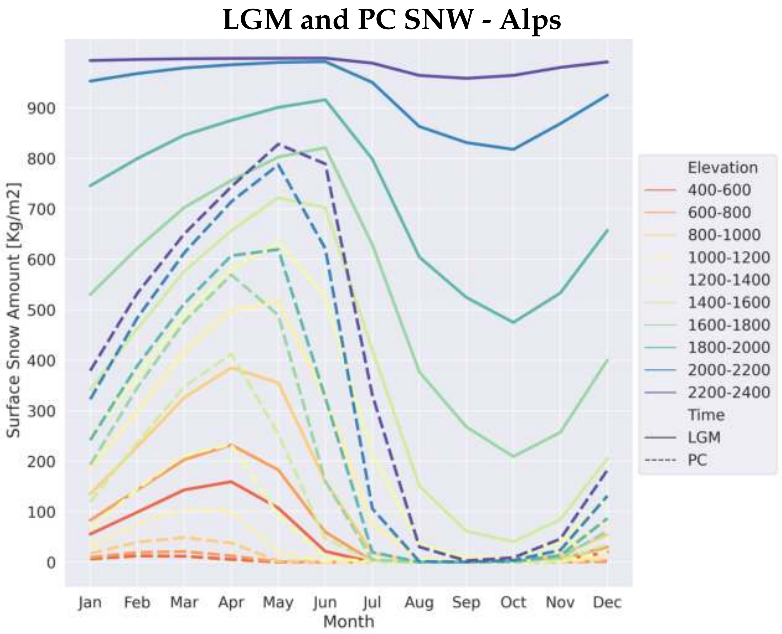
LGM and PC SNW - Alps

FIGURE 4.28: Monthly mean surface snow amount of LGM (solid) a and PC (dashed) over the Alps. The colours represent different elevation bands, with the reference of the LGM topography.

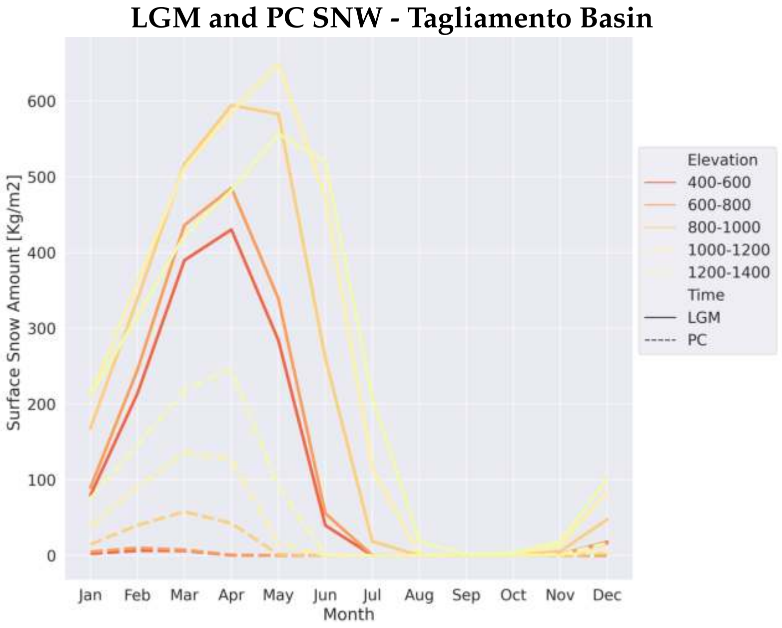
LGM and PC SNW - Tagliamento Basin

FIGURE 4.29: Monthly mean surface snow amount of LGM (solid) and PC over the Tagliamento Basin. The colours represent different elevation bands, with the reference of the LGM topography.

band (1200 to 1400 m a.s.l.), poorly represented in the Tagliamento basin (figure 4.29). Considering that the model output was given in $kg\,m^{-2}$, this may have two meanings: *i)* The snowfalls in the southeastern Alps were richer in moisture than the snowfalls in the rest of the Alps, or *ii)*, assuming a constant snow density throughout the Alps, in the southeastern Alps there was more snow on the ground than in the rest of the

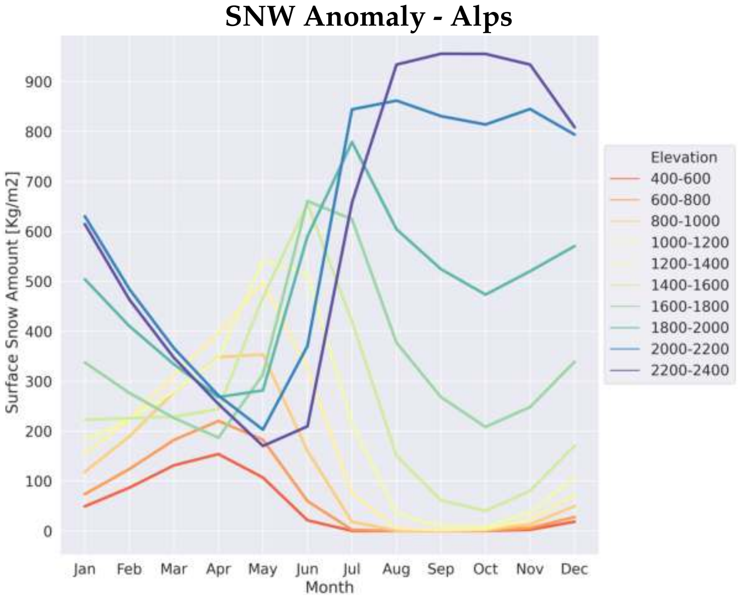

FIGURE 4.30: Monthly mean surface snow amount anomaly over the Alps. The colours represent different elevation bands, with the reference of the LGM topography.

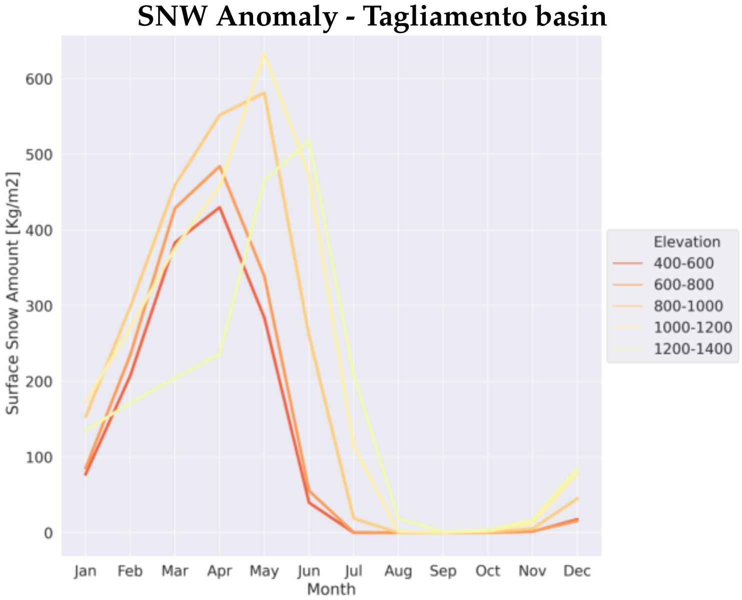

FIGURE 4.31: Monthly mean surface snow amount bias over the Tagliamento basin. The colours represent different elevation bands, with the reference of the LGM topography.

alpine chain, due to a favourable combination of precipitation and melting.

In the Alps, the minimum snow amount on the ground occurred in September above 1400 m a.s.l., from August to September from 1200 to 1400 m a.s.l., from July to September from 800 to 1200 m a.s.l., and from June to September at the lower elevations (figure 4.28). Thus the beginning of the melting season occurred earlier at lower elevations, but everywhere ended in September, when the first consistent snowfalls used to occur. LGM data support the possibility of summer snowfalls

even at low altitude due to small oscillations in the snow amount occurring during summer at all the elevations.
In the Alps, the largest anomaly in the snow amount is caused by the rising of the ELA from LGM to PC. This anomaly occurred during summer and autumn at the highest elevation (figure 4.30). In particular, above 1200 m a.s.l. the snow covered the ground all year-round. Indeed, this altitude marks the lower limit of the permanent snow-coverage at the LGM and when over a glacier it can represent the ELA. When compared with the Alps, the Tagliamento basin shows larger surface snow amount anomaly in spring, while in summer it presents slightly smaller anomalies than the Alps, also considering only the elevation between 400 and 1400 m a.s.l. (figure 4.31. This occurs because during winter the Tagliamento basin received much more snow precipitation than at the PC, but very few snow remained over the summer, due to its low elevation, which was closed to the ELA (1100 to 1300 m a.s.l., Monegato, 2012) and the southward exposition. These data show that from January to June, the Tagliamento basin was particularly snowy, consistent with the whole Alpine chain, but during summer the surface snow amount was much lower the rest of the Alps due to the intense melting that occurred at its low elevations.

4.2.9 Snow Melting

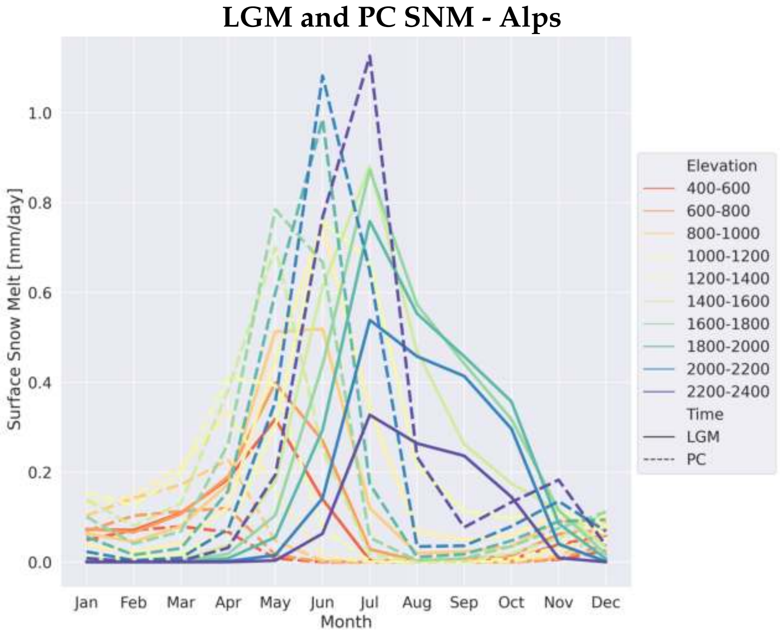

FIGURE 4.32: Monthly mean surface snow melt of LGM (solid) and PC over the Tagliamento Basin. The colours represent different elevation bands, with the reference of the LGM topography.

The snow melting at the LGM was, in average, larger than at the PC as a consequence of the higher snow amount on the ground from March-April to November (figure 4.28). During winter and early spring the cold LGM temperatures prevented

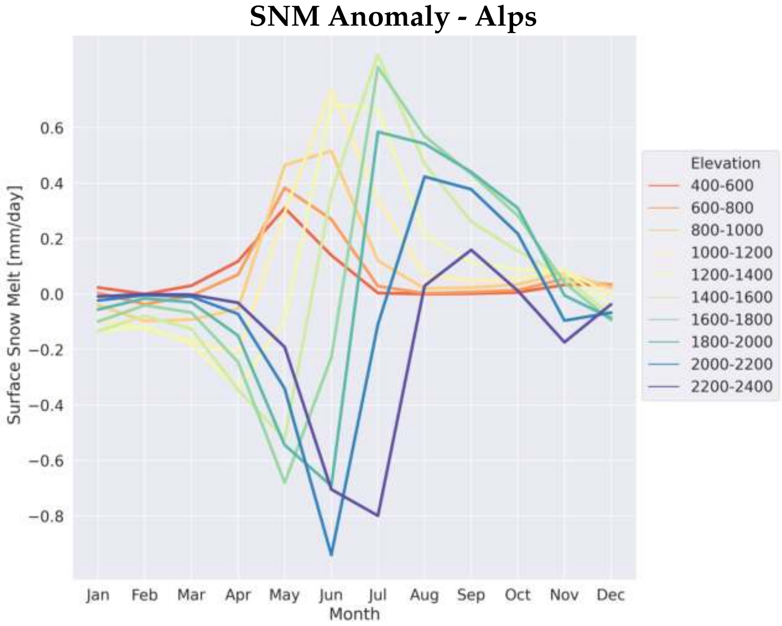

FIGURE 4.33: Monthly mean surface snow melt anomaly over the Alps. The colours represent different elevation bands, with the reference of the LGM topography.

massive melting phenomena, in particular at high altitude, where the LGM-PC anomaly was negative (figure 4.33). The snow melting season at the LGM started later and lasted longer than in pre-industrial times because of the colder condition that extended the duration of winter and the larger snow amount that remained over the summer (figure 4.32). At the LGM, the melting season began in March below 1200 m a.s.l., in April and May above and lasted to September. The melting was important, pushing the permanent snow limit above 1200 to 1400 m a.s.l. within September.

At the PC the maximum melting values (about $1\,\mathrm{mm\,d^{-1}}$) occurred above 2000 m a.s.l. between late spring and summer, but there was a second peak, of smaller intensity, in correspondence of the autumn snowfalls (figure 4.32). On the contrary, at the LGM the peak of melting was between 1000 and 2000 m a.s.l.. Out of this altitudinal range there are two distinct situations: Below 1000 m a.s.l. the melting started with the fist snowfalls of September, had a peak in April and rapidly decreased within June, when no more snow remained in the ground. Above 2000 m a.s.l. the melting started in April, with the peak occurred in June, but with less intensity than at the intermediate elevations. This because the cold temperatures in altitude prevented melting phenomena despite the large amount of snow on the ground.

Above 1600 m a.s.l. the annual melting curve was not centred around the peak (in June), but presented a tail until October, when the cold temperatures abruptly stopped the melting (figure 4.32). The convexity of the curve may indicate the melting of new snow, deposited by summer snowfalls, which was characterised by lower density and faster melting compared with the older snow. At these elevations some snow

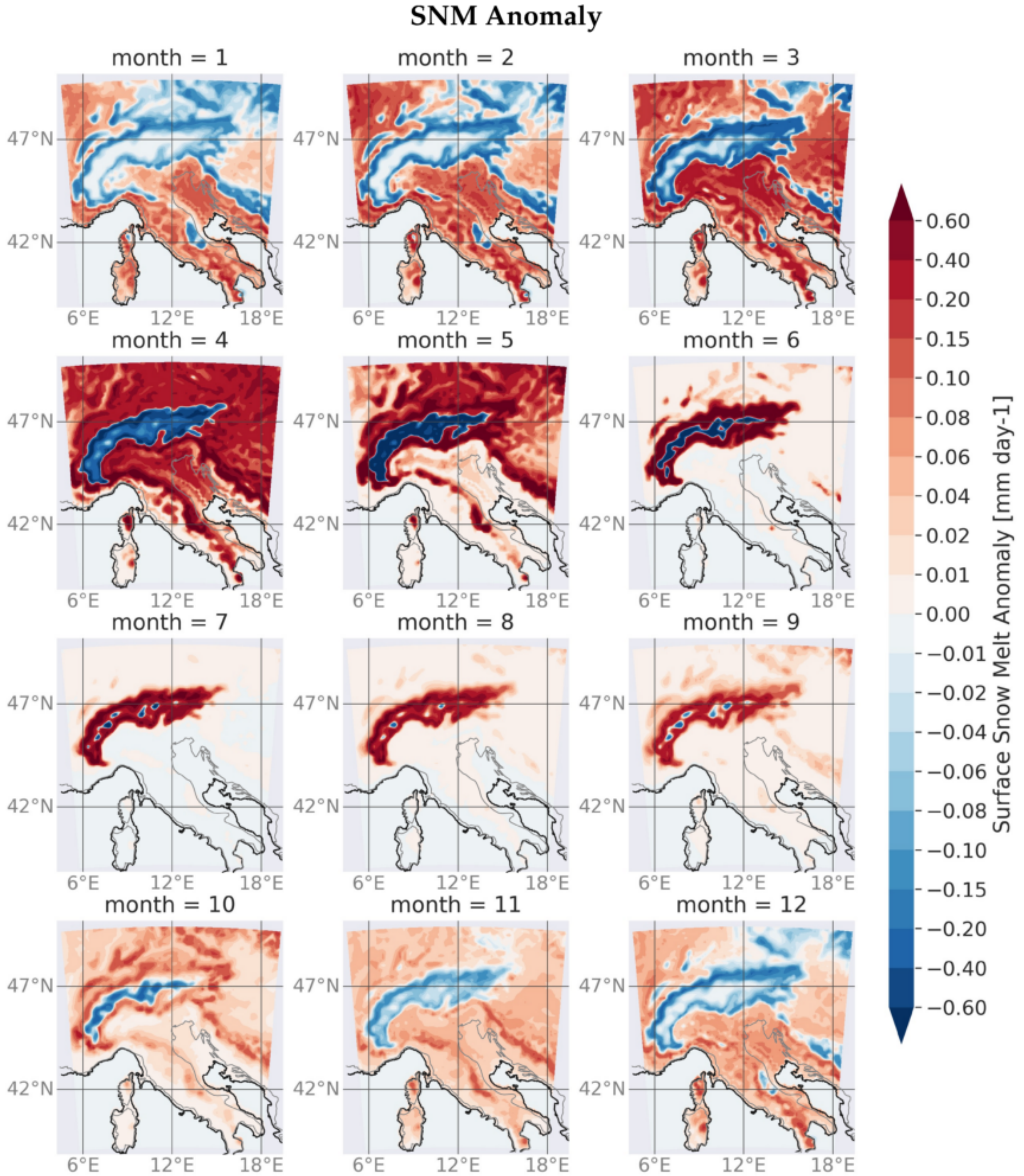

FIGURE 4.34: Monthly mean snow melt anomaly averaged over 19 years.

always remained on the ground.

Below 1000 to 1200 m a.s.l. the LGM-PC anomaly was always positive suggesting that there was snow available for melting (figure 4.33). Above this elevation the melting anomaly was negative until the late spring-early summer due to the cold temperature of the LGM that prevented the melting. On the contrary at the PC late spring-early summer was the time with the highest melting values. Between late-summer to early autumn the melting anomaly (figure 4.34) was positive above 1000 to 1200 m a.s.l., because of the large availability of snow to melt compared to the PC.

The Tagliamento basin presented higher values of snow melting at all the elevations if compared to the average values, at the same altitudes in the Alps (figure 4.33 and

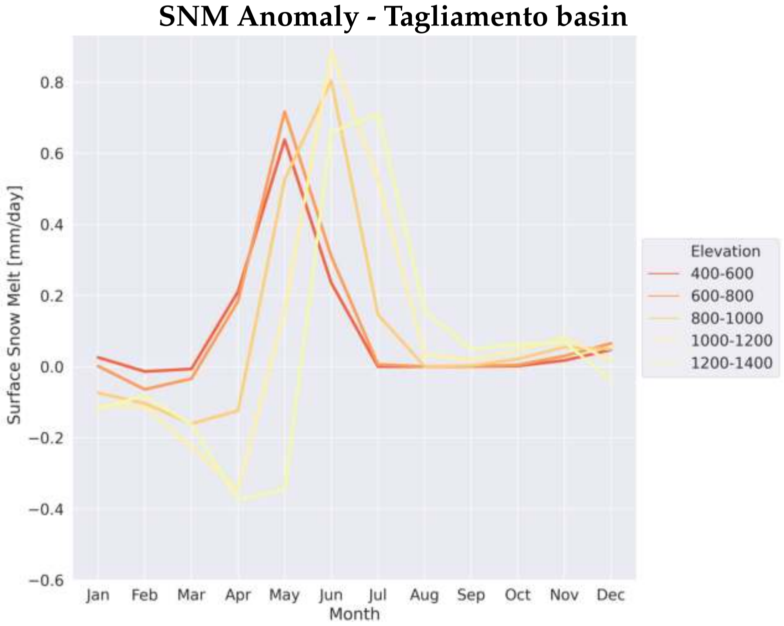

FIGURE 4.35: Monthly mean surface snow melt anomaly over the Tagliamento basin. The colours represent different elevation bands, with the reference of the LGM topography.

4.35). This reflects the larger amount of snow on the ground in the Tagliamento glacier compared with areas at same elevations in the rest of the Alps. Due to the low elevation of this basin, the yearly LGM curve does not show the skewness towards the autumnal month, as for the Alps, but above 1000 m a.s.l. the surface snow melting in summer was larger than 0 mm d^{-1}. This indicates that a certain amount of snow remained on the ground all year-round above 1000 m a.s.l. also in the Tagliamento basin.

4.2.10 Runoff

The runoff is an important variable in the study of the hydrological cycle and presents marked differences between LGM and PC. It can be distinguished into surface and total. The total runoff (figure 4.36 and 4.37) includes the percolation of water into the ground and is higher than the surface runoff (figure 4.38).

Both the runoffs show similar trends for the PC, while for the LGM they show different patterns, in particular during summer and above 1400 m a.s.l. . This may be a consequence of the below-freezing point temperatures at high elevations during the LGM, condition that prevents the presence of liquid water at the surface.

Considering the total runoff anomaly, the values were positive in summer and negative in winter at low elevation (figure 4.36). Above 1200 to 1400 m a.s.l. the runoff anomaly was positive between June and September and negative between October and May, with two peaks corresponding to late-spring and October (figure 4.39). The anomaly shows a delay in the beginning of the melting season of the LGM respect

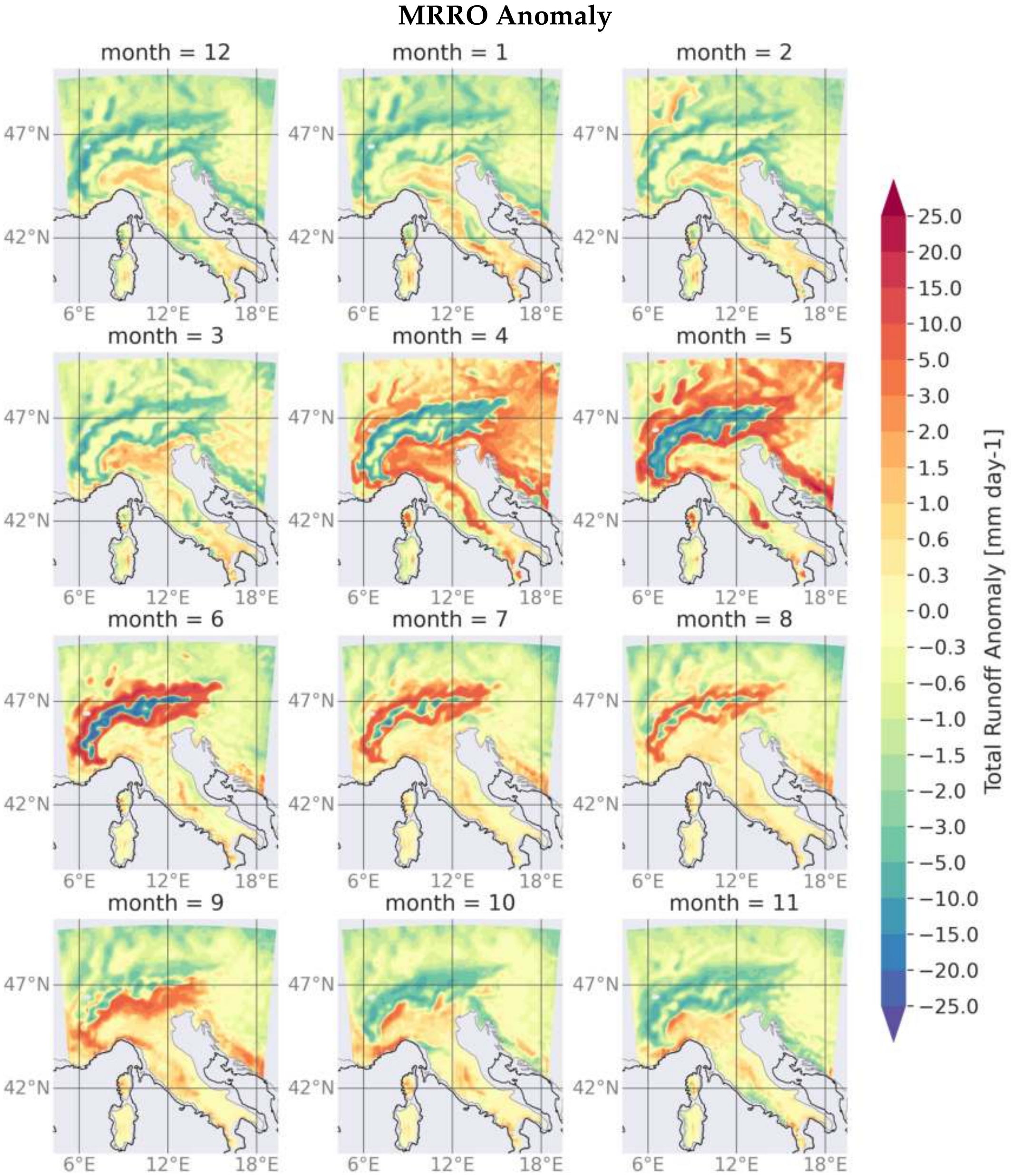

FIGURE 4.36: Monthly mean surface runoff anomaly averaged over 19 years.

to the PC above 1200 m a.s.l.. Below this elevation the runoff anomaly reflects the presence of snow at the LGM but not at the PC.

At the LGM the peak in the runoff occurred from May to July from 400 to 1600 m a.s.l., above this elevation the runoff decreased with a pattern already shown by the yearly melting curve (figure 4.37). Indeed, the runoff presented a skew that extended from July to October with a low steepness. This shape may indicate the runoff of melting water from new snowfalls, occurred during summer.

The PC on the contrary shows a well defined peak during summer (later than in the LGM), whose values rise with the elevation as a consequence the high amount of snow at high altitude during the PC.

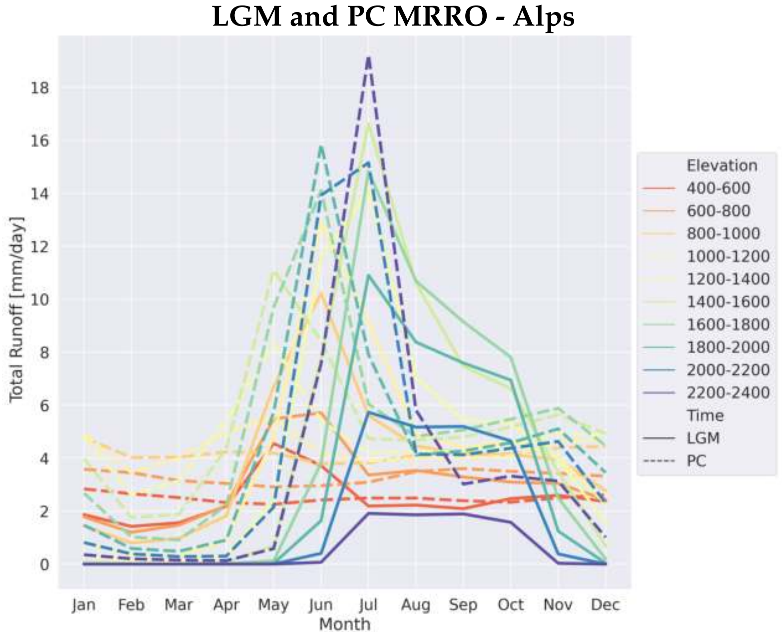

FIGURE 4.37: Monthly mean total runoff of LGM (solid) and PC (dashed) over the Alps. The colours represent different elevation bands, with the reference of the LGM topography.

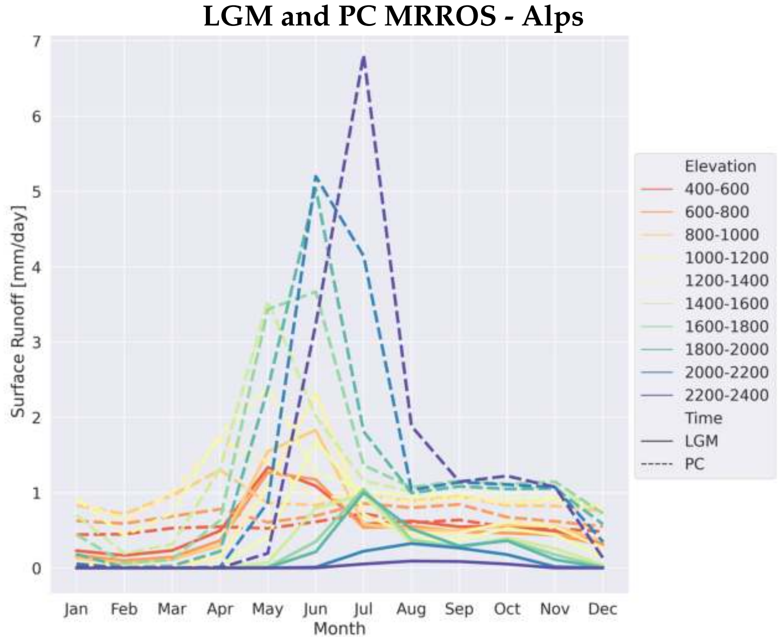

FIGURE 4.38: Monthly mean surface runoff of LGM (solid) and PC (dashed) over the Alps. The colours represent different elevation bands, with the reference of the LGM topography.

The strong correlation between snow melting and runoff is highlighted by the presence of the highest runoff values in the alpine region during the melting season. During spring and autumn the runoff over the Alps was minimum, but it showed high values in the piedmont areas, where the temperatures were favourable to melt

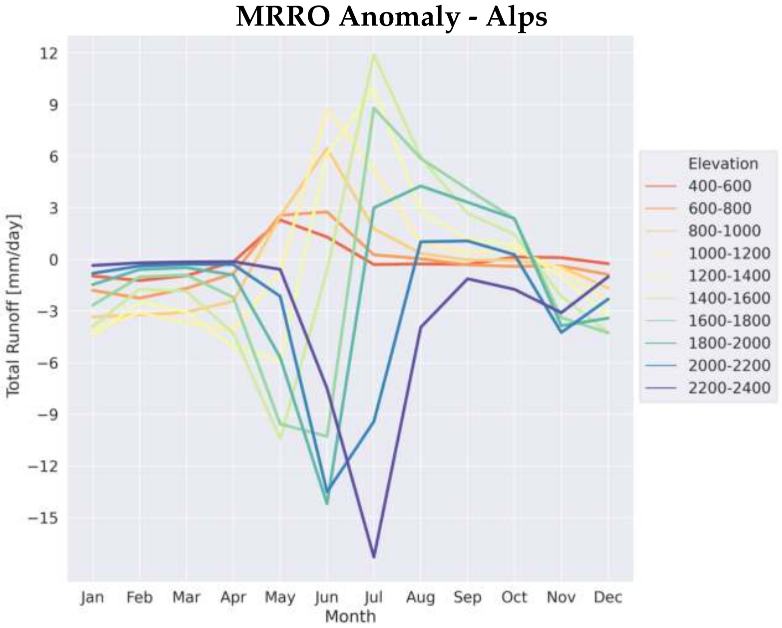

FIGURE 4.39: Monthly mean total runoff anomaly over the Alps. The colours represent different elevation bands, with the reference of the LGM topography.

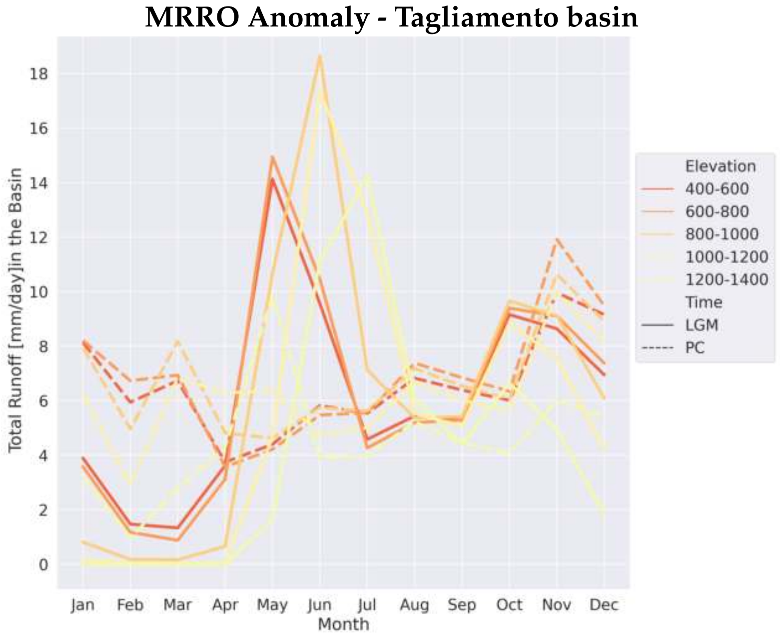

FIGURE 4.40: Monthly mean total runoff anomaly over the Tagliamento Basin. The colours represent different elevation bands, with the reference of the LGM topography.

the snow on the ground.

The Tagliamento basin presents two peaks one from late spring to summer, as the rest of the Alps, and one, of smaller intensity, in September (figure 4.40). At the elevation of the Tagliamento basin the rest of the Alps does not show the second peak. This matches with the high LGM precipitation rate during autumn in the southern Alps compared to the other alpine sectors.

4.2.11 Evaporation

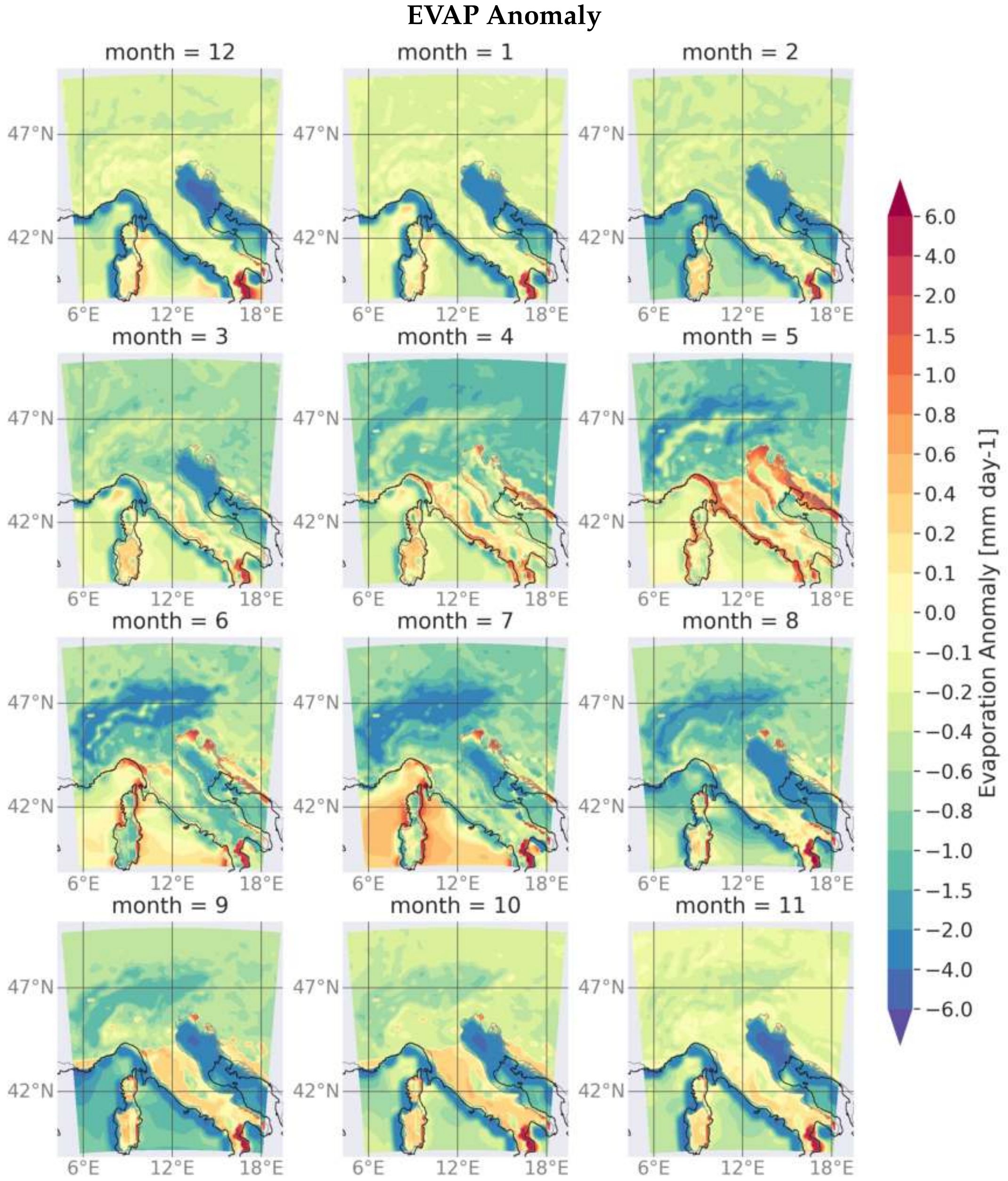

FIGURE 4.41: Monthly mean evaporation anomaly averaged over 19 years.

The higher pre-industrial temperatures and the different vegetation favour higher monthly mean evaporation compared to the LGM. The largest evaporation anomaly is recorded along the coastlines due to the modification of the terrain between the two simulations and over the Alps during the melting season with variations dependent on the altitude. At the LGM the evaporation was more relevant than in the PC in spring and autumn over the Apennines and on the Balkan coast. This pattern, clearly different from the alpine region pattern, may depend on a combination of factors:

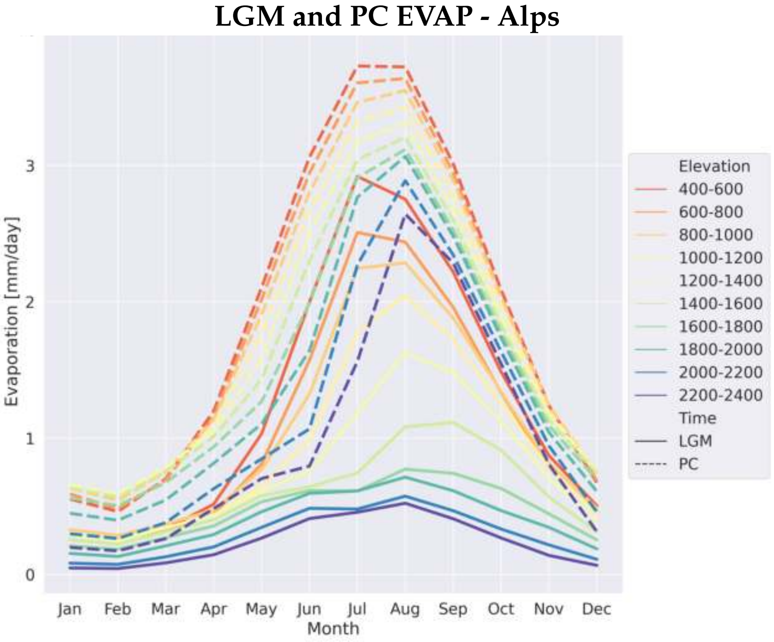

FIGURE 4.42: Monthly mean evaporation of LGM (solid) and PC (dashed) over the Alps. The colours represent different elevation bands, with the reference of the LGM topography.

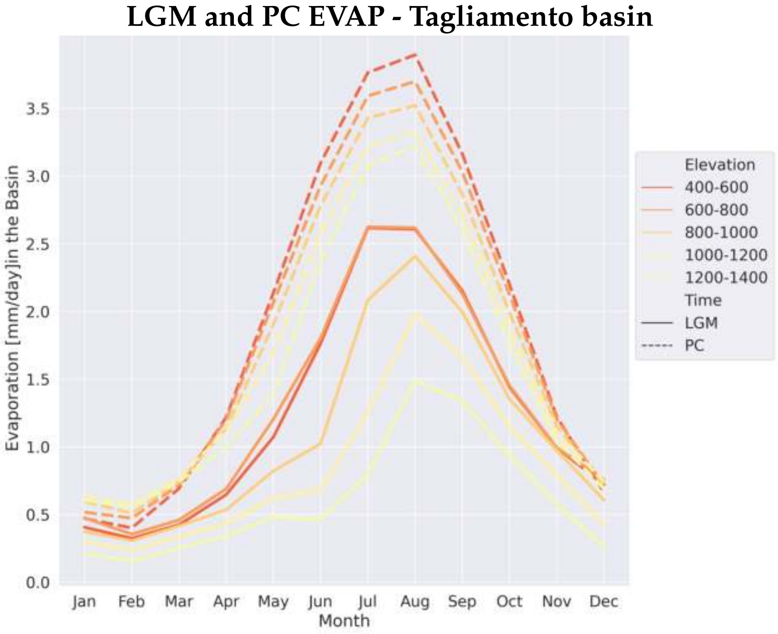

FIGURE 4.43: Monthly mean evaporation of LGM (solid) and PC (dashed) over the Tagliamento Basin. The colours represent different elevation bands, with the reference of the LGM topography.

i) the abundance of water available from melting and surface runoff, **ii)** the higher temperatures and *iii)* the vegetation (figure 4.41).

The evaporation annual cycle shows a bell-shaped curve around June-July for both LGM and PC (figure 4.42). The variation of evaporation with the elevation was larger at the LGM, with 2.5 mm d^{-1} between lower and higher elevation, compared with the PC, when the range was of 1 mm d^{-1}. A similar pattern was also observed in the vertical temperature range of LGM and PC.

In the Tagliamento basin the average monthly evaporation at different elevation was generally lower than over the whole Alps at the same elevations (figure 4.43). This may reflect the trend shown by *i)* Near Surface Air Temperatures (TAS), that in the Alps, between 400 and 1400 m a.s.l. are about 2 °C warmer than in the Tagliamento basin and *ii)* Surface Temperatures (TS) that in the Alps, between 400 and 1400 m a.s.l. are about 3 °C warmer than in the Tagliamento basin.

4.3 Months with anomalous pattern

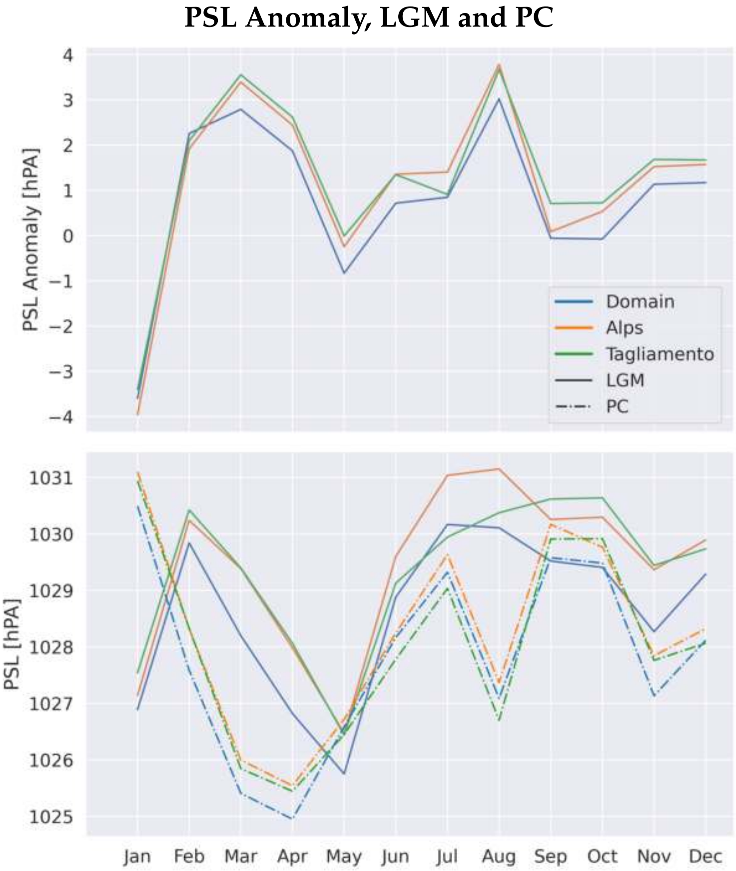

FIGURE 4.44: Monthly mean sea level pressure of LGM (solid) and PC (dashed) over the domain (blue), Alps (orange) and Tagliamento Basin (green).

From the above study of the primary output variables it appears as if the behaviour of some months is not aligned with the more general seasonal trend. It is worth analysing these situations more in depth, in particular for what concerns the sea level pressure (figure 4.11) and precipitation anomalies (figure 4.13) of January.

Indeed, the January sea level pressure anomaly is negative while in all the other

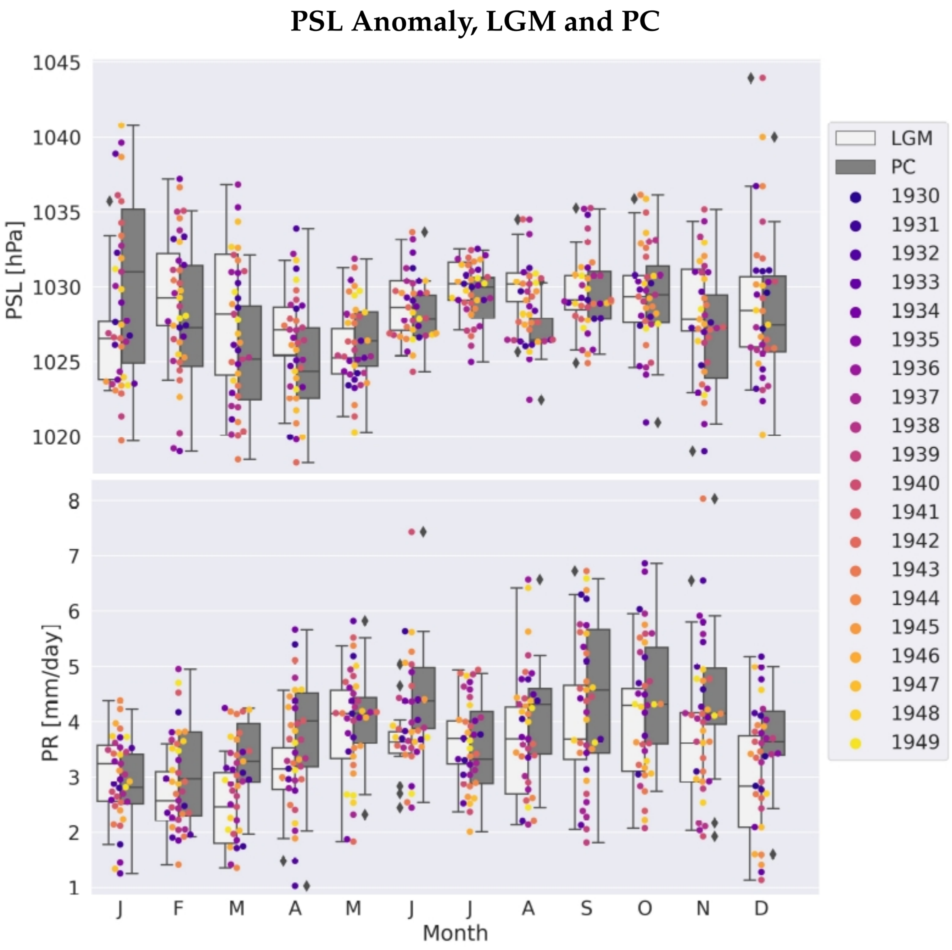

FIGURE 4.45: Box-plot representing the LGM (grey boxes and PC (white boxes) monthly mean year-by-year of PSL (above) and PR (below). The different years are drawn as coloured circles and the outliers as black diamonds.

month, particularly during winter it is positive. The case is similar for the precipitation anomaly, which presents a positive anomaly in January with a well defined boundary between wetter and drier LGM conditions on the main alpine divide, while November, December, February and March show mainly drier LGM conditions compared to the PC over the whole domain.

From LGM to PC the annual cycle changed and in general presented a shift of one month between the two simulations, with the PC anticipating the LGM. January may result particularly anomalous for precipitation and sea level pressure due to the fact that in January occur the maximum seasonal values of one simulation time and the minimum seasonal values in the other simulation time, as shown for the sea level pressure by the figure 4.44.

In order to investigate the cause of this anomalous behaviour, in particular with regards to the month of January, a study of the outliers and a jackknifing approach were applied to the data. The outliers were intended as the monthly means of the individual years falling out of the 99 percentiles. Figure 4.45 shows the monthly statistical distribution as box-plot for the monthly mean PSL and PR. The outliers are present in several months (PSL: January, June,August, September. October, and December; PR: April, May, June, August, September November, and December) but January shows outliers only in the LGM sea level pressure. Thus according to this analysis there is not a correspondence between anomalous months in the monthly mean maps (figure 4.11 and 4.13) and the presence of outliers in the monthly means of the individual years (figure 4.45).

The second applied approach was a leave-one-out jackknifing technique. This approach requires to systematically leave out each observation of a dataset, constituted by *n* elements, and then calculate the statistical metrics of *n-1* elements, *n* times. Thus, for each of the 19 years of the simulations we produced a map of a given variable (pr,prc and psl) averaged over 18 years. This method did not highlighted any problematic data as all the maps showed a similar pattern in every month.

The last analysis focused on the possibility that a particular day in every January caused unreliable data, but again no problematic years nor days were found.

Observing the sea level pressure anomaly, January presents particularly low values when compared to the winter mean. This anomaly may be explained by a change in the annual cycle between LGM and PC. Indeed, in January the LGM sea level pressure showed the lowest winter values, while at the PC it showed the highest values (figure 4.44). This could possibly cause a significant negative anomaly in the January sea level pressure.

Concerning the precipitation there are more factors that might contribute to anomalous patterns:

i the large monthly and spatial variability of the total precipitation (figures 4.13 and 4.17), which may determine large anomalies in a particular region;

ii the shift of about one month in the monthly mean patterns, already observed for the sea level pressure;

iii the combination between stratiform and convective precipitation. In the Alps stratiform precipitation was predominant during winter (table 4.3), both at the LGM and PC. In January, but not in the other winter months, the total precipitation anomaly reflected the pattern of the stratiform precipitation anomaly, with a well defined boundary between the northern Alps negative anomaly and the southern Alps positive anomaly. This points out that eventually the stratiform precipitation covered the convective precipitation signal in January, but why this occurred only in January is still not clear.

These elements only contribute to complicate the understanding of January precipitation, but do not explain its behaviour. Indeed, the positive convective precipitation anomaly over the Apennines (4.14) is not reliable, due to the lower LGM average temperatures and the consequent more stable and less energetic atmosphere compared to pre-industrial times, that do not represent the ideal background for convection.

4.4 MPI-ESM-P and RegCM4 models comparison

To conclude the analysis of the climate model simulations employed in this study we briefly address the topic of the added values in a qualitative way. A comparison between RCM and ESM paleoclimatic simulations provides new references to the added values in the paleoclimate modelling field (Armstrong et al., 2019; Ludwig et al., 2019). Being the domain of study reach in orographic features it is the ideal terrain to test the performance of a RCM and compare its results with a lower resolution Earth's system model.

Armstrong et al. (2019) found that the RCM applied to paleoclimate showed improved spatial pattern and enhanced anomalies in the jet stream, but when compared to the proxy reconstructions no apparent improvements was identified. In the case of our study (figure 4.23) only four proxies falls in the RegCM4 domain. Among these proxies three are in agreement with our RegCM4 model result. In the domain shown for the MPI-ESM-P model 23 proxies from Bartlein et al. (2010) are present and 10 fits with the MPI-ESM-P simulation, but only two are located in the smaller RegCM4 domain. Thus in this study, the RCM has not only improved the spatial pattern increasing the information in the mountain areas, but has also increased the agreement between proxy reconstruction and model from 50 % (MPI-ESM-P) to 75 % (RegCM4).

A comparison of models precipitation (figure 4.46) and temperature(figure 4.47) anomalies evidence the increased detail of the RCM simulations particularly over the Alps and Apennines, where the anomaly values are maximum. The MPI-ESM-P model produce almost uniform anomalies over the Italian peninsula, Adriatic Sea and Balkans, as its resolution can not resolve these three elements. On the contrary, the RCM shows temperature and precipitation gradients that can be associated to the elevation and land-sea mask.

In particular the MPI-ESM-P model present over the Apennines a slightly positive anomaly, but the increased resolution of the RCM allow to capture the spatial distribution of positive and negative precipitation anomaly areas.

To conclude the RCM provided new and more detailed information about PC and LGM climate condition respect to the MPI-MPI-P simulation. The discrepancies between proxies and models can be attributable to intrinsic error of both methods but also to resolution-dependent issues.

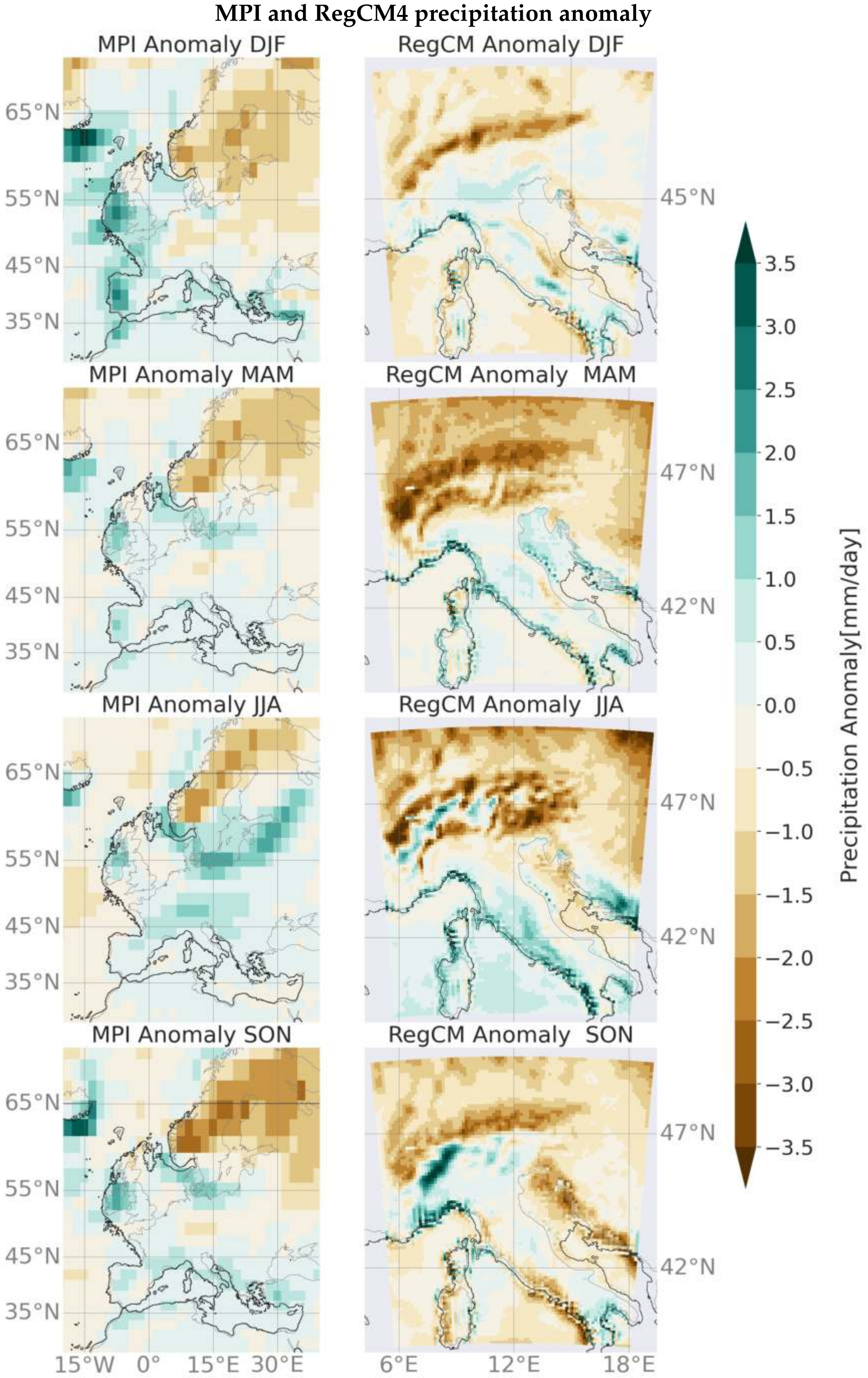

FIGURE 4.46: MPI-ESM-P (left) and RegCM4 (right) seasonal mean precipitation anomaly.

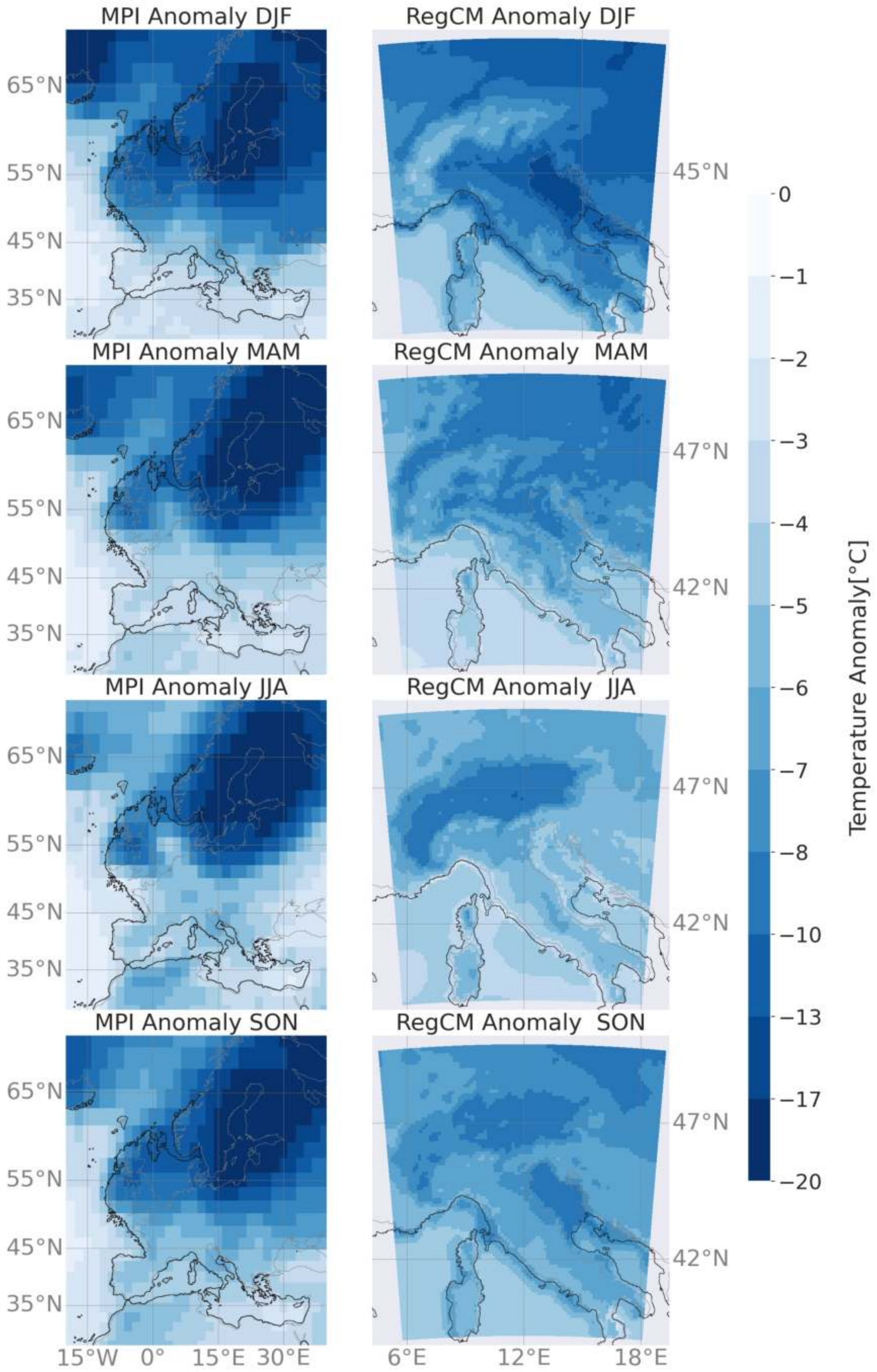

FIGURE 4.47: MPI-ESM-P (left) and RegCM4 (right) seasonal mean temperature anomaly.

Chapter 5

Equilibrium-Line Altitude

The Equilibrium-Line Altitude allows to relate glacier changes to variations in the climate conditions (Lie et al., 2003; Mcgrath et al., 2017; Zemp et al., 2008). According to Cogley et al. (2011), the ELA is the spatially averaged altitude of the set of points on the surface of the glacier where the climatic mass balance is zero at a given moment. Of interest for this study is the environmental ELA, which represents the regional altitude of zero mass balance in the absence of shading, avalanching, debris-cover and topography-dependent effects (Anderson et al., 2018). This means that the environmental ELA is only determined by regional climatic factors such as temperature and precipitation.

In this work the environmental ELA (hereafter referred to as *envELA*) calculations are performed following the methodology presented by Žebre et al. (2020), which is based on the equation of Ohmura and Boettcher (2018).

The main scientific questions addressed by this chapter are:

i) Is RegCM4.7 able to reproduce the climatic conditions suitable for an extended glaciation over the Alps during the LGM? (section 5.1)

ii) What is the spatial pattern of the LGM envELA over the domain? (section 5.2)

iii) How much did the envELA rise from the LGM to the PC? (section 5.2)

In order to answer the second and third questions, a bias correction was applied to the RegCM data before calculating the envELA.

5.1 Assessment of model simulations by means of envELA

The envELA represents the theoretical elevation above sea level where a glacier can form (Anderson et al., 2018; Žebre et al., 2020). Here we want to apply this definition to understand whether RegCM4.7 is able to produce the right combination of temperature and precipitation to support the existence of a glacier where we know from the literature that a glacier existed and whether the grid-cells where this condition is satisfied lie below the model topography. The main idea is that the area

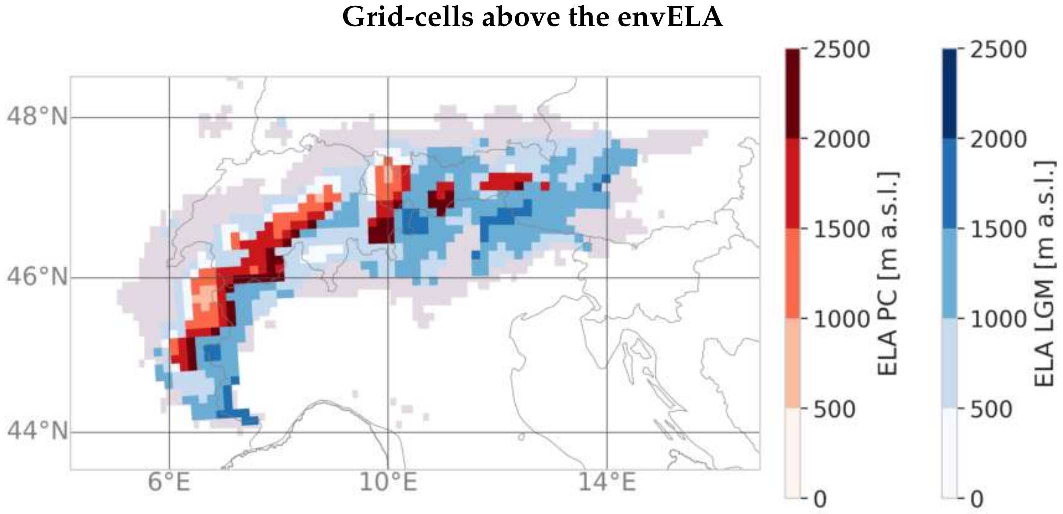

FIGURE 5.1: LGM (blue) and PC (red) envELA and potential glacier extension, i.e. the grid-cells where the envELA is lower than the surface elevation. In grey the LGM glacier extension according to the literature.

contoured by the set of grid-cells where the envELA intersects the model topography has the right conditions for the existence of a glacier. Thus if this area lies over the glacier map of LGM or PC, we can say that RegCM performs well in representing glacier-suitable condition for that time. This fact is extremely important in order to model the LGM reliably.

The envELA found in this section is strictly related to the model topography and climate and do not necessarily represent the true ELA, except where the model topography equals the real topography. This connection between model topography and envELA is due to the model's finite resolution and the resulting smoothing of its topography, which is more pronounced in correspondence with relatively small orographic features such as mountain tops and steep gradients.

The envELA was calculated for both the LGM and PC simulations, following the approach presented by Žebre et al. (2020), which is based on an empirical equation that relates mean summer temperature and total annual precipitation (Ohmura and Boettcher, 2018):

$$P_a = 5.87T_{JJA}^2 + 230T_{JJA} + 966 \tag{5.1}$$

where P_a is the RegCM total annual precipitation in mm and T_{JJA} is the RegCM mean summer air temperature in °C.

Differently from Žebre et al. (2020), who calculated the envELA for every year in a given time range, here the envELA was obtained by averaging temperature and precipitation over the 19 yr of the simulations, as the glaciers were considered at a steady-state during the simulation time.

The processing flow described by Žebre et al. (2020) involves the application of the equation 5.1 grid-cell by grid-cell using the RegCM4.7 total annual precipitation as

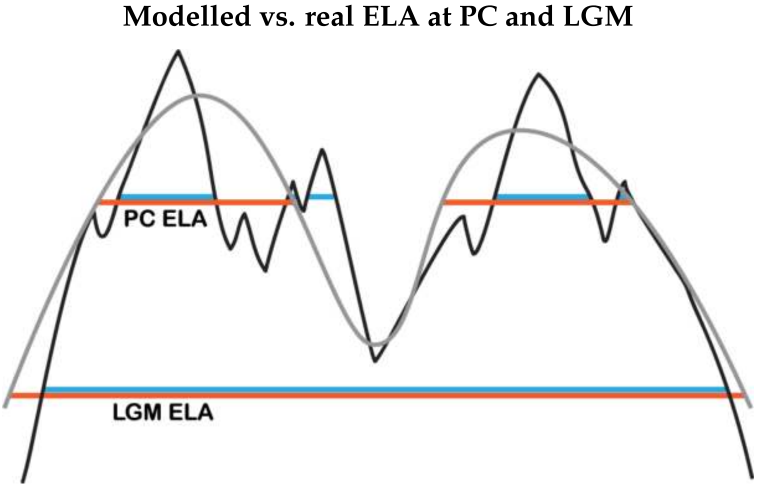

FIGURE 5.2: Schematic sketch of the model orography (grey) with the model extrapolated envELA (red) vs. the real orography (black) with the real ELA (blue) for LGM and PC.

input for P_a in order to calculate the T_{JJA}. The height difference between the modelled T_{JJA} and the RegCM4.7 mean summer temperature (T_{RCM}) is calculated for every grid-cell by applying the summer environmental lapse rate of 0.65 °C/100m. Then the resulting height difference is subtracted from the RegCM4.7 model topography (DEM_{RCM}):

$$envELA = DEM_{RCM} - [(T_{JJA} - T_{RCM}) * 100/0.65] \tag{5.2}$$

In the grid-cells where the height difference is negative, the envELA is lower than the RegCM4.7 topography, and the presence of a glacier is possible. Figure 5.1 shows the grid-cells where a glacier can potentially exist according to the calculated envELA for the LGM and PC.
A further check requires to compare the grid-cells where a glacier can potentially exist with the glacier map of a reference time. The glacier extension should enclose the envELA, as the ELA in a steady-state glacier is not located at the glacier front but instead separates ablation and accumulation areas.

This approach does not claim to reproduce the real ELA at PC and LGM accurately, but rather we wanted to employ the modelled envELA to test RegCM4.7. We focus on the ability of RegCM to reproduce the adequate LGM conditions for the subsistence of a glacier, and we check whether this condition is satisfied in an area that was effectively glacier-covered at the LGM (figure 5.1).

5.1.1 Results and discussion

It resulted that just few grid-cells fall out of the area that was effectively glacier-covered at the LGM. Concerning the PC, the envELA showed a withdrawal with respect to the LGM, as expected, but the grid-cells where a glacier could potentially

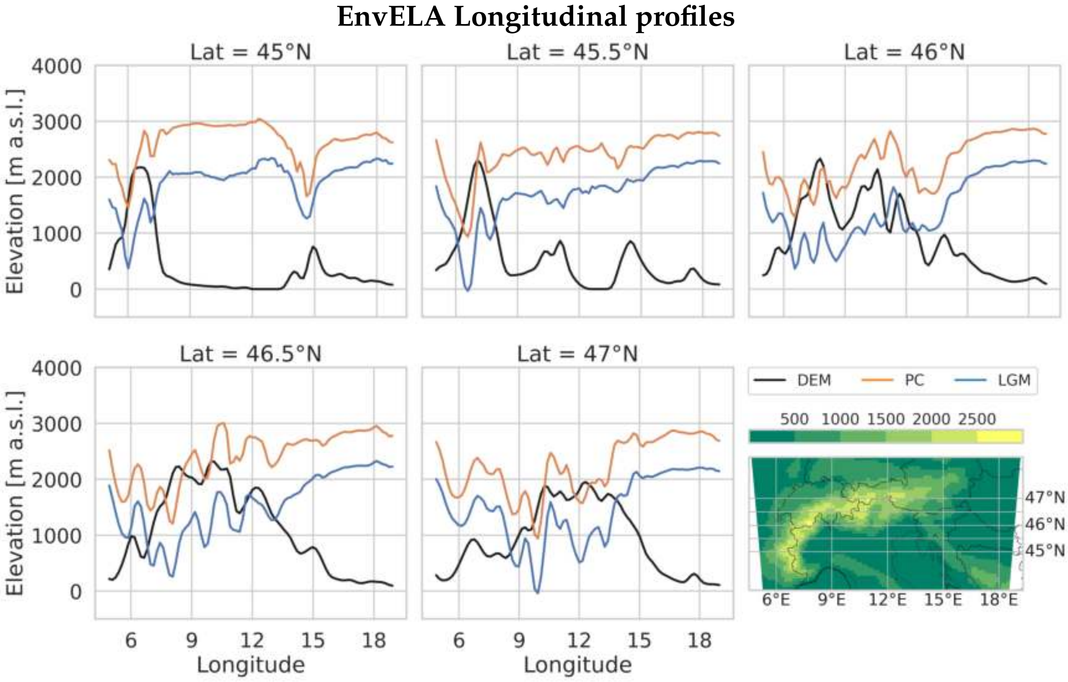

FIGURE 5.3: Longitudinal transects of the LGM (blue) and PC (orange) modelled envELA across the Alps calculated from the RegCM4.7 mean summer temperature and total annual precipitation averaged over the 19 yr of the simulations. In the lower right corner the model topography in m a.s.l..

exist exceeded PC glacier extension (figure 5.1).

This difference between LGM and PC can be explained by the differences between the real and the model topography, as shown in figure 5.2. Indeed, at the LGM the glaciers extensively covered the Alps, reaching low elevations and also several valley floors, and the modelled envELA for the LGM is almost everywhere below both the real and model topography in the Alps. At the PC the glacier front withdrew, causing desegregation of the LGM extended ice bodies and reducing the glaciers extension. In the Alps the PC ELA often lies above the real topography but below the modelled one. This occurs especially at high elevation, where the real topography is jagged, but the model topography is smooth.

The method presented in this section did not allow to calculate the envELA over the whole alpine chain, as it showed unreasonably low values in the western Alps (0 to 500 m a.s.l. for the LGM and 1500 m a.s.l. for the PC compared to the values between 1500 and 1850 m a.s.l. found by Federici et al. (2016) and Forno et al. (2010) for the LGM and the value of 2800 m a.s.l. found by Cossart et al. (2012) and Federici et al. (2016) for the PC; figure 5.3). Too high precipitation or too low temperature for the Western alpine region may explain this behaviour since the envELA is calculated starting from the empirical equation 5.1, which is based upon these two variables.

In figure 5.4, five transects across the Alps at different latitudes highlight the longitudinal distribution of the total annual precipitation and mean temperatures. The

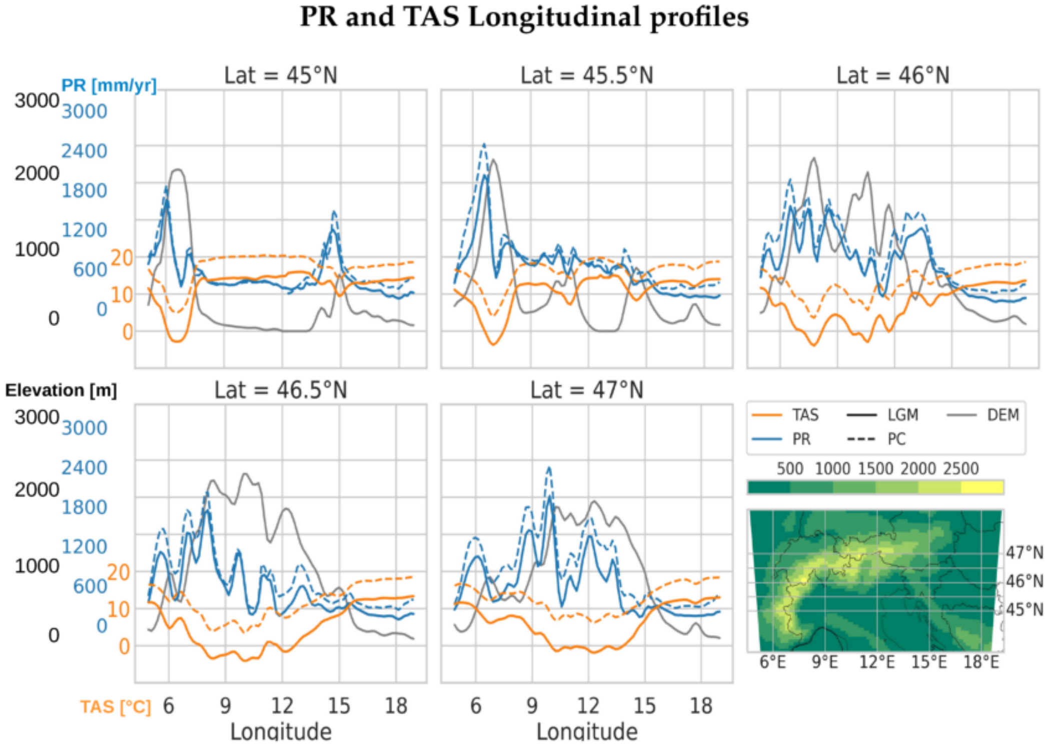

FIGURE 5.4: Longitudinal transects of the LGM (solid lines) and PC (dashed lines) TAS (orange) and PR (blue) across the Alps. In grey the model topography also represented in the lower right corner as a map.

topography represented in figures 5.3 and 5.4 is the PC model topography, as it corresponds to the present-day topography. This makes it possible to compare the result of this thesis with other works.

Concerning the temperature, it was applied a correction based on the environmental lapse rate (0.65 °C/100m) to the LGM data in order to take into account the 120 m of elevation difference between LGM and PC.

The precipitation pattern in the external western Alps presents extremely high precipitation both at the LGM and PC (figure 5.4) around some circle-shaped spots (figure 4.12.a). Present-day observations (figure 4.12.b; Isotta et al., 2014) show high precipitation values in the external western Alps caused by the Atlantic air masses, but the highest values are recorded in Ticino, Julian and Carnic Alps due to southerly flows.

Figure 5.3 and 5.4 show similar patterns between the envELA and the total annual precipitation, with the peaks located in the western alpine chain, up-wind with respect to Atlantic air masses, while the negative peaks of temperature are centred around topography maxima.

This data suggests that RegCM4.7 overestimates the orographic precipitation in the external western Alps, and this negatively affects the envELA calculations performed with equations 5.1 and 5.2. A possible explanation can be found in the model customisation (performed by comparing a PC simulation with present-day observations) that was focused particularly on the precipitation in the southeastern Alps. Thus the chosen set of customisation parameters may not be the ideal one for the western alpine sector.

In support of this hypothesis there are the ELA values found by Kuhlemann et al. (2008), Monegato (2012) and Tintor (2005) for the small LGM glaciers of Julian Prealps. In this region the envELA found following the methodology presented by Žebre et al. (2020) is about 1000 m a.s.l. and fits with the values shown by Monegato (2012), where the ELA was estimated to range from 1130 to 1200 m a.s.l.. Kuhlemann et al. (2008) assessed the LGM ELA in the southeastern Alps to values below 1300 m a.s.l. while Tintor (2005) proposed a value around 1000 m a.s.l..

5.2 EnvELA with bias-corrected data

As seen in the previous section (5.1), our RegCM4.7 model simulation overestimates the precipitation in both the LGM and PC runs. Thus, a first-order bias correction was applied before calculating the envELA with equations 5.1 and 5.2.

The pre-industrial RegCM4.7 annual total precipitation and summer mean temperature were averaged over the simulation time (19 years) and then compared with two observational datasets reduced and averaged over the time range 1871–1900, indicative for the pre-industrial time. Precipitation and temperature were bias-corrected with the Long-term Alpine Precipitation Reconstruction (LAPrec; Auer et al., 2007; Isotta et al., 2014) and the Historical Instrumental climatological Surface Time series of the greater Alpine region (HISTALP; Auer et al., 2007) respectively.

The biases between model and observations were estimated for the pre-industrial simulation but were assumed to remain constant in time and were then used to bias-correct also the LGM precipitation and temperature model outputs. This is a strong assumption, however, due to the lack of observations for the LGM, we can not separately bias-correct pre-industrial and LGM temperature and precipitation. Additionally, this allows to compare the two bias-corrected simulations evenly.

The precipitation was corrected assuming a simple linear scaling, as:

$$P_{corr} = \frac{\overline{P_{LAPREC(1871-1900)}}}{\overline{P_{PC-RCM(19yr)}}} * P_{m,RCM(19yr)}, \tag{5.3}$$

where $\overline{P_{LAPREC(1871-1900)}}$ is the yearly precipitation total from the LAPrec dataset averaged over the period 1871-1900, $\overline{P_{PC-RCM(19yr)}}$ is the yearly precipitation total from the pre-industrial RegCM4.7 simulation averaged over 19 years, and $P_{m,RCM(19yr)}$ is the monthly total precipitation for the RegCM4.7 simulations (PC and LGM) averaged

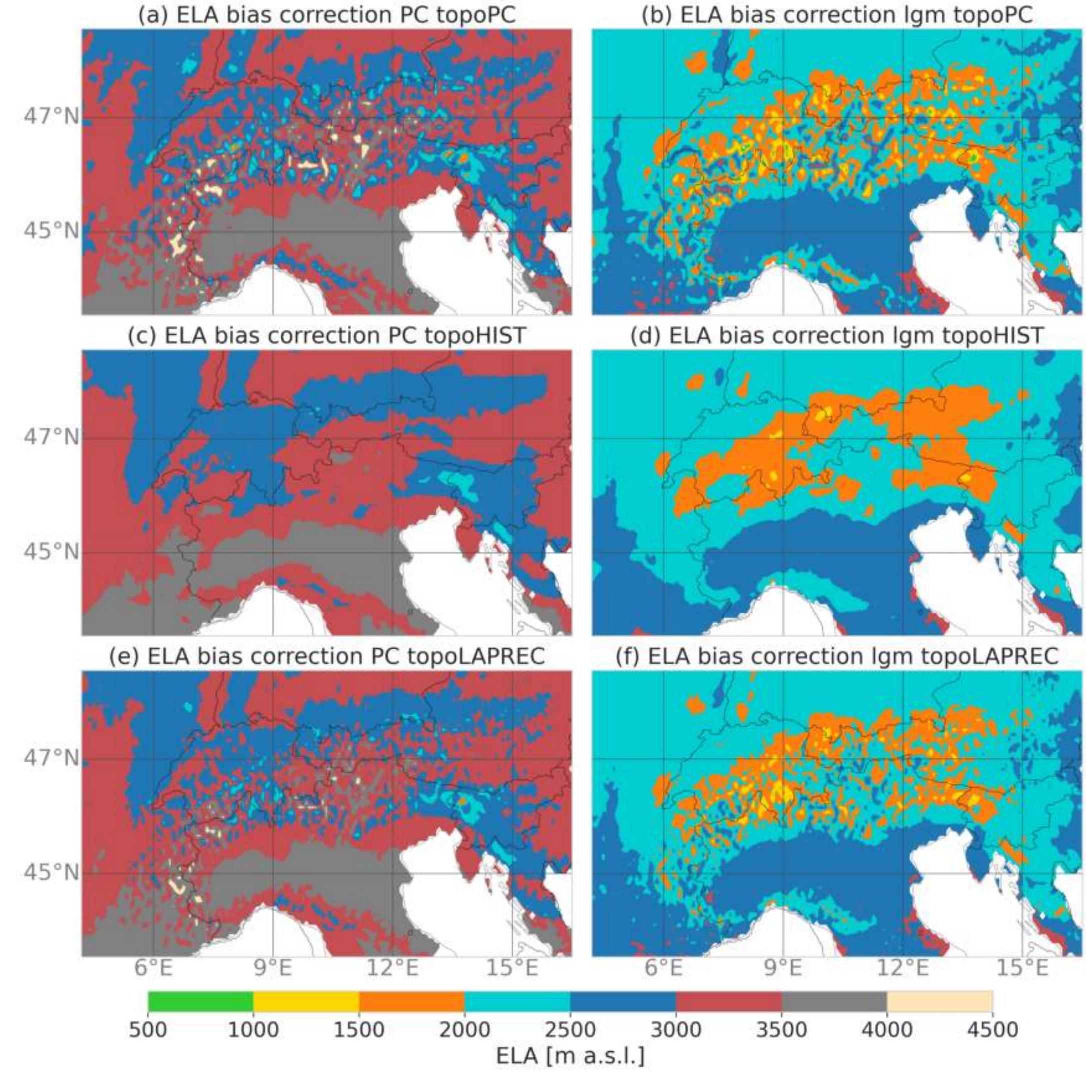

FIGURE 5.5: EnvELA for the PC (a, c, e) and LGM (b, d, f) after the application of a first-order bias correction. The topography used in the calculations is the RegCM4.7 model topography (a, b), the HISTALP topography (c, d) and the LAPrec topography (e, f).

over 19 years.

The temperature bias correction was performed according to the following equation:

$$TS_{corr} = TS_{m,RCM(19yr)} - (\overline{TS_{HIST(1871-1900)}} - \overline{TS_{PC-RCM(19yr)}}), \tag{5.4}$$

where $TS_{m,RCM(19yr)}$ is the summer monthly mean temperature of the RegCM4.7 simulations (PC and LGM) averaged over 19 years, $\overline{TS_{HIST(1871-1900)}}$ is the summer mean temperature from HISTALP dataset averaged over the period 1871–1900, and $\overline{TS_{PC-RCM(19yr)}}$ is the summer mean temperature from the pre-industrial RegCM4.7 simulation averaged over 19 years.

Both P_{corr} and TS_{corr} were then averaged along the time dimension. By using this

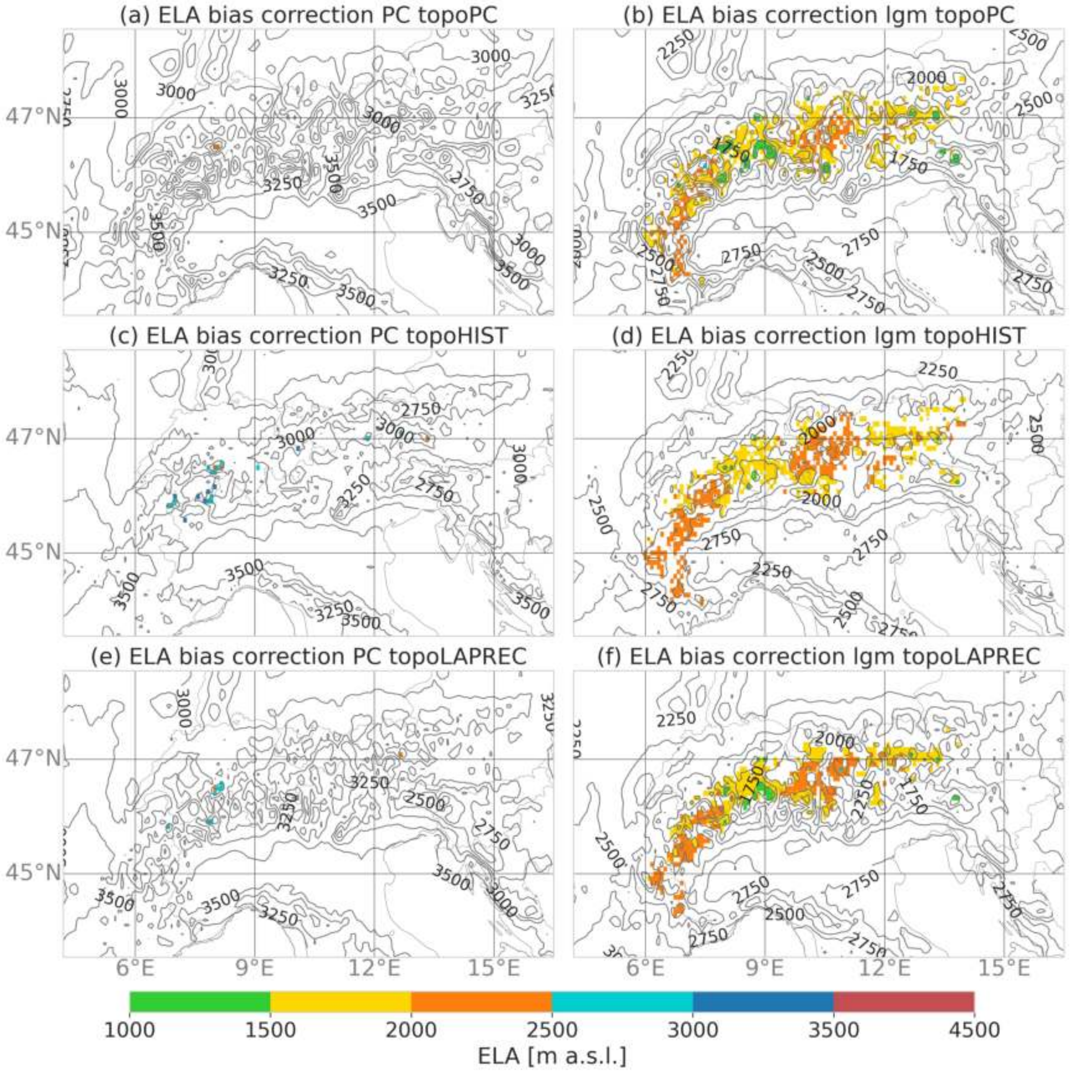

FIGURE 5.6: EnvELA for the PC (a, c, e) and LGM (b, d, f) after the application of a first-order bias correction. With colours, the grid-cells where the envELA is below the RegCM4.7 model topography (a, b), the HISTALP topography (c, d) and the LAPrec topography (e, f). To produce these maps it was applied to the envELA calculated with the RegCM4.7 (a, b) and LAPrec topography (e, f) a multidimensional gaussian filter.

precipitation and temperature spatially distributed values in equation 5.1, it was possible to obtain an average bias-corrected PC and LGM envELA over the domain (figure 5.5).

The envELA was calculated according to equation 5.2 using the RegCM4.7 model topography (figures 5.5.a and b), HISTALPS topography (figures 5.5.c and d), and LAPrec topography (figures 5.5.e and f), with the aim of observing how the topography influences the resulting envELA.

LAPrec, HISTALP and the RegCM4.7 output use different horizontal grids, thus all the dataset were interpolated onto the HISTALP equidistant grid of about 6 × 9 km resolution before the bias corrections and envELA calculations. The interpolation applied was the distance-weighted average remapping method of the Climate Data Operators software (CDO; Schulzweida, 2019), which, according to Torma et al. (2015), produces the most consistent spatial patterns among several interpolation methods in a complex-terrain region, such as the Alps.

5.2.1 Results and Discussion

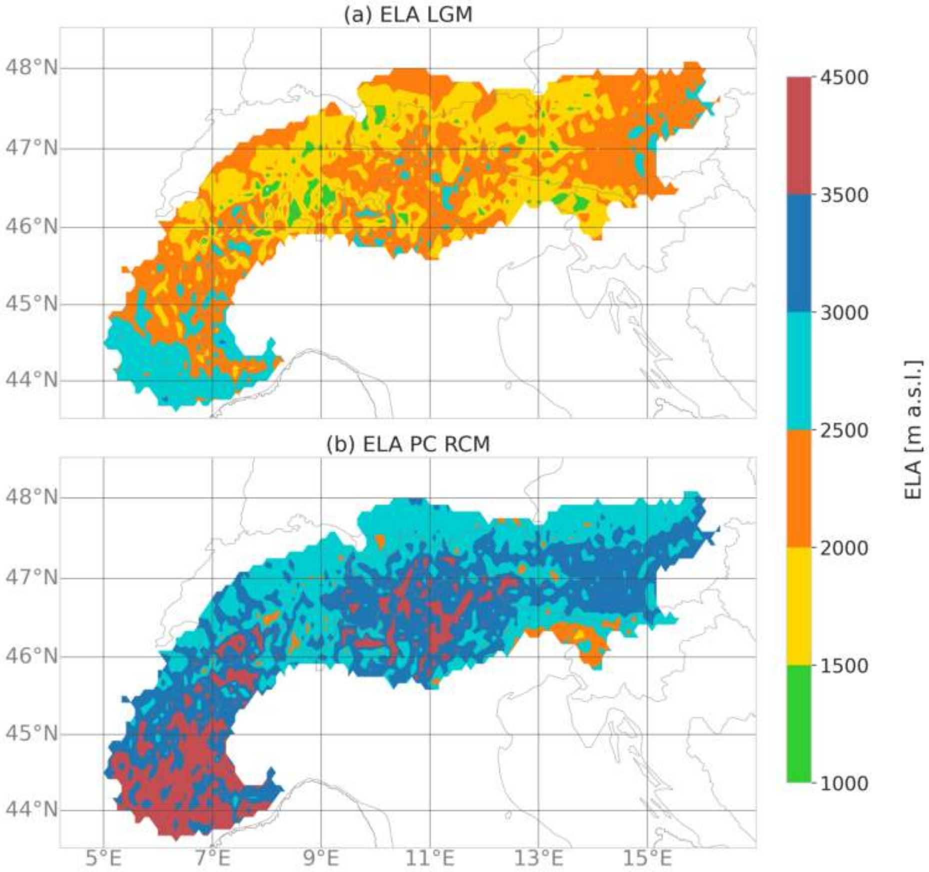

FIGURE 5.7: EnvELA averaged between the three topographic scenarios for the greater alpine region for the LGM (a) and PC (b).

Despite the remapping applied to the RegCM4.7 topography, the native resolution of the RegCM4.7 model simulation is lower compared to that of the observational datasets, which causes different spatial patterns between the three topographies. Indeed, the scenarios produced with the RegCM4.7 (figure 5.5.a, b) and LAPrec topography (figure 5.5.e, f) show higher spatial variability compared to the HISTALP data (figure 5.5.c, d). This occurs because the temperature used in equation 5.1 to calculate the envELA is obtained from HISTALP, which fits well with its own topography. However, when it is used with LAPrec or RegCM topographies, it produces an envELA pattern characterised by high spatial variability, probably due to a slight spatial mismatch between the climatic and topographic datasets.

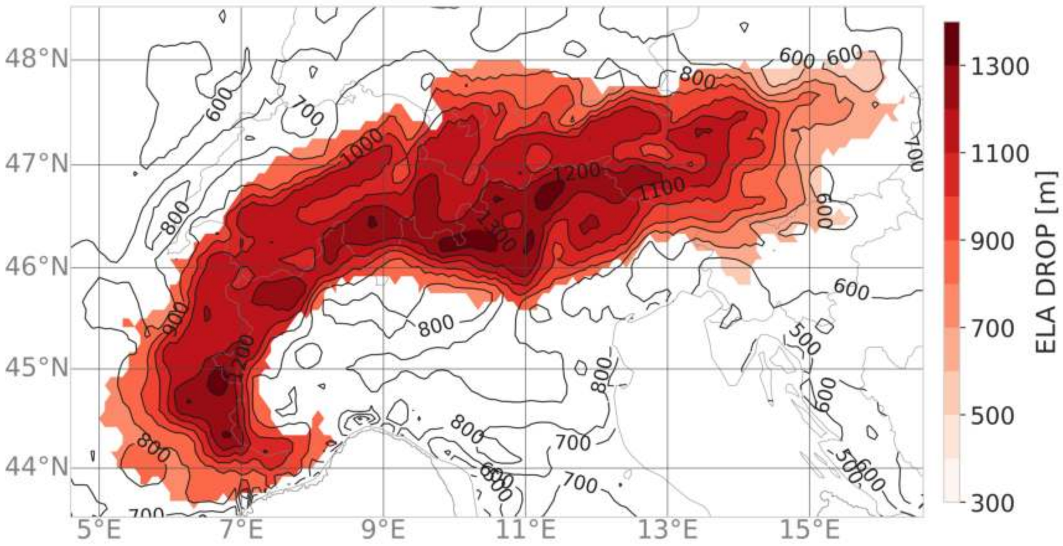

FIGURE 5.8: EnvELA depression between LGM and PC.

	RCM	HALP	LAPR	mean
PC	3085	3106	3104	3098
LGM	2094	2115	2114	2108
PC obs	3087	3109	3107	3101
$\Delta[LGM - PC]$	991	990	990	990

TABLE 5.1: Average envELA calculated for the three topographic datasets (RegCM4.7 = RCM, HIASTALP = HALP, and LAPrec = LAPR) and the envELA depression. PC_{obs} is obtained by HISTALP and LAPrec datasets for the period 1871-1900.

However, for both PC and LGM, the main features of the calculated envELA are in common between the three topographies, as shown by figures 5.5 and 5.6. Table 5.1 shows that the envELA values averaged over the great alpine region present extremely close values for the three topographic scenarios, with maximum spread between higher and lower mean envELA per scenario equal to 22 m. Thus hereafter, the envELA is given as the average of the three scenarios (figure 5.7).

The highest envELA values are located in the western and central Alps, while the lowest values are present in the Ticino, Julian and Carnic Alps and more generally, on the northern rim of the Alps (figure 5.7). Tables 5.2 and 5.3 present the envELA variability by latitude and longitude, respectively. The highest envELA are found for PC, LGM and PC_{obs} between 44 and 45 °N and between 5 and 7 °E. The lowest values are found between 47 and 48 °N, and between 13 and 15 °E for PC and PC_{obs} and

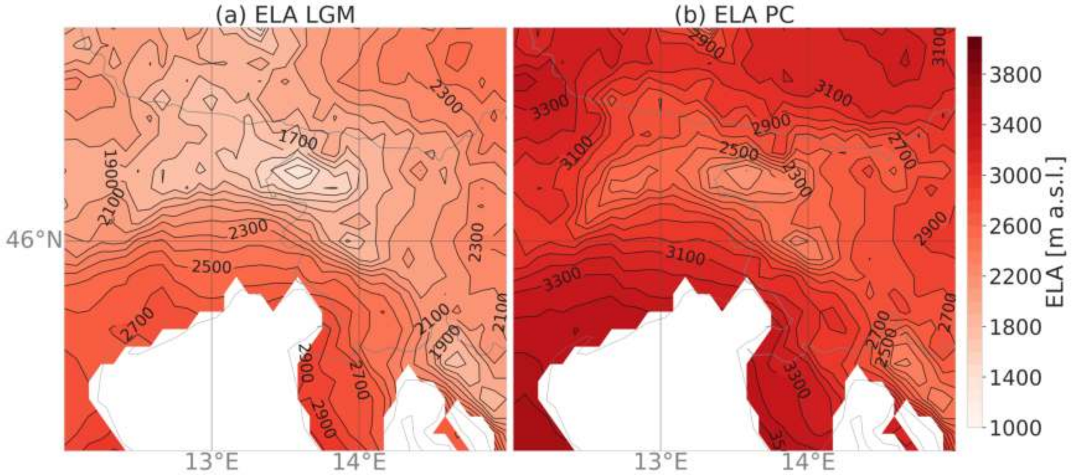

FIGURE 5.9: EnvELA for LGM (a) and (b), in the southeastern Alps. The black lines represent the envELA every 100 m.

between 46 and 47 °N and 11 and 13 °E for LGM. The average envELA values over the greater alpine region are 2108 m a.s.l. for the LGM and 3098 m a.s.l. for the PC.

In general, compared to the literature, the calculation overestimates the envELA values by about 200 to 500 m. The calculated LGM envELA results between 1250 and 1750 m a.s.l. in the Julian Alps (figure 5.9.a) compared to the value of 1000 to 1300 m a.s.l. found by Colucci et al. (2014), Kuhlemann et al. (2008), Monegato (2012) and Tintor (2005). Higher values are produced over the Velebit mountains (figures 5.5 and 5.9.a) where the calculated envELA ranges between 1400 and 1900 m a.s.l., compared to the values of 1200 to 1500 m a.s.l. found by Kuhlemann et al. (2008), Sarıkaya et al. (2020) and Žebre et al. (2014). The values for the Pennine and Graian Prealps are estimated on average around 2000 m a.s.l., with only isolated spots characterised by lower envELA that fits the ELA calculated by Forno et al. (2010), equal to 1500 m a.s.l.. In the Maritime Alps, the modelled envELA resulted between 2000 and 2500 m a.s.l., which is higher than the values found by Federici et al. (2016), which range from 1685 to 1845 m a.s.l.. In the northern Apennines the calculated envELA values show isolated grid-cells reaching the value of 1750 m a.s.l., about 400 to 500 m higher than the value proposed by Kuhlemann et al. (2008).
The PC calculated envELA agrees with the Little Ice Age (LIA; or PC for this study) values found in the literature. Colucci (2016) calculated the LIA ELA for the Julian Alps using the accumulation area ratio (AAR) method, which resulted in 2275 and 2486 m a.s.l. for the Canin and Triglav glaciers respectively. The calculated envELA in the southeastern Alps fits well with these data, showing values between 1800 and 2300 m a.s.l. (figures 5.7.b and 5.9.b). Concerning the western Alps, the calculated envELA values are between 200 and 300 m above the values of 3000 and 3100 m a.s.l. and 2841 and 2818 m a.s.l. found in the Ecrins group (Cossart et al., 2012) and in Maritime Alps (Federici et al., 2016).

Figures 5.6.a, c and e show that in the PC simulations only few grid-cells in the Northern and North-Western Alps present an envELA lower than the topography, while at the LGM the potentially glacierised area that lies above the envELA is extended over the whole alpine chain (figure 5.6.b, d, f). This result does not represent the number of glaciers present at the pre-industrial time over the Alps nor the effective PC glacier extension, but highlights those grid-cells that show suitable conditions for the development of a glacier.

The small number of glacierised cells at the PC is thus attributable to the low resolution of the model and observational datasets topographies compared to the small scale of the cirque and valley glaciers that survived around the highest summits (van Husen, 2000) at the time. These ice bodies, on average, cover a smaller surface compared to the area of the HISTALP grid-cells, over which all other datasets are remapped. Concerning the LGM (figure 5.6.b, d, f), the grid-cells with suitable conditions to host a glacier fall within the LGM glacierised area found in the literature (Ehlers and Gibbard, 2004). Particularly interesting for this study is the presence of low elevation envELA in the Julian Alps.

	44°-45°N	**45°-46°N**	**46°-47°N**	**47°-48°N**
PC	3490	3174	3048	2922
LGM	2496	2156	1986	2011
PC obs	3493	3178	3051	2923
$\Delta[LGM - PC]$	994	1108	1062	911

TABLE 5.2: EnvELA averaged between the three topographic scenarios (RegCM4.7, HISTALP and LAPrec) shown by latitude (every 1° between 44° and 48°N). PC and LGM are the RegCM4.7 model outputs and Δ[LGM-PC] is their difference, while PC_{obs} is the envELA obtained by HISTALP and LAPrec datasets for the period 1871-1900.

	5°-7°E	**7°-9°E**	**9°-11°E**	**11°-13°E**	**13°-15°E**
PC	3374	3117	3075	3045	2879
LGM	2382	2070	2008	1985	2010
PC obs	3380	3121	3078	3048	2881
$\Delta[LGM - PC]$	992	1047	1067	1060	869

TABLE 5.3: EnvELA averaged between the three topographic scenarios (RegCM4.7, HISTALP and LAPrec) shown by latitude (every 2° between 5° and 15°E). PC and LGM are the RegCM4.7 model outputs and Δ[LGM-PC] is the envELA depression, while PC_{obs} is the envELA obtained by HISTALP and LAPrec datasets for the period 1871-1900.

The envELA depression (figure 5.8 and table 5.1) is calculated between LGM and PC and, on average, is equal to 990 m over the Alps. This value is close to the values of 1000 to 1200 m proposed by Ivy-Ochs et al. (2006a,b). The envELA depression varies with latitude and longitude, with the largest depression in the south-central Alps, between 45 and 46 °N and 9 and 11 °E (tables 5.2 and 5.3). The western Alps also present high values of envELA depression (1200 m), while in the eastern Alps the values are smaller. This longitudinal gradient goes against the trend proposed by Federici et al. (2016) and Ivy-Ochs et al. (2006a), who suggest an average ELA depression equal to 980 m in the south-western Alps and 1000 to 1200 m in the central and eastern Alps.

In general, even though the calculated envELA values after the bias correction are overestimated, the application of the bias correction improved the spatial pattern of the envELA compared to the patterns shown in section 5.1. Additionally, we have to consider that the LGM ELA values we use as a reference to validate our results are not observational data. Indeed, these values come from reconstructions based on geomorphological evidence, models, and the application of typical AAR values. The ELA found in these reconstructions is affected by the fact that the typical AAR is defined from a statistical sample of glaciers and may not be the ideal value for a specific study site. Moreover, the geomorphological reconstructions return an ELA that is site-dependent.

On the contrary, our reconstruction, based on the method proposed by Žebre et al. (2020), is independent of local, small-scale (smaller than 12 km) topo-climatic conditions, as it is sensitive only to the main climatic patterns over the domain.

Chapter 6

Discussion

This project studies the paleoclimate following an approach based on the application of a high resolution (12 km) regional climate model. Paleoclimatic studies are more commonly performed by means of proxy data or low-resolution ESM. The use of a high-resolution model overcomes the weaknesses of these two methods, given the spatio-temporal continuity and the detailed information produced by our approach. Additionally, the use of the regional climate model RegCM allows to address questions about specific precipitation patterns, discriminating convective and stratiform precipitation.

The ESM proved to reproduce correctly the large-scale PC and LGM atmospheric circulation, providing appropriate initial and boundary condition for the RCM simulations. We have performed two double nested RegCM runs, in which we simulated the climatic conditions over the Alps and the Apennines at the pre-industrial and LGM times. The simulations were forced by a low-resolution ESM, and the final resolution of the analysed datasets is equal to 12 km.

This chapter presents the results obtained from the RegCM simulations, highlighting the connections between the different variables presented in chapter 4 and the implications of the RegCM individual fields onto the atmospheric circulation. The atmospheric circulation is then related to the glaciers distribution, particularly in the southern Alps. The results were analysed for the whole domain, with a particular focus on the Tagliamento basin.
This chapter is structured in two sections: one dedicated to the entire simulation domain (section 6.1), and one focused on the southeastern Alps around the Tagliamento Glacier (section 6.2). The latter is the key area of interest for this study, whose main objective was the evaluation of the atmospheric pattern responsible for the onset and maintenance of the Tagliamento glacier.

6.1 Simulated LGM over the study domain

The modelling approach followed in this thesis allowed to capture with high resolution the spatial distribution of the main atmospheric circulation pattern that characterised the LGM over the Italian Peninsula.
Our results *(i)* highlight the importance of the Alps as European climate divide, *(ii)* evidence the lee-side development of a cyclonic circulation that caused precipitation from the Apennines to the Balkans and the southeastern Alps, being in this way responsible for the expansion of several glaciers in these regions, and *(iii)* allow to capture the driving elements involved in the hydrologic balance with continuity in time.

The main drivers of the European climate are the North Atlantic atmospheric and oceanic circulation and the European orography. This is valid for the present-day as well as for the LGM. The position of the polar front determines which regions receive more precipitation, but on the other side, the Alps constitutes an important orographic barrier that blocks or deviate the air masses flowing over Europe, strongly influencing the climate.

Alps as a climate divide

In the RegCM simulations produced for this study, both precipitation and winds patterns show marked differences between the northern and southern alpine domains. In agreement with the proxy reconstructions (Duprat-Oualid et al., 2017; Monegato et al., 2015; Sirocko et al., 2016; Tzedakis, 2005; Watts et al., 1996), the RegCM simulations suggest much drier LGM conditions throughout Europe compared to the pre-industrial time (−15 % on average over the domain, −40 % in Central Europe and +30 % over the Tyrrhenian Sea), with the southern alpine region being relatively wetter than the northern alpine foreland (figure 4.13). This difference is particularly pronounced for convective precipitation, which showed a marked (−50 %) reduction over Central Europe and an increase (+30 %) in the Tyrrhenian region during summer (figure 4.14).
Convective phenomena are triggered by water and energy fluxes, thus reduced temperature may induce lower convective precipitation, but at the same time also cold air outbreaks can destabilise the lower troposphere leading to convection. This second case was suggested by Kuhlemann et al. (2008) to explain the cyclogenesis in the Tyrrhenian Sea when polar air was funnelled through the Rhone valley. Over the domain, the near-surface air temperature anomaly was equal to −6.6 °C, with June being the month with the smallest anomaly (−4.3 °C) and December the month with the largest anomaly (−8.9 °C). The temperature anomaly evidenced a meridional gradient with a minimum anomaly in the Tyrrhenian region and maximum in the northeastern alpine foreland (figure 4.24). This pattern was also found by Kuhlemann

et al. (2008), who reconstructed the temperature anomaly from ELA depression between LGM and present. However, our data show a smaller temperature anomaly over the domain compared to Kuhlemann et al. (2008) but are in agreement with the data of Wu et al. (2007) for Central Italy.

Central Europe was characterised by a dry and continental climate as a consequence of the reduced westerlies that in the present-day determine maritime conditions. However, despite this main pattern, the model simulations also highlighted a high precipitation rate along the western rim of the Alps for both LGM and PC. Using the envELA (section 5.1) as a proxy for the LGM precipitation and present-day observation as a reference for PC, it results that the RegCM overestimates the precipitation in this alpine sector. This bias is probably determined by the joint effect of too strong MPI-ESM-P westerly winds and non-ideal customisation of the RegCM system for the external Alps.
Concerning the atmospheric circulation, the westerly winds that blew all year round over the northern alpine foreland were much weaker if compared with the pre-industrial time (figure 4.21). On the contrary, the southern alpine region was subject to stronger winds, supporting a southward shift of the North Atlantic jet (Florineth and Schlüchter, 2000; Luetscher et al., 2015; Monegato et al., 2017). In particular, the southern region presented a seasonal variability characterised by the alternation between the winter northwesterly flows, a cyclonic circulation centred between the Gulf of Genoa and the Po Valley in the intermediate seasons, and the summer westerly flows.

Atmospheric circulation in the southern alpine region

The atmospheric patterns that characterise the southern region of the domain are the main drivers for the precipitation in the southern Alps, Apennines and Balkans and consequently feed the glaciers of these mountain chains.
At the LGM the Tyrrhenian region underwent persistent incursions of polar air that was funnelled western of the Alps, through the Rhone valley. The polar air descended as a northwesterly flow towards the Tyrrhenian Sea and was then deflected eastward at a latitude that oscillated from winter to summer between 38 and 45 °N (figure 6.1). This latitudinal displacement was possibly forced by the North Atlantic jet stream, which was subject to small seasonal variations and that at the LGM was located further South than today (Monegato et al., 2017).
During winter, the northwesterly winds were particularly persistent, probably due to the increased sea level pressure and temperature gradient between the northern and the southern parts of the domain, which enhanced the meridional geostrophic circulation. Indeed, our results show a marked NE-SW sea level pressure gradient,

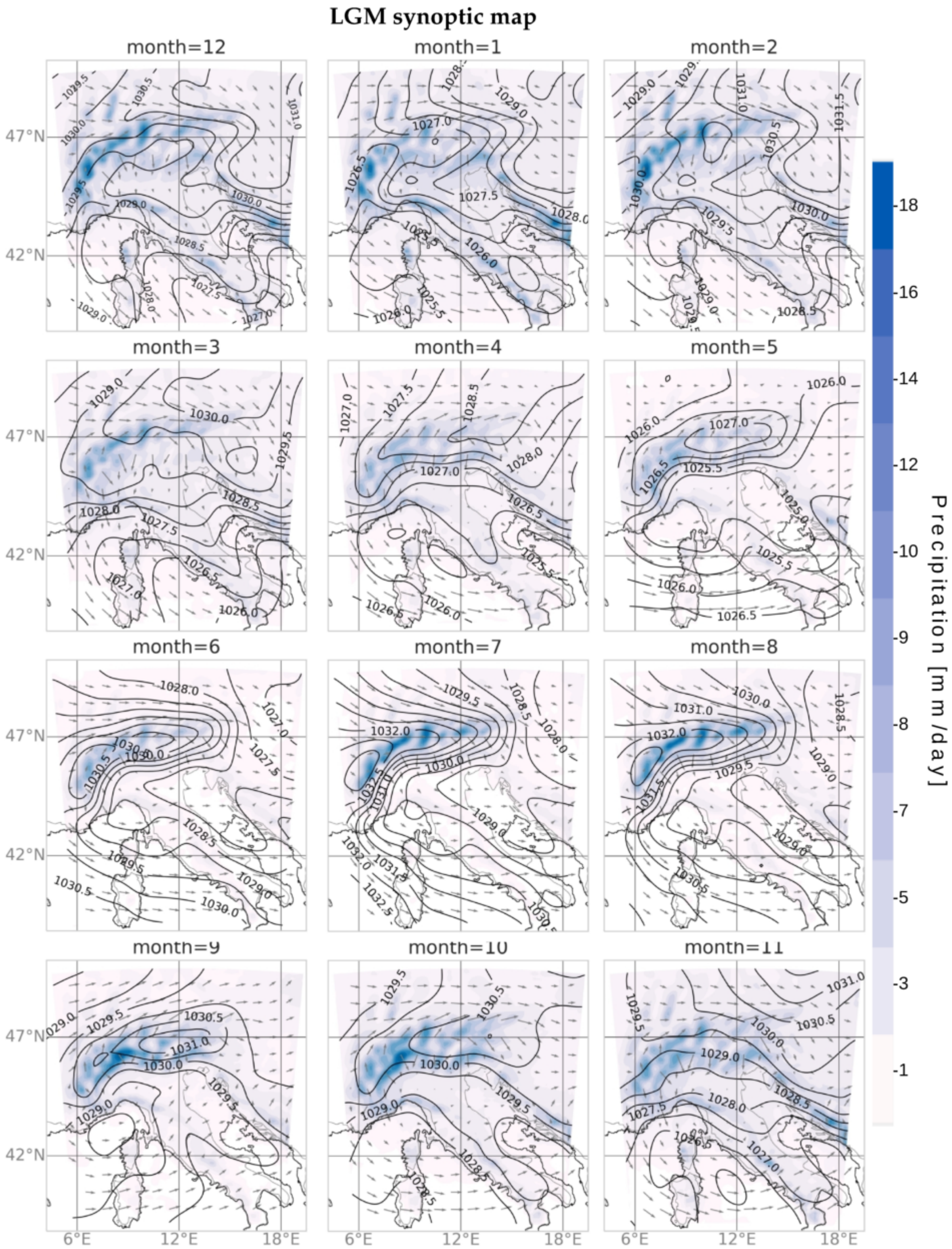

FIGURE 6.1: Synoptic circulation at the LGM: sea level pressure is represented as black lines, precipitation is in blue and winds in grey.

with a permanent high-pressure system over the Fennoscandian ice sheet and a low-pressure system centred over the Tyrrhenian Sea. An analogous pattern, with colder temperature in the northeastern sector of the domain and warmer temperature over the Tyrrhenian region, was also shown by the near-surface air temperature.
Convective precipitation associated with a cyclonic circulation affected the entire Tyrrhenian region, the Apennines and Balkans from May to September and in a smaller amount also the southern Alps. During summer, when the main winds over the central Apennines were purely westerly, the precipitation occurred further South (figures 4.14, 4.16 and 6.1). This precipitation had convective nature and was probably triggered by the contrast between the cold polar air that reached the warmer Tyrrhenian Sea surface, as suggested by Kuhlemann et al. (2008). This convective precipitation, together with the wind pattern, supports the idea of a cyclonic circulation over the Tyrrhenian Sea that triggered precipitation along a storm track extending in the eastern direction. Thus the regions mostly affected by the Stau-Foehn induced precipitation were the western Apennines, the southern Balkans, and in a smaller amount the southeastern Alps, which are located in the upwind side with respect to the Mediterranean jet. In all these regions, despite the low elevation, the southerly exposure and latitude, several glaciers developed.

The situation described in this section is only the average seasonal pattern, indeed from the weather evolution produced with 6-hourly plots, it is possible to observe the complexity of the atmospheric circulation and its variability. Lee-side cyclones developed from the western Mediterranean to central and southern Italy also in winter, with a variable location of the centre of the low-pressure system. This determines precipitation patterns that affected different areas of the domain, according to the cyclone centre location.
During winter, westerly winds were sometimes channelled through the Gulf of Genoa, leading to precipitation in the southern Alps and northern Apennines. The Adriatic region was hit by strong and frequent Bora events associated with dry conditions over the region, particularly in winter. This agrees with the findings of Ludwig et al. (2020), who related, by the mean of 8.5 km resolution RCM simulations, dust emissions and Bora events that affected the Adriatic region at the LGM. Both dust emission and Bora events were at their maximum during winter and early spring, when the vegetation was at its minimum and the climate was in average dryer compared to the rest of the year. Indeed since at the LGM the northern Adriatic was land covered, the air masses from northeast, if not already moisty, did not collect further humidity and did not produce Stau-Foehn intense precipitation in the eastern flank of the Apennines. This Bora-induced precipitation occurred more frequently during the warmer months. In the future it will be interesting to statistically characterise these events with a circulation weather type approach in order to study their frequency, also in relation to present-day conditions.

Figure 6.1 depicts the atmospheric circulation over the domain. To summarise, our data suggest an alternation of winter and summer conditions: the first characterised by a persistent meridional flow, and the second by a zonal flow. This zonal flow is also responsible for the precipitation in the southern Alps, Apennines and Balkans. These results fit with the hypothesis advanced by Kuhlemann et al. (2008) that was based on proxy reconstruction and with the data produced by Jost et al. (2005) through the use of the high-resolution (0.44° × 0.44° about 35 × 35 km) climate model HadRM. Compared with these studies, we provide higher-resolution, quantitative information about seasonality and spatial variability of the atmospheric circulation focused on the Alps and Apennines.

Hydrological balance

The modelling approach allowed us to reconstruct the average annual cycle of the analysed variables and gave us the instruments to study the relationship between the hydrological fields.
Snow cover was present from October to May in the largest part of the domain (figure 4.27), and the minimum snow amount was reached between August and September in the mountainous areas (figure 4.28). The beginning of the melting season occurred earlier at lower elevations, but everywhere ended in September, when the first consistent snowfalls usually occurred. Additionally, our results support the possibility of summer snowfalls even at low altitude, fact that represents a useful indicator of the climate condition. Moreover, summer snowfalls feed and protect glaciers from intense summer ablation.
The melting season was particularly long because of the large snow amount that remained over the summer (figure 4.28). From May to September, the melting was important (figure 4.32), pushing the permanent snow limit at about 1300 m a.s.l. within September. Above 1500 m a.s.l. the monthly mean temperatures were always below 0 °C (figure 4.25), preventing extensive melting phenomena.

The strong correlation between snow melting and runoff is highlighted by the presence of the highest runoff values in the alpine region during the melting season (figure 4.36). During spring and autumn the runoff over the Alps was minimum, but it showed high values in the piedmont areas, where the temperatures were favourable to melt the snow on the ground.

Glaciers

From the outcomes about the altitude of the snow limit and summer freezing level, presented in the previous section, one could expect the ELA location at about 1300 to 1500 m a.s.l. over the Alps. This value would fit with the ELA reconstructed using geomorphological techniques (Colucci et al., 2014; Federici et al., 2016; Forno et al.,

2010; Monegato, 2012; Sarıkaya et al., 2020) but is much lower (800 to 600 m) than the average envELA calculated in section 5.2. This discrepancy is possibly attributable to the method used to calculate the envELA (chapter 5), which is dependent on mean summer temperature and total annual precipitation (both biases corrected). Thus the envELA is independent of the local topo-climatic condition to which a real glacier is exposed.
In our envELA calculation we used, following the method of Ohmura and Boettcher (2018) and Žebre et al. (2020), the mean summer temperature (bias corrected with observational mean summer temperature). However, applying into equation 5.1 colder temperature (mean summer temperature bias corrected with annual mean temperature), the average LGM envELA matched the geomorphological reconstructions. Since the PC envELA calculated from bias corrected data fits well with the geomorphological ELA reconstruction for the LIA, the discrepancy encountered between LGM envELA and LGM ELA reconstructed from geomorphological evidence is not attributable to errors in the methodology, but instead could be ascribed to too high LGM temperature. Something similar was also found by Kuhlemann et al. (2008), who obtained better results comparing his ELA depression with annual average SST instead of summer average SST. This may indicate that during the LGM (and more in general during a glacial phase), the summer melting, being less intense than today, had a different weight with regards to the glacier behaviour. The reason this happens is not clear, but it is possibly related to a shorter length of the melting season and to the effect of frequent summer snowfall, which determines more wintry-like condition, especially if compared with today. Indeed the methods of (Ohmura and Boettcher, 2018; Žebre et al., 2020) are base on empirical equations developed according to present-day conditions.

The glaciers of the circum-Mediterranean region are highly sensitive to the smallest variation in temperature and precipitation, but at the same time, they influence the atmospheric circulation in their area. An example observed in our simulations is the development of intense katabatic winds that from the Alps flowed towards the planes. In part, these winds could be determined by the interpolation applied to the surface pressure in order to calculate the sea level pressure. However, considering the atmospheric processes, the strong thermal gradient between the extended glaciers over the Alps and the warmer surrounding planes could cause the wind-field to diverge in correspondence of the main alpine ridge due to the formation of katabatic flows. The katabatic winds cooled and dried the Po Valley and Friulian Plains, especially during the warmest months when the snow cover in the planes was minimum and the thermal gradient was maximum.

6.2 Simulated climate in the Tagliamento Glacier basin

The prime objective of this thesis is the analysis of the LGM atmospheric circulation over the Tagliamento Glacier basin, with particular attention to the timing of the precipitation. The glacial periods in this area have already been characterised especially concerning the LGM and LIA, by the mean of geomorphological and sedimentological evidence (Colucci, 2016; Colucci and Žebre, 2016; Monegato, 2012; Monegato et al., 2015, 2007). This project represents the first experiment based on a high-resolution regional climate model that aims at investigating specifically the southeastern Alps, and more in general, to our knowledge, it is one of the highest resolution modelling studies that employs a RCM on the paleoclimate (Ludwig et al., 2020, 2018).

The southeastern Alps are one of the wettest regions in Europe (Isotta et al., 2014) and at the LGM hosted a glacial complex characterised by relatively small accumulation basins located at low elevation. The most extended glacier of the area was the Tagliamento Glacier, whose piedmont lobe expanded into the plane. Several studies estimated the ELA in the southeastern Alps and Prealps between 1000 and 1200 m a.s.l. (Monegato, 2012; Tintor, 2005), lower than the average southern alpine glaciers ELA. These elements make the southeastern Alps a unique case study for the application of a high-resolution climate model focused on the atmosphere-cryosphere interactions.
In this section we analyse the climatic conditions that supported the Tagliamento glacier expansion and maintenance, particularly for what concerns precipitation and hydrological balance.

The precipitation in the southeastern Alps was mainly related to *(i)* the cyclonic circulation that developed at the LGM between the western Mediterranean and the southern Italy and *(ii)* to the convective phenomena in the northern Adriatic during the melting season. These patterns led to a persistent relatively wet area in the southeastern Alps all year-round (figure 4.19). This wet spot was located in the southern part of the Tagliamento glacier basin and was determined by both stratiform precipitation during the whole year and convective precipitation from late spring to early autumn (figures 4.16 and 4.17).
Our precipitation data supports higher convective activity in the Tagliamento basin compared to the rest of the Alps in late spring and early autumn, when, indeed, the convective precipitation anomaly is minimum (figure 6.2.b). The RegCM simulation also highlights the occurrence of stratiform precipitation that prevails during the coldest months and at the highest elevations (figure 6.2.c). Only the 38 % of annual precipitation are of convective nature, but this precipitation occurs mainly in summer and occasionally as snowfalls. They are thus extremely important to preserve the glacier from melting.
The average monthly precipitation amount in the Tagliamento basin was higher

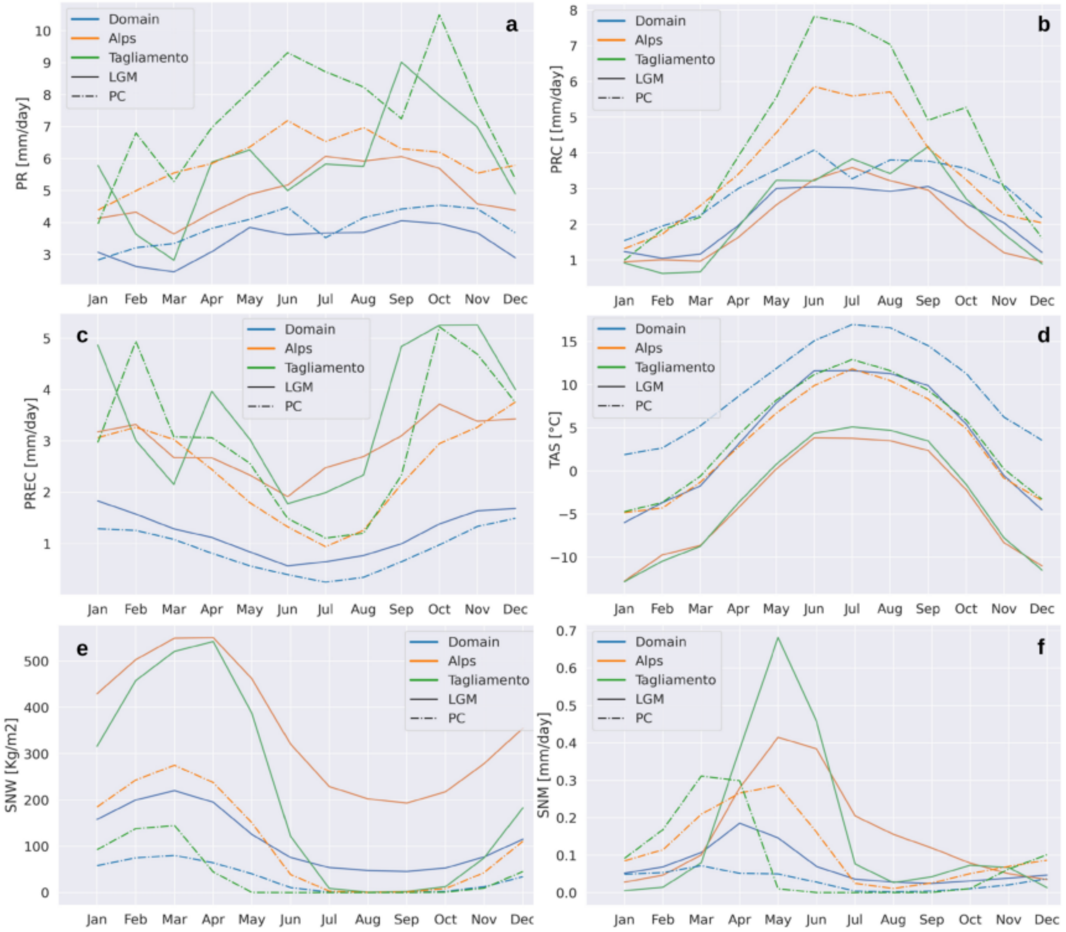

FIGURE 6.2: Total (a), convective (b) and stratiform (c) precipitation, near-surface air temperature (d), surface snow amount (e) and surface snow melting (f). The coloured lines represent the whole domain (blue), the Alps (orange) and the Tagliamento basin (green) for the LGM (solid line) and PC (dashed line).

than the average precipitation amount in the Alps at the same elevation (and even at higher elevations; figure 4.17). The only exception occurred in March, which showed particularly low values, while maximum precipitation occurred in September (figure 6.2.a). Considering the average monthly temperature and the surface snow amount, it is likely that this autumn precipitation frequently occurred in the form of snowfalls, particularly above 800 to 1000 m a.s.l., interrupting the melting season and feeding the Tagliamento glacier (figure 4.29 and 6.2.e).

In the Tagliamento basin, the surface snow amount (given in km) was always higher compared to the entire Alpine chain in the same altitudinal band (figure 4.28 and 4.29). Assuming a constant snow density throughout the Alps, we can explain the higher snow amount with a higher snow thickness in the southeastern Alps compared to the rest of the alpine chain due to a favourable combination of precipitation and melting. Above 1300 m a.s.l. the snow-covered the ground all year-round. Thus, this altitude marked the lower limit of the permanent snow-cover at the LGM and when over a glacier, it potentially represented the ELA. In section 6.1, we have already augmented the discrepancy between the envELA calculated in section 5.2 and the ELA obtained from geomorphological reconstruction. In the southeastern Alps the envELA overestimates the calculated geomorphologiacally reconstructed ELA by about 250 to 450 m. Indeed, the calculated LGM envELA results between 1250 and 1750 m a.s.l. in the Julian Alps compared to the value of 1000 to 1300 m a.s.l. found by (Colucci et al., 2014; Kuhlemann et al., 2008; Monegato et al., 2007; Tintor, 2005).

When compared with the Alps, the Tagliamento basin showed a larger surface snow amount anomaly in spring, while in summer it presented slightly smaller anomalies. This occurs because during winter the Tagliamento basin received much more snowy precipitation than the rest of the Alpine chain, but very little snow remained over the summer due to the intense melting that occurred at the low elevations of the Tagliamento basin (figure 6.2.e). In September a further increase in the melting was recorded, which is attributable to the new snowfalls that occurred in the early autumn (figure 6.2.f).
The Tagliamento basin presented higher values of snow melting if compared to the average values, at the same altitudes, in the Alps during spring and summer. This reflects the larger amount of snow on the ground in the southeastern Alps compared with areas at the same elevations in the rest of the alpine chain.

These data can explain why such an extended glacier as the Tagliamento glacier could form in a low-elevation and southerly exposed flack. Here the precipitation was higher than the average precipitation over the Alps and in the late-summer to early-autumn frequent snowfalls fed and protected the glacier surface from melting. Indeed despite the snowfalls, the summer melting was higher in the Tagliamento basin than on average in the rest of the Alps.
To summarise, the origin of the precipitation in the southeastern Alps are mainly attributable to southerly flows, but also westerly and easterly/northeasterly air masses led to occasional precipitation.

Chapter 7

Conclusions, Innovations and Future Works

This study represents the first work with such a high-resolution that focuses on the interaction between atmosphere and cryosphere in the past. This is also one of the first time that the atmospheric circulation over the southeastern Alps was investigated by the mean of a paleoclimate model (Ludwig et al., 2020). Thus, this study has the potential to set the grounds for other similar experiments which could focus on different regions or times, or that could test different models with eventually the non-hydrostatic core, reaching in this way an even higher resolution.

The primary aim of this PhD project was the evaluation of the atmospheric circulation that at the Last Glacial Maximum led to the onset and maintenance of the Tagliamento glacier. We developed a chain of three climate model simulations with increasing resolution in order to extract the fields involved in the glaciological and hydrological cycles. Our final aim was to characterise, with high spatio-temporal resolution, the precipitation patterns that influenced the southeastern Alps at the LGM.

To achieve this goal, we devised a modelling approach based on a chain of two climate models. For first, the Max Planck Institute for Meteorology Earth System Model (MPI-ESM-P; Stevens et al., 2013), compliant with PMIP3/CMIP5 protocols (Paleoclimate Modelling Intercomparison Project; Braconnot et al., 2012), provided the large scale framework for pre-industrial and LGM time. Then, the Regional Climate Model RegCM4.7 developed by the ICTP (Elguindi et al., 2014; Giorgi et al., 2012) was nested into the MPI-ESM-P in two steps of increasing resolution (50 km and 12 km).
In order to adapt the RegCM4.7 to work for LGM conditions over the southeastern alpine region, the LGM run was provided with a tailored reconstruction of land-use datasets. A land-use map representing the distribution of vegetation at the LGM and a land-ocean mask that took into account the retreat of the coastline due to the glacier expansion were created and tested.

Our results show a general good performance of the reproduced land-use datasets, but some improvements are still possible, particularly for what concerns the vegetation in central Italy and the western Italian coast. However, these regions fall out of the area of our major interest, the southeastern Alps, and in general did not prove to modify the main atmospheric patterns over the domain.
The ESM validation was performed with a focus on the jet-stream position and strength, temperature and precipitation anomalies. The RegCM setting was validated over the domain in terms of mean annual, seasonal and monthly winds, precipitation and temperature, showing good model performance and entitling us to use the model for paleoclimate simulations.
Accomplished the testing and validation phase, two 20-years long numerical simulations have been performed with RegCM4.7 at the resolution of 12 km. The simulations were forced with paleoclimate model data at the LGM standard (21 ka BP) and at the pre-industrial time. Orbital parameters and greenhouse gas concentrations were set accordingly to the time that was simulated.

7.1 Main Outcomes

The LGM and PC simulations have been analysed, studying both the whole domain and the Tagliamento glacier basin and comparing the LGM with the pre-industrial results, in order to find the anomaly between the two time periods.
Our main outcome is that the use of a high-resolution RCM highlights the atmospheric circulation patterns responsible for the development of the main glaciers in the southeastern Alps, but also Apennines and Balkans. Indeed, even though the uncertainties regarding the initial and boundary conditions for a paleoclimate model study are inherently larger than the uncertainties for a present-day study, the model proved to be capable of reproducing climate fields that matched with proxies and other modelling reconstructions. Coherently with most literature, our results showed colder LGM temperature (−6.6 °C on average) and much drier condition (−15 %) than today over the study domain.
These elements prove that not only the RegCM performed well, but that also the initial and boundary conditions we reconstructed had a good quality. Furthermore, our data shows over the domain an alternation between winter and summer conditions characterised by meridional and zonal flows, respectively, with the predominance of stratiform or convective precipitations according to the season.

With this thesis, we provide high-resolution, quantitative information about seasonality and spatial variability of the atmospheric circulation over the Alps and Apennines. Thanks to this approach, we have been able to quantify stratiform and convective precipitations and address their origin. This result is certainly innovative in the framework of paleoclimate studies.

In particular, in relation to the southeastern Alps, we observed that:

- in the southeastern Alps the precipitation (both liquid and solid) was higher than the average precipitation over the whole alpine chain (particularly at the same Tagliamento basin elevation) and in the late-summer to early-autumn frequent snowfalls fed and protected the glacier surface from melting;
- the main precipitation in the domain originated from a cyclonic circulation that developed in the Tyrrhenian region and more rarely from the westerly or easterly incursion of moist air masses. This aspect, in particular, requires further investigation in order to statistically characterise these events in terms of their frequency, also in relation with present-day conditions; however, the cyclonic circulation was responsible for the precipitation in the up-wind side of the southern Alps, Apennines and Balkans and consequently was likely the cause of the development of the glaciers in these regions;
- the southeastern Alps were affected by both convective and stratiform precipitation: from spring to autumn in the northern Adriatic the convective phenomena prevailed, while during the rest of the year southerly and westerly stratiform precipitation were dominant. Summer snowfalls, even at low elevation, were likely to happen;
- we found a discrepancy between calculated envELA, modelled snowline and freezing level, and ELA values found in the literature. This discrepancy is possibly attributable to the fact that the method used to calculate the envELA (chapter 5) is independent of the local topo-climatic condition to which a real glacier is exposed. Additionally, we have to mention that the maximum LGM Tagliamento glacier expansion occurred at 26 ka BP while the ESM is run at the LGM standard (21 ka BP) when the waning of the Tagliamento glacier was already started.

7.2 Future Works

This work represents the first paleoclimate study that aims at investigating the atmospheric patterns of a small region with a high-resolution (12 km). Therefore this study opens the doors to a whole set o new possible experiments.

In particular, the investigation and assessment of the precipitation patterns, especially when convective phenomena are involved, is the ideal field of application for a convective-permitting model, which is already available in the newest version of the RegCM. The use of the non-hydrostatic core would allow to reach a resolution of up to about 3 km that could potentially highlight small scale, topography-related features.

This study is based on single ESM and RCM, initialised with a unique set of initial and boundary conditions. In this way, the assessment of the uncertainty of our method is not possible. We thus propose, as future development, to expand the current methodology following an ensemble approach. A first step in this direction could consist of using multiple driving ESMs, which would allow a better estimation of the uncertainty, especially in the study of a small area such as the Tagliamento basin. This would increase the number of samples involved in the calculation of the statistical metrics.

In the near future, further development of the current work could concern the investigation of other areas in addition to the Tagliamento glacier. These areas could be the Dora Baltea and the Garda catchment, which are the main glacial analogous of the Tagliamento glacier in the southern Alps, and the central Apennines and the Balkans, which are exposed to the same mesoscale flows of the southeastern Alps.

In order to integrate the results obtained in this thesis, it would be important to statistically characterise the precipitation occurring in the southeastern Alps in terms of frequency and origin with a Weather Type approach (Jones et al., 1993). In this way, we could, for example, compare the frequency of LGM Bora events with present-day conditions or precisely track the movements of the cyclonic circulation centre and relate it with the precipitation distribution.

In this context, to trace the LGM Mediterranean storm track, it would be interesting to expand the study domain to the western and southern Mediterranean regions and central Europe up to the limit of the Fennoscandian ice sheet.

Finally, being this project dedicated to the atmosphere-cryosphere interaction, a future development concerns the full coupling of the RegCM system with a glacier model.

In conclusion, our work, which is based on a high-resolution modelling approach, proved to be able to capture the precipitation patterns responsible for the onset of the Tagliamento glacier. The results show good agreement with the available paleoclimatic reconstruction, even if some work is still required in the evaluation of the envELA. This project set the grounds for several future studies and adds new quantitative information about the atmospheric circulation at the LGM.

Appendix A

LGM Vegetation throughout the domain

In order to represent the vegetation distribution used in the LGM simulation a literature review was performed. Here, the LGM vegetation will be detailed according to the latitudinal division of the domain followed in the section 3.2.2.

Northern Alps

The Central Europe at the LGM was confined between the Fennoscandian ice sheet and the Alps, and appeared as a vast dry plain beaten by strong winds. Due to the intensity of the dust activity and the proximity of an ice sheet, the environment around the margins of the Fennoscandian Ice Sheet were characterised by a glacial desert with moss and some grass (Sirocko et al., 2016).
Duprat-Oualid et al. (2017) studied a pollen record from the Bergsee, located in the southern piedmont of the Black Forest at an altitude of 382 m a.s.l. (N 47°34′20″, E 7°56′11″). The vegetation pattern points to a landscape dominated by a boreal forest-steppe. This bioma is characteristic of cold regions with a limited, but sufficient availability of moisture, fact underliend by the prensence of Betula and Helianthemum, absent in dryer environments. The proportion between tree and steppic taxa is equal to 2:8, with a contribution of Birch, Salix and Pinus for trees and Artemisia, Helianthemum, and Poaceae for steppic taxa.
From Bunker (Germany, N 51°22′3″, E 7°39′53″) and Spannagel (Austria, 2521 m a.s.l., N 47°4′49″, E 11°40′18″) caves there is no evidence of speleothems growth during the MIS2, which is sign of dryness (Fuhrmann et al., 2020). Pollen data from these caves confirm higher grass and herbs content and lower tree pollen percentages, with Birch and Pine present only in traces (Sirocko et al., 2016).

Duprat-Oualid et al. (2017) underline how the vegetation pattern is influenced, in addition to the elevation, also by the distance from the North Atlantic (longitudinal gradient) and ice sheets (latitudinal gradient). Indeed, at St. Anne Lake, located in the Carpathians at 946 m a.s.l. (N 46°7′35″, E 25°53′17″), the record is dominated by Pinus (40 %) and Juniperus (10 %). The distribution of the vegetation shows 45 % of conifer tree, 45 % of grassland and 10 % of shrub, with temperate deciduous trees and shrubs likely present at lower altitude (Magyari et al., 2014). This pattern is in contrast with the Bergsee record, which presents a dominance of herbaceous steppic taxa. The difference between the two sites may be explained by the increased continentality of St. Anne Lake, characterised by warmer and drier summers (Duprat-Oualid et al., 2017).

Southern Alps

The moisture gradient increased from the semiarid Adriatic alluvial Plain towards a wide braided river area, whose water was supplied by glaciers. Ground water availability together with orographic precipitation (Luetscher et al., 2015) are the main drivers for the vegetation development in the southeastern Alps.
The Adriatic alluvial plain, being far from the Alpine chain, experienced dry condition. Here the environment was semi-desertic and the main taxa were Artemisia and Juniperus with sporadic Pine (Monegato et al., 2015).
At the contrary, the low altitude mountains and the piedmont belt are located on the wetter side of the moisture gradient and presents a boreal forest (Pinus cembra, Pinus abies, Larix decidua, Pinus sylvestris and different Betula) without temperate broad-leaved deciduous trees. In this area the taxa distribution is driven by the altitudinal moisture gradient and by the soil conditions. Swiss stone pine and Larch coexist with Spurce in the uppermost tree belt, until the tree line (800 m a.s.l. Ravazzi et al., 2004). Here the ground is well-drained and limits the forest development.
The glacifluvial fans, richer in water, were covered by Dwarf Mountain, Scots pines and Spruce.
Records from Euganei Hills and Dinaric foreland prove the occurrence of Fagus, Abies, Tilia, and Carpinus in the region. These taxa are present only in microrefugia for broad-leaved trees. While the lowland between the mountainous area and the steppic Adriatic plane points to a pine forests (Pinus mugo and Pinus cembra).

In the west Garda region climate conditions and the glacial activity are likely to have prevented tree expansion (Ravazzi et al., 2012). Pollen records show the absence of an extended forest and the landscape is steppic (Artemisia, Helianthemum, Ephedra and Chenopods). Evidence from Val Borlezza (Ravazzi et al., 2012) shows the presence of Pinus cembra, Pinus sylvestris and Pinus mugo. Figure A.1, from Monegato et al. (2015), exhaustively represent the vegetation pattern in the southern Alps.

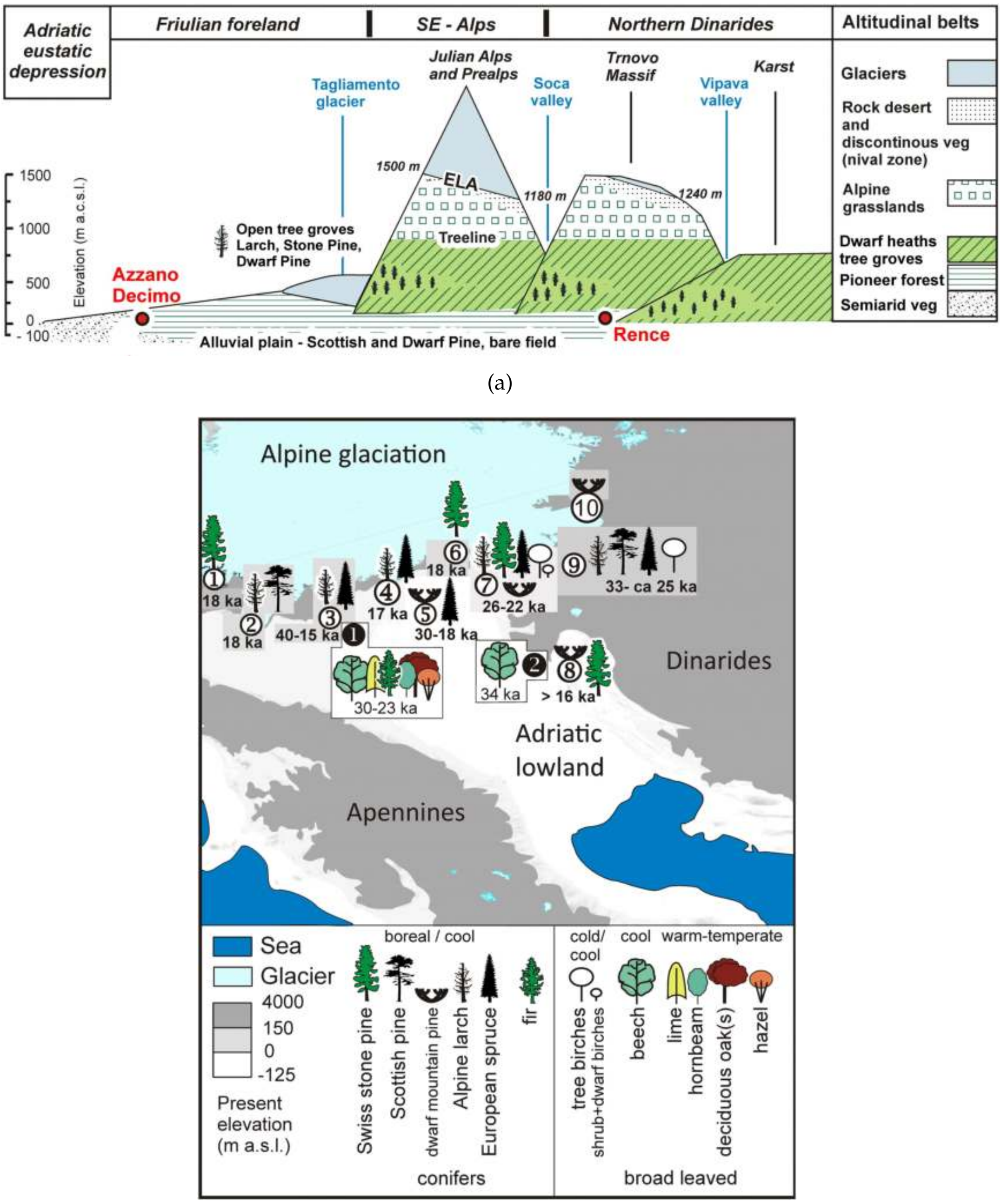

(a)

(b)

FIGURE A.1: Modified from Monegato et al. (2015). Vegetation pattern at LGM in the southern Alps. A.1a: Latitudinal section of southeastern Alps and Dinarides representing the paleoecological and paleobotanical record at the LGM. A.1b: Tree and shrub presence in the northern Adriatic during the LGM. White numbers represent woody component in zonal ecosystems. Black numbers represent woody component in micro-habitats.

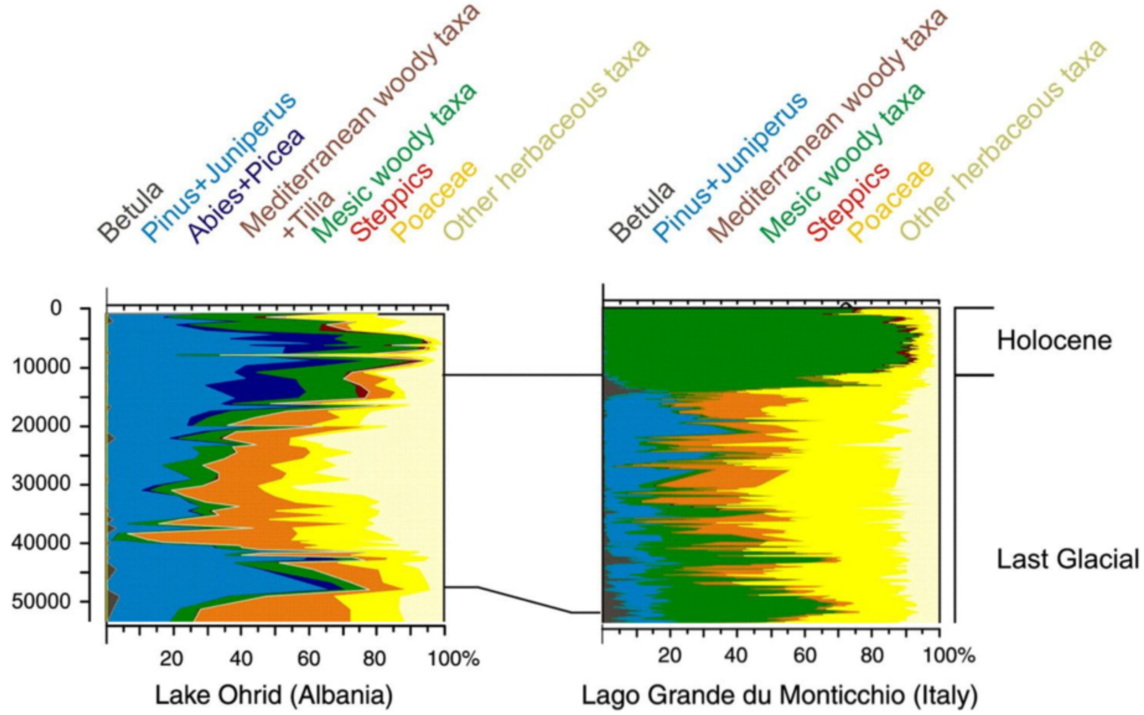

FIGURE A.2: Modified from Lézine et al. (2010). Comparison between Ohrid (Lézine et al., 2010) and Monticchio (Brauer et al., 2007) pollen data. The synthetic pollen diagrams show the main vegetation types of the two pollen sites.

Pyrenees, Apennines and Balkans

In this area, Monticchio Lake (Italy, 656 m a.s.l., N 40°56′0″, E 15°35′0″) constitutes an important site of study for paleo-environmental reconstructions of the last glacial. The environmental conditions in South-Central Italy and Balkans let the Quaternary sedimentary sequences undisturbed (Tzedakis, 2005). Moreover, tephra layer deposited by the large number of active volcano of the region, make possible the correlation and dating of sediment-cores coming from Mediterranean region. The sediment core extracted from Monticchio Lake allowed radiometric and tephro-chronological dating of the last 76.3 ka (Watts et al., 1996). According to Watts et al. (1996) the South-Central Italy was steppic: Herb dominated (75%, especially Artemisia and Chenopodiaceae) and the environment was almost treeless, except for Juniperus and Pinus, but the letter may not have been present locally. Deciduous tree were rare and the climate was extremely dry.

Record data from Castiglione valley (44 m a.s.l., N 41°53′30″, E 12°45′35″; Alessio et al., 1986) and Vico Lake (507 m a.s.l., N 42°20′0″, E 12°16′0″; Leroy et al., 1996) confirm the steppic and dry environment. These sites well represent the latitudinal and altitudinal extension of the steppic bioma in Central Italy at the LGM.

The southern Po alluvional plane was extremely dry (Monegato et al., 2015), as already pointed out for the southern Alps region.

The Balkan area, as shown by Sadori et al. (2016) and Lézine et al. (2010) for the Lake Ohrid (705 m a.s.l., N 40°55′0″, E 20°40′30″) and by Lawson et al. (2004) for Lake Ioannina (470 m a.s.l., N 39°45′0″, E 20°51′0″), was characterised by open vegetation, mainly steppe, with abundance of herbaceous taxa (Gramineae, Artemisia, Poaceae, Chenopodiaceae and Cyperaceae). Pinus persisted with low to medium values (9 to 77 %). The presence of sparse montane and mesophilous taxa, as the Quercus robur was recorded, testifying a wetter climate compared to the Apennines. The orographic setting triggered the relatively high precipitation on the south-west Balkans, which provided condition for the persistence of thermophilous trees during the arid glacial stages of the Quaternary. However, it is likely that these taxa survived in refugia characterised by favourable topo-climatic conditions (Lawson et al., 2004). A comparison between the bioma of Monticchio Lake and Ohrid Lake is shown in figure A.2.

Finally, Carrión et al. (2003) studied late glacial deposits (20 to 17 cal ka BP) from the Sierra de Segura (Spain, 780 m a.s.l., N 38°1′0″, E 2°47′0″), were he found Pinus pinaster, deciduous Quercus, evergreen Quercus, Ericaceae, Corylus, Betula, and Fraxinus, in pollen percentages always below 10. This data, show that tree taxa survived in altitude in the southern Europe during the LGM. Hence, presents several similarities with the Balkans record (Lawson et al., 2004).

Appendix B

ELA reconstructions over the Alps

To improve the methodology proposed in the section 5.1 and as an alternative to the bias correction proposed in the section 5.2, here we test different precipitation datasets (table B.1) to calculate the envELA.
As result, eight envELA scenarios were produced by applying the equations 5.1 and 5.2. In all the scenarios the temperature T_{RCM} (eq. 5.2) used to calculate the envELA is the RegCM4.7 summer near-surface air temperature averaged over the 19 yr of the simulation, while the total annual precipitation datasets, P_a, differs according to the scenario. Only one scenario (scenario a) used the RegCM4.7 precipitation, the other were based on the LAPrec and HISTALP datasets. The climate records of the LAPrec observational dataset were reduced to cover the period 1971 to 2000 and than were averaged along the time dimension.

#	Precipitation Datasets	Time Covered
a	RCM	LGM
b	LAPrec	PD
c	$LAPrec - (68 * \delta T[LGM - PD])$	LGM-PD
d	$LAPrec - 10\,\%$	LGM-PD
e	$LAPrec - \delta PR[LGM - PC] - 3\,\%$	LGM-PD
f	$LAPrec - \delta PR[LGM - PC] - (68 * \delta T[PC - PD])$	LGM-PD
g	$LAPrec - (68 * \delta T[LGM - PC])$	LGM-PC
h	$LAPrec - \delta PR[LGM - PC]$	LGM-PC

TABLE B.1: Precipitation datasets used to calculate the eight envELA scenarios. Scenario *a* is based on the RegCM4.7 precipitation dataset and is the case already presented in the section 5.1; scenario *b* uses the PD observation without correction, scenarios *c*, *d*, *e* and *f* use precipitation dataset covering the time range LGM- PD (present-day), and scenarios *g* and *h* are based on the dataset referring to the time range LGM-PC and do not apply any corrections for the time range PC-PD.

envELA scenarios

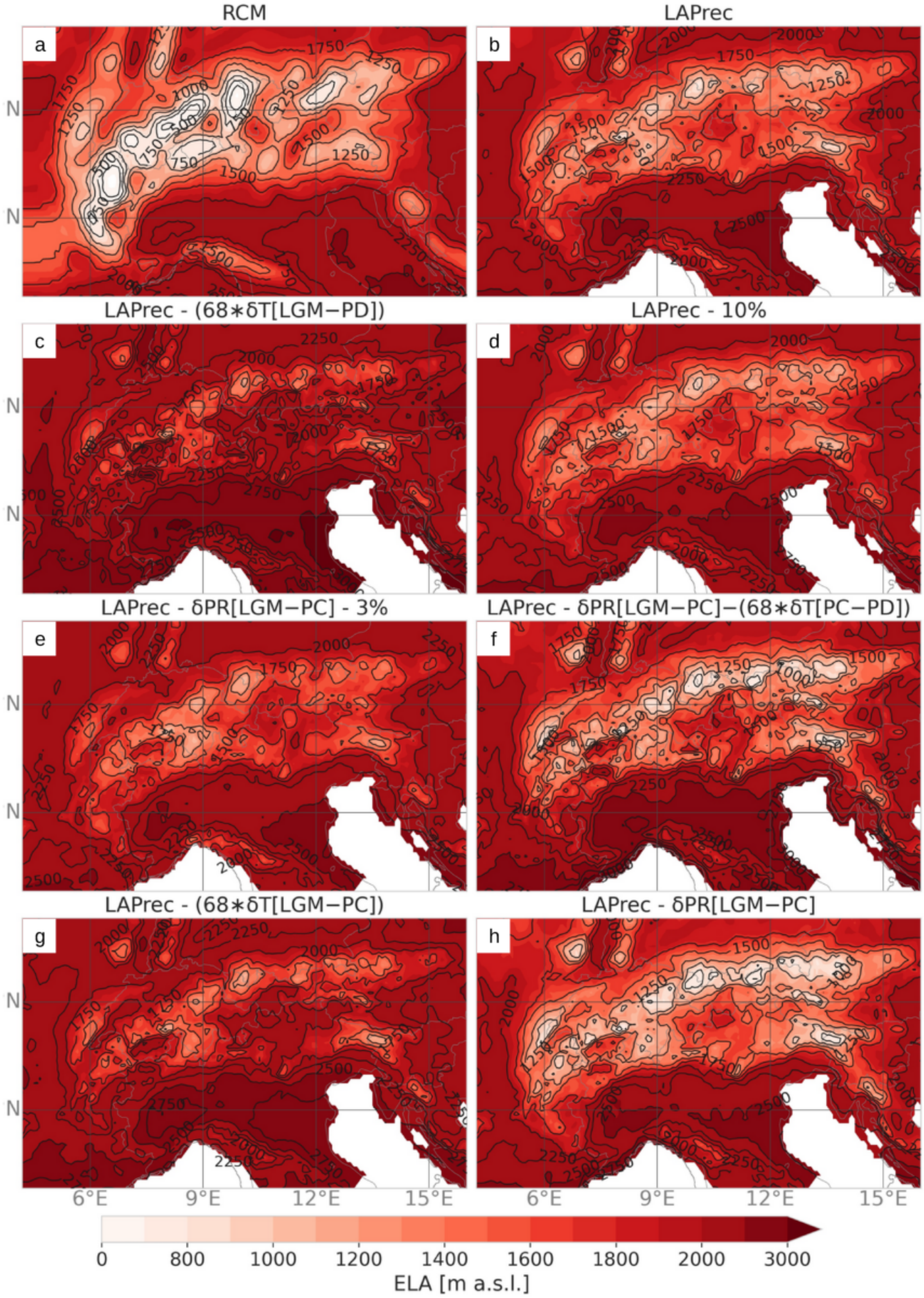

FIGURE B.1: envELA scenarios produced with the equation 5.1 to test the different correction to LAPrec dataset in order to represent LGM conditions.

Scenario a

This scenario (figure B.1.a) has already been presented in the section 5.1.
RegCM4.7 simulation outputs were used for both temperature and precipitation datasets, after having averaged the summer near-surface air temperature and the total annual precipitation over the 19 years the simulation. Among all the scenarios this is the most consistent in terms of methodology as both temperature and precipitation were produced in the same model simulation.
The envELA obtained by applying the equations 5.1 and 5.2 returns values in line with the works of Colucci et al. (2014), Kuhlemann et al. (2008), Monegato (2012) and Tintor (2005) for the southeastern Alps. The envELA calculated for the Dinaric Alps ranges between 1300 and 1600 m a.s.l. in agreement with Kuhlemann et al. (2008), Sarıkaya et al. (2020) and Žebre et al. (2014), and the values for the Pennine and Graian Prealps fit the values of 1500 m a.s.l. found by Forno et al. (2010).
Differently from the southern rim of the Alps, the western and north-western sectors of the alpine chain show unexpected low values due to the RegCM4.7 overestimation of the precipitation (see section 5.1).

Scenario b

The second scenario presented (figure B.1.b) shows reliable values across the Alps, with a rise of the envELA from East to West: the highest values in the Maritime Alps (1500 to 1750 m a.s.l.) and inner dry alpine zone (1500 m a.s.l.) and lowest values in the northern and southeastern Alps (1000 to 1200 m a.s.l.).
Although this scenario fits well with the LGM proxies, it is not completely reliable as the precipitation are provided by LAPrec dataset that refers to the years range 1971 to 2000.

Scenario c

In this scenario (figure B.1.c) we wanted to correct the LAPrec dataset in order to account for the LGM precipitation. Thus the LAPrec dataset was modified according to the methodology proposed by Seguinot et al. (2018) that considered a correction of 68 mm of precipitation for every °C of temperature difference. The temperature difference was calculated between the LGM RegCM4.7 near-surface air temperature averaged over the 19 yr of the simulation and the HISTALP dataset averaged between 1971 and 2000. The precipitation for the scenario *c* were corrected as:

$$PR_{cor} = LAPrec - (68 * \delta T[LGM_{RCM} - PD_{HISTALP}]) \tag{B.1}$$

where $LAPrec$ is the original LAPrec dataset and $\delta T[LGM_{RCM} - PD_{HISTALP}]$ is the temperature difference between LGM RegCM4.7 near-surface air temperature

(LGM_{RCM}) and the present-day HISTALP temperature ($PD_{HISTALP}$).
Before performing the calculation of the equation B, to the HISTALP dataset was applied a multidimensional gaussian filter with σ equal to 0.8, in order to produce a light smoothing of the HISTALP temperature that reduced the high spatial variability of this dataset, that was not found in the RegCM and LAPrec datasets. Without this filter the envELA resulted extremely noisy and it was not possible to clearly identify its spatial pattern over the Alps.
The result of this scenario shows too high envELA all over the Alps, but in particular in the western and central sectors (figure B.1.c)

Scenario d

As for the scenario *c*, in the scenario *d* (figure B.1.d) we wanted to correct the LAPrec dataset in order to account for the LGM-PD precipitation anomaly. In this case to LAPrec dataset was applied a constant reduction of 10 % over the whole domain, that returned envELA values in line with the studies of Colucci et al. (2014), Forno et al. (2010), Kuhlemann et al. (2008), Monegato (2012), Sarıkaya et al. (2020), Tintor (2005) and Žebre et al. (2014).
The reduction of 10 % respect to present-day differs from the values of precipitation decrease from LGM to the present found by Becker et al. (2016) who, using a glacier flow model, estimated a decrease of 20 % in the northern Alps and 47 % in the southern Alps with a corresponding cooling of 12 °C. Analogously by the mean of a mass balance model Heyman et al. (2013) assessed the LGM precipitation reduction from 75 to 25 % and Peyron et al. (1998) derived from proxies, mean annual precipitation 60 to 20 % lower than today for the northern Alps. The value of 10 % we applied to correct LAPrec temperature is clearly lower than the values proposed by the literature but the envELA pattern that results from its application is aligned with the results from other works.

Scenario e

In the scenario *e* (figure B.1.e) we corrected the LAPrec dataset in order to account for the LGM precipitation. It was applied to the LAPrec dataset a correction given by the percentual difference between the LGM and PC RegCM4.7 precipitation plus an amount equal to 3 % in order to consider the precipitation difference between PC and present-day. Several values were tested and the 3 % was the one that performed better considering the calculated envELA values. However, the values are slightly too high compared with the literature (Kuhlemann et al., 2008). The correction was calculate as:

$$PR_{cor} = LAPrec - \delta PR[LGM_{RCM} - PC_{RCM}] - 3 \tag{B.2}$$

where $LAPrec$ is the original LAPrec dataset and $\delta PR[LGM_{RCM} - PC_{RCM}]$ is the temperature difference between RegCM4.7 LGM PR (LGM_{RCM}) and RegCM4.7 PC PR temperature (PC_{RCM}).

Scenario f

In the scenario f (figure B.1.f) a correction was applied to LAPrec dataset in order to account for the LGM-PD precipitation difference. It was applied to the LAPrec dataset a correction given by the percentual difference between the LGM and PC RegCM4.7 precipitation plus an amount that considered the precipitation anomaly in the time range PC-PD. This was calculated with the methodology proposed by Seguinot et al. (2018) and already explained in the *scenario c*. The idea behind this scenario is similar to that one of scenario e but it was applied a different method to calculate the precipitation anomaly between PC and PD. Also in this case it was applied a multidimensional gaussian filter to smooth the HISTALP dataset used in the correction based on the Seguinot et al. (2018) method. The precipitation for the scenario f were corrected as:

$$PR_{cor} = LAPrec - \delta PR[LGM_{RCM} - PC_{RCM}] - (68 * \delta T[LGM_{RCM} - PD_{HISTALP}]) \tag{B.3}$$

where $LAPrec$ is the original LAPrec dataset, $\delta PR[LGM_{RCM} - PC_{RCM}]$ is the precipitation anomaly between LGM and PC and $\delta T[LGM_{RCM} - PD_{HISTALP}]$ is the temperature difference between RegCM4.7 near-surface air temperature and the HISTALP temperature.

The result fits well with other works across all the Alpine range, fro east (Colucci et al., 2014; Kuhlemann et al., 2008; Monegato, 2012; Sarıkaya et al., 2020; Tintor, 2005; Žebre et al., 2014) to west Forno et al. (2010).

Scenario g

In this scenario (figure B.1.g) we only corrected the LAPrec dataset for the LGM-PC anomaly. The time range PC-PD was not considered. The correction used the methodology proposed by Seguinot et al. (2018) that set a correction of 68 mm of precipitation for every °C of temperature difference. The temperature difference was calculated between the LGM and PC RegCM4.7 near-surface air temperature averaged over the 19 yr of the simulation. The precipitation for the scenario g was corrected as:

$$PR_{cor} = LAPrec - (68 * \delta T[LGM_{RCM} - PC_{RCM}]) \tag{B.4}$$

where $LAPrec$ is the original LAPrec dataset and $\delta T[LGM_{RCM} - PC_{RCM}]$ is the temperature difference between LGM and PC RegCM4.7 near-surface air temperature.

The calculated envELA present too high values almost everywhere in the domain, but particularly in the western and central Alps.

Scenario h

As in the scenario *g*, in the scenario *h* (figure B.1.h) we only corrected the LAPrec dataset for the LGM-PC anomaly, without considering the time range PC-PD. In this case the correction applied to LAPrec dataset was given by the percentual difference between the LGM and PC RegCM4.7 precipitation. The precipitation for the scenario *h* were corrected as:

$$PR_{cor} = LAPrec - \delta PR[LGM_{RCM} - PC_{RCM}] \tag{B.5}$$

where $LAPrec$ is the original LAPrec dataset, $\delta PR[LGM_{RCM} - PC_{RCM}]$ is the precipitation anomaly between LGM and PC in the RegCM4.7 simulations.
This scenario produces values that locally are too low as the case of the Julian Alps with an envELA of 750 m a.s.l. and the northern alpine rim with values below 750 m a.s.l..

Among all the tests performed, the scenario *f* is the one that performs better and that is supported by the more consistent method covering all the time between LAPrec$_{1971\text{-}2000}$ and the LGM is the scenario *f*.

Bibliography

Abe-Ouchi, A., Segawa, T. and Saito, F. (2007). 'Climatic Conditions for modelling the Northern Hemisphere ice sheets throughout the ice age cycle'. In: *Climate of the Past* 3.3, pp. 423–438. DOI: `10.5194/cp-3-423-2007`.

Adam, J. C. and Lettenmaier, D. P. (2003). 'Adjustment of global gridded precipitation for systematic bias'. In: *Journal of Geophysical Research: Atmospheres* 108.D9, n/a–n/a. DOI: `10.1029/2002jd002499`.

Ahn, J. and Brook, E. J. (2014). 'Siple Dome ice reveals two modes of millennial CO_2 change during the last ice age'. In: *Nature Communications* 5.1. DOI: `10.1038/ncomms4723`.

Ahn, J., Wahlen, M., Deck, B. L., Brook, E. J., Mayewski, P. A., Taylor, K. C. and White, J. W. C. (2004). 'A record of atmospheric CO_2 during the last 40,000 years from the Siple Dome, Antarctica ice core'. In: *Journal of Geophysical Research: Atmospheres* 109.D13, n/a–n/a. DOI: `10.1029/2003JD004415`.

Alessio, M., Allegri, L., Bella, F., Calderoni, G., Cortesi, C., Dai Pra, G., De Rita, D., Esu, D., Follieri, M., Improta, S., Magri, D., Narcisi, B., Petrone, V. and Sadori, L. (1986). '^{14}C dating, geochemical features, faunistic and pollen analyses of the uppermost 10 m core from Valle di Castiglione (Rome, Italy)'. In: 25, pp. 287–308.

Amante, C. and Eakins, B. (Mar. 2009). 'ETOPO1 1 Arc-Minute Global Relief Model: procedures, data sources and analysis'. In: DOI: `10.7289/V5C8276M`.

Anderson, R. S., Anderson, L. S., Armstrong, W. H., Rossi, M. W. and Crump, S. E. (2018). 'Glaciation of alpine valleys: The glacier–debris-covered glacier–rock glacier continuum'. In: *Geomorphology* 311, pp. 127–142. DOI: `10.1016/j.geomorph.2018.03.015`.

Annan, J. and Hargreaves, J. C. (2013). 'A new global reconstruction of temperature changes at the Last Glacial Maximum'. In: *Climate of the Past* 9.1, pp. 367–376. DOI: `10.5194/cp-9-367-2013`.

Armstrong, E., Hopcroft, P. O. and Valdes, P. J. (2019). 'Reassessing the value of regional climate modeling using paleoclimate simulations'. In: *Geophysical Research Letters* 46.21, pp. 12464–12475. DOI: `10.1029/2019GL085127`.

Auer, I. et al. (2007). 'HISTALP-historical instrumental climatological surface time series of the Greater Alpine Region'. In: *International Journal of Climatology* 27.1, pp. 17–46. DOI: `10.1002/joc.1377`.

Ban, N., Schmidli, J. and Schär, C. (2014). 'Evaluation of the convection-resolving regional climate modeling approach in decade-long simulations'. In: *Journal of Geophysical Research: Atmospheres* 119.13, pp. 7889–7907. DOI: `10.1002/2014JD021478`.

Bartlein, P. J. et al. (2010). 'Pollen-based continental climate reconstructions at 6 and 21 ka: a global synthesis'. In: *Climate Dynamics* 37.3-4, pp. 775–802. DOI: `10.1007/s00382-010-0904-1`.

Becker, P., Seguinot, J., Jouvet, G. and Funk, M. (2016). 'Last Glacial Maximum precipitation pattern in the Alps inferred from glacier modelling'. In: *Geographica Helvetica* 71.3, pp. 173–187. DOI: `10.5194/gh-71-173-2016`.

Berg, J. van den, Wal, R. S. W. van de, Milne, G. A. and Oerlemans, J. (2008). 'Effect of isostasy on dynamical ice sheet modeling: A case study for Eurasia'. In: *Journal of Geophysical Research* 113.B5. DOI: `10.1029/2007jb004994`.

Berger, A. (1978). 'Long-term variations of caloric insolation resulting from the Earth's orbital elements'. In: *Quaternary research* 9.2, pp. 139–167.

Bowen, D. Q. (2009). 'Last Glacial Maximum'. In: *Encyclopedia of paleoclimatology and ancient environments*. Ed. by V. Gorni. Dordrecht, The Netherlands: Springer Science & Business Media. Chap. 11, pp. 493–495. DOI: `10.1007/978-1-4020-4411-3_122`.

Braconnot, P. et al. (2007). 'Results of PMIP2 coupled simulations of the Mid-Holocene and Last Glacial Maximum – Part 1: experiments and large-scale features'. In: *Climate of the Past* 3.2, pp. 261–277. DOI: `10.5194/cp-3-261-2007`.

Braconnot, P., Harrison, S. P., Kageyama, M., Bartlein, P. J., Masson-Delmotte, V., Abe-Ouchi, A., Otto-Bliesner, B. and Zhao, Y. (2012). 'Evaluation of climate models using palaeoclimatic data'. In: *Nature Climate Change* 2.6, pp. 417–424. DOI: `10.1038/nclimate1456`.

Brauer, A., Allen, J. R., Mingram, J., Dulski, P., Wulf, S. and Huntley, B. (2007). 'Evidence for last interglacial chronology and environmental change from Southern Europe'. In: *Proceedings of the National Academy of Sciences* 104.2, pp. 450–455. DOI: `10.1073/pnas.0603321104`.

Broccoli, A. and Manabe, S. (1987). 'The influence of continental ice, atmospheric CO2, and land albedo on the climate of the last glacial maximum'. In: *Climate dynamics* 1.2, pp. 87–99. DOI: `10.1007/bf01054478`.

Carrión, J. S., Yll, E. I., Walker, M. J., Legaz, A. J., Chaín, C. and López, A. (2003). 'Glacial refugia of temperate, Mediterranean and Ibero-North African flora in south-eastern Spain: new evidence from cave pollen at two Neanderthal man sites'. In:

Global Ecology and Biogeography 12.2, pp. 119–129. DOI: 10.1046/j.1466-822x.2003.00013.x.

Ciarlo, J. M. et al. (2020). ‘A new spatially distributed added value index for regional climate models: the EURO-CORDEX and the CORDEX-CORE highest resolution ensembles’. In: *Climate Dynamics*, pp. 1–22.

Clark, P. U., Dyke, A. S., Shakun, J. D., Carlson, A. E., Clark, J., Wohlfarth, B., Mitrovica, J. X., Hostetler, S. W. and McCabe, A. M. (2009). ‘The Last Glacial Maximum’. In: *Science* 325.5941, pp. 710–714. ISSN: 0036-8075. DOI: 10.1126/science.1172873.

Clark, P. U. and Mix, A. C. (2002). ‘Ice sheets and sea level of the Last Glacial Maximum’. In: *Quaternary Science Reviews* 21.1-3, pp. 1–7. DOI: 10.1016/s0277-3791(01)00118-4.

CLIMAP Project Members (1976). ‘The surface of the ice-age earth’. In: *Science* 191.4232, pp. 1131–1137. DOI: 10.1126/science.191.4232.1131.

CLIMAP Project Members (1981). *Seasonal reconstructions of the Earth’s surface at the last glacial maximum*. Map and Chart Series 36.

Cogley, J. G., Hock, R., Rasmussen, L., Arendt, A., Bauder, A., Braithwaite, R., Jansson, P, Kaser, G, Möller, M, Nicholson, L et al. (2011). ‘Glossary of glacier mass balance and related terms’. In: *IHP-VII technical documents in hydrology* 86. DOI: 10.14430/arctic4151.

Cohmap Members (1988). ‘Climatic changes of the last 18,000 years: observations and model simulations’. In: *Science*, pp. 1043–1052. DOI: 10.1126/science.241.4869.1043.

Colgan, W., Box, J. E., Ribeiro, S. and Kjeldsen, K. K. (2019). ‘Sea-level rise in Denmark: bridging local reconstructions and global projections’. In: *Geological Survey of Denmark and Greenland Bulletin* 43. DOI: 10.34194/geusb-201943-01-01.

Collins, W. D., Bitz, C. M., Blackmon, M. L., Bonan, G. B., Bretherton, C. S., Carton, J. A., Chang, P., Doney, S. C., Hack, J. J., Henderson, T. B., Kiehl, J. T., Large, W. G., McKenna, D. S., Santer, B. D. and Smith, R. D. (2006). ‘The Community Climate System Model Version 3 (CCSM3)’. In: *Journal of Climate* 19.11, pp. 2122 –2143. DOI: 10.1175/JCLI3761.1.

Colucci, R. R. (2016). ‘Geomorphic influence on small glacier response to post-Little Ice Age climate warming: Julian Alps, Europe’. In: *Earth Surface Processes and Landforms* 41.9, pp. 1227–1240. DOI: 10.1002/esp.3908.

Colucci, R. R. and Guglielmin, M. (2015). ‘Precipitation–temperature changes and evolution of a small glacier in the southeastern European Alps during the last 90 years’. In: *International Journal of Climatology* 35.10, pp. 2783–2797. DOI: 10.1002/joc.4172.

Colucci, R. R., Monegato, G. and Žebre, M. (2014). 'Glacial and proglacial deposits of the Resia Valley (NE Italy): new insights on the onset and decay of the last Alpine Glacial Maximum in the Julian Alps'. In: *Alpine and Mediterranean Quaternary* 27.2, pp. 85–104.

Colucci, R. R. and Žebre, M. (2016). 'Late Holocene evolution of glaciers in the southeastern Alps'. In: *Journal of Maps* 12.sup1, pp. 289–299. DOI: `10.1080/17445647.2016.1203216`.

Coppola, E, Verdecchia, M, Tomassetti, B and Visconti, G (2003). 'CHYM: A grid based Hydrological Model'. In: *Proceedings of International Symposium on Remote Sensing of Environment, Honolulu, Hawaii*.

Correggiari, M, Roveriand, F and Trincardi, A (1996). 'Late Pleistocene and Holocene evolution of the north Adriatic Sea'. In: *Il Quaternario* 9.2, pp. 697–704.

Cossart, E., Fort, M., Bourlès, D., Braucher, R., Perrier, R. and Siame, L. (2012). 'Deglaciation pattern during the Lateglacial/Holocene transition in the southern French Alps. Chronological data and geographical reconstruction from the Clarée Valley (upper Durance catchment, southeastern France)'. In: *Palaeogeography, Palaeoclimatology, Palaeoecology* 315, pp. 109–123. DOI: `10.1016/j.palaeo.2011.11.017`.

Dahl-Jensen, D., Albert, M., Aldahan, A., Azuma, N, Balslev-Clausen, D, Baumgartner, M., Berggren, A.-M., Bigler, M., Binder, T., Blunier, T. et al. (2013). 'Eemian interglacial reconstructed from a Greenland folded ice core'. In: *Nature* 493.7433, p. 489. DOI: `10.1038/nature11789`.

Dai, Y., Zeng, X., Dikinson, R. E., Baker, I., Bonan, G. B., Bosilovich, M. G., Denning, A. S., Dirmeyer, P. A., Houser, P. R., Niu, G., Oleson, K. W., Schlosser, C. A. and Yang, Z.-L. (2003). 'The Common Land Model'. In: *Bulletin of the American Meteorological Society* 84, pp. 1013–1023.

Danielson, J. J. and Gesch, D. B. (2011). *Global multi-resolution terrain elevation data 2010 (GMTED2010)*. Tech. rep. US Geological Survey. DOI: `10.3133/ofr20111073`.

Davies, H. and Turner, R. E. (1977). 'Updating prediction models by dynamical relaxation: An examination of the technique'. In: *Quarterly Journal of the Royal Meteorological Society* 103.436, pp. 225–245. DOI: `10.1002/qj.49710343602`.

Dee, D. P. et al. (2011). 'The ERA-Interim reanalysis: Configuration and performance of the data assimilation system'. In: *Quarterly Journal of the royal meteorological society* 137.656, pp. 553–597. DOI: `10.1002/qj.828`.

Denis, B., Laprise, R. and Caya, D. (2003). 'Sensitivity of a regional climate model to the resolution of the lateral boundary conditions'. In: *Climate Dynamics* 20.2, pp. 107–126. DOI: `10.1007/s00382-002-0264-6`.

Dickinson, E, Henderson-Sellers, A and Kennedy, J (1993). 'Biosphere-atmosphere transfer scheme (BATS) version 1e as coupled to the NCAR community climate model'. In: DOI: `10.5065/D67W6959`.

Dickinson, R. E., Errico, R. M., Giorgi, F. and Bates, G. T. (1989). 'A regional climate model for the western United States'. In: *Climatic change* 15.3, pp. 383–422. DOI: `10.1007/bf00240465`.

Duprat-Oualid, F., Rius, D., Bégeot, C., Magny, M., Millet, L., Wulf, S. and Appelt, O. (2017). 'Vegetation response to abrupt climate changes in Western Europe from 45 to 14.7 k cal a BP: the Bergsee lacustrine record (Black Forest, Germany)'. In: *Journal of Quaternary Science* 32.7, pp. 1008–1021. DOI: `10.1002/jqs.2972`.

Ehlers, J. and Gibbard, P. L. (2004). *Quaternary glaciations-extent and chronology: part I: Europe*. Elsevier.

Elguindi, N., Bi, X., Giorgi, F., Nagarajan, B., Pal, J., Solmon, F., Rauscher, S., Zakey, A., O'Brien, T., Nogherotto, R. et al. (2014). *Regional climate model RegCM: reference manual version 4.5*. Tech. rep. Abdus Salam ICTP, Trieste.

Farnsworth, A., Lunt, D. J., O'Brien, C. L., Foster, G. L., Inglis, G. N., Markwick, P., Pancost, R. D. and Robinson, S. A. (2019). 'Climate Sensitivity on Geological Timescales Controlled by Nonlinear Feedbacks and Ocean Circulation'. In: *Geophysical Research Letters* 46.16, pp. 9880–9889. DOI: `10.1029/2019gl083574`.

Federici, P. R., Ribolini, A. and Spagnolo, M. (2016). 'Glacial history of the Maritime Alps from the Last Glacial Maximum to the Little Ice Age'. In: *Geological Society, London, Special Publications* 433.1, pp. 137–159. DOI: `10.1144/sp433.9`.

Feldberg, M. J. and Mix, A. C. (2003). 'Planktonic foraminifera, sea surface temperatures, and mechanisms of oceanic change in the Peru and south equatorial currents, 0-150 ka BP'. In: *Paleoceanography* 18.1, n/a–n/a. DOI: `10.1029/2001pa000740`.

Flato, G. et al. (2013). 'Evaluation of Climate Models'. In: *Climate Change 2013: The Physical Science Basis. Contribution of Working Group I to the Fifth Assess-ment Report of the Intergovernmental Panel on Climate Change*. Ed. by T. Stocker, D. Qin, G.-K. Plattner, M. Tignor, S. Allen, J. Boschung, A. Nauels, Y. Xia, V. Bex and P. Midgley. Cambridge, United Kingdom and New York, NY, USA: Cambridge University Press, pp. 801–866. DOI: `10.1017/cbo9781107415324.021`.

Flato, G. M. (2011). 'Earth system models: an overview'. In: *Wiley Interdisciplinary Reviews: Climate Change* 2.6, pp. 783–800. DOI: `10.1002/wcc.148`.

Florineth, D. (Jan. 1998). 'Surface geometry of the Last Glacial Maximum (LGM) in the southeastern Swiss Alps (Graubünden) and its paleoclimatological significance'. In: *Eiszeitalter und Gegenwart* 48, pp. 23–37. DOI: `10.3285/eg.48.1.03`.

Florineth, D. and Schlüchter, C. (2000). ‘Alpine Evidence for Atmospheric Circulation Patterns in Europe during the Last Glacial Maximum’. In: *Quaternary Research* 54.3, pp. 295–308. DOI: `10.1006/qres.2000.2169`.

Fontana, A., Monegato, G., Zavagno, E., Devoto, S., Burla, I. and Cucchi, F. (2014a). ‘Evolution of an Alpine fluvioglacial system at the LGM decay: The Cormor megafan (NE Italy)’. In: *Geomorphology* 204, pp. 136 –153. ISSN: 0169-555X. DOI: `10.1016/j.geomorph.2013.07.034`.

Fontana, A., Mozzi, P. and Bondesan, A. (2008). ‘Alluvial megafans in the Venetian–Friulian Plain (north-eastern Italy): evidence of sedimentary and erosive phases during Late Pleistocene and Holocene’. In: *Quaternary International* 189.1, pp. 71–90. DOI: `10.1016/j.quaint.2007.08.044`.

Fontana, A., Mozzi, P. and Marchetti, M. (2014b). ‘Alluvial fans and megafans along the southern side of the Alps’. In: *Sedimentary Geology* 301, pp. 150–171. DOI: `10.1016/j.sedgeo.2013.09.003`.

Forno, M. G., Gianotti, F. and Gianluca, R. (2010). ‘Significato paleoclimatico dei rapporti tra il glacialismo principale e quello tributario nella bassa Valle della Dora Baltea’. In: *Il Quaternario - Italian Journal of Quaternary Sciences* 23.1, pp. 105–124.

Fuhrmann, F., Diensberg, B., Gong, X., Lohmann, G. and Sirocko, F. (2020). ‘Aridity synthesis for eight selected key regions of the global climate system during the last 60 000 years’. In: *Climate of the Past* 16.6, pp. 2221–2238. DOI: `10.5194/cp-16-2221-2020`.

Gillespie, A. and Molnar, P. (1995). ‘Asynchronous maximum advances of mountain and continental glaciers’. In: *Reviews of Geophysics* 33.3, pp. 311–364. DOI: `10.1029/95rg00995`.

Giorgetta, M. A., Roeckner, E., Mauritsen, T., Bader, J., Crueger, T., Esch, M., Rast, S., Kornblueh, L., Schmidt, H., Kinne, S. et al. (2013). *The atmospheric general circulation model ECHAM6-model description*. Tech. rep. Max-Planck-Institut für Meteorologie.

Giorgi, F, Gutowski, J and William, J (2015). ‘Regional dynamical downscaling and the CORDEX initiative’. In: *Annual Review of Environment and Resources* 40, pp. 467–490. DOI: `10.1093/acrefore/9780190228620.013.784`.

Giorgi, F, Marinucci, M., DeCanio, G and Bates, G. (1993). ‘Development of a second generation regional climate model (REGCM2), Cumulus cloud and assimilation of lateral boundary conditions’. In: *Mon Wea Rev* 121, pp. 2814–2832. DOI: `10.1175/1520-0493(1993)121<2814:doasgr>2.0.co;2`.

Giorgi, F., Pal, J. S., Bi, X., Sloan, L., Elguindi, N. and Solmon, F. (2006). ‘Introduction to the TAC special issue: The RegCNET network’. In: *Theoretical and Applied Climatology* 86.1-4, pp. 1–4. DOI: `10.1007/s00704-005-0199-z`.

Giorgi, F. (1990). 'Simulation of regional climate using a limited area model nested in a general circulation model'. In: *Journal of Climate* 3.9, pp. 941–963. DOI: `10.1175/1520-0442(1990)003<0941:sorcua>2.0.co;2`.

Giorgi, F. (2019). 'Thirty years of regional climate modeling: where are we and where are we going next?' In: *Journal of Geophysical Research: Atmospheres* 124.11, pp. 5696–5723. DOI: `10.1029/2018JD030094`.

Giorgi, F. and Bates, G. T. (1989). 'The climatological skill of a regional model over complex terrain'. In: *Monthly Weather Review* 117.11, pp. 2325–2347. DOI: `10.1175/1520-0493(1989)117<2325:tcsoar>2.0.co;2`.

Giorgi, F., Jones, C., Asrar, G. R. et al. (2009). 'Addressing climate information needs at the regional level: the CORDEX framework'. In: *World Meteorological Organization (WMO) Bulletin* 58.3, p. 175.

Giorgi, F. et al. (2012). 'RegCM4: model description and preliminary tests over multiple CORDEX domains'. In: *Climate Research* 52, pp. 7–29. DOI: `10.3354/cr01018`.

Gómez-Navarro, J., Montávez, J., Wagner, S and Zorita, E (2013). 'A regional climate palaeosimulation for Europe in the period 1500-1990-Part 1: Model validation.' In: *Climate of the Past* 9.4. DOI: `10.5194/cp-9-1667-2013`.

Goosse, H., Brovkin, V, Fichefet, T., Haarsma, R, Huybrechts, P., Jongma, J, Mouchet, A., Selten, F, Barriat, P.-Y., Campin, J.-M. et al. (2010). 'Description of the Earth system model of intermediate complexity LOVECLIM version 1.2'. In: *Geoscientific Model Development* 3, pp. 603–633. DOI: `10.5194/gmd-3-603-2010`.

Grell, G. a., Dudhia, J. and Stauffer, D. (1994). *A description of the fifth-generation Penn State/NCAR Mesoscale Model (MM5)*. Tech. rep. December, p. 121. DOI: `10.5065/D60Z716B`.

Haeberli, W., Hoelzle, M., Paul, F. and Zemp, M. (2007). 'Integrated monitoring of mountain glaciers as key indicators of global climate change: the European Alps'. In: *Annals of glaciology* 46, pp. 150–160. DOI: `10.3189/172756407782871512`.

Harris, I., Jones, P., Osborn, T. and Lister, D. (2013). 'Updated high-resolution grids of monthly climatic observations - the CRU TS3.10 Dataset'. In: *International Journal of Climatology* 34.3, pp. 623–642. DOI: `10.1002/joc.3711`.

Haylock, M. R., N. Hofstra, A.M.G. Klein Tank, E.J. Klok, P.D. Jones and New., M (2008). 'A European daily high-resolution gridded dataset of surface temperature and precipitation'. In: *Journal of Geophysical Research-Atmospheres*. DOI: `10.1029/2008JD010201`.

Heyman, B. M., Heyman, J., Fickert, T. and Harbor, J. M. (2013). 'Paleo-climate of the central European uplands during the last glacial maximum based on glacier mass-balance modeling'. In: *Quaternary Research* 79.1, pp. 49–54. DOI: `10.1016/j.yqres.2012.09.005`.

Hird, J., DeLancey, E., McDermid, G. and Kariyeva, J. (2017). 'Google Earth Engine, Open-Access Satellite Data, and Machine Learning in Support of Large-Area Probabilistic Wetland Mapping'. In: *Remote Sensing* 9.12, p. 1315. DOI: `10.3390/rs9121315`.

Hughes, P. D. and Woodward, J. C. (2008). 'Glacial and periglacial environments'. In: *The Physical Geography of the Mediterranean*. Ed. by J. Woodward. Oxford University Press, pp. 353–383. DOI: `10.1177/0959683610361291`.

Hughes, P. D., Gibbard, P. L. and Ehlers, J. (2013). 'Timing of glaciation during the last glacial cycle: evaluating the concept of a global 'Last Glacial Maximum'(LGM)'. In: *Earth-Science Reviews* 125, pp. 171–198. DOI: `10.1016/j.earscirev.2013.07.003`.

Isotta, F. A. et al. (2014). 'The climate of daily precipitation in the Alps: development and analysis of a high-resolution grid dataset from pan-Alpine rain-gauge data'. In: *International Journal of Climatology* 34.5, pp. 1657–1675. DOI: `10.1002/joc.3794`.

Ivy-Ochs, S., Kerschner, H., Kubik, P. W. and Schlüchter, C. (2006a). 'Glacier response in the European Alps to Heinrich Event 1 cooling: the Gschnitz stadial'. In: *Journal of Quaternary science* 21.2, pp. 115–130. DOI: `10.1002/jqs.955`.

Ivy-Ochs, S., Kerschner, H., Reuther, A., Maisch, M., Sailer, R., Schaefer, J., Kubik, P. W., Synal, H and Schluchter, C (2006b). 'The timing of glacier advances in the northern European Alps based on surface exposure dating with cosmogenicˆ 1ˆ 0Be,ˆ 2ˆ 6Al,ˆ 3ˆ 6Cl, andˆ 2ˆ 1Ne'. In: *Special Papers-Geological Society of America* 415, p. 43. DOI: `10.1130/2006.2415(04)`.

Ivy-Ochs, S., Kerschner, H., Reuther, A., Preusser, F., Heine, K., Maisch, M., Kubik, P. W. and Schlüchter, C. (2008). 'Chronology of the last glacial cycle in the European Alps'. In: *Journal of Quaternary Science: Published for the Quaternary Research Association* 23.6-7, pp. 559–573.

Ivy-Ochs, S., Schäfer, J., Kubik, P. W., Synal, H.-A. and Schlüchter, C. (2004). 'Timing of deglaciation on the northern Alpine foreland (Switzerland)'. In: *Eclogae Geologicae Helvetiae* 97.1, pp. 47–55. DOI: `10.1007/s00015-004-1110-0`.

Jansen, E., Overpeck, J., Briffa, K., Duplessy, J., Joos, F, Masson-Delmotte, V, Olago, D, Otto-Bliesner, B, Peltier, W., Rahmstorf, S, Ramesh, R, Raynaud, D., Rind, D., Solomina O. Villalba, R. and Zhang, D. (2007). 'Paleoclimate'. In: *Climate change: the physical science basis; contribution of Working Group I to the Fourth Assessment Report of the Intergovernmental Panel on Climate Change*. Ed. by S. Solomon, D. Qin, M. Manning, Z. Chen, M. Marquis, K. Averyt, M. Tignor and H. Miller. Cambridge, United Kingdom and New York, NY, USA: Cambridge University Press. URL:

https://www.ipcc.ch/site/assets/uploads/2018/02/ar4-wg1-chapter6-1.pdf.

Jia, X., Lee, J.-Y., Lin, H., Hendon, H. and Ha, K.-J. (2014). 'Interdecadal change in the Northern Hemisphere seasonal climate prediction skill: Part II. Predictability and prediction skill'. In: *Climate dynamics* 43.5-6, pp. 1611–1630. DOI: 10.1007/s00382-020-05494-x.

Jones, P., Hulme, M and Briffa, K. (1993). 'A comparison of Lamb circulation types with an objective classification scheme'. In: *International Journal of Climatology* 13.6, pp. 655–663.

Jost, A, Lunt, D, Kageyama, M, Abe-Ouchi, A, Peyron, O, Valdes, P. and Ramstein, G (2005). 'High-resolution simulations of the last glacial maximum climate over Europe: a solution to discrepancies with continental palaeoclimatic reconstructions?' In: *Climate Dynamics* 24.6, pp. 577–590. DOI: 10.1007/s00382-005-0009-4.

Ju, L., Wang, H. and Jiang, D. (2007a). 'Simulation of the Last Glacial Maximum climate over East Asia with a regional climate model nested in a general circulation model'. In: *Palaeogeography, Palaeoclimatology, Palaeoecology* 248.3-4, pp. 376–390. DOI: 10.1016/j.palaeo.2006.12.012.

Ju, L., Wang, H. and Jiang, D. (2007b). 'Simulation of the Last Glacial Maximum climate over East Asia with a regional climate model nested in a general circulation model'. In: *Palaeogeography, Palaeoclimatology, Palaeoecology* 248.3-4, pp. 376–390. DOI: 10.1016/j.palaeo.2006.12.012.

Kageyama, M., Nebout, N. C., Sepulchre, P., Peyron, O., Krinner, G., Ramstein, G. and Cazet, J.-P. (2005). 'The Last Glacial Maximum and Heinrich Event 1 in terms of climate and vegetation around the Alboran Sea: a preliminary model-data comparison'. In: *Comptes Rendus Geoscience* 337.10-11, pp. 983–992. DOI: 10.1016/j.crte.2005.04.012.

Kageyama, M. et al. (2018). 'The PMIP4 contribution to CMIP6 – Part 1: Overview and over-arching analysis plan'. In: *Geoscientific Model Development* 11.3, pp. 1033–1057. DOI: 10.5194/gmd-11-1033-2018.

Kageyama, M. et al. (2020). 'The PMIP4-CMIP6 Last Glacial Maximum experiments: preliminary results and comparison with the PMIP3-CMIP5 simulations'. In: DOI: 10.5194/egusphere-egu2020-11153.

Källen, E. (1996). *HIRLAM documentation manual, System 2.5.SMHI*. Tech. rep. SMHI, Norrköping, Sweden.

Kanamitsu, M. and De Haan, L. (2011). 'The Added Value Index: A new metric to quantify the added value of regional models'. In: *Journal of Geophysical Research: Atmospheres* 116.D11. DOI: 10.1029/2011jd015597.

Karl, T. R. and Trenberth, K. E. (2003). 'Modern global climate change'. In: *science* 302.5651, pp. 1719–1723. DOI: `10.1126/science.1090228`.

Kelly, M. A., Buoncristiani, J.-F. and Schlchter, C. (2004). 'A reconstruction of the last glacial maximum (LGM) ice-surface geometry in the western Swiss Alps and contiguous Alpine regions in Italy and France'. In: *Eclogae Geologicae Helvetiae* 97.1, pp. 57–75. DOI: `10.1007/s00015-004-1109-6`.

Kettner, A. J. and Syvitski, J. P. (2008). 'Predicting discharge and sediment flux of the Po River, Italy since the Last Glacial Maximum'. In: *Analogue and Numerical Modelling of Sedimentary Systems: From Understanding to Prediction*. Wiley-Blackwell Oxford, UK. DOI: `10.1002/9781444303131.ch7`.

Kirtman, B. et al. (2013). 'Near-term climate change: Projections and predictability'. In: *Climate Change 2013. The Physical Science Basis. Contribution of Working Group I to the Fifth Assessment Report of the Intergovernmental Panel on Climate Change*. Ed. by T. Stocker, D. Qin, G.-K. Plattner, M. Tignor, S. Allen, J. Boschung, A. Nauels, Y. Xia, V. Bex and P. Midgley. Cambridge, United Kingdom and New York, NY, USA: Cambridge University Press. URL: `http://pure.iiasa.ac.at/id/eprint/10550/`.

Kotlarski, S. et al. (2014). 'Regional climate modeling on European scales: a joint standard evaluation of the EURO-CORDEX RCM ensemble'. In: *Geoscientific Model Development* 7.4, pp. 1297–1333. DOI: `10.5194/gmd-7-1297-2014`.

Koutavas, A. (2002). 'El Nino-Like Pattern in Ice Age Tropical Pacific Sea Surface Temperature'. In: *Science* 297.5579, pp. 226–230. DOI: `10.1126/science.1072376`.

Kuhlemann, J., Rohling, E. J., Krumrei, I., Kubik, P., Ivy-Ochs, S. and Kucera, M. (2008). 'Regional synthesis of Mediterranean atmospheric circulation during the Last Glacial Maximum'. In: *Science* 321.5894, pp. 1338–1340. DOI: `10.1126/science.1157638`.

Kuhn, M. (1995). 'The mass balance of very small glaciers'. In: *Zeitschrift für Gletscherkunde und Glazialgeologie* 31.1, pp. 171–179.

Kutzbach, J., Gallimore, R. and Guetter, P. (1991). 'Sensitivity experiments on the effect of orbitally-caused insolation changes on the interglacial climate of high northern latitudes'. In: *Quaternary International* 10, pp. 223–229.

Kutzbach, J. E. and Guetter, P. J. (1986). 'The influence of changing orbital parameters and surface boundary conditions on climate simulations for the past 18 000 years'. In: *Journal of the Atmospheric Sciences* 43.16, pp. 1726–1759. DOI: `10.1175/1520-0469(1986)043<1726:tiocop>2.0.co;2`.

Laîné, A., Kageyama, M., Salas-Mélia, D., Voldoire, A., Riviere, G., Ramstein, G., Planton, S., Tyteca, S. and Peterschmitt, J. Y. (2009). 'Northern hemisphere storm tracks during the last glacial maximum in the PMIP2 ocean-atmosphere coupled models: energetic study, seasonal cycle, precipitation'. In: *Climate Dynamics* 32.5, pp. 593–614. DOI: `10.1007/s00382-008-0391-9`.

Lambeck, K., Rouby, H., Purcell, A., Sun, Y. and Sambridge, M. (2014). 'Sea level and global ice volumes from the Last Glacial Maximum to the Holocene'. In: *Proceedings of the National Academy of Sciences* 111.43, pp. 15296–15303. DOI: `10.1073/pnas.1411762111`.

Langford, Z., Kumar, J., Hoffman, F., Norby, R., Wullschleger, S., Sloan, V. and Iversen, C. (2016). 'Mapping Arctic plant functional type distributions in the Barrow Environmental Observatory using WorldView-2 and LiDAR Datasets'. In: *Remote Sensing* 8.9, p. 733. DOI: `10.3390/rs8090733`.

Laprise, R., De Elia, R, Caya, D, Biner, S, Lucas-Picher, P., Diaconescu, E, Leduc, M, Alexandru, A, Separovic, L et al. (2008). 'Challenging some tenets of regional climate modelling'. In: *Meteorology and Atmospheric Physics* 100.1-4, pp. 3–22. DOI: `10.1007/s00703-008-0292-9`.

Laskar, J., Robutel, P., Joutel, F., Gastineau, M., Correia, A. C. M. and Levrard, B. (2004). 'A long-term numerical solution for the insolation quantities of the Earth'. In: *Astronomy & Astrophysics* 428.1, pp. 261–285. DOI: `10.1051/0004-6361:20041335`.

Lavorel, S., Díaz, S., Cornelissen, J. H. C., Garnier, E., Harrison, S. P., McIntyre, S., Pausas, J. G., Pérez-Harguindeguy, N., Roumet, C. and Urcelay, C. (2007). 'Plant functional types: are we getting any closer to the Holy Grail?' In: *Terrestrial ecosystems in a changing world*. Springer, pp. 149–164. DOI: `10.1007/978-3-540-32730-1_13`.

Lawson, I., Frogley, M., Bryant, C., Preece, R. and Tzedakis, P. (2004). 'The Lateglacial and Holocene environmental history of the Ioannina basin, north-west Greece'. In: *Quaternary Science Reviews* 23.14-15, pp. 1599–1625. DOI: `10.1016/j.quascirev.2004.02.003`.

Lea, D. W. (2000). 'Climate Impact of Late Quaternary Equatorial Pacific Sea Surface Temperature Variations'. In: *Science* 289.5485, pp. 1719–1724. DOI: `10.1126/science.289.5485.1719`.

Leroy, S., Giralt, S., Francus, P. and Seret, G. (1996). 'The high sensitivity of the palynological record in the Vico maar lacustrine sequence (Latium, Italy) highlights the climatic gradient through Europe for the last 90 ka'. In: *Quaternary Science Reviews* 15.2, pp. 189 –201. ISSN: 0277-3791. DOI: `https://doi.org/10.1016/0277-3791(95)00023-2`.

Lie, Øyvind, Dahl, S. O. and Nesje, A. (2003). 'A theoretical approach to glacier equilibrium-line altitudes using meteorological data and glacier mass-balance records from southern Norway'. In: *The Holocene* 13.3, pp. 365–372. DOI: `10.1191/0959683603hl629rp`.

Lisiecki, L. E. and Raymo, M. E. (2005). ‘A Pliocene-Pleistocene stack of 57 globally distributed benthic δ18O records’. In: *Paleoceanography* 20.1. DOI: `10.1029/2004pa001071`.

Lisiecki, L. E. and Stern, J. V. (2016). ‘Regional and global benthic δ18O stacks for the last glacial cycle’. In: *Paleoceanography* 31.10, pp. 1368–1394. DOI: `10.1002/2016pa003002`.

Ludwig, P., Gavrilov, M. B., Markovic, S. B., Ujvari, G. and Lehmkuhl, F. (2020). ‘Simulated regional dust cycle in the Carpathian Basin and the Adriatic Sea region during the Last Glacial Maximum’. In: *Quaternary International*. DOI: `10.1016/j.quaint.2020.09.048`.

Ludwig, P., Gómez-Navarro, J. J., Pinto, J. G., Raible, C., Wagner, S. and Zorita, E. (2019). ‘Perspectives of regional paleoclimate modeling’. In: *Annals of the New York Academy of Sciences* 1436.1, pp. 54–69. DOI: `10.1111/nyas.13865`.

Ludwig, P., Pinto, J. G., Raible, C. C. and Shao, Y. (2017). ‘Impacts of surface boundary conditions on regional climate model simulations of European climate during the Last Glacial Maximum’. In: *Geophysical Research Letters* 44.10, pp. 5086–5095. DOI: `10.1002/2017gl073622`.

Ludwig, P., Schaffernicht, E. J., Shao, Y. and Pinto, J. G. (2016). ‘Regional atmospheric circulation over Europe during the Last Glacial Maximum and its links to precipitation’. In: *Journal of Geophysical Research: Atmospheres* 121.5, pp. 2130–2145. DOI: `10.1002/2015jd024444`.

Ludwig, P., Shao, Y., Kehl, M. and Weniger, G.-C. (2018). ‘The Last Glacial Maximum and Heinrich event I on the Iberian Peninsula: A regional climate modelling study for understanding human settlement patterns’. In: *Global and Planetary Change* 170, pp. 34–47. DOI: `10.1016/j.gloplacha.2018.08.006`.

Luetscher, M., Boch, R., Sodemann, H., Spötl, C., Cheng, H., Edwards, R. L., Frisia, S., Hof, F. and Müller, W. (2015). ‘North Atlantic storm track changes during the Last Glacial Maximum recorded by Alpine speleothems’. In: *Nature Communications* 6, p. 6344. DOI: `10.1038/ncomms7344`.

Lézine, A.-M. et al. (2010). ‘Lake Ohrid, Albania, provides an exceptional multi-proxy record of environmental changes during the last glacial–interglacial cycle’. In: *Palaeogeography, Palaeoclimatology, Palaeoecology* 287.1, pp. 116 –127. ISSN: 0031-0182. DOI: `10.1016/j.palaeo.2010.01.016`.

Magyari, E. K., Veres, D, Wennrich, V, Wagner, B, Braun, M, Jakab, G, Karátson, D, Pál, Z, Ferenczy, G., St-Onge, G et al. (2014). ‘Vegetation and environmental responses to climate forcing during the Last Glacial Maximum and deglaciation in the East Carpathians: attenuated response to maximum cooling and increased biomass burning'. In: *Quaternary Science Reviews* 106, pp. 278–298. DOI: `10.1016/j.quascirev.2014.09.015`.

Martínez, I., Keigwin, L., Barrows, T. T., Yokoyama, Y. and Southon, J. (2003). 'La Niña-like conditions in the eastern equatorial Pacific and a stronger Choco jet in the northern Andes during the last glaciation'. In: *Paleoceanography* 18.2, n/a–n/a. DOI: `10.1029/2002pa000877`.

Martinson, D. G., Pisias, N. G., Hays, J. D., Imbrie, J., Moore, T. C. and Shackleton, N. J. (1987). 'Age Dating and the Orbital Theory of the Ice Ages: Development of a High-Resolution 0 to 300,000-Year Chronostratigraphy'. In: *Quaternary Research* 27.1, pp. 1–29. DOI: `10.1016/0033-5894(87)90046-9`.

Maselli, V., Hutton, E. W., Kettner, A. J., Syvitski, J. P. and Trincardi, F. (2011). 'High-frequency sea level and sediment supply fluctuations during Termination I: an integrated sequence-stratigraphy and modeling approach from the Adriatic Sea (Central Mediterranean)'. In: *Marine Geology* 287.1-4, pp. 54–70. DOI: `10.1016/j.margeo.2011.06.012`.

Masson-Delmotte, V. et al. (2013). 'Information from paleoclimate archives'. In: *Climate Change 2013: The Physical Science Basis. Contribution of Working Group I to the Fifth Assessment Report of the Intergovernmental Panel on Climate Change*. Ed. by Q. D. Stocker T.F., G.-K. Plattner, M. Tignor, S. Allen, J. Boschung, A. Nauels, Y. Xia, V. Bex and P. Midgley. Cambridge, United Kingdom and New York, NY, USA: Cambridge University Press. DOI: `10.1017/cbo9781107415324.013`.

McCaa, J. R. and Bretherton, C. S. (2004). 'A new parameterization for shallow cumulus convection and its application to marine subtropical cloud-topped boundary layers. Part II: Regional simulations of marine boundary layer clouds'. In: *Monthly weather review* 132.4, pp. 883–896. DOI: `10.1175/1520-0493(2004)132<0883:anpfsc>2.0.co;2`.

Mcgrath, D., Sass, L, O'Neel, S., Arendt, A and Kienholz, C (2017). 'Hypsometric control on glacier mass balance sensitivity in Alaska and northwest Canada'. In: *Earth's Future* 5.3, pp. 324–336. DOI: `10.1038/s41558-018-0093-1`.

Merz, N., Raible, C. C. and Woollings, T. (2015). 'North Atlantic Eddy-Driven Jet in Interglacial and Glacial Winter Climates'. In: *Journal of Climate* 28.10, pp. 3977–3997. DOI: `10.1175/jcli-d-14-00525.1`.

Monegato, G. (2012). 'Local glaciers in the Julian Prealps (NE Italy) during the Last Glacial Maximum'. In: *Alpine and Mediterranean Quaternary* 25.1, pp. 5–14. ISSN: 2279-7335.

Monegato, G., Ravazzi, C., Culiberg, M., Pini, R., Bavec, M., Calderoni, G., Jež, J. and Perego, R. (2015). 'Sedimentary evolution and persistence of open forests between the south-eastern Alpine fringe and the Northern Dinarides during the Last Glacial

Maximum'. In: *Palaeogeography, palaeoclimatology, palaeoecology* 436, pp. 23–40. DOI: `10.1016/j.palaeo.2015.06.025`.

Monegato, G., Ravazzi, C., Donegana, M., Pini, R., Calderoni, G. and Wick, L. (2007). 'Evidence of a two-fold glacial advance during the last glacial maximum in the Tagliamento end moraine system (eastern Alps)'. In: *Quaternary Research* 68.2, pp. 284–302. DOI: `10.1016/j.yqres.2007.07.002`.

Monegato, G., Scardia, G., Hajdas, I., Rizzini, F. and Piccin, A. (2017). 'The Alpine LGM in the boreal ice-sheets game'. In: *Scientific reports* 7.1, p. 2078. DOI: `10.1038/s41598-017-02148-7`.

Neelin, J. D., Bracco, A., Luo, H., McWilliams, J. C. and Meyerson, J. E. (2010). 'Considerations for parameter optimization and sensitivity in climate models'. In: *Proceedings of the National Academy of Sciences* 107.50, pp. 21349–21354. DOI: `10.1073/pnas.1015473107`.

NGRIP (2004). 'High-resolution record of Northern Hemisphere climate extending into the last interglacial period'. In: *Nature* 431, pp. 147–151. DOI: `10.1038/nature02805`.

Oerlemans, J. (1980). 'Model experiments on the 100,000-yr glacial cycle'. In: *Nature* 287.5781, pp. 430–432. DOI: `10.1038/287430a0`.

Ohmura, A. and Boettcher, M. (2018). 'Climate on the equilibrium line altitudes of glaciers: theoretical background behind Ahlmann's P/T diagram'. In: *Journal of Glaciology* 64.245, pp. 489–505. DOI: `https://doi.org/10.1017/jog.2018.41`.

Oleson, K. W., Niu, G.-Y., Yang, Z.-L., Lawrence, D. M., Thornton, P. E., Lawrence, P. J., Stöckli, R., Dickinson, R. E., Bonan, G. B., Levis, S., Dai, A. and Qian, T. (2008). 'Improvements to the Community Land Model and their impact on the hydrological cycle'. In: *Journal of Geophysical Research: Biogeosciences* 113.G1, n/a–n/a. DOI: `10.1029/2007jg000563`.

Oleson, K. W. et al. (2013). *Technical Description of version 4.5 of the Community Land Model (CLM)*. Tech. rep. Boulder, CO: NCAR Technical Note NCAR/TN-503+STR, p. 422. DOI: `10.5065/D6RR1W7M`.

Pal, J. S., Small, E. E. and Eltahir, E. A. (2000). 'Simulation of regional-scale water and energy budgets: Representation of subgrid cloud and precipitation processes within RegCM'. In: *Journal of Geophysical Research: Atmospheres* 105.D24, pp. 29579–29594. DOI: `10.1029/2000jd900415`.

Pavan, V. et al. (2018). 'High resolution climate precipitation analysis for north-central Italy, 1961–2015'. In: *Climate Dynamics* 0.0, pp. 1–19. ISSN: 14320894. DOI: `10.1007/s00382-018-4337-6`.

Peltier, W. and Fairbanks, R. G. (2006). ‘Global glacial ice volume and Last Glacial Maximum duration from an extended Barbados sea level record’. In: *Quaternary Science Reviews* 25.23-24, pp. 3322–3337. DOI: `10.1016/j.quascirev.2006.04.010`.

Penck, A. and Brückner, E. (1909). *Die alpen im Eiszeitalter*. Vol. 3. CH Tauchnitz.

Peyron, O., Guiot, J., Cheddadi, R., Tarasov, P., Reille, M., Beaulieu, J.-L. de, Bottema, S. and Andrieu, V. (1998). ‘Climatic reconstruction in Europe for 18,000 yr BP from pollen data’. In: *Quaternary research* 49.2, pp. 183–196. DOI: `10.1006/qres.1997.1961`.

Pinto, J. G. and Ludwig, P. (2020). ‘Extratropical cyclone characteristics over the North Atlantic and Western Europe during the Last Glacial Maximum’. In: DOI: `10.5194/egusphere-egu2020-6659`.

Pitman, A. L. (2003). ‘The evolution of, and revolution in, land surface schemes designed for climate models’. In: *International Journal of Climatology* 23, pp. 479–510. DOI: `10.1002/joc.893`.

Prömmel, K., Geyer, B., Jones, J. M. and Widmann, M. (2010). ‘Evaluation of the skill and added value of a reanalysis-driven regional simulation for Alpine temperature’. In: *International Journal of Climatology: A Journal of the Royal Meteorological Society* 30.5, pp. 760–773. DOI: `10.1002/joc.1916`.

Antonioli, F and Vai, G. B., eds. (Jan. 2004). *An outline of the flora and vegetation of Adriatic basin (Northern Italy and eastern side of the Apennine) during the Last Glacial Maximum*. Firenze, pp. 15–20.

Ravazzi, C., Badino, F., Marsetti, D., Patera, G. and Reimer, P. J. (2012). ‘Glacial to paraglacial history and forest recovery in the Oglio glacier system (Italian Alps) between 26 and 15 ka cal BP’. In: *Quaternary Science Reviews* 58, pp. 146 –161. ISSN: 0277-3791. DOI: `https://doi.org/10.1016/j.quascirev.2012.10.017`.

Renssen, H, Isarin, R., Jacob, D, Podzun, R and Vandenberghe, J (2001). ‘Simulation of the Younger Dryas climate in Europe using a regional climate model nested in an AGCM: preliminary results’. In: *Global and Planetary Change* 30.1-2, pp. 41–57. DOI: `10.1016/S0921-8181(01)00076-5`.

Ritz, S. P., Stocker, T. F. and Joos, F. (2011). ‘A coupled dynamical ocean–energy balance atmosphere model for paleoclimate studies’. In: *Journal of Climate* 24.2, pp. 349–375. DOI: `10.1175/2010jcli3351.1`.

Roeckner, E, Dümenil, L, Kirk, E, Lunkeit, F, Ponater, M, Rockel, B, Sausen, R and Schlese, U (1989). *The Hamburg version of the ECMWF model (ECHAM)*. Tech. rep. CAS/JSC Working Group on Numerical Experimentation, pp. 7–1.

Russo, E. and Cubasch, U. (2016). 'Mid-to-late Holocene temperature evolution and atmospheric dynamics over Europe in regional model simulations'. In: *Climate of the Past* 12.8, pp. 1645–1662. DOI: `10.5194/cp-12-1645-2016`.

Sadori, L. et al. (2016). 'Pollen-based paleoenvironmental and paleoclimatic change at Lake Ohrid (south-eastern Europe) during the past 500 ka'. In: *Biogeosciences* 13.5, pp. 1423–1437. DOI: `10.5194/bg-13-1423-2016`.

Sarıkaya, M. A., Stepišnik, U., Žebre, M., Çiner, A., Yıldırım, C., Vlahović, I., Tomljenović, B., Matoš, B. and Wilcken, K. M. (2020). 'Last glacial maximum deglaciation of the Southern Velebit Mt. (Croatia): insights from cosmogenic 36Cl dating of Rujanska Kosa'. In: *Mediterranean Geoscience Reviews* 2.1, pp. 53–64. DOI: `10.1007/s42990-020-00030-9`.

Sato, H., Ito, A., Ito, A., Ise, T. and Kato, E. (2015). 'Current status and future of land surface models'. In: *Soil Science and Plant Nutrition* 61, pp. 34–47. DOI: `http://dx.doi.org/10.1080/00380768.2014.917593`.

Schaefer, J. M. (2006). 'Near-Synchronous Interhemispheric Termination of the Last Glacial Maximum in Mid-Latitudes'. In: *Science* 312.5779, pp. 1510–1513. DOI: `10.1126/science.1122872`.

Schaffernicht, E. J., Ludwig, P. and Shao, Y. (2020). 'Linkage between dust cycle and loess of the Last Glacial Maximum in Europe'. In: *Atmospheric Chemistry and Physics* 20.8, pp. 4969–4986. DOI: `10.5194/acp-20-4969-2020`. URL: `https://doi.org/10.5194%2Facp-20-4969-2020`.

Schulzweida, U. (Oct. 2019). *CDO User Guide*. DOI: `10.5281/zenodo.3539275`. URL: `https://doi.org/10.5281/zenodo.3539275`.

Seguinot, J., Ivy-Ochs, S., Jouvet, G., Huss, M., Funk, M. and Preusser, F. (2018). 'Modelling last glacial cycle ice dynamics in the Alps'. In: *The Cryosphere* 12.10, pp. 3265–3285. DOI: `https://doi.org/10.5194/tc-12-3265-2018`.

Shalaby, A., Zakey, A. S., Tawfik, A. B., Solmon, F., Giorgi, F., Stordal, F., Sillman, S., Zaveri, R. A. and Steiner, A. L. (2012). 'Implementation and evaluation of online gas-phase chemistry within a regional climate model (RegCM-CHEM4)'. In: *Geoscientific Model Development* 5.3, pp. 741–760. DOI: `10.5194/gmd-5-741-2012`.

Shi, X. and Lohmann, G. (2016). 'Simulated response of the mid-Holocene Atlantic meridional overturning circulation in ECHAM6-FESOM/MPIOM'. In: *Journal of Geophysical Research: Oceans* 121.8, pp. 6444–6469. DOI: `10.1002/2015jc011584`.

Sirocko, F., Knapp, H., Dreher, F., Förster, M., Albert, J., Brunck, H., Veres, D., Dietrich, S., Zech, M., Hambach, U., Röhner, M., Rudert, S., Schwibus, K., Adams, C. and Sigl, P. (2016). 'The ELSA-Vegetation-Stack: Reconstruction of Landscape Evolution Zones (LEZ) from laminated Eifel maar sediments of the last 60,000years'. In: *Global* *and Planetary Change* 142, pp. 108 –135. ISSN: 0921-8181. DOI: `https://doi.org/10.1016/j.gloplacha.2016.03.005`.

Small, E. E., Sloan, L. C., Hostetler, S. and Giorgi, F. (1999). 'Simulating the water balance of the Aral Sea with a coupled regional climate-lake model'. In: *Journal of Geophysical Research: Atmospheres* 104.D6, pp. 6583–6602. DOI: `10.1029/98jd02348`.

Smiatek, G., Kunstmann, H. and Senatore, A. (2016). 'EURO-CORDEX regional climate model analysis for the Greater Alpine Region: Performance and expected future change'. In: *Journal of Geophysical Research: Atmospheres* 121.13, pp. 7710–7728. DOI: `doi:10.1002/2015JD024727`.

Solmon, F., Giorgi, F. and Liousse, C. (2006). 'Aerosol modelling for regional climate studies: application to anthropogenic particles and evaluation over a European/African domain'. In: *Tellus B* 58.1. DOI: `10.3402/tellusb.v58i1.16792`.

Stevens, B. et al. (2013). 'Atmospheric component of the MPI-M Earth system model: ECHAM6'. In: *Journal of Advances in Modeling Earth Systems* 5.2, pp. 146–172. DOI: `10.1002/jame.20015`.

Strandberg, G., Brandefelt, J., Kjellstro¨ M, E. and Smith, B. (2011). 'High-resolution regional simulation of last glacial maximum climate in Europe'. In: *Tellus A: Dynamic Meteorology and Oceanography* 63.1, pp. 107–125. DOI: `10.1111/j.1600-0870.2010.00485.x`.

Tang, J., Niu, X., Wang, S., Gao, H., Wang, X. and Wu, J. (2016). 'Statistical downscaling and dynamical downscaling of regional climate in China: Present climate evaluations and future climate projections'. In: *Journal of Geophysical Research: Atmospheres* 121.5, pp. 2110–2129. DOI: `https://doi.org/10.1002/2015JD023977`.

Thackray, G. D., Owen, L. A. and Yi, C. (2008). 'Timing and nature of late Quaternary mountain glaciation'. In: *Journal of Quaternary Science: Published for the Quaternary Research Association* 23.6-7, pp. 503–508. DOI: `10.1002/jqs.1225`.

Thum, T, Räisänen, P, Sevanto, S, Tuomi, M., Reick, C, Vesala, T, Raddatz, T, Aalto, T, Järvinen, H, Altimir, N et al. (2011). 'Soil carbon model alternatives for ECHAM5/JSBACH climate model: evaluation and impacts on global carbon cycle estimates'. In: *Journal of Geophysical Research: Biogeosciences* 116.G2. DOI: `10.1029/2010JG001612`.

Tiedtke, M (1996). 'An extension of cloud-radiation parameterization in the ECMWF model: The representation of subgrid-scale variations of optical depth'. In: *Monthly weather review* 124.4, pp. 745–750. DOI: `10.1175/1520-0493(1996)124<0745:aeocrp>2.0.co;2`.

Timmermann, A., Justino, F., Jin, F.-F, Krebs, U. and Goosse, H. (2004). 'Surface temperature control in the North and tropical Pacific during the last glacial maximum'. In: *Climate Dynamics* 23.3-4, pp. 353–370. DOI: 10.1007/s00382-004-0434-9.

Tintor, W (2005). *Zum Spätglazial in den nördlichen Tälern der italienischen Julischen Alpen*. na.

Torma, C., Giorgi, F. and Coppola, E. (2015). 'Added value of regional climate modeling over areas characterized by complex terrain-Precipitation over the Alps'. In: *Journal of Geophysical Research: Atmospheres* 120.9, pp. 3957–3972. DOI: 10.1002/2014jd022781.

Trincardi, F., Cattaneo, A., Asioli, A., Correggiari, A. and Langone, L. (1996). 'Stratigraphy of the late-Quaternary deposits in the central Adriatic basin and the record of short-term climatic events'. In: *Memorie-Istituto Italiano di Idrobiologia* 55, pp. 39–70.

Turuncoglu, U. U., Dalfes, N., Murphy, S. and DeLuca, C. (2013). 'Toward self-describing and workflow integrated Earth system models: A coupled atmosphere-ocean modeling system application'. In: *Environmental Modelling & Software* 39, pp. 247–262. DOI: 10.1016/j.envsoft.2012.02.013.

Tzedakis, P. (2005). 'Towards an understanding of the response of southern European vegetation to orbital and suborbital climate variability'. In: *Quaternary Science Reviews* 24.14-15, pp. 1585–1599. DOI: 10.1016/j.quascirev.2004.11.012.

van Husen, D. (2000). 'Geological processes during the Quaternary'. In: *Mitteilungen der Österreichischen Geologischen Gesellschaft* 92.1999, pp. 135–156.

Van Vuuren, D. P., Edmonds, J., Kainuma, M., Riahi, K., Thomson, A., Hibbard, K., Hurtt, G. C., Kram, T., Krey, V., Lamarque, J.-F. et al. (2011). 'The representative concentration pathways: an overview'. In: *Climatic change* 109.1-2, p. 5.

Voelker, A. H. L., Sarnthein, M., Grootes, P. M., Erlenkeuser, H., Laj, C., Mazaud, A., Nadeau, M.-J. and Schleicher, M. (1998). 'Correlation of Marine 14C Ages from the Nordic Seas with the GISP2 Isotope Record: Implications for 14C Calibration Beyond 25 ka BP'. In: *Radiocarbon* 40.1, pp. 517–534. DOI: 10.1017/s0033822200018397.

Wake, L. and Marshall, S. (2015). 'Assessment of current methods of positive degree-day calculation using in situ observations from glaciated regions'. In: *Journal of Glaciology* 61.226, pp. 329–344. DOI: 10.3189/2015jog14j116.

Watts, W., Allen, J. and Huntley, B (1996). 'Vegetation history and palaeoclimate of the last glacial period at Lago Grande di Monticchio, southern Italy'. In: *Quaternary Science Reviews* 15.2-3, pp. 133–153. DOI: 10.1016/0277-3791(95)00093-3.

Wilson, M., Henderson-Sellers, A, Dickinson, R. E. and Kennedy, P. (1987). ‘Sensitivity of the Biosphere–Atmosphere Transfer Scheme (BATS) to the inclusion of variable soil characteristics’. In: *Journal of Climate and Applied Meteorology* 26.3, pp. 341–362.

Wirsig, C., Zasadni, J., Christl, M., Akçar, N. and Ivy-Ochs, S. (2016). ‘Dating the onset of LGM ice surface lowering in the High Alps’. In: *Quaternary Science Reviews* 143, pp. 37–50. DOI: `10.1016/j.quascirev.2016.05.001`.

Wu, H., Guiot, J., Brewer, S. and Guo, Z. (2007). ‘Climatic changes in Eurasia and Africa at the last glacial maximum and mid-Holocene: reconstruction from pollen data using inverse vegetation modelling’. In: *Climate Dynamics* 29.2-3, pp. 211–229. DOI: `10.1007/s00382-007-0231-3`.

Yokoyama, Y., Lambeck, K., De Deckker, P., Johnston, P. and Fifield, L. K. (2000). ‘Timing of the Last Glacial Maximum from observed sea-level minima’. In: *Nature* 406.6797, pp. 713–716. DOI: `10.1038/35021035`.

Yokoyama, Y. et al. (2018). ‘Rapid glaciation and a two-step sea level plunge into the Last Glacial Maximum’. In: *Nature* 559.7715, pp. 603–607. DOI: `10.1038/s41586-018-0335-4`.

Zakey, A. S., Solmon, F. and Giorgi, F. (2006). ‘Implementation and testing of a desert dust module in a regional climate model’. In: *Atmospheric Chemistry and Physics* 6.12, pp. 4687–4704. DOI: `10.5194/acp-6-4687-2006`.

Žebre, M., Colucci, R. R., Giorgi, F., Glasser, N. F., Racoviteanu, A. E. and Del Gobbo, C. (2020). ‘200 years of equilibrium-line altitude variability across the European Alps (19012100)’. In: *Climate Dynamics*, pp. 1432–0894. DOI: `10.1007/s00382-020-05525-7`.

Žebre, M., Stepišnik, U. and Kodelja, B. (2014). ‘Traces of Pleistocene glaciation on Trnovski Gozd’. In: *Dela* 0.39, p. 157. DOI: `10.4312/dela.39.9.157-170`.

Zemp, M., Paul, F., Hoelzle, M. and Haeberli, W. (2008). ‘Glacier fluctuations in the European Alps, 1850–2000’. In: *Darkening Peaks Glacier Retreat Sci. Soc.*

Zickfeld, K., Eby, M., Weaver, A. J., Alexander, K., Crespin, E., Edwards, N. R., Eliseev, A. V., Feulner, G., Fichefet, T., Forest, C. E. et al. (2013). ‘Long-term climate change commitment and reversibility: an EMIC intercomparison’. In: *Journal of Climate* 26.16, pp. 5782–5809. DOI: `10.1175/JCLI-D-12-00584.1`.